# LABORATORY ELECTRICAL DC RESISTIVITY OF SERPENTINITE, GRAPHITE, OXIDE AND SULFIDE MINERALS

THAMARA JULIA DA CRUZ SATURNINO

A THESIS SUBMITTED TO THE FACULTY OF GRADUATE STUDIES IN PARTIAL FULFILLMENT OF THE REQUIREMENTS FOR THE DEGREE OF MASTER OF SCIENCE

GRADUATE PROGRAM IN EARTH AND SPACE SCIENCE
YORK UNIVERSITY
TORONTO, ONTARIO

December 2019

# Abstract

Radar remote sensing and Ground Penetrating Radar (GPR) are effective techniques for geological subsurface investigations. Planetary missions, such as Apollo-17 and Chang'e-3, have used GPR as a tool for investigating the Earth's moon surface. Electrical DC resistivity of chalcopyrite, galena, graphite, hematite, ilmenite, magnetite, pyrite, pyrrhotite and serpentinite was assessed using a Cryogen-Free Measurement System (CFMS) over a temperature range of 10K-300K. The objective of this work is to contribute to radar and Ground Penetrating Radar sensing data interpretation as electrical DC conductivity (or its inverse, resistivity) is related to radar signal loss. The samples were characterized by analyzing the hand specimens and by using a petrographic microscope. Semi quantitative chemical composition has been assessed by using a Scanning Electronic Microscope (SEM) attached to an Electron Dispersive Spectroscopy detector (EDS). Linear regression was executed for understanding the linearity of the relationship between current and voltage. The temperature dependence of resistivity was determined for each sample.

# Acknowledgments

I would like to thank my supervisor Michael Daly for the opportunity and for all the support that made this work possible. I am very thankful for everything you have done.

I am also very grateful for the Planetary Instrumentation Laboratory team at York university for the friendship and assistance. I am especially thankful to Cosette Gilmour, Emmanuel Lalla, James Freemantle, Kristen Cote, Menelaos Konstantinidis and Pamela Such.

I would like to thank my family, from Brazil and Italy, for all the love someone could have and for always being extraordinarily supportive. Thank you, mom and dad, (Maria José de Fatima Da Cruz Saturnino and João Raimundo Saturnino) for everything you sacrificed to make my dreams come true. Thanks to my wonderful partner, Mirco Stella for being tremendously patient and understanding. I love you, my family, more than anything.

# Contents

# List of tables

# List of figures

# 1 Introduction

Radar sensing methods are very functional for observing surface structures, bulk chemical properties, subsurface attributes and contrasting geologic zones (Campbell, 2002). The technique has been previously used for lunar subsurface exploration with the Apollo Lunar Sounder Experiment (ALSE) on board with the Apollo-17 lunar mission, with the objective of detecting subsurface discontinuities and generation of a lunar surface profile (Porcello, et al., 1974). Similarly, the Lunar Penetrating Radar (LPR) in the Chang'e-3 spacecraft, landed in 2013, was used for mapping of lunar regolith and detection of subsurface geologic structures (Fang, et al., 2014). Furthermore, the European Space Agency (ESA) has planned the usage of Ground Penetrating Radar (GPR) on Mars for geological shallow subsurface investigation. The Water Ice Subsurface Deposit Observation on Mars (WISDOM) radar is part of the upcoming 2020 ESA-Roscosmos ExoMars Rover mission.

The intent of this work is to contribute to Ground Penetrating Radar and Radar imaging system data processing and interpretation, since electrical DC conductivity (or its inverse, resistivity) is related to signal loss of these methods, as DC conductivity is associated to complex dielectric permittivity. Nine minerals and one rock sample (serpentinite) were used for electrical Direct Current resistivity assessment. The mineral assemblage consists of graphite (crystalline carbon); oxides: hematite ($Fe_2O_3$ – iron oxide), ilmenite ($FeTiO_3$ – iron titanium oxide), magnetite and magnetite lodestone ($Fe_3O_4$ - iron oxide); and sulfides: chalcopyrite ($CuFeS_2$ – copper iron sulfide), galena (PbS – lead sulfide), pyrite ($FeS_2$ – iron sulfide), and pyrrhotite ($Fe_{(1-x)}S$ – iron sulfide). The samples were characterized by hand specimen examination and by using a petrographic microscope. Scanning electron microscopy (SEM) coupled to an electron-dispersive X-ray spectrometer (EDS) was used for chemical elements distribution within the samples. Electrical resistivity measurements were executed with the Cryogen-Free Measurement System (CFMS) over a temperature range of 10K-300K, with 10K increment. Such low temperatures were selected with the intent that the present study will contribute for future planetary geophysical missions. Planetary surfaces, such as the lunar poles, can reach temperatures as low as 30K (Vasavada, et al., 2012).

## 1.1 Research objectives

The main objective of this work is to elaborate a methodology for performing DC resistance measurements using the Cryogen-free Measurement System (CFMS), by (Cryogenic Ltd, 2014), that it is more appropriate for rock samples.

In addition to that, the intent of this project is to create a database of electrical DC resistivity values of terrestrial samples which could be used to improve Ground Penetrating Radar and Radar sensing data analysis and interpretations.

## 1.2 Electrical resistance, resistivity and conductivity

Electrical resistance (R) is defined as the amount of electric current flow that can pass through a material and it is measured by the ratio between the voltage (V) and current (I) applied to it. This relationship is also known as Ohm's law. The unit for resistance is ohm (Ω). (Daintith, 2010)

$$R = \frac{V}{I}$$

Materials which follow a linear pattern on a voltage versus current graph plot are known as ohmic (Halliday, Resnick, & Krane, 1992). Some materials that are known for not pursuing this characteristic, nonohmic, are light bulb filaments and diodes.

Resistance is associated to the length and cross-sectional area of a given material and can also be expressed as:

$$R = \rho \frac{L}{A}$$

where ρ, resistivity, is a proportionality constant with unit in ohm·meter (Ω·m). Resistivity is an intrinsic property of a material and it is in fact known as specific resistance. (Cutnel & Johnson, 1995) It may be mentioned that resistivity is temperature dependant:

$$\rho = \rho_0[1 + \alpha(T - T_0)]$$

where T is temperature and ρ0 at temperature T0 (Cutnel & Johnson, 1995) (Giancoli, 1988). For metallic conductors, resistivity is proportionality constant to temperature (Ghosh, 2010).

Electrical conductivity (σ), on the other hand, is a property of a material that is defined as the potential to conduct electric current and, consequently, is the inverse of resistivity (Daintith, 2010):

$$\sigma = \frac{1}{\rho}$$

The unit for electrical conductivity is siemens per meter, S·m-1. The materials can be categorized into conductors, semiconductors and dielectrics, according to its conductivity. Conductors are highly conductive as a result of free electrons present on the valence shell. In contrast, dielectrics have very low conductivity as the electrons are strongly attracted to its nucleus (Kumar, 2010).

## 1.3 Radar remote sensing

Radar remote sensing is a technique for surface exploration that uses electromagnetic emission in the microwave range of the spectrum to obtain several information of the target area, such as geometry, roughness and even chemical features. The emitted signal is modified by the target due to its physical properties. The aspects of the target object can be identified according to the characteristics of the reemitted energy, the spectral signature of the object (Elachi, 1988) (Campbell, 2002). Some ground-breaking discoveries were possible as a result of radar remote sensing. To give an instance, volcanic features on Mars and sulfur volcanic activity on Io, Jupiter's moon, were recorded by spaceborne sensors (Elachi, 1988).

The basic constituents of a radar remote sensing structure are illustrated on Figure 1. The transmitter irradiates microwave signals to the surface, which in turn, reflects and/or scatters the energy to the receiver. The signal gathered by the receiver is processed according to the objectives of the surveying. The transmitter/receiver switch (T/R switch) is present in the equipment that carries only one antenna and shifting between transmitting and receiving detector is necessary (Ulaby, 2014).

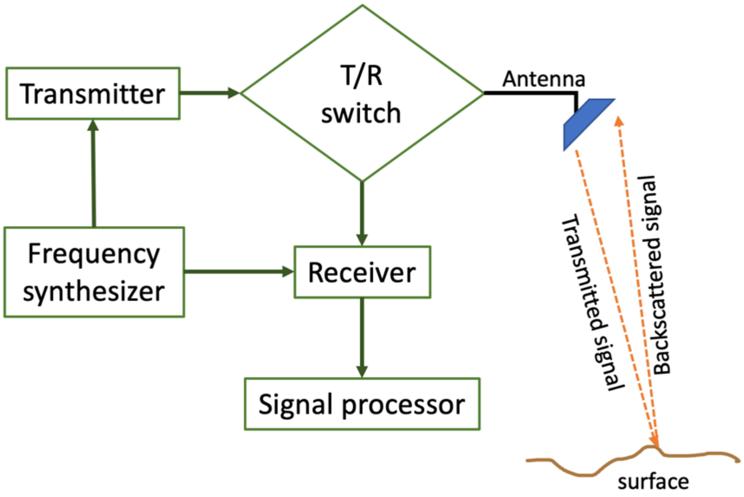

Figure 1: Constituents of a radar remote sensing structure (Modified from Ulaby (2014)).

There are many types of microwave sensors (Figure 2) and these diversifications contribute to the application of these techniques in a complexity of purposes and fields of study. The microwave sensors can be divided into two main groups: passive (also known as radiometers) and active, also called radars. Radiometers are used for thermal emission observations and lack of transmitters, in contrast with radars where a transmitter is used to illuminate the surface to be examined. The two main groups, passive and active sensors, have two categories each: real-aperture and synthetic aperture (Ulaby, 2014). Aperture is a feature, an opening on the antenna, that creates images by the captured signal that is reflected back to it. On radar surveys, the signals can be combined throughout a flight track, to simplify a long antenna. This method is defined as synthetic aperture (Harding Jr, Miller, Swift, & Wright, 2001). Radiometers and sounders are two types of real-aperture passive sensors. Synthetic-aperture passive sensors can be one-dimensional or two-dimensional. Regarding real-aperture radars, they are classified as scatterometers, altimeters, side-looking airborne radars (SLAR) and meteorological radars. Under the synthetic aperture active sensors there are: synthetic-aperture radars (SAR), inverse synthetic-aperture radar (ISAR), and interferometric synthetic-aperture radar (InSAR) (Ulaby, 2014).

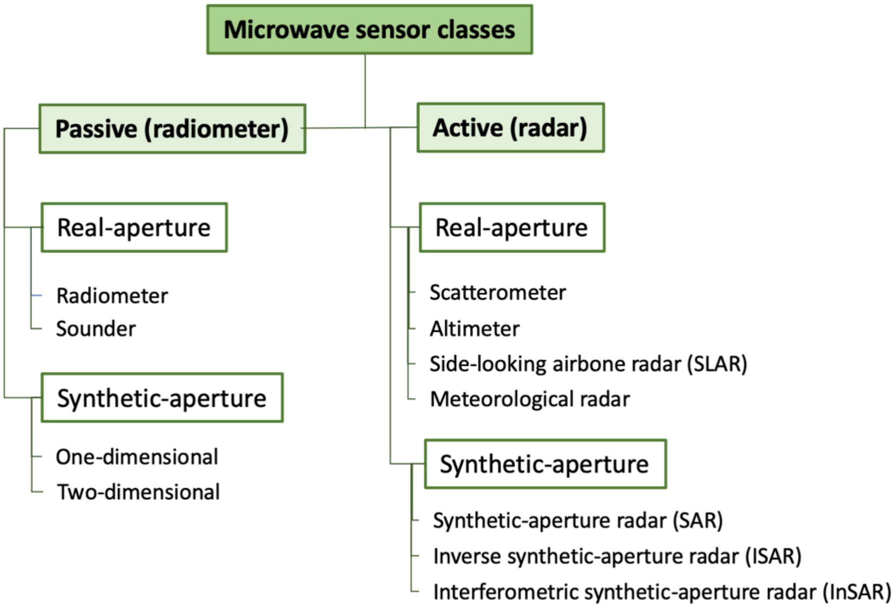

Figure 2: Classification of microwave sensors (Modified from Ulaby (2014)).

## 1.4 Ground penetrating radar

Ground penetrating radar (GPR) is a tool for subsurface exploration with several applications. This method has been used for a variety of study fields, such as agriculture, mining, archeology and civil engineering. (Daniels, 2004) (Persico, 2014). Furthermore, GPR technique has been considered as a potential apparatus for future planetary exploration, more specifically for lunar and Mars surface investigation, on account of its "small size, light weight, high resolution and simple operational system" (Ali & Shieh, 2014). Studies varying antenna settings and heights above the surface to understand how that would impact the data of a GPR mounted on a rover on lunar surface was accessed by (Angelopoulos, Redman, Pollard, Haltigin, & Dietrich, 2014). Targeting Mars inspection, researchers have designed a mini GPR rover (Kim, Carnes, & Ulmer, 2012) intended to contribute for comprehending Mars stratigraphy, that could reveal presence of water-ice layers. Additionally, the inspection would assist to identify the best areas for sampling. The rover has been already tested by the authors in Hawaii at the Kilauea Southwest Rift, a Mars analogue site.

A central unit, two antennas, one transmitting and one receiving, and a computer configure the major elements of a GPR system (Figure 3). An electromagnetic pulse (in the microwave range) is produced by the central unit and the transmitting antenna propagates the electromagnetic waves into the subsurface. The receiving antenna receives the signal reflected by the buried material or discontinuities. A computer allows the user to visualize the data simultaneously while collecting it (Persico, 2014).

Dielectric constant (ε) and the electrical conductivity (σ) of the target area are crucial parameters in GPR surveying as they can determine the penetration range of the experiment. For instance, deeper layers are reached on surfaces with low conductivity and dielectric constant compared to regions of higher dielectric constant and conductivity, because the signal is less attenuated within those conditions allowing the signal to propagate more profound (Schrott, Otto, Götz, & Geilhausen, 2013). Aside from that, the penetration depth is also reliant on the antenna and its applied frequency. The lower the frequency, the deeper the inspection can be. However, lower frequencies also provide lower quality images compared to higher frequencies. Frequencies below 200 MHz are considered low, and over 700MHz up to 3000MHz are defined as high frequencies (Persico, 2014).

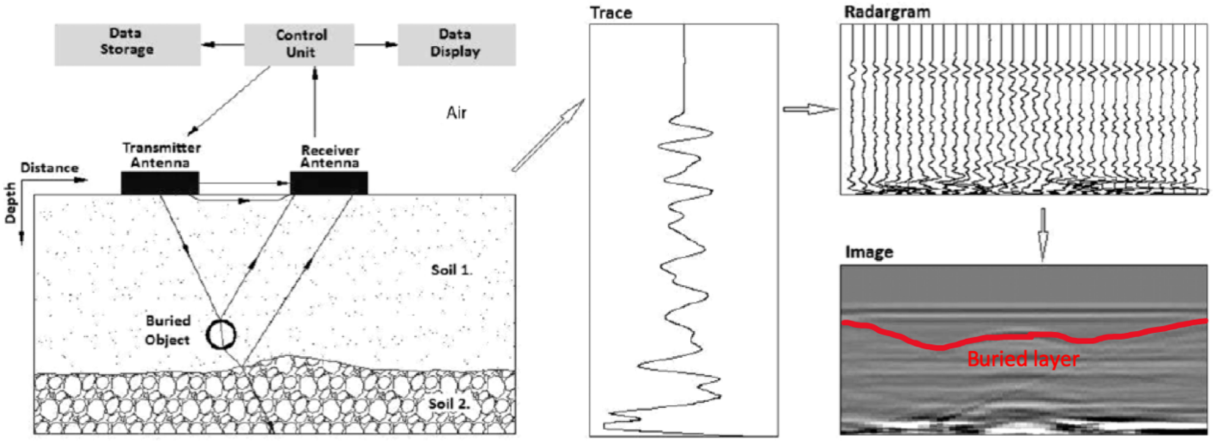

Figure 3: GPR system componentes (Ayala-Cabrera, Herrera, Montalvo, & Pérez-García, 2011).

## 1.5 Application of electrical conductivity in radar and GPR data interpretation

The electric field of the radio waves polarizes the materials it interacts with and induces an electric field within them. These materials can be categorized in conductors or dielectrics where conductors have free charge carriers and allow the currents to penetrate the materials relatively easily while dielectrics have few charge carriers. For dielectric materials the dipole moment is correlated to the total electric field and complex electric susceptibility as shown in the formula (Griffiths, 1981 apud Campbell, 2002):

$$P = \varepsilon_0 \mathcal{X}_e E$$

Where:

P = dipole moment;

E = total electric field;

$\varepsilon_0$ = permittivity of free space = $8.85 \times 10^{-12}$ F/m.

$X_e$= electric susceptibility

The total field can be determined by calculating the electric displacement (D) using the formula (Campbell, 2002):

$$D = \varepsilon_0 E + P = \varepsilon E$$

Where:

$\varepsilon = \varepsilon_0 (1 + \mathcal{X}_e)$ = complex permittivity of the medium.

The ratio between the complex permittivity and permittivity of free space is the dielectric constant (or relative permittivity), $\varepsilon_r$ (Campbell, 2002).

Regarding to the magnetic side of the electromagnetic field we can make an association among the magnetic dipole moment per unit volume, the net field and the dimensionless magnetic susceptibility (Campbell, 2002):

$$M = \mathcal{X}_m H$$

Where:

M = the magnetic dipole moment per unit volume;

H = the net field;

Xm = the magnetic susceptibility.

And the complex permeability is (Campbell, 2002):

$$\mu = \mu_0(1 + \mathcal{X}_m)$$

Where:

$\mu$ = complex permeability;

$\mu_0$ = permeability of free space = $4\pi \times 10^{-7}$ H/m.

Permittivity, permeability and conductivity of a material determine its electromagnetic loss (Boivin, Hickson, Tsai, Ghent, & Daly, 2018). If we break the complex dielectric permittivity and complex magnetic permeability into their real and imaginary parts, where the real part represents the amount of energy that can be stored while the imaginary part expresses the amount of lost energy (Stillman & Olhoeft, 2008), the electrical DC conductivity is associated to complex dielectric permittivity, in its imaginary part as an additional function (Feldman, Gusev, & Vasilyeva, 2012):

$$\frac{\sigma_0}{\varepsilon_0 \omega}$$

Where:

$\sigma_0$ = DC conductivity;

$\omega$ = Angular (radian) frequency.

The depth of penetration of an electromagnetic signal, such as radar and GPR, is defined by the loss tangent ($\delta$) which is also affected by conductivity as expressed in the equation:

$$tan\delta_e = \frac{\varepsilon'' + \frac{\sigma}{\omega\varepsilon_0}}{\varepsilon'_r}$$

Where:

$\delta_e$ = total electrical loss tangent;

$\varepsilon'_r$ = real part of the relative complex permittivity;

$\varepsilon''_r$ = imaginary part of the relative complex permittivity;

The contribution of this work to radar and GPR is to provide electrical resistivity/conductivity of minerals/rocks to be used in signal loss calculations, as conductivity is a parameter that affects loss tangent as shown above. Often when interpreting radar data, assumptions about physical characteristics of the target are made. By knowing values of electrical properties of the target materials these interpretations would be more accurate. Moreover, these measurements were conducted at a very low temperature range (10K to 300K), which could be applied to radar and GPR planetary explorations where such temperatures can be found. Permittivity analysis for application in radar have been previously studied. Assessment of complex permittivity using coaxial airline has been studied for application of radar data interpretation of Near-Eath Asteroids (NEAs). The authors analyzed permittivity of powdered alumina and dunite in correlation to bulk density, using silica aerogel to alter the bulk density (Hickson, et al., 2018). Similarly, Boivin, Hickson, Tsai, Ghent, & Daly (2018) developed a method to measure permittivity of serpentinite blended with carbonaceous materials in different concentration ratios to understand the effects of carbonaceous materials on attenuation of radar signals. The material chosen by the authors is similar in composition to Bennu asteroid's regolith. They used a coaxial transmission airline within 400MHz to 8.5GHz frequency range.

# 2 Experimental apparatus

## 2.1 Petrographic microscope

The mineral samples used in this work have a high purity but mineralogical characterization using a petrographic microscope was still needed. Even though the samples appear to be mostly homogeneous during hand specimen examination, some heterogeneity/impurity could be observed. Impurities can influence the overall electrical resistivity/conductivity of the specimen, so their identification is important for a better understanding of the physical properties of the chosen samples. Furthermore, the petrographic microscope was applied for investigating habit, texture, alteration, size, anisotropy, internal reflections, fracture, cleavage, twinning and other features of the minerals/rock.

The equipment used for petrographic investigation was an Olympus BX-53P (Figure 4) combined with the software package Olympus STREAM for capturing and processing images. The mineral samples are opaque, so they were analyzed under the reflected light while serpentine was examined using the transmitted light. For analyzing under the reflected light, the samples were cut into slabs using an IsoMet Low Speed Cutter and polished using a rotary rock polishing machine (SMART CUT™ LP from UKAM Industrial Superhard Tools). The serpentinite was sent to Vancouver Petrographics Ltd for thin section preparation.

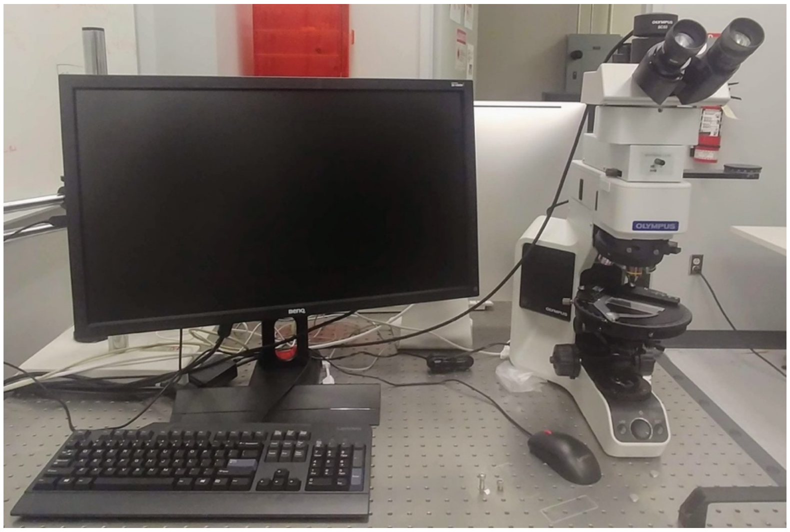

Figure 4: Olympus BX-53P petrographic microscope.

## 2.2 Scanning Electron Microscope (SEM)

Scanning electron microscopy (SEM) was performed at the Planetary Instrumentation Laboratory (PIL, at York University) using a Tescan VEGA3 model (Figure 5) coupled to an electron-dispersive X-ray spectrometer (EDS) and to a back-scattered electron detector (BSE). The BSE component was applied to obtain grey-scale images of the samples. The EDS was used for semi-quantitative chemical composition assessment. An electron beam hits the specimen causing inner shell ionization and causes electronic escaping from inner shells forming a gap where the electron was. Another electron from higher energy shells sometimes replaces the lost electron and emanates X-ray energy. Because these X-rays are specific to each element, it allows us to determine the chemistry of samples (Kuo, 2014). The usage of SEM in this work is valuable even for samples that appear very homogenous on hand specimen examination.

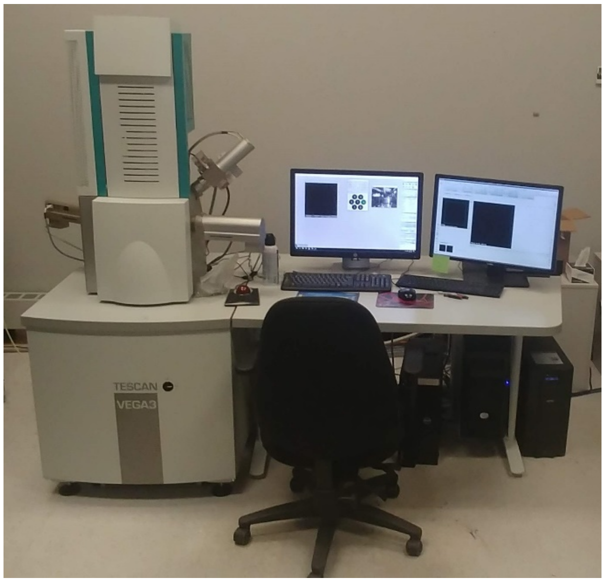

Figure 5: Scanning electron microscope (SEM) at the Planetary Instrumentation Laboratory (PIL, at York University).

## 2.3 Cryogen Free Measurement System

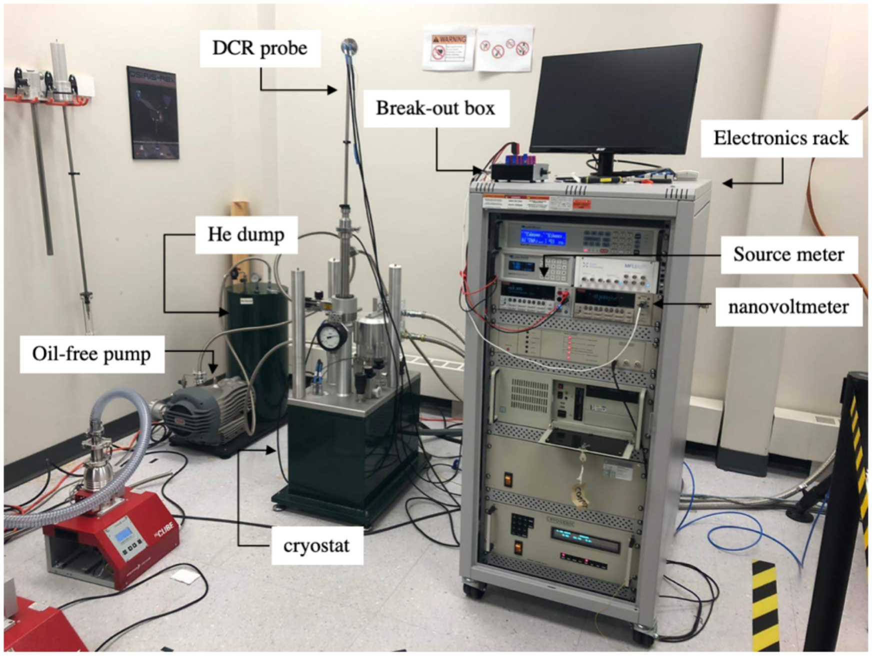

The DC resistance measurements were conducted at PIL by using the Cryogen Free Measurement System (CFMS) (Figure 6). The CFMS allows magnetic and electric measurements in a temperature range from 1.6K to 400K, with standard deviation of 0.3Mk for temperature at 3K and 8.0Mk at 250K, and magnetic fields between 5 and 9T (Cryogenic Ltd, 2014). It is composed by a superconducting magnet with an integrated Variable Temperature Insert (VTI). The machine detects resistance varying from 100 nΩ to 1 GΩ with an accuracy of 0.1% across range of 1Ω to 1MΩ. It has a voltage range capacity of 10 nV to 100 V and current range from 1 nA to 1 A for DC electrical conductivity (Cryogenic Ltd, 2014).

The main components of the CFMS system are: cryocooler, cryostat, superconducting magnets, temperature control of sample, thermometry, electronic rack and software.

There are several magnetic and electric measurements that can be performed using the CFMS and each measurement requires a different probe. The resistivity measurements probe is composed by the probe, sample platform, break-out box and voltage and current meters.

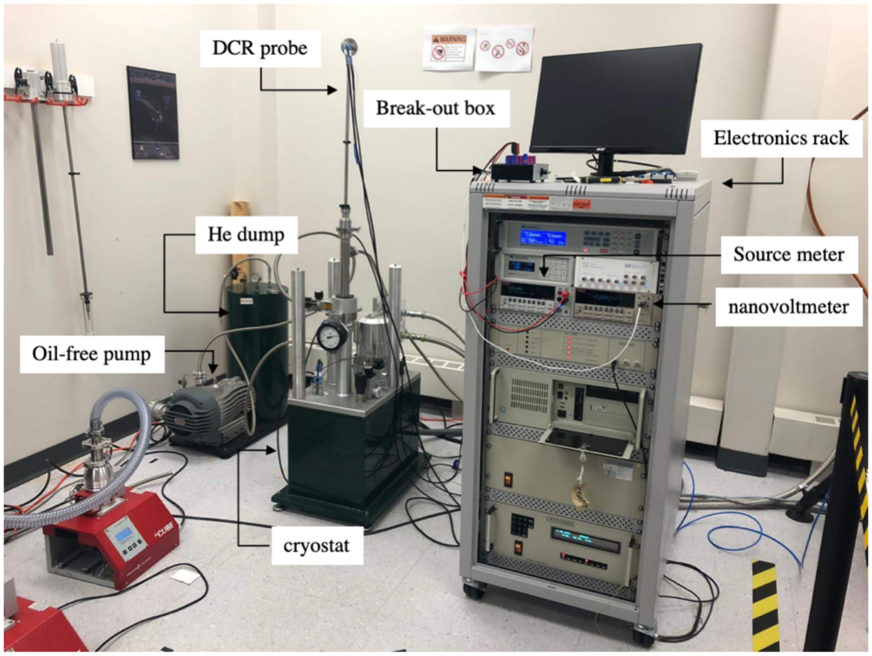

Figure 6: Cryogen Free Measurement System (CFMS).

### *2.3.1 Main components of the CFMS system*

#### *2.3.1.1 Cryocooler system*

The cryocooler system is the part of the equipment that allows the materials to reach cryogenic temperatures. It is composed of a helium compressor, a power source and a cooling water source (Cryogenic Ltd, 2014). The cryocooler used in this project is a Pulse Tube (PT) type model SRP-062 by Sumitomo Heavy Industries Ltd. The cooling is reached by the controlled expansion of the helium gas. The cryocooler is composed by a first and second stage. The first stage cools the radiation shield and pre-cools the circulation helium while the second stage cools the magnet and the variable temperature insert (VTI) (Cryogenic Ltd, 2014).

#### *2.3.1.2 Cryostat*

The cryostat is the vacuum chamber of the system that guarantees thermal protection to the VTI and superconducting magnets (Cryogenic Ltd, 2014). The cryocooler is attached to the cryostat.

#### *2.3.1.3 Superconducting magnets*

The superconducting magnets are copper solenoids positioned vertically and wired with a filament of niobium titanium (NbTi) superconducting wire (Cryogenic Ltd, 2014). Magnetic measurements were not conducted in this work.

#### *2.3.1.4 Temperature control of the sample*

The temperature of the sample is controlled by the variable temperature insert (VTI). The cryogenic temperatures are reached as a result of the low pressure of the VTI and the latent heat of helium vaporisation (Cryogenic Ltd, 2014). The circulation of helium gas in a close circuit allows cooling the VTI and sample. The VTI cooling circuit is represented on Figure 7. The helium is stored in the helium dump at room temperature and pumped into the system by the oil-free pump. The helium flows from the dump to the VTI circuit by the helium gas inlet and it is purified by a charcoal filter. Then the gas is cooled to 40K after passing by the first stage heat exchanger. On the second stage the gas reaches 4K and the condensed gas is accumulated in the helium pot and then it keeps cooling until 1.6K after passing through the needle valve. After that, according to the user's setting for temperature the helium can be warmed by the VTI heat exchanger which passes through the sample at the top of the VTI and flows to the helium dump where the process is reinitiated (Cryogenic Ltd, 2014).

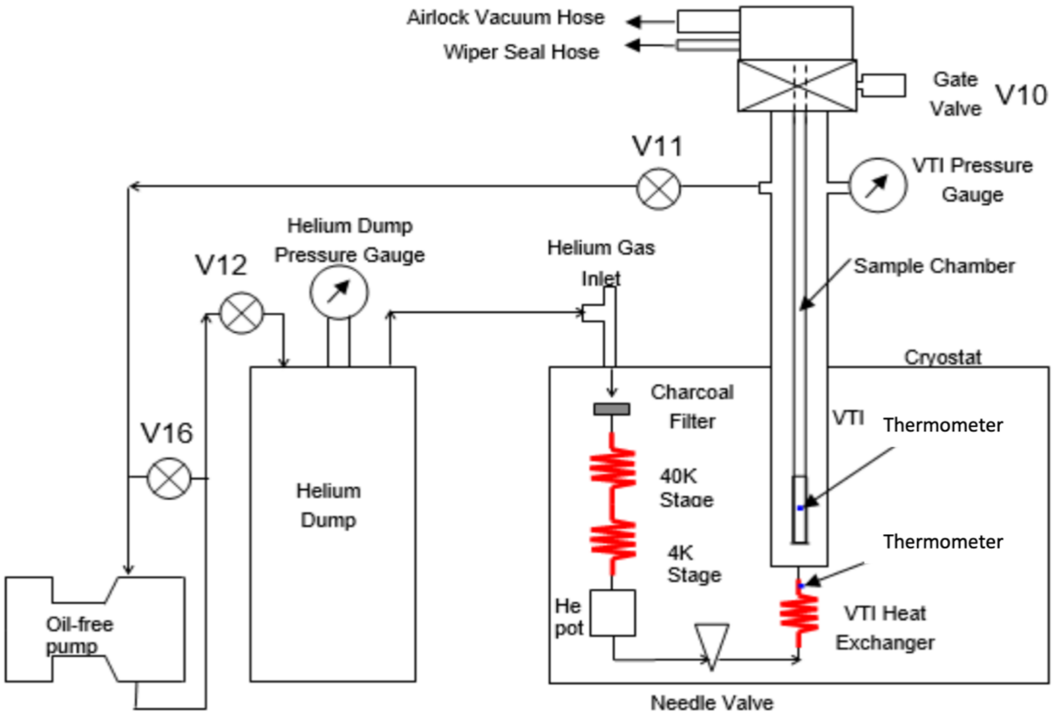

Figure 7: VTI cooling circuit (Modified from Cryogenic Ltd (2014)).

#### 2.3.1.5 *Thermometry*

The CFMS comprises different types of thermometers: carbon ceramic sensors (CCS), Cernox$^{TM}$ and platinum resistance thermometers. The CCS sensitivity increases with the decrease of temperature and it is applied where magnetoresistance is small. The Cernox$^{TM}$ is used at the VIT and on the sample probe, where no sensitivity to magnetic field is important. The platinum resistance thermometers have good sensitivity at high temperature and are applied on the heated probes (Cryogenic Ltd, 2014).

#### 2.3.1.6 *Electronic racks*

The main pieces of the electronics rack are the temperature controller, temperature monitor and magnet power supply. The temperature controller regulates the temperature of the sample, VTI heat exchanger and helium pot. The temperature monitor tracks the different thermometers within the system and reads the hall sensor. The magnet power supply protects and energise the superconducting magnets (Cryogenic Ltd, 2014).

#### *2.3.1.7 Software*

The CFMS can be controlled using the measurement system software. The software also allows the user to choose the type of measurement, load and remove probes, edit a sequence and control the system electronics.

### ***2.3.2 Main components of the resistivity measurements probe***

#### *2.3.2.1 Resistivity probe*

The resistivity probe (Figure 8) is composed by two connectors on the top: one for electrical contact for the heater and thermometer (a 6-pin fischer connector), and one for electrical contact to the samples (a 12-pin fischer connector). The probe is loaded to the system through an airlock and the height is adjusted by a clamp located on the top of the probe. The sample platform is attached at the bottom of the probe (Cryogenic Ltd, 2014).

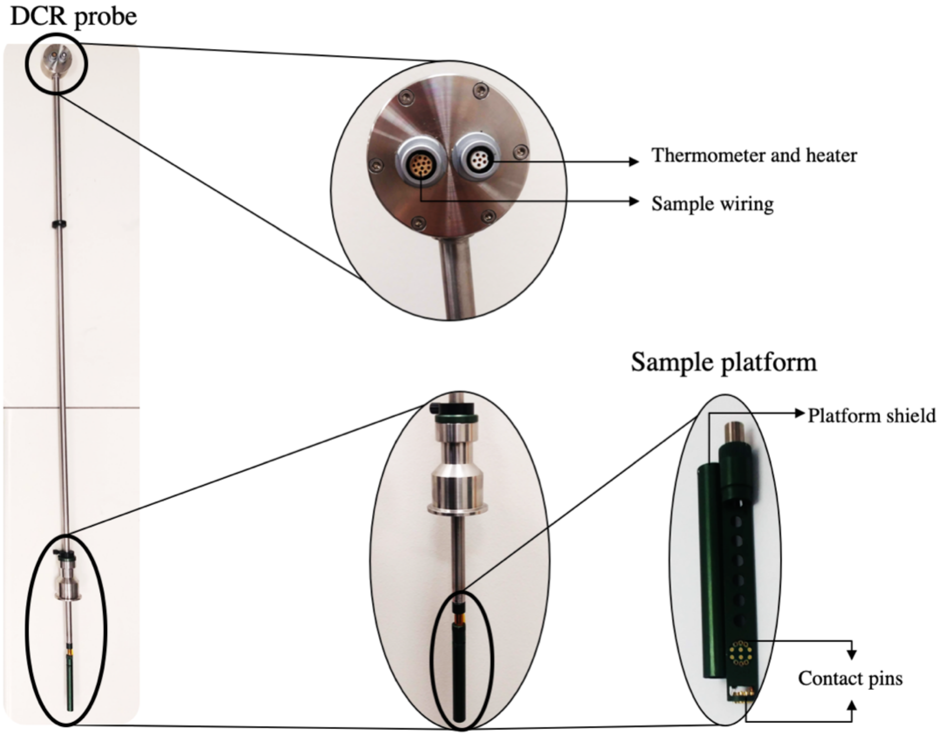

Figure 8: sample probe (Cryogenic Ltd, 2014).

### *2.3.2.2 Sample platform*

The main parts of the sample platform (Figure 9) are a CERNOX$^{TM}$ thermometer, a 100 Ω auxiliary heater and two sample sockets. The sockets are positioned in different directions, one vertical and one horizontal to the platform and probe and each of them has six contacts. These contacts are numbered and correspond to the numbers on the break-out box.

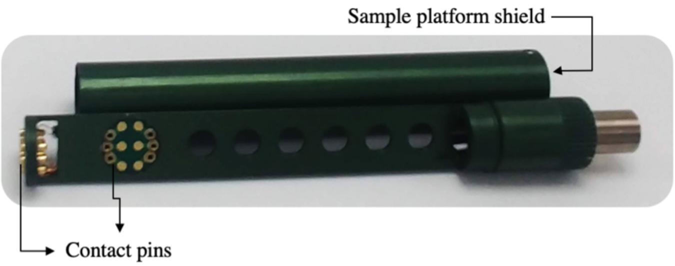

Figure 9: Sample platform with contacts pins.

### *2.3.2.3 Break-out box*

The break-out box (Figure 10) connects the sample to the system and allows current and voltage to be supplied and measured between any numbered contact pins on the sample sockets. The connection points on the break-out box are numbered and correspond to the pins on the sample sockets from the sample platform. The sample platform can also be attached to the break-out box to check electrical connection before starting the measurement (Cryogenic Ltd, 2014).

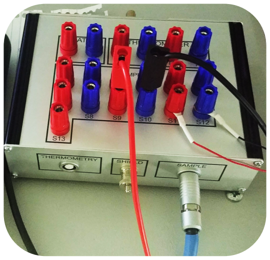

Figure 10: Break-out box.

### *2.3.2.4 Voltage and current meters*

The CFMS is supplied with a Keithley 2400 source meter (Figure 11) and a Keithley 2182A nanovoltmeter (Figure 12) for electrical measurements. The source meter is connected to the break-out box with banana plugs while the nanovoltmeter is connected with a 4-wire cable. This nanovoltmeter comprises 2 sets of 4-wire cable nominated channel-1 and channel-2.

Figure 11: Keithley 2400 source meter.

Figure 12: Keithley 2182A nanovoltmeter.

# 3 Samples

The sample selected for this work consists of nine minerals and one rock, where four of them are classified as sulfides (chalcopyrite, galena, pyrite and pyrrhotite), four as oxides (ilmenite, magnetite, magnetite lodestone and hematite), and one as native element (graphite). The rock chosen is a serpentinite. The minerals were acquired from Ward's Natural Science Establishment, Inc. and the serpentinite was provided by the Royal Ontario Museum (ROM).

## 3.1 Chalcopyrite

### *3.1.1 Hand sample examination*

The chalcopyrite ($CuFeS_2$ – copper iron sulfide), Ward's catalogue number 470025-374, are from Durango, Mexico. The samples are approximately 3cm to 4 cm each and have a brass-yellow color, metallic luster, with some dark-gray mineral association of sphalerite (Figure 13). The samples are slightly weathered characterized by a bronze color. The grains are fine to coarse with a massive texture. The streak has a greenish black color. The sample has no cleavage.

Figure 13: Chalcopyrite hand specimen.

### *3.1.2 Petrography*

Most of the sample, 90%, is composed by chalcopyrite and the other 10% consists of intrusions (Figure 14). Chalcopyrite has a dark yellow color with some brownish spots, typically observed on this mineral. The grains are fine with massive texture. Intrusions of anhedral sphalerite, medium gray color, measuring from approximately 30µm to 1mm in length, were found. Arsenopyrite is also associated to the sample with light gray anhedral crystals, usually around sphalerite, with sizes varying from 20µm to 600µm in lenghth, roughly. Very fine pyroxene trace minerals, 100µm and smaller, black color, were also observed.

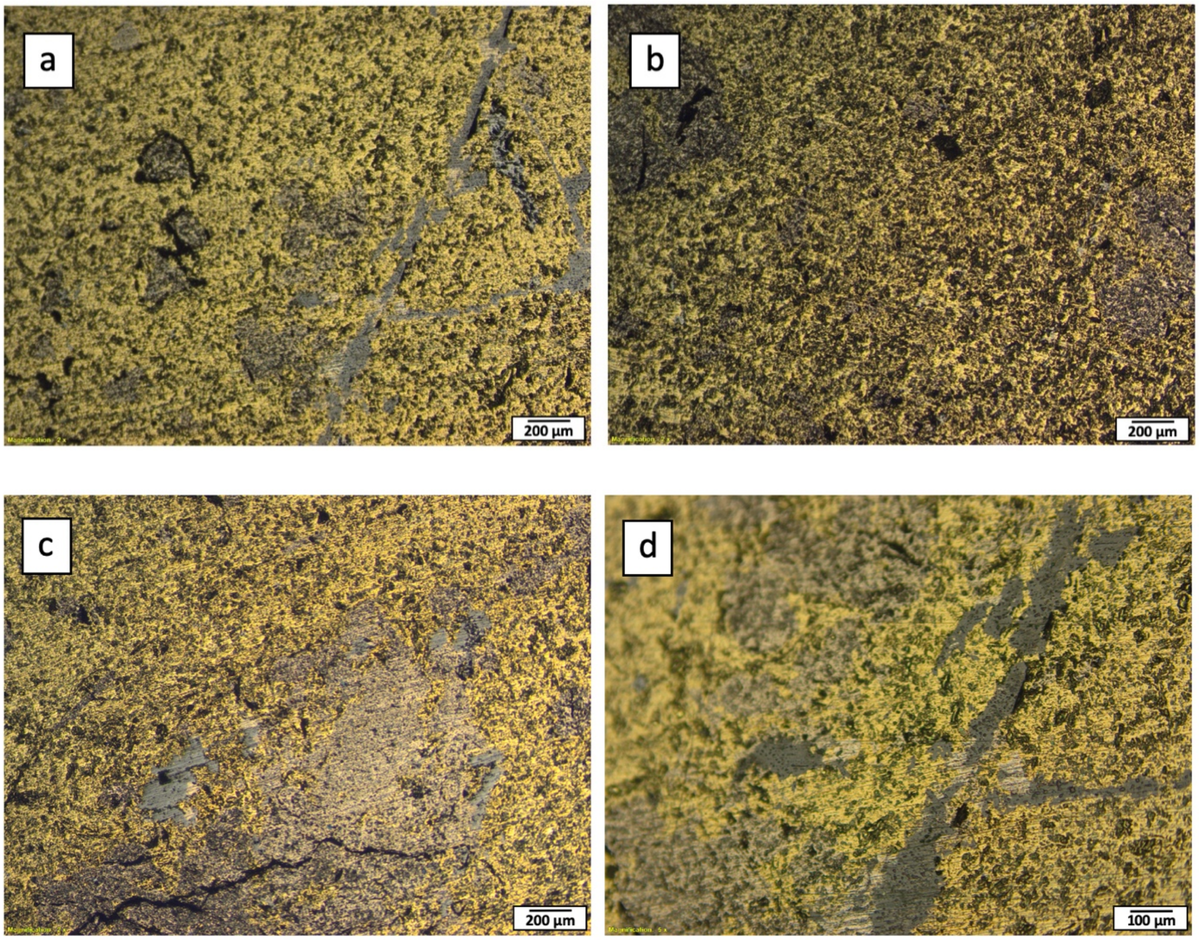

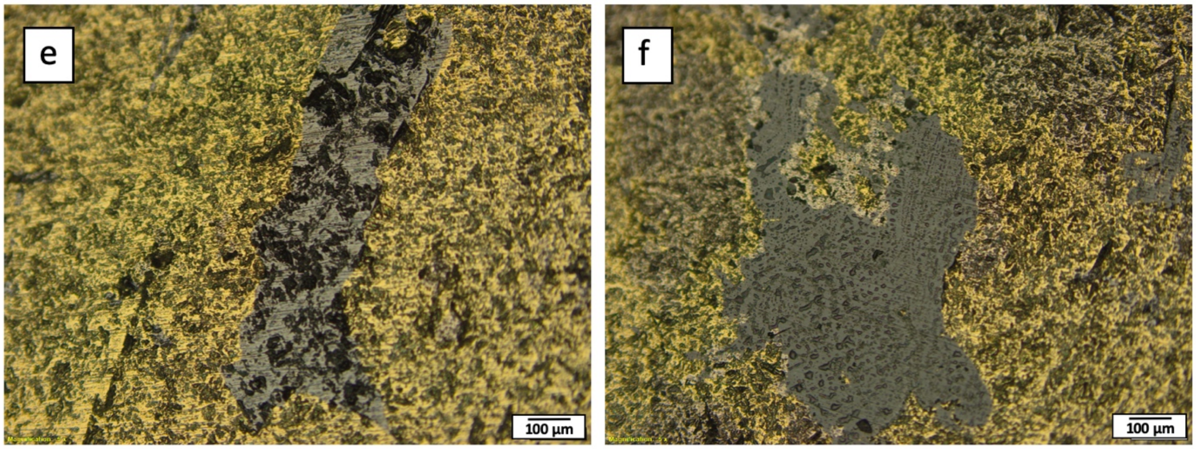

Figure 14: Chalcopyrite under reflected light microscope (a) chalcopyrite (dark yellow), sphalerite (medim gray) and pyroxene minerals (black). Scale bar: 200μm; (b) chalcopyrite with some pyroxene minerals and arsenopyrite intrusions. Scale bar: 200μm; (c) arsenopyrite, sphalerite and opaque minerals intrusions in chalcopyrite. Scale bar: 200μm; (d)sphalerite intrusion with arsenopyrite. Scale bar: 100μm; (e) sphalerite intrusion in chalcopyrite. Scale bar: 100μm; (f) sphalerite (medium gray) intrusion surrounded by arsenopyrite (light gray) in chalcopyrite. Scale bar: 100μm.

## 3.2 Galena

### *3.2.1 Hand sample examination*

The galena samples (PbS – lead sulfide), Ward's catalogue number 479226-330 are from Brushy Creek (Missouri, USA). The samples measure from 2cm to 3 cm (Figure 15) and are composed by over 90% of galena. The mineral has a dark gray color, metallic lust and black streak. The crystals are coarse in a massive texture with perfect cleavage in two directions forming a right angle. Chalcopyrite ($CuFeS_2$) is present in the samples as a mineral association, in brass-yellow color with fine crystals in irregular shape.

Figure 15: Galena hand specimen.

### *3.2.2 Petrography*

Galena is intruded by quartz. Quartz is found in anhedral habit, transparent, with crystals size varying from approximately 25µm to 1mm (Figure 16).

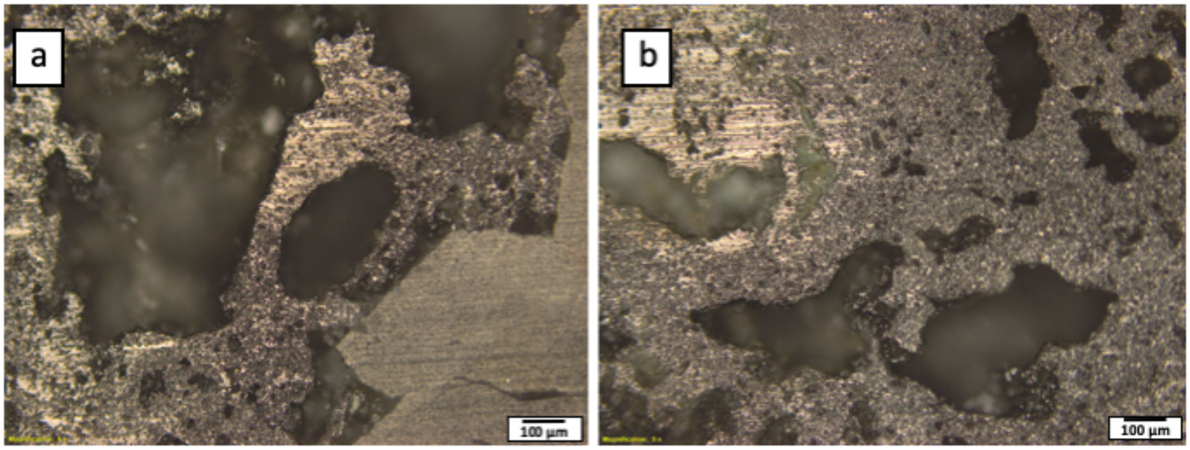

Figure 16: Quartz in galena. (a)(b)Quartz crystals are transparent and anhedral. Scale bar: 100µm

Galena occurs in light grey color with massive texture and showing two directions of cleavage forming a right angle and distinctive triangular pits (Figure 17).

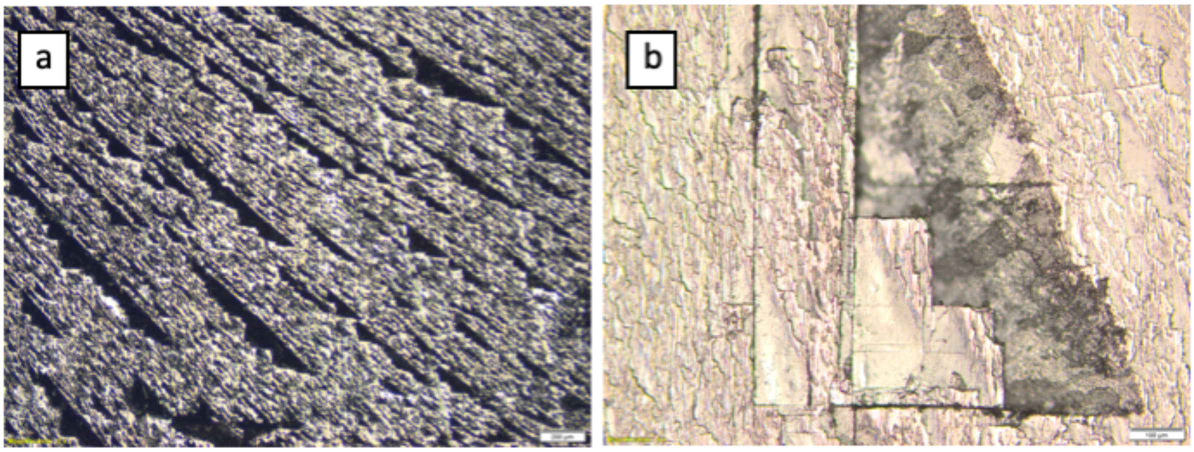

Figure 17: Galena sample under reflected light microscope (a) Galena exhibiting distinctive triangular pits. Scale bar: 200µm; (b) Galena with two cleavage directions forming right angle. Scale bar: 100µm;

## 3.3 Graphite

### *3.3.1 Hand sample examination*

The graphite samples (C - carbon), Ward's catalogue number 470025-594, are from Colombo, Sri Lanka (Figure 18). The specimens are pure and measure from 3cm to 4cm, approximately. The mineral has a dark gray color, black streak, metallic lust and foliated texture. The samples have perfect cleavage on the direction of the foliation. No weathering and mineral associations were observed.

Figure 18: Graphite hand specimen.

### 3.3.2 Petrography

The graphite sample is composed by 100% of graphite (Figure 19). The crystals are very fine, dark gray colored with strong reflection pleochroism varying from white to black. Foliation could not be observed.

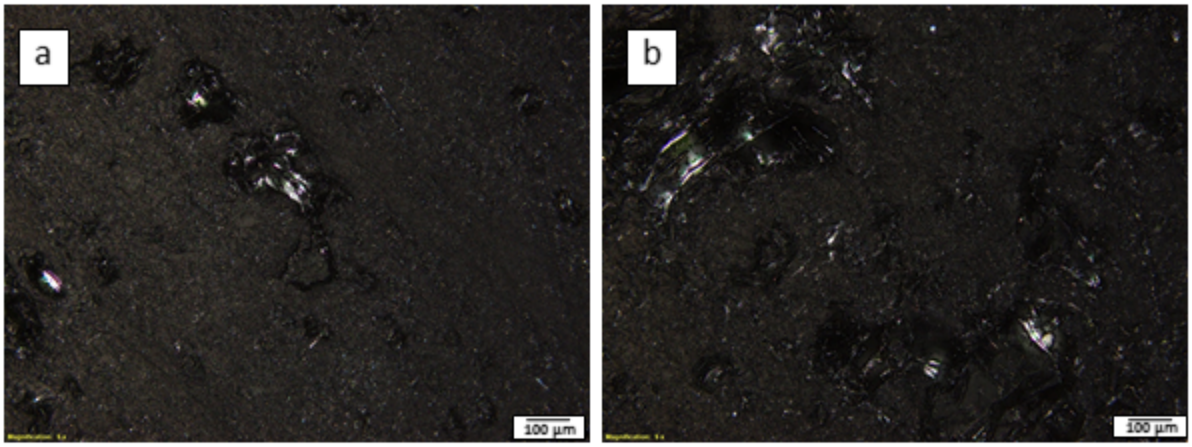

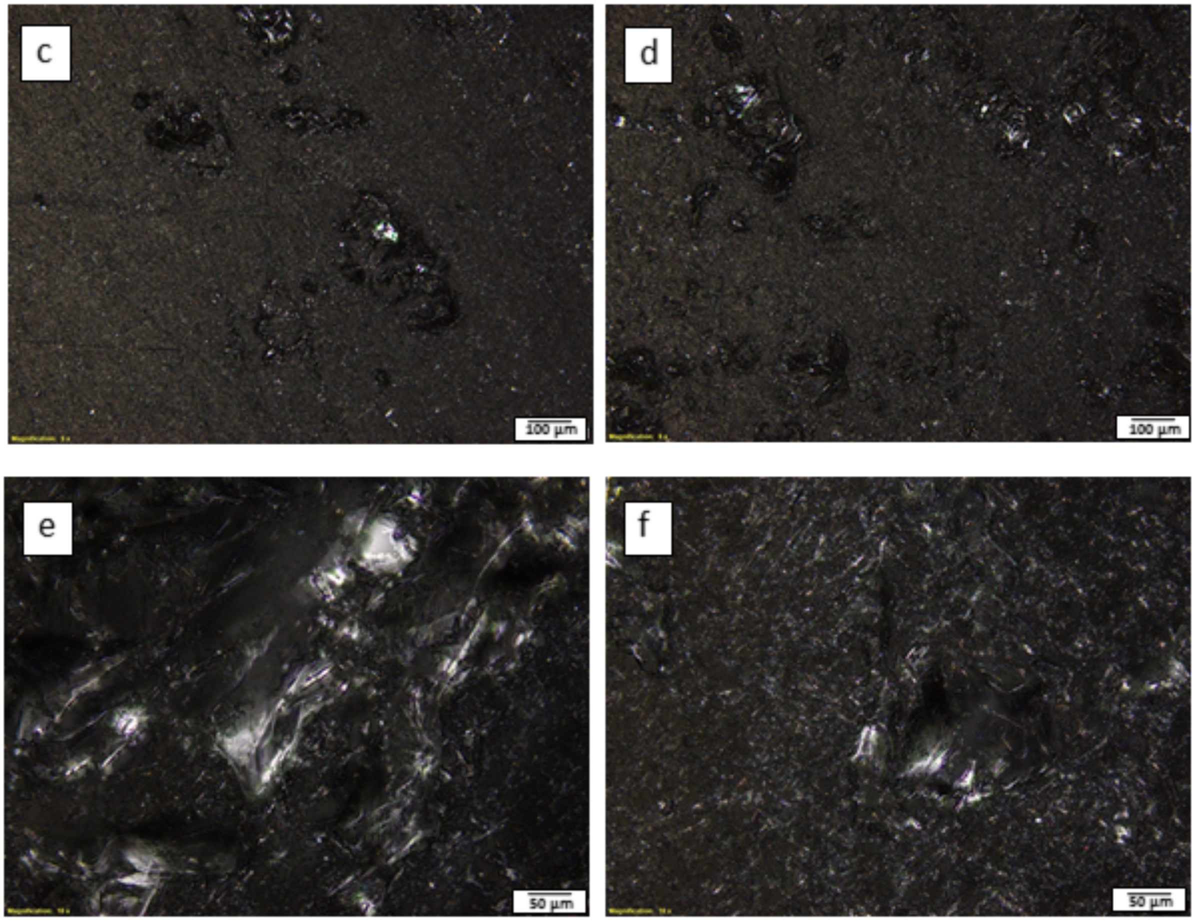

Figure 19: Graphite sample under reflected light microscope (a) Scale bar: 100µm; (b) Scale bar: 100µm; (c) Scale bar: 100µm; (d) Scale bar: 100µm; (e) Scale bar: 50µm; (f) Scale bar: 50µm.

## 3.4 Hematite

### *3.4.1 Hand sample examination*

The hematite ($Fe_2O_3$ – iron oxide) hand samples (Figure 20), Ward's catalogue number 470025-642, are from Republic (Michigan – USA). Hematite is silver-gray colored with splendent lust and bright red streak. It consists of very fine crystals in a micaceous habit. Some red colored spots were observed, which means that the sample is slightly oxidized. The sample is mainly composed by hematite, over 90%, however some fine veins of silica are present in the sample.

Figure 20: Hematite hand specimen.

### *3.4.2 Petrography*

Intrusions of quartz were found in hematite samples (Figure 21). Quartz occur as transparent, subhedral to euhedral phenocrysts. It shows bright internal reflections and some crystals have hematite inclusions. Some of the phenocrysts are relict grains of probably olivine or pyroxene. Quartz grains measure from 20µm to 1mm in length, approximately.

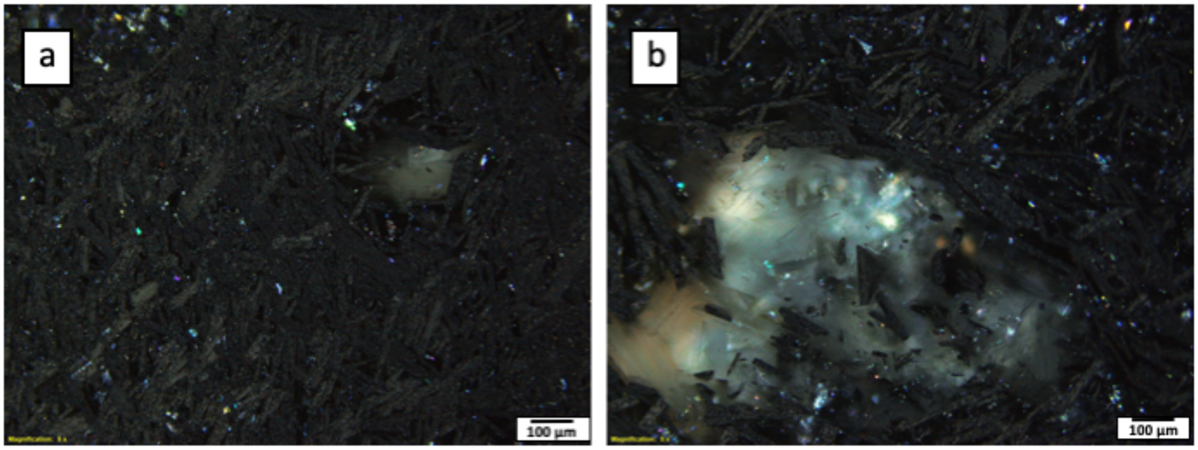

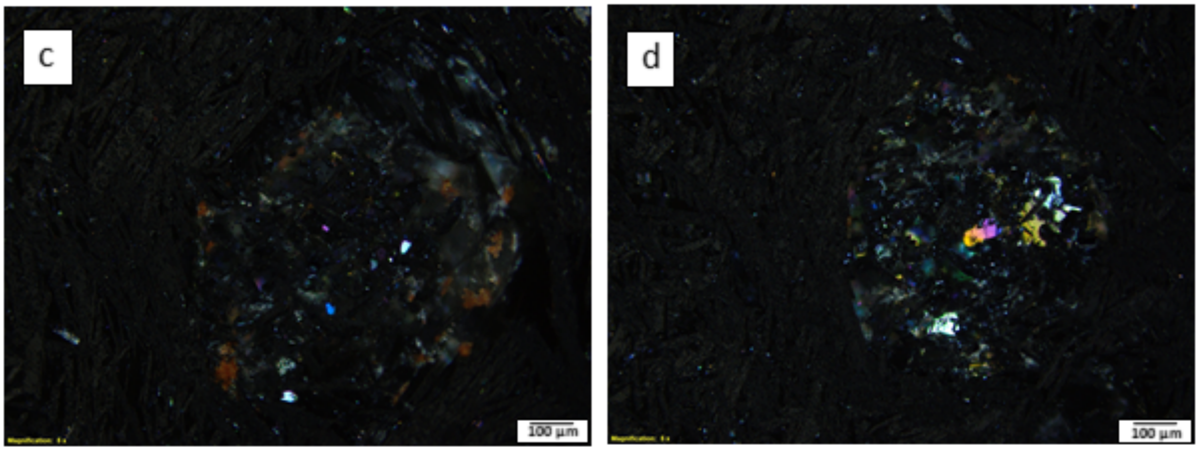

Figure 21: Hematite sample under reflected light microscope. (a)Subhedral quartz in hematite. Scale bar: 100µm; (b) Quartz phanerocrystal in hematite with hematite also occurring as inclusions. Scale bar: 100µm; (c) relict grain of olivine or pyroxene. Scale bar: 100µm; (d) relict grain substituted by silica. Scale bar: 100µm.

By observing the sample under the microscope (Figure 22), the hematite was characterized as part of the matrix of the sample, associated to a translucent iridescent mineral, described in the chalcography section above. Most of the sample, over 90%, is composed by the matrix. Hematite occurs in euhedral micaceous shape and massive texture, with crystals measuring from 50µm to 250µm, approximately.

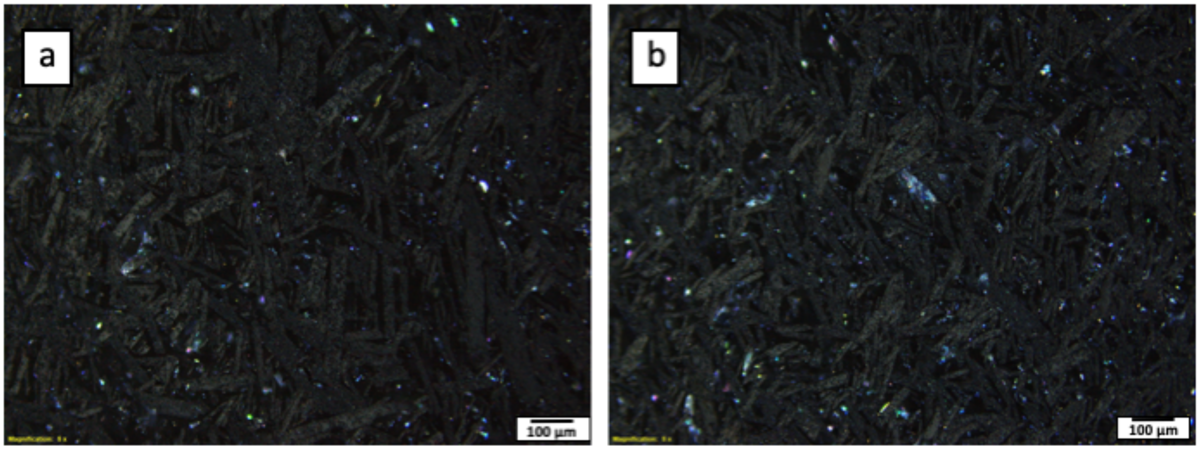

Figure 22: Hematite sample under reflected light microscope. (a)(b) hematite in the matrix. Scale bar: 100μm.

## 3.5 Ilmenite

### *3.5.1 Hand sample examination*

The ilmenite samples ($FeTiO_3$ – iron titanium oxide), Ward's catalogue number 470025-650, are from Saint Urbain-QC, Canada (Figure 23). The hand specimens measure 2cm to 5cm. The mineral has a black color, black streak and metallic lust. The crystals are coarse sized with tabular habit in a massive texture. The samples are slightly weathered characterized by a redish brown color. No cleavage and mineral associations were observed.

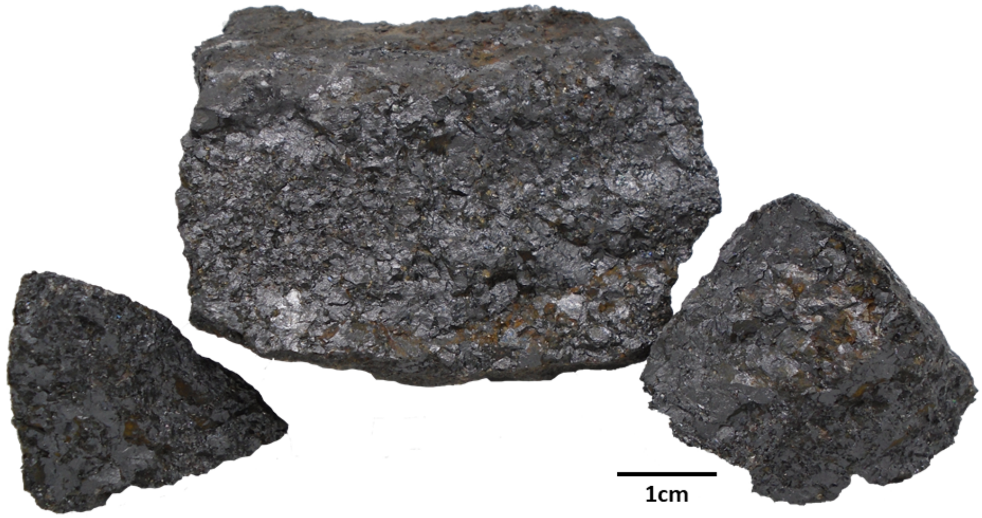

Figure 23: Ilmenite hand specimen.

### *3.5.2 Petrography*

Mineral associations of quartz and rutile were found in ilmenite samples (Figure 24). Quartz occurs with fine to coarse crystals, measuring from 30μm to 1.5mm, roughly. The grains are transparent white in color, exhibiting bright internal reflections. Rutile is also present in the sample with crystal sizes varying from 30μm to 200μm in length. The crystals are dark brown color, associated to chalcopyrite and quartz. It often occurs as veins measuring up to 400 μm in length.

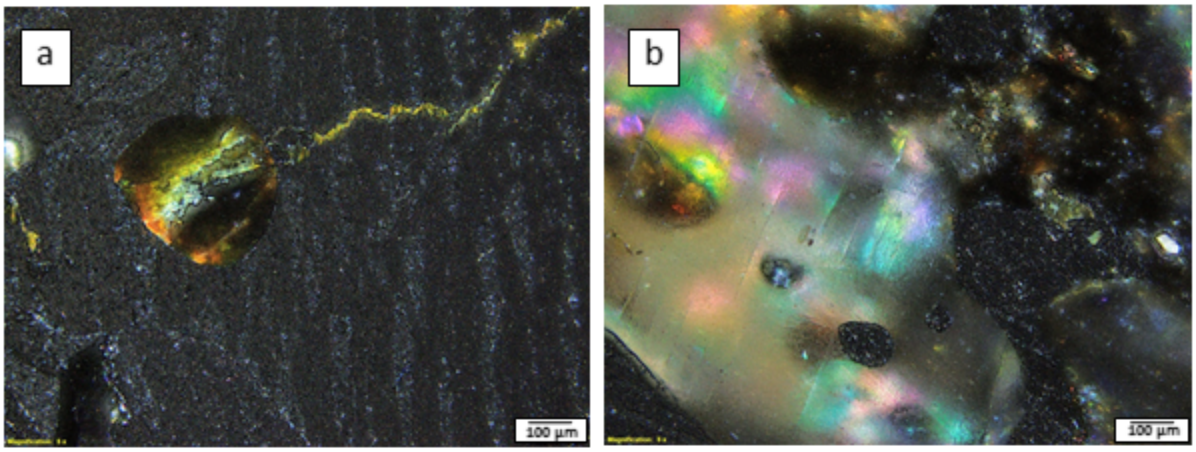

Figure 24: (a) Rutile crystal and vein in ilmenite. Scale bar: 100μm. (b) Quartz in ilmenite. Scale bar: 100μm.

Ilmenite appears in coarse crystals, up to 1.5mm, with anhedral to subhedral shape and dark grey color (Figure 25). Over 90% of the sample is composed by ilmenite. Intrusions of chalcopyrite, brass-yellow, anhedral habit, measuring 100μm to 250μm, are present in the sample. Triple junction of ilmenite was observed with hematite exsolution lamellae (light gray).

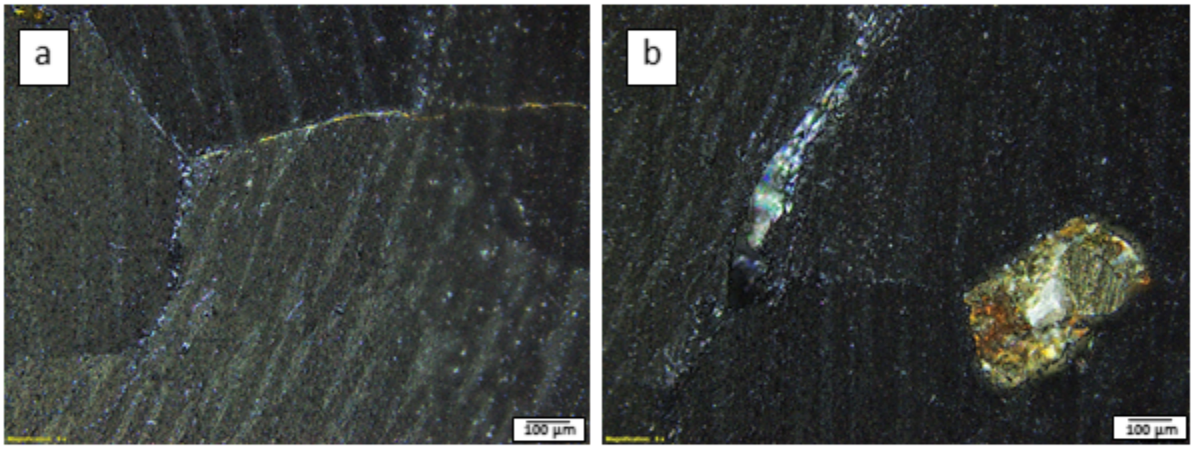

Figure 25: Ilmenite sample under reflected light microscope (a) Triple junction of ilmenite (dark gray) with hematite exsolution lamellae (light gray) Scale bar: 100µm; (b) Chalcopyrite in ilmenite. Scale bar: 100µm.

## 3.6 Magnetite

### *3.6.1 Hand sample examination*

The magnetite samples ($Fe_3O_4$ - iron oxide), Ward's catalogue number 470025-672, are from Ishemig, Michigan, USA (Figure 26). The hand specimens are 2cm to 4 cm wide, have dark gray color, metallic lust and black streak. The crystals are fine and anhedral. Some fine veins of quartz are present in the sample.

Figure 26: Magnetite hand specimen.

### *3.6.2 Petrography*

Quartz grains are present in the magnetite samples (Figure 27). The crystals are fine and with anhedral habit, often showing bright internal reflections. It usually occurs as veins measuring up to 1.6mm in length.

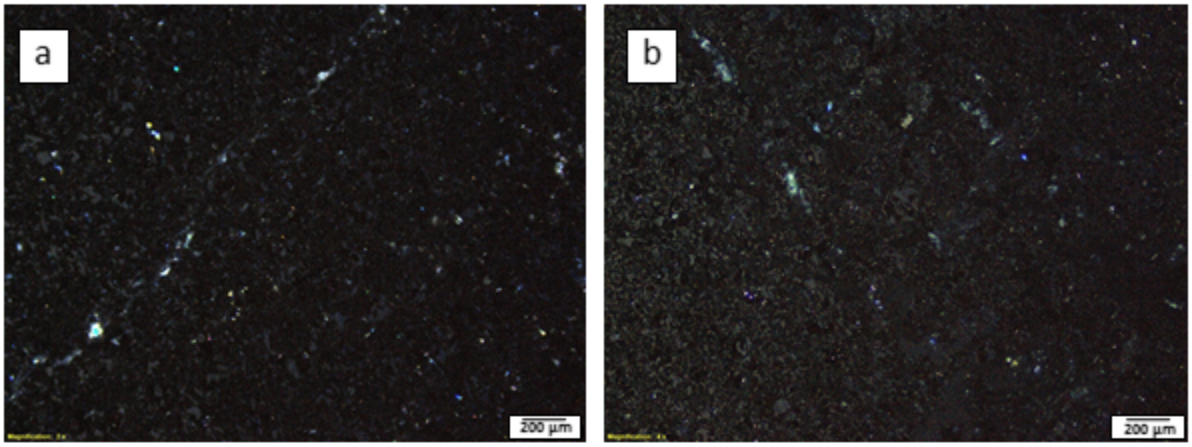

Figure 27: (a)(b) Quartz veins in magnetite. Scale bar: 200µm.

Magnetite occurs in the sample in dark gray fine crystals and anhedral habit (Figure 28). Intrusions of chalcopyrite are present in light yellow, anhedral to subhedral habit and varying from 100µm to 300µm length crystals. Hematite, medium gray color, is also included in the sample with minerals exhibiting anhedral to subhedral habit, measuring from 50µm t0 200µm, approximately.

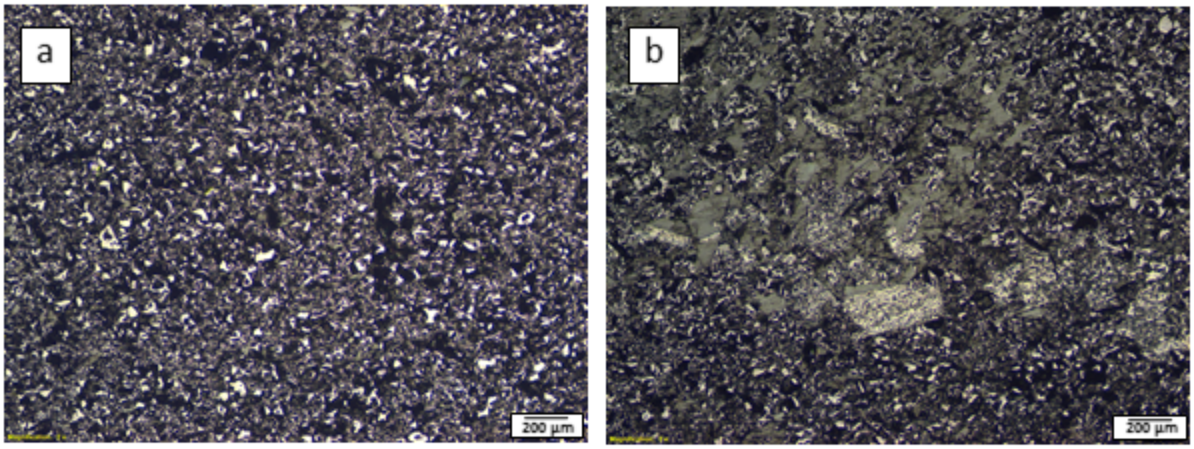

Figure 28: Magnetite sample under reflected light microscope (a) Magnetite dark gray fine crystals and anhedral habit .Scale bar: 200µm; (b)Chalcopyrite and hematite in magnetite Scale bar: 200µm.

## 3.7 Magnetite lodestone

### ***3.7.1 Hand sample examination***

The magnetite lodestone samples ($Fe_3O_4$ - iron oxide), Ward's catalogue number 470025-678, are from Iron Co., Utah, USA (Figure 29). The samples measure from 3cm to 4.5cm wide, approximately. Magnetite lodestone has dark gray color, metallic lust and black streak. The crystals are fine in a massive texture. Sulfide mineral intrusions, dark yellow, anhedral and fine to medium size grains, were observed. Magnetism was observed with some smaller particles of the sample attracted around them.

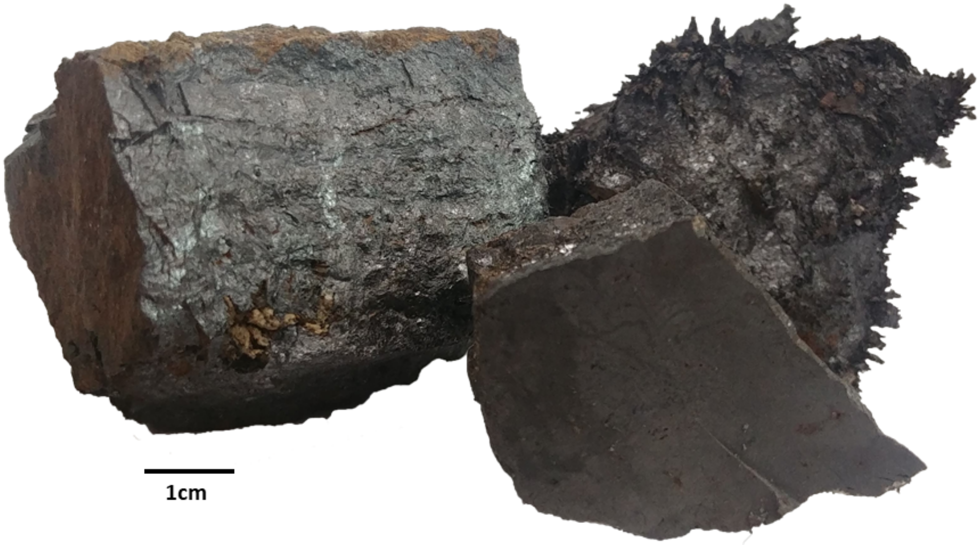

Figure 29: Magnetite lodestone hand specimen.

### *3.7.2 Petrography*

Mineral associations of quartz, realgar and orpiment were found in magnetite lodestone samples (Figure 30). Quartz occurs in anhedral to subhedral grains in transparent to milky white color. The crystals measrure from 10µm to 200µm, approximately, and some of them are elongated. Realgar, brownish red, occurs associated to orpiment, orange. Realgar and orpiment crystals have anhedral to subhedral shape, with sizes varying from 10µm to 500µm, often surrounding or surrounded by quartz. Some realgar crystals were crystalized in veins.

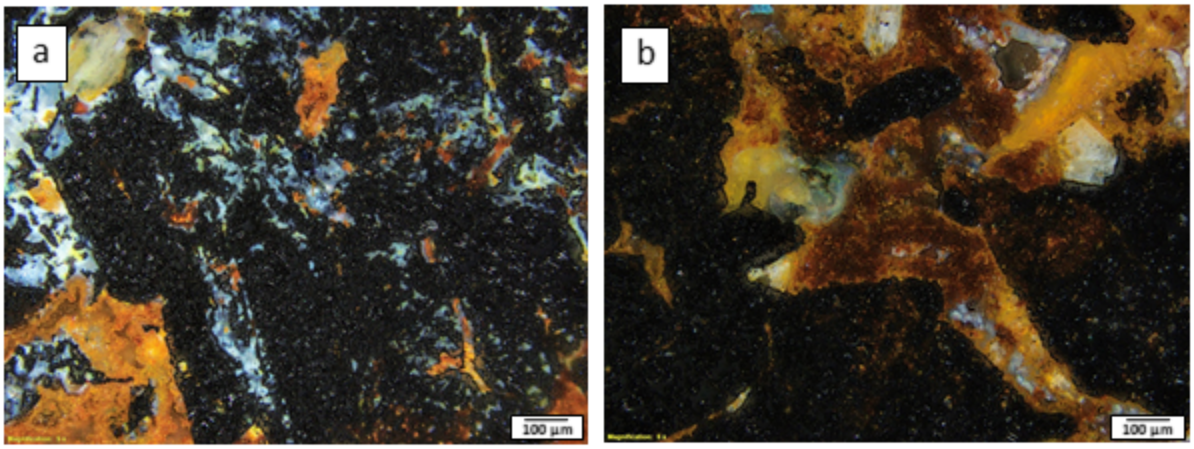

Figure 30: (a) (b) Quartz, realgar and orpiment in magnetite lodestone. Scale bar: 100µm;

Magnetite lodestone occur in very Fine crystals in dark black color and anhedral habit and high relief (Figure 31).

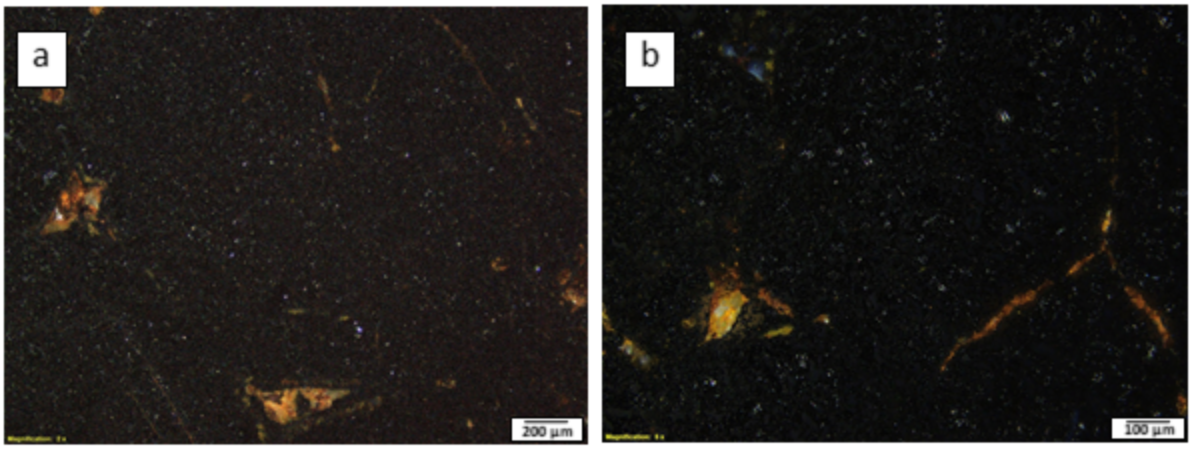

Figure 31: Magnetite lodestone sample under reflected light microscope (a) Scale bar: 200µm; (b) Scale bar: 100µm.

## 3.8 Pyrite

### 3.8.1 *Hand sample examination*

The pyrite hand specimens ($FeS_2$ – iron sulfide), Ward's catalogue number 470154-900, are from Navajun, Spain (Figure 32). The samples are approximately 2cm wide, are pure cubic crystals with penetration twinning. The minerals have brass yellow color, metallic luster and black streak. Medium size white and transparent crystals of quartz inclusions were observed on pyrite slabs.

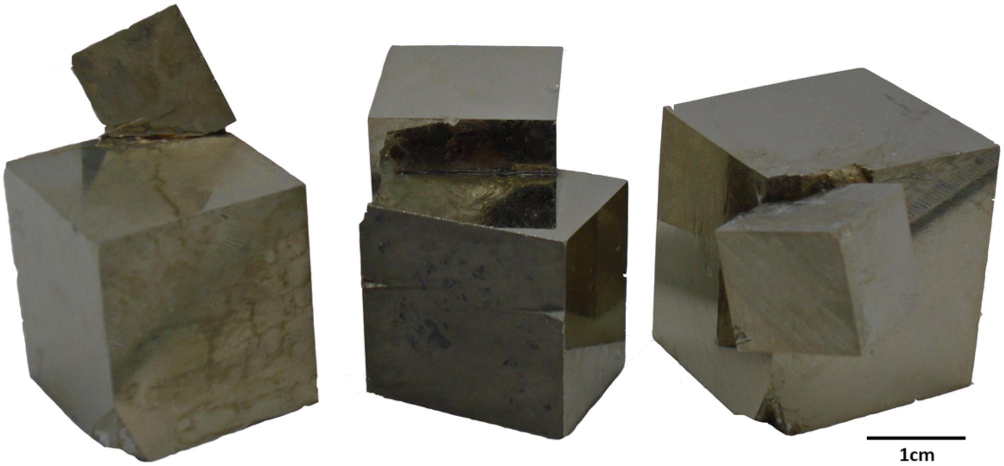

Figure 32: Pyrite hand specimen.

### 3.8.2 *Petrography*

Quartz inclusions were observed in pyrite samples (Figure 33). Quartz occurs in transparent anhedral crystals, measuring from 20μm to 2.5mm, approximately, show bright internal reflections.

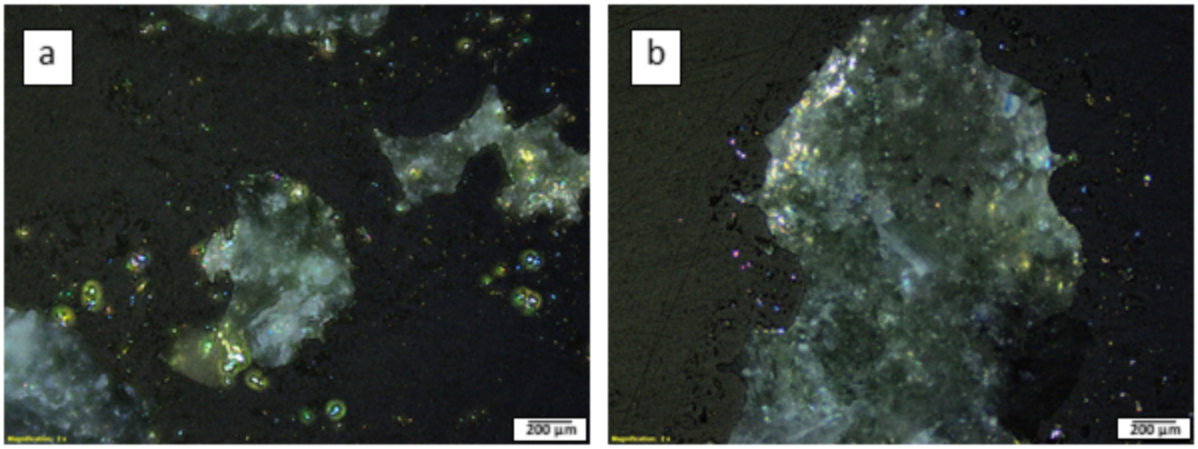

Figure 33: (a)(b) Quartz inclusions in pyrite. Scale bar: 200µm;

Pyrite under the microscope has a light yellow color with no pleochroism and no internal reflections (Figure 34). The mineral inclusions, quartz, shown in gray color, were described in the item above.

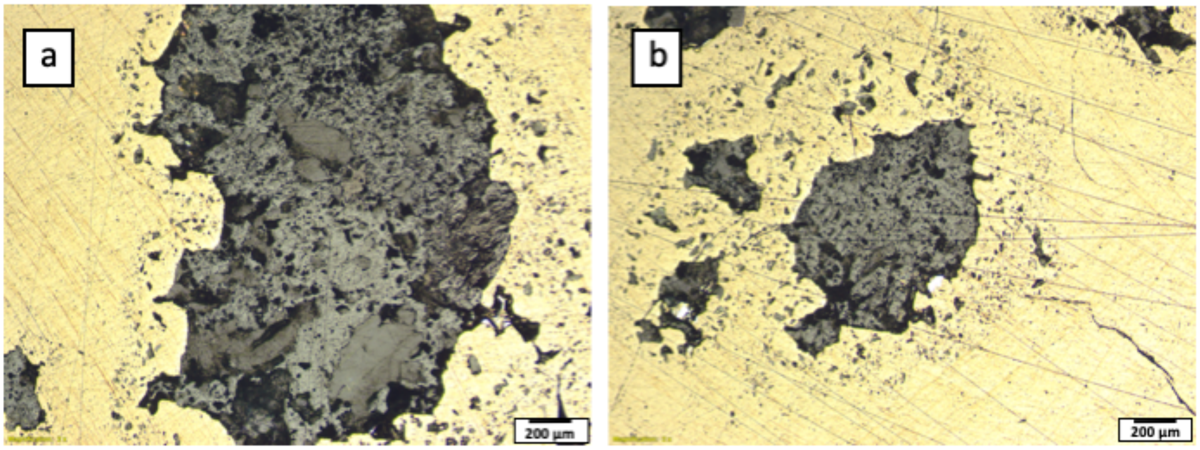

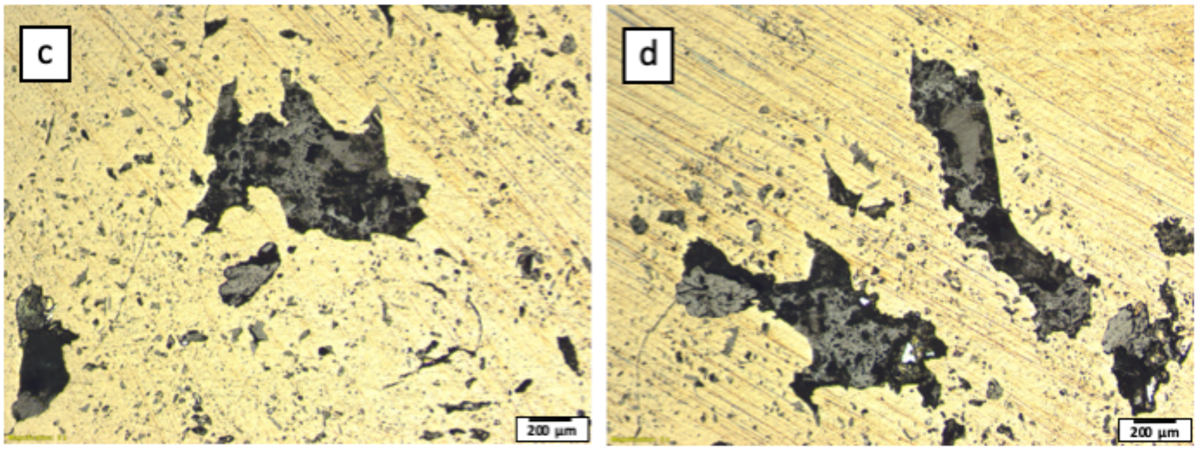

Figure 34: Pyrite sample under reflected light microscope (a) (b)(c)(d)Scale bar: 200µm.

## 3.9 Pyrrhotite

### *3.9.1 Hand sample examination*

Pyrrhotite samples ($Fe_{(1-x)}S$ – iron sulfide), Ward's catalogue number 470025-750, are from Galax, Virginia, USA (Figure 35). The hand specimens measure approximately 2cm to 4cm in length, have brown color, metallic luster and black streak. The grains are fine with massive texture. Inclusions of quartz (white), chalcopyrite (dark yellow) and sphalerite (gray) were observed. The inclusions are fine and anhedral.

Figure 35: Pyrrhotite hand specimen.

### 3.9.2 *Petrography*

Quartz intrusions were found in pyrrhotite samples. It occurs in white transparent color with habit varying from anhedral to subhedral (Figure 36). The crystals appear as polycrystalline aggregates, where individual grains are typically between 100µm and 200µm wide.

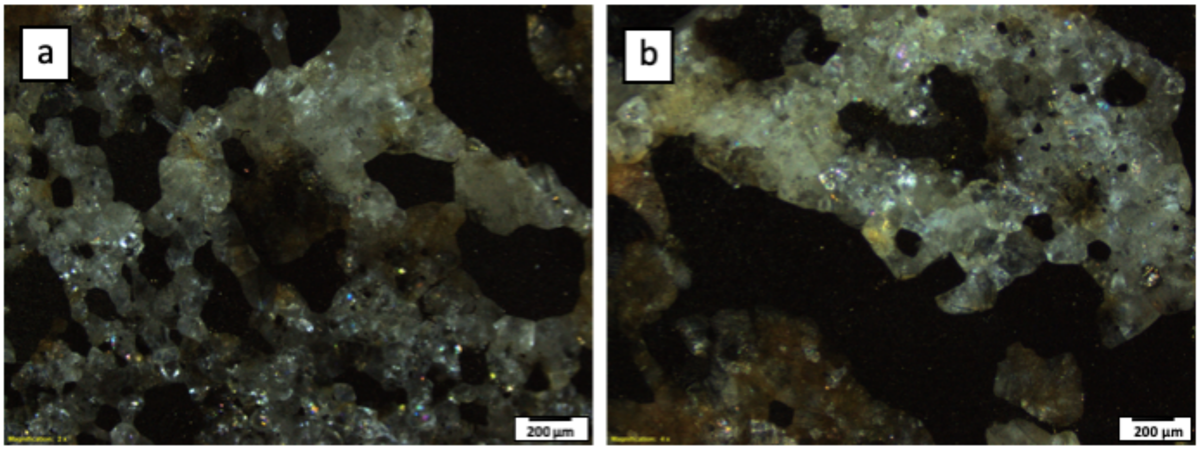

Figure 36: (a)(b) Polycrystalline aggregates of quartz in pyrrhotite. Scale bar: 200µm;

Pyrrhotite occurs in dull yellow color and anhedral grains (Figure 37) and it comprises more than 90% of the sample. Inclusions of chalcopyrite, sphalerite and were also observed. Chalcopyrite has a darker yellow color than pyrrhotite. It appears with anhedral habit and often associated to quartz, measuring from 30µm to 1mm, approximately. Sphalerite, light gray, anhedral, with crystals size varying from 30µm to 100µm.

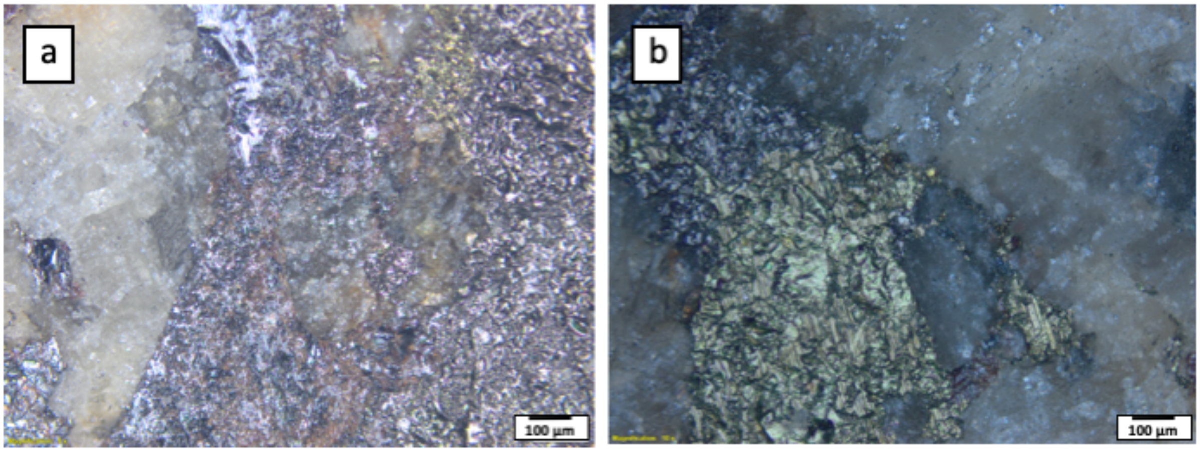

Figure 37: Pyrrhotite sample under reflected light microscope (a) Sphalerite and chalcopyrite in pyrrhotite. Scale bar: 100µm; (b) Chalcopyrite in pyrrhotite. Scale bar: 100µm.

## 3.10 Serpentinite

### *3.10.1 Hand sample examination*

Metamorphic rock with greenish black matrix and light green porphyroblasts (Figure 38). The grains of the matrix are very fine with massive texture, formed by serpentine and opaque minerals. The porphyroblasts are composed by unoriented and very fine fibrous crystals, which presumably is talc or chrysotile.

Figure 38: Serpentinite hand specimen.

### *3.10.2 Petrography*

Metamorphic rock composed by serpentine, opaque minerals, talc and relitic olivine (Figure 39). The majority of the sample, approximately 70%, consists of serpentine minerals. Serpentine occur in pale yellow color with variations in tabular and elongated habits and low birefringence expressed by first order interference colors. The opaque minerals occur in vein-like texture and are potentially magnetite formed by hydrous alteration of the protolith (iron rich minerals such as pyroxenes and olivines). Talc occurs in pale brown color, moderate relief and anomalous low interference color. Olivine occurs as relict serpentinized grains, with anomalous brown interference color, high relief and characteristic cracks

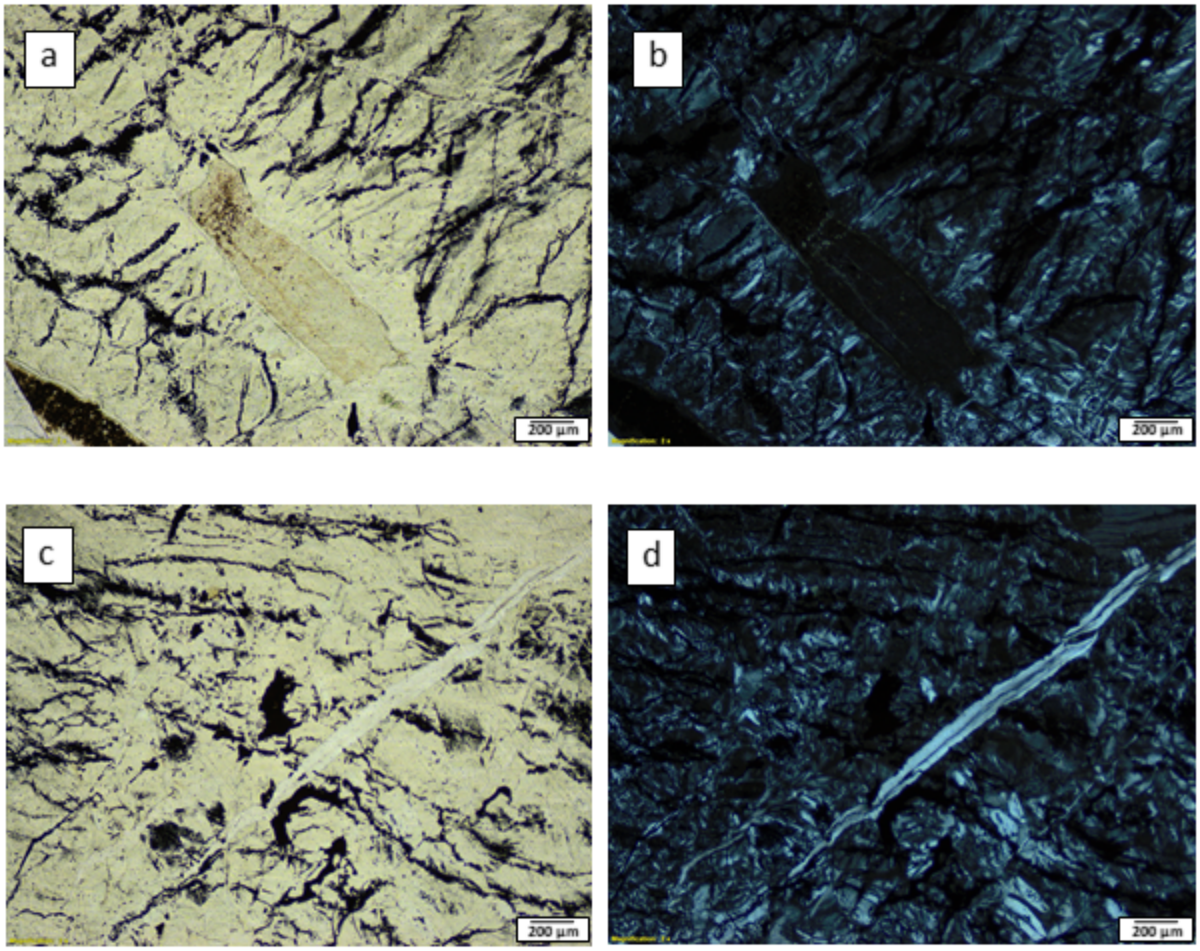

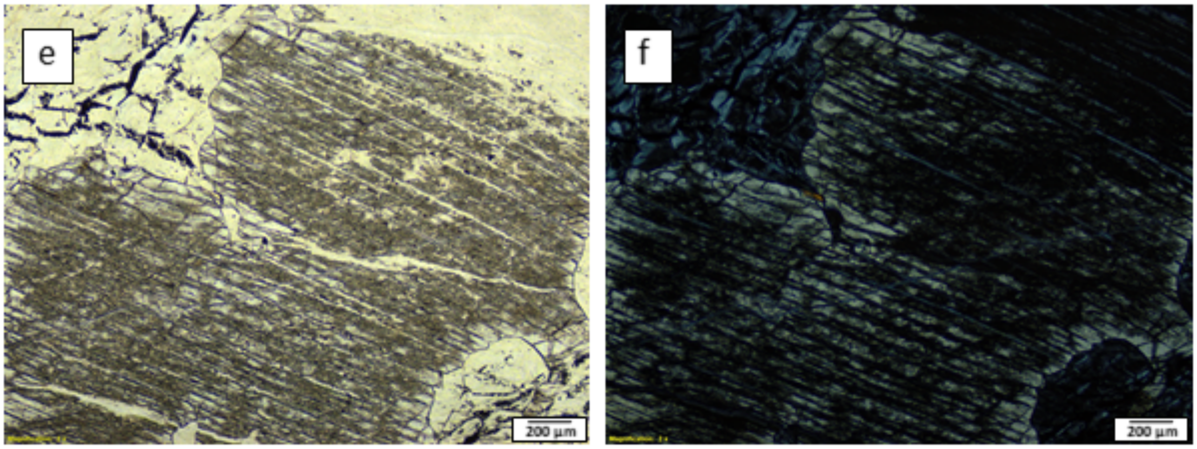

Figure 39: Serpentinite sample under transmitted light microscope (a) Talc in serpentinite sample with plane-polarized light. Scale bar: 200µm; (b) Talc in serpentinite sample with cross-polarized light Scale bar: 200µm; (c) Serpentinite with plane-polarized light. Scale bar: 200µm; (d) Serpentinite with cross-polarized light. Scale bar: 200µm; (e) Relict olivine with plane-polarized light. Scale bar: 200µm; (f) Relict olivine with cross-polarized light. Scale bar: 200µm.

# 4 Methodology and experimental techniques

## 4.1 Scanning electron microscope

For the scanning electron microscope (SEM) measurements, samples were prepared by cutting a slab of the mineral/rock using a slow cutter saw followed by polishing using a rotary polisher. It is important to polish the samples for a clearer distinction of the minerals. The samples are mounted by attaching the polished slab to the aluminum sample holder using a carbon adhesive tape.

Before inserting the samples in the machine, the nitrogen that circulates in the machine needs to be pumped to depressurize the equipment. After the pumping is complete the samples are inserted and each sample is put in a numbered sample slot. Upon analysis of the samples the equipment is vacuumed and the slot number of the target sample is selected so the stage moves and the chosen sample is centered. Thereafter the electron beam is turned on at the lowest energy, 5eV, and the grey-scale image is produced. To improve the quality of the image some parameters need to be adjusted, such as magnification, beam speed and working distance between the detector and sample stage. The grey-scale is associated to the composition of the sample. In other words, different shades of grey represent different composition within the sample.

The sample and its features are observed from a larger scale to a smaller scale. Once the SEM-BSE analysis is complete, the target area is selected for a composition identification using the EDS detector. For EDS purposes it is ideal that the sample scale is smaller or equal to 50 micrometers. The electron energization might be adjusted according to the sample and the number of counts per second detected by the EDX on the EDX software.

On the EDS software the detector is turned on and the first step is to execute a preview scan of the sample. The preview scan will show the number of counts per second (cps) of the image. To start the EDS measurements a minimum of 1000 cps is required. If the image has less than 1000 cps some parameters need to be adjusted, for instance, the beam size, working distance, beam speed and in particular, beam energy intensity. When at least 1000 cps is reached, the sample image is captured using the EDS detector. Once the image is scanned the point analyses can be started. Points of interest are selected on the sample to generate a compositional spectrum of each point.

Within the spectra the relative percentage of each element is estimated. Those values are later used to estimate the mineral content of the sample.

Furthermore, an EDS map can be generated. After selecting the target area, the image is scanned and a colored map is created where each color corresponds to a different element present in the sample.

## 4.2 Direct current electrical resistance measurements

The sample mounting for the direct current electrical resistance (DCR) measurements was developed as one of the main objectives of this project. The supplier suggests two different approaches for mounting the samples and both demonstrated to be inappropriate for minerals and rocks analysis. The first method is soldering the sample on the sample holder provided (Figure 40a). Soldering minerals and rocks can cause reactions and alterations to the samples. That means that this method is not suitable for this work since the results would not be reliable for the target minerals/rock.The second approach offered by the supplier is attaching the sample to the sample holder using silver epoxy (Figure 40b). Several attempts were made following this technique; however, it was very challenging to connect the sides of the sample to the gold pins of the holder considering the size of the samples and the texture of the epoxy before cured. Additionally, it was not possible to acquire electrical connections through this method. Failing to mount the samples according to the recommendations on the manual, a third technique was created (Figure 40c). It consists on soldering copper wires to a copper plate and attaching them to the sides of the sample using silver epoxy. The sample was then soldered to the holder. This method did not work because when the sample was being soldered to the holder the heat was melting the solder between the copper plates and copper wires. Finally, the method that was possible to successfully mount the sample for the electrical measurements in this work is described in detail in the section bellow (Figure 40d).

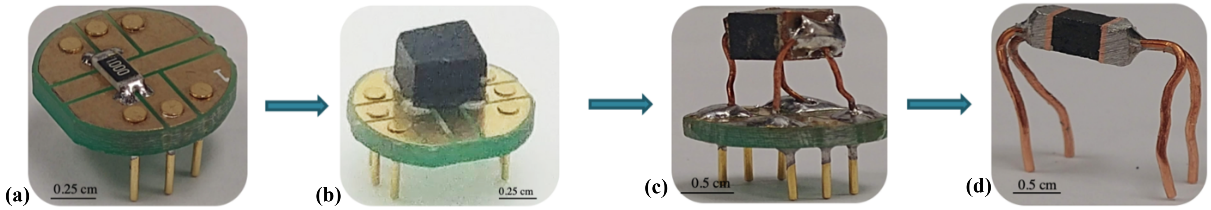

Figure 40: Different sample mounting approaches tested in this project. (a) a resistor soldered to the sample holder; (b) sample attached to the holder using silver epoxy; (c) third mounting technique using copper wires soldered to a copper plate and attaching them to the sides of the sample using silver epoxy and then soldering it to the holder; (d) sample mounting developed and using in this work.

### *4.2.1 Sample preparation*

The minerals and rock selected were cut into a parallelepiped shape with axis size of 5mm (Figure 41a) or less using a low speed circular saw (See the dimensions of each sample in Appendix D). The samples were then polished using a rotary polishing machine to remove any topographic irregularities on the surface. Following the polishing, to prepare the structure for the electrical wiring, a 3 mm thick copper plate (Figure 41b) was polished using a medium grade sand paper to remove superficial oxidation and sterilized with isopropanol. The copper plate was then cut into 5mm x 5mm pieces. A 0.5mm thick uncap copper wire was cut into approximately 4 cm long pieces. Each piece of wire was fold in half (Figure 41c) and soldered to the center of each piece of copper plate (Figure 41c). This structure was subsequently attached to two opposing sides of every sample using silver epoxy (Figure 41e).

The silver epoxy comes in two parts: A the epoxy, and B, the hardener. Equal amounts of each part were measured using an analytical scale and mixed together for two minutes. There are two options for curing the epoxy. The first option is to heat it for 15 minutes at 75°C-100°C. Alternatively, curing can be achieved at room temperature in 24 hours. The first method did not work for this project because the epoxy became very friable. After the epoxy was cured, each sample was polished to remove any excess of epoxy (Figure 41f).

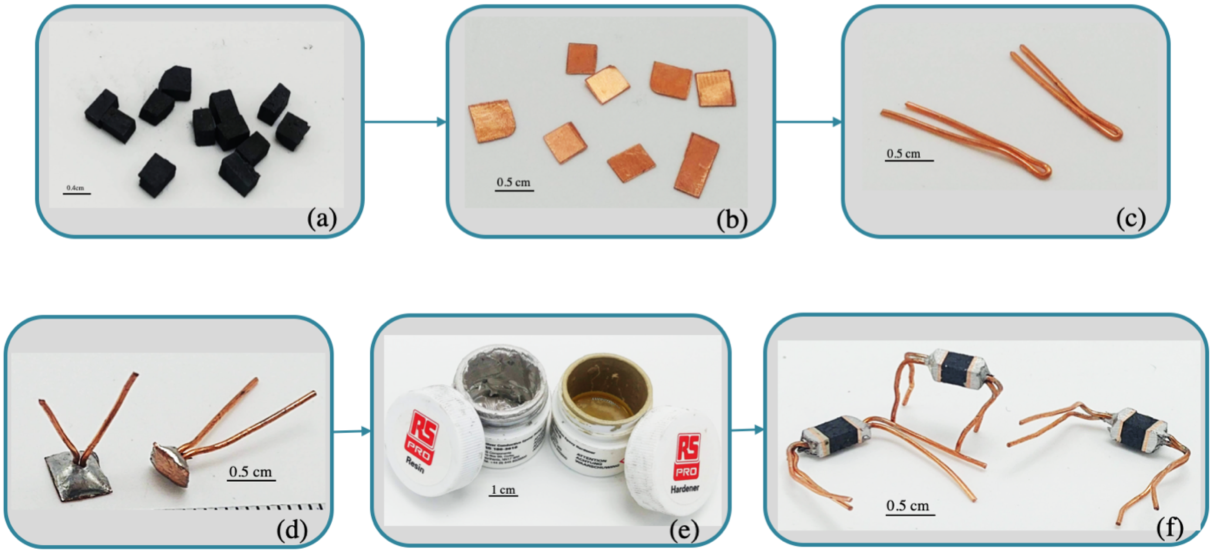

Figure 41: Sample preparation method developed (a) sample cut to size; (b) 3mm thick copper plates; (c) copper wires; (d) copper wires soldered to copper plates; (e) silver epoxy; (f) final product.

### *4.2.2 Measurement arrangement*

The DCR measurement setup is shown in Figure 42. The sample-wire system was attached to the sample platform. The platform has two sample slots so it can be placed perpendicular or parallel to the magnetic field if magnetic measurements are also executed. Each of the four wires of the sample was connected to a numbered pin on the platform. For this work, the pins used were numbers 7, 8, 11 and 12. These pin numbers correspond with the terminal numbers on the break-out-box. The sample platform was connected to the break-out-box and the resistance between pins was checked using a digital nanovoltmeter to ensure that the sample was properly wired. Once the electrical contacts were confirmed, the connections on the break-out-box were configured and the platform was attached to the DCR sample probe. The channel one wires from the nanovoltmeter, one black and one red, were connected to the first two numbered terminals on the break-out-box (7 and 8). The two banana plugs from the source meter were connected to the two other terminals (11 and 12). The helium gas valve that flushes the sample before loading and removing the probe to remove contaminants was opened. The equipment software was started and on “select measurement” option the “DCR” analysis was chosen and followed by “sample load”. The probe was connected to the airlock using an o-ring clamp and the height of the probe was adjusted using another clamp that comes attached to the probe. The thermometer/heater cable was attached to the probe and to the Lakeshore temperature controller. The gate valve was closed and after pressing “OK” on the software, the helium was flushed to the sample. Following this, the probe was lowered, inserting it to the cryostat. Subsequently, the 12-pin cable (sample wiring) was attached to the probe and to the break-out-box completing the sample loading process.

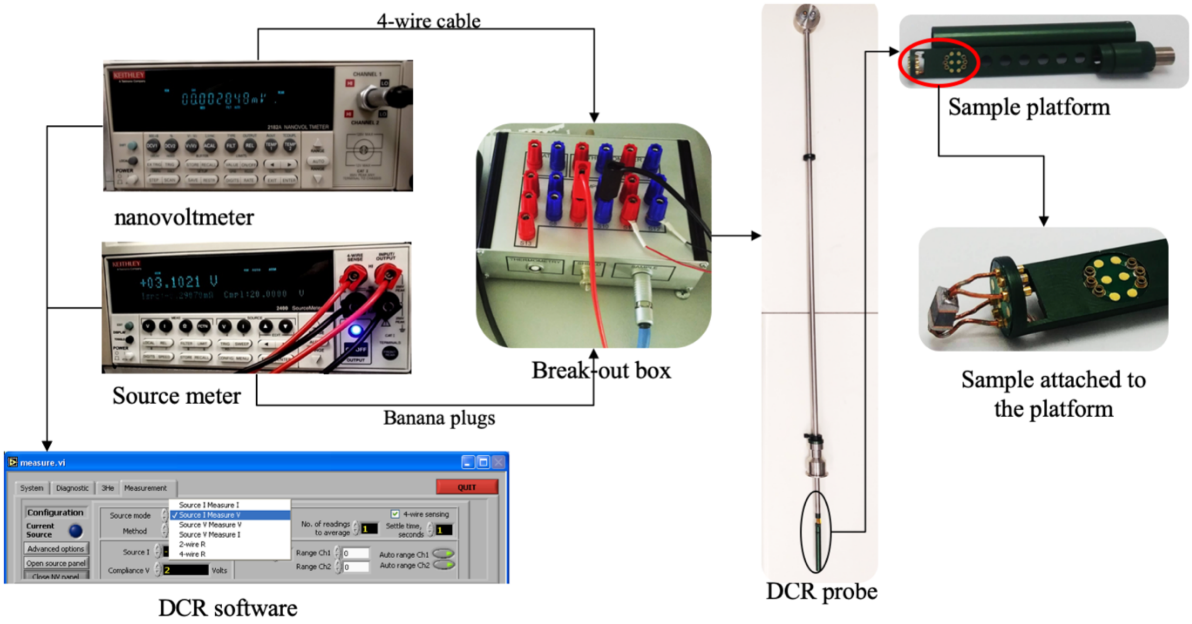

Figure 42: Simplified DC resistance measurement setup using CFMS. Adapted from Cryogenic Ltd. (2014).

### 4.2.3 *Measurement configuration*

After the sample probe was inserted in the system, the measurement configuration was defined by using the option “edit sequence” on the equipment software. On the sequence editor tab, the directory where the data was saved and the file name were chosen. The current and voltage before measurement were set to zero. DC current was selected as curve variable with a step curve type. The step size and turnpoints varied according to the sample. For this work two sequences with different turnpoints and step sizes were used. For the samples: galena, graphite and ilmenite the sequence 1 was used, as shown on Table 1, and for the samples: calchopyrite, magnetite crystalline, magnetite lodestone, pyrite, pyrrhotite, serpentinite and specularite the sequence 2 was applied (table 2). For both sequences the ramp rate was 1A/min with 1 second settling time and 3 readings per point. The temperature was set to be the parameter 1 for both sequences where the lowest temperature was 10K and the highest 300K with a 10K increment. The sequences represented on tables 1 and 2 were executed for each temperature from the parameter 1. The measurement configuration button on the sequence editor was selected to specify the measurement type, method and other experiment parameters. The measurement was set to source current and measure voltage using the simple method. The simple method means that the resistance will be measured using the applied current and measured voltage. For the source meter the source I was set as 0.001 Amp and the compliance volt to 80V and 1 second of settle time. For the voltmeter the channel 1 was selected because the channel 2 was not used for these experiments, with an autorange mode and 1 second delay between readings. Subsequently the sequence editor was closed and the sequence was executed by selecting “execute sequence” on the software menu.

After the sequence was complete the probe was removed by pressing the “remove probe” option on the software. The probe was lifted until above the gate valve, the gate valve was closed and the system flushed helium to the sample. After the helium was flushed the airlock was opened and the probe completely removed.

Table 1: DCR sequence 1

| **Turnpoints (Amps)** | **Step size (Amps)** |
|---|---|
| 1E-9 | 1E-10 |
| 1E-8 | 1E-9 |
| 1E-7 | 1E-8 |
| 1E-6 | 1E-7 |
| 1E-5 | 1E-6 |
| 0 | 1E-5 |

Table 2: DCR sequence 2

| **Turnpoints (Amps)** | **Step size (Amps)** |
|---|---|
| 1E-6 | 1E-7 |
| 1E-5 | 1E-6 |
| 1E-4 | 1E-5 |
| 1E-3 | 1E-4 |
| 0 | 1E-3 |

# 5 Results

## 5.1 EDS maps

### *5.1.1 Chalcopyrite*

The resulted EDS map (Figure 43) provides an estimation of the chemical composition of chalcopyrite sample and its inclusions. The individual element maps are illustrated on the side. The elements detected by the method in this sample were oxygen, sulfur, iron and copper. As expected, copper, iron and sulfur are present in the matrix, which is composed by chalcopyrite. Three mineral inclusions could be observed by the EDS maps. The inclusion shown in orange is an iron rich sulfide and it is evolved by an iron oxide mineral (in pink). The third inclusion, in brownish gray, is also a sulfide, with no iron or copper content, but other elements were not expressed on the map for this particular mineral.

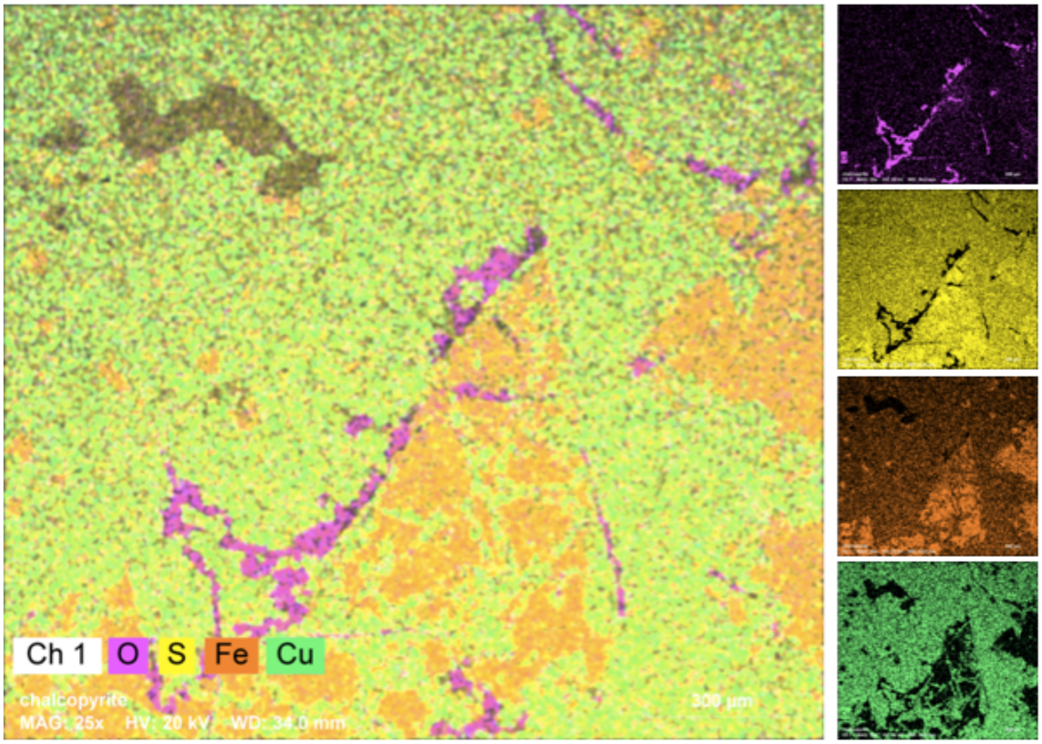

Figure 43: EDS map with elemental composition of chalcopyrite. Images on the side are partial EDS elements maps representing oxygen, sulfur, iron and copper, respectively (from top to bottom).

### *5.1.2 Galena*

The resulted EDS map (Figure 44) provides an estimation of the chemical composition of galena sample and its inclusion. The individual element maps are illustrated on the side. The elements detected by the method in this sample were oxygen, sulfur, lead, iron, arsenic and copper. As expected, sulfur and lead are present in the matrix, which is composed by galena. Additionally, oxygen, iron and arsenic were also observed in the matrix as contaminants. The inclusion shown in grey is composed by oxygen, iron and copper.

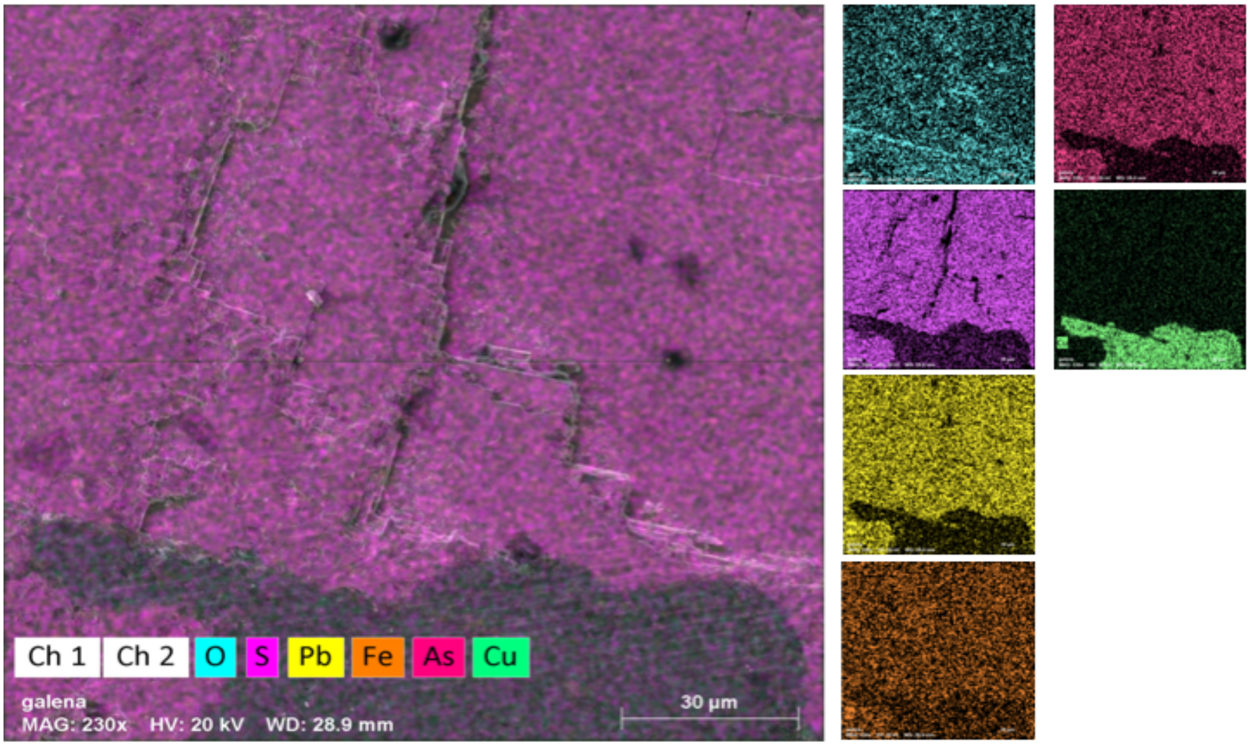

Figure 44: EDS map with elemental composition of galena. Images on the side are partial EDS elements maps representing oxygen, sulfur, lead, iron, arsenic and copper, respectively (from top to bottom).

### *5.1.3 Graphite*

The resulted EDS map (Figure 45) provides an estimation of the chemical composition of graphite. The individual element maps are illustrated on the side. The elements detected by the method in this sample were carbon, oxygen, magnesium and tantalum. The sample is very homogeneous and no inclusions were observed, however, contaminants are present (oxygen, magnesium and tantalum).

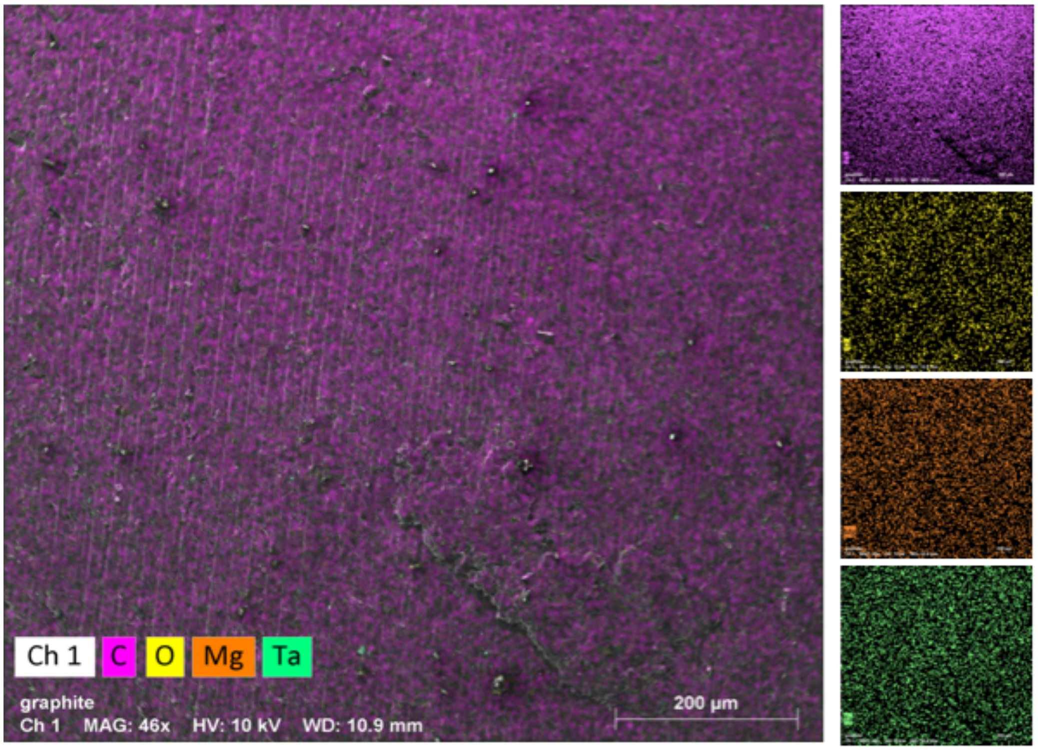

Figure 45: EDS map with elemental composition of graphite. Images on the side are partial EDS elements maps representing carbon, oxygen, magnesium and tantalum, respectively (from top to bottom).

### *5.1.4 Hematite*

The resulted EDS map (Figure 46) provides an estimation of the chemical composition of hematite sample and its inclusions. The individual element maps are illustrated on the side. The elements detected by the method in this sample were oxygen, aluminum, silicon, iron, magnesium and sodium. As expected, oxygen and iron are present in the matrix, which is composed by hematite. Three mineral inclusions could be observed by the EDS maps. The inclusion shown in pink (top left) is composed by oxygen, aluminum, silicon and sodium. The inclusion in greyish pink (top) associated to the previous inclusion is formed by oxygen, aluminum, silicon, iron and magnesium. The third inclusion, also in pink but with bladed shape, is composed by oxygen, silicon and iron.

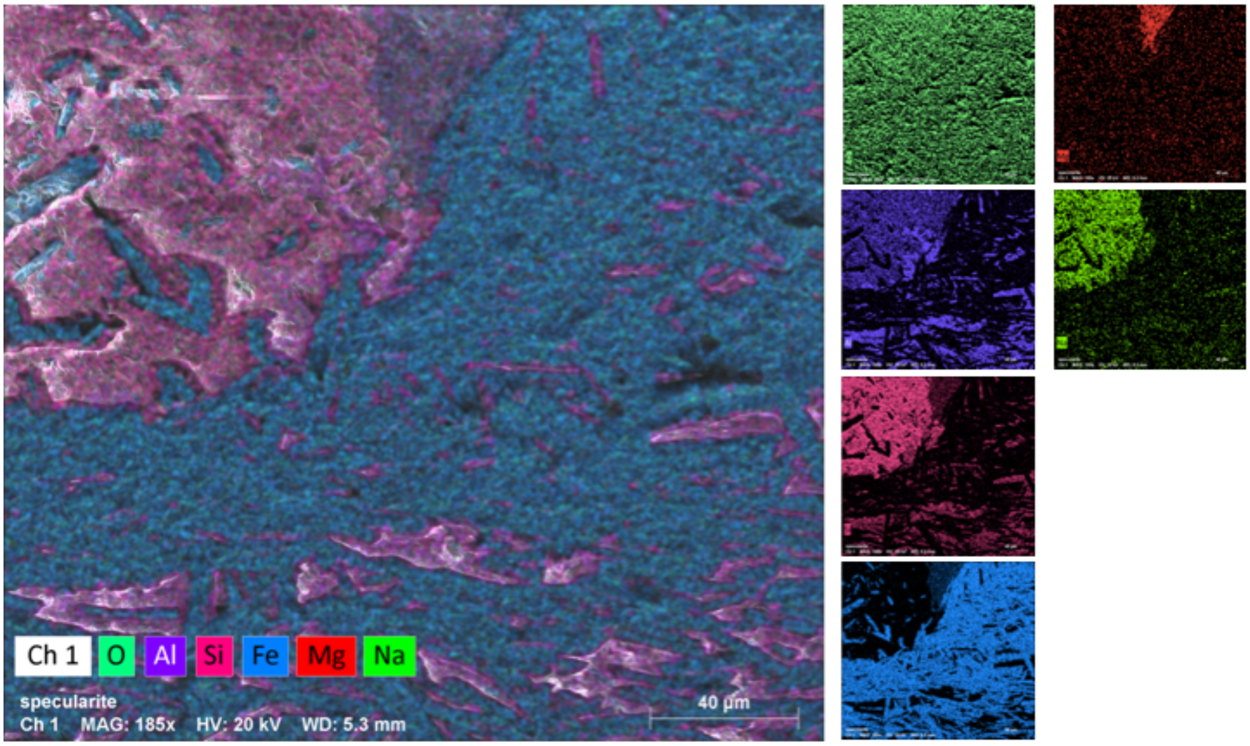

Figure 46: EDS map with elemental composition of hematite. Images on the side are partial EDS elements maps representing oxygen, aluminum, silicon, iron, magnesium and sodium, respectively (from top to bottom).

### *5.1.5 Ilmenite*

The resulted EDS map (Figure 47) provides an estimation of the chemical composition of ilmenite sample and its inclusions. The individual element maps are illustrated on the side. The elements detected by the method in this sample were oxygen, silicon, titanium, iron, calcium, magnesium, sodium and aluminum. As expected, oxygen, iron and titanium are present in the matrix, which is composed by ilmenite. Two mineral inclusions could be observed by the EDS maps. One of the inclusions (bright green) is composed by oxygen, silicon, magnesium and aluminum. The second (dull green) inclusion has a very similar composition to the first one, but it has calcium and sodium instead of magnesium, which suggested that one is product of alteration of another, also considering the topology of these crystals, associated to each other.

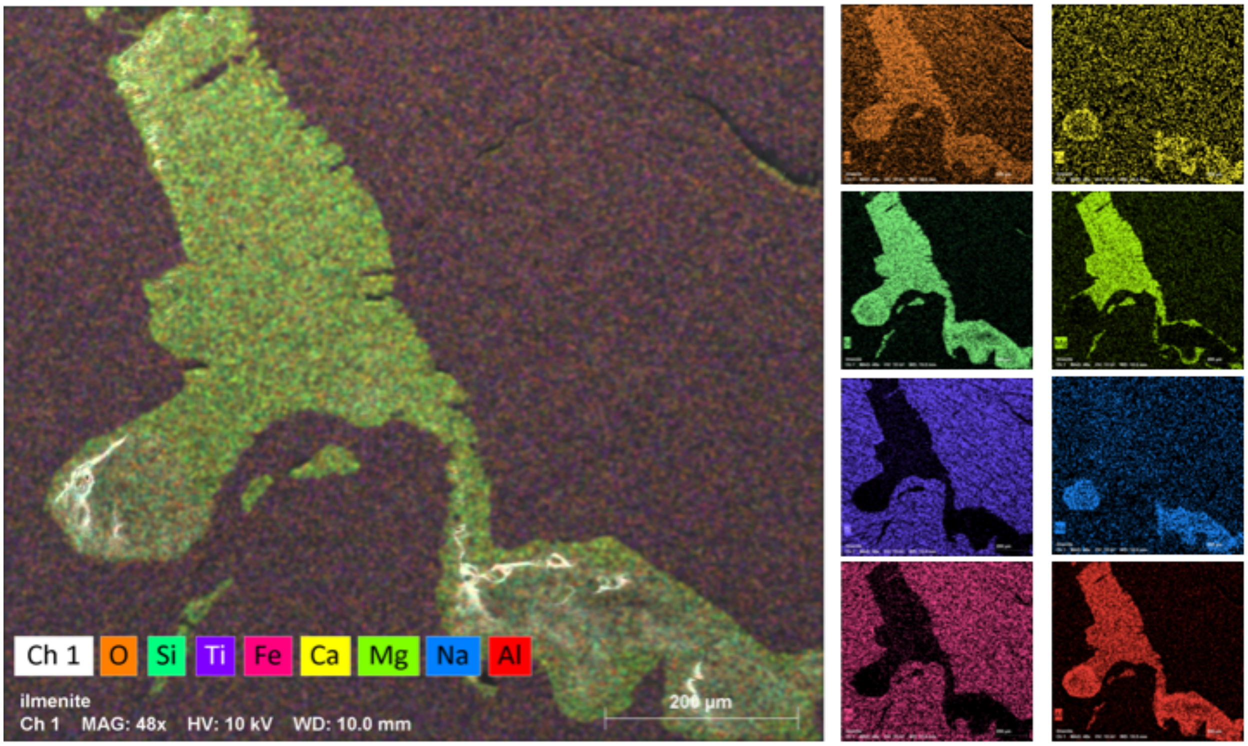

Figure 47: EDS map with elemental composition of ilmenite. Images on the side are partial EDS elements maps representing oxygen, silicon, titanium, iron, calcium, magnesium, sodium and aluminum, respectively (from top to bottom).

### *5.1.6 Magnetite*

The resulted EDS map (Figure 48) provides an estimation of the chemical composition of magnetite sample and its inclusions. The individual element maps are illustrated on the side. The elements detected by the method in this sample were iron, oxygen, silicon, calcium, potassium and aluminum. As expected, iron and oxygen are present in the matrix, which is composed by magnetite. Two mineral inclusions could be observed by the EDS maps. The inclusion shown in light orange is composed by oxygen, silicon, potassium and aluminum. Another inclusion, shown in green, is also present in the sample and it is composed by calcium and oxygen.

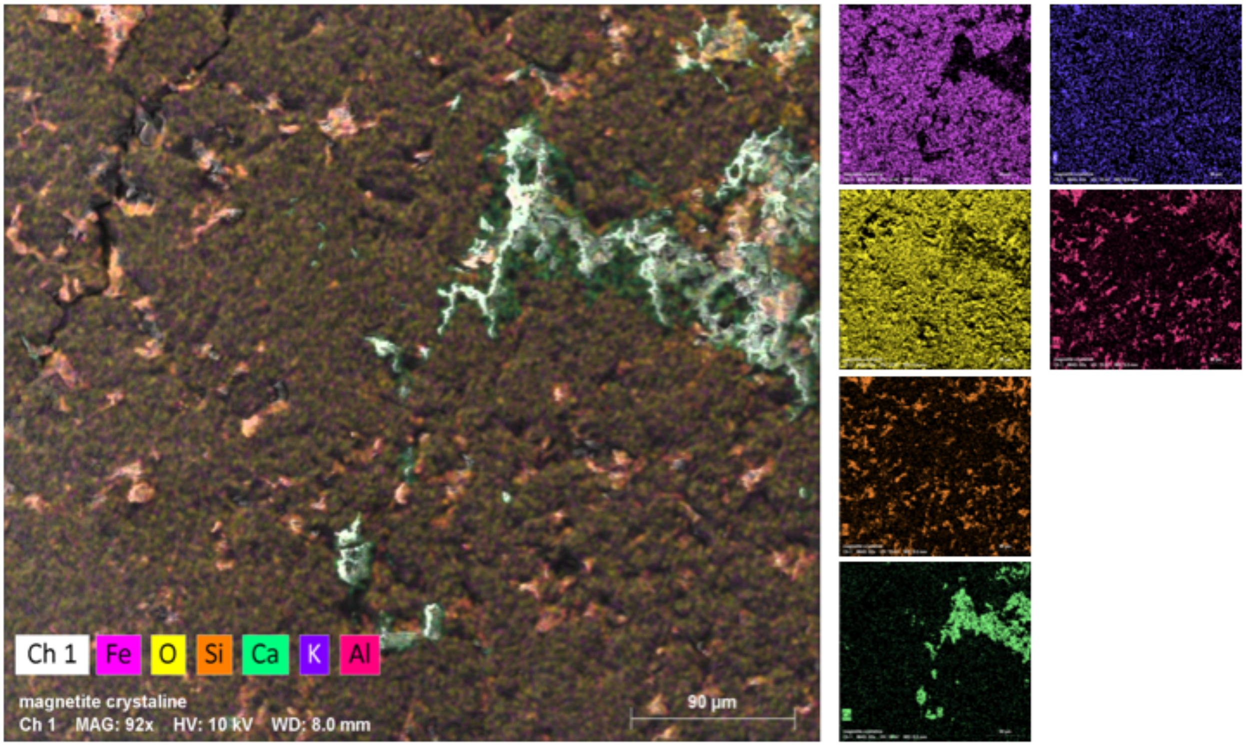

Figure 48: EDS map with elemental composition of magnetite. Images on the side are partial EDS elements maps representing iron, oxygen, silicon, calcium, potassium and aluminum, respectively (from top to bottom).

### *5.1.7 Magnetite lodestone*

The resulted EDS map (Figure 49) provides an estimation of the chemical composition of magnetite lodestone sample and its inclusions. The individual element maps are illustrated on the side. The elements detected by the method in this sample were oxygen, silicon, iron, calcium, cobalt and gold. As expected, iron and oxygen are present in the matrix, which is composed by magnetite. Additionally, cobalt and gold are also observed in the matrix. Two mineral inclusions could be observed by the EDS maps. The inclusion shown in orange is composed by oxygen, silicon and gold. Another inclusion, shown in pink, is composed by calcium and gold.

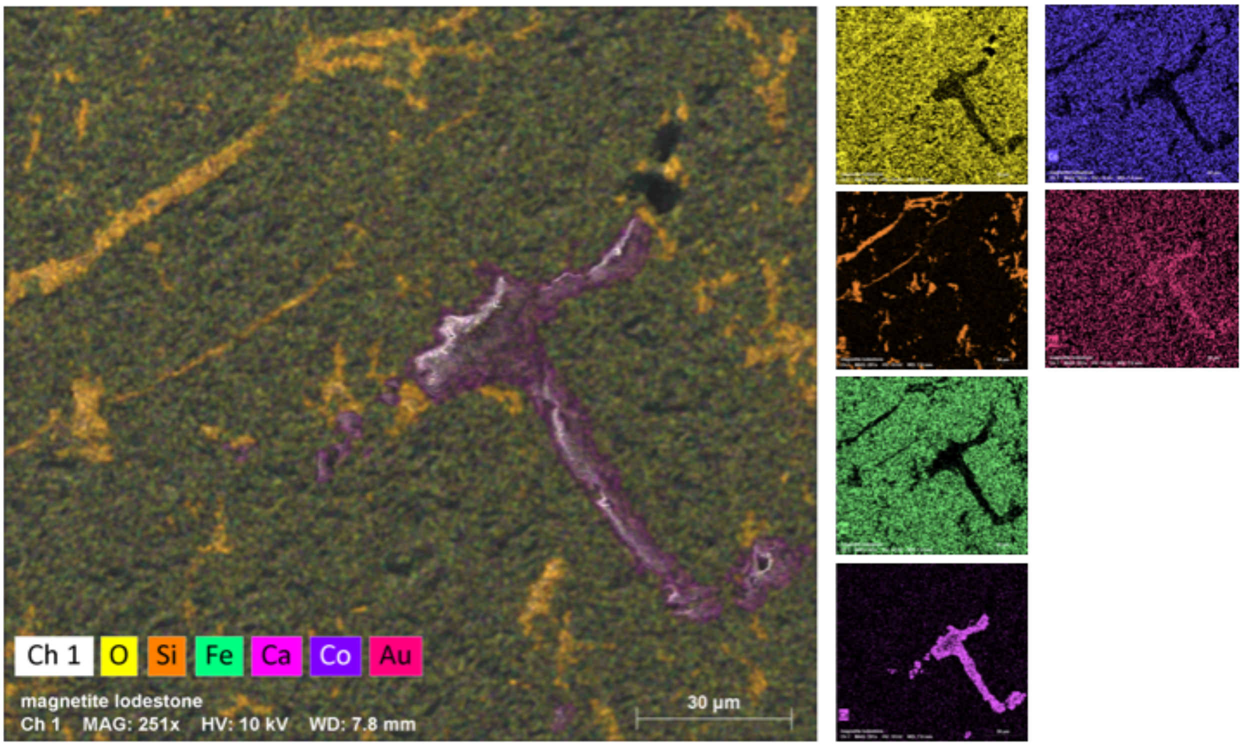

Figure 49: EDS map with elemental composition of magnetite lodestone. Images on the side are partial EDS elements maps representing oxygen, silicon, iron, calcium, cobalt and gold, respectively (from top to bottom).

### *5.1.8 Pyrite*

The resulted EDS map (Figure 50) provides an estimation of the chemical composition of pyrite sample and its inclusions. The individual element maps are illustrated on the side. The elements detected by the method in this sample were oxygen, silicon, titanium, iron, calcium, magnesium, sodium, aluminum and sulfur. As expected, sulfur and iron are present in the matrix, which is composed by pyrite. Additionally, titanium, magnesium and sodium are also observed in the matrix. Two mineral inclusions could be observed by the EDS maps. The inclusion shown in orange is composed by oxygen, silicon, magnesium and sodium. Another inclusion, shown in light green, is composed by calcium, magnesium, sodium and aluminum.

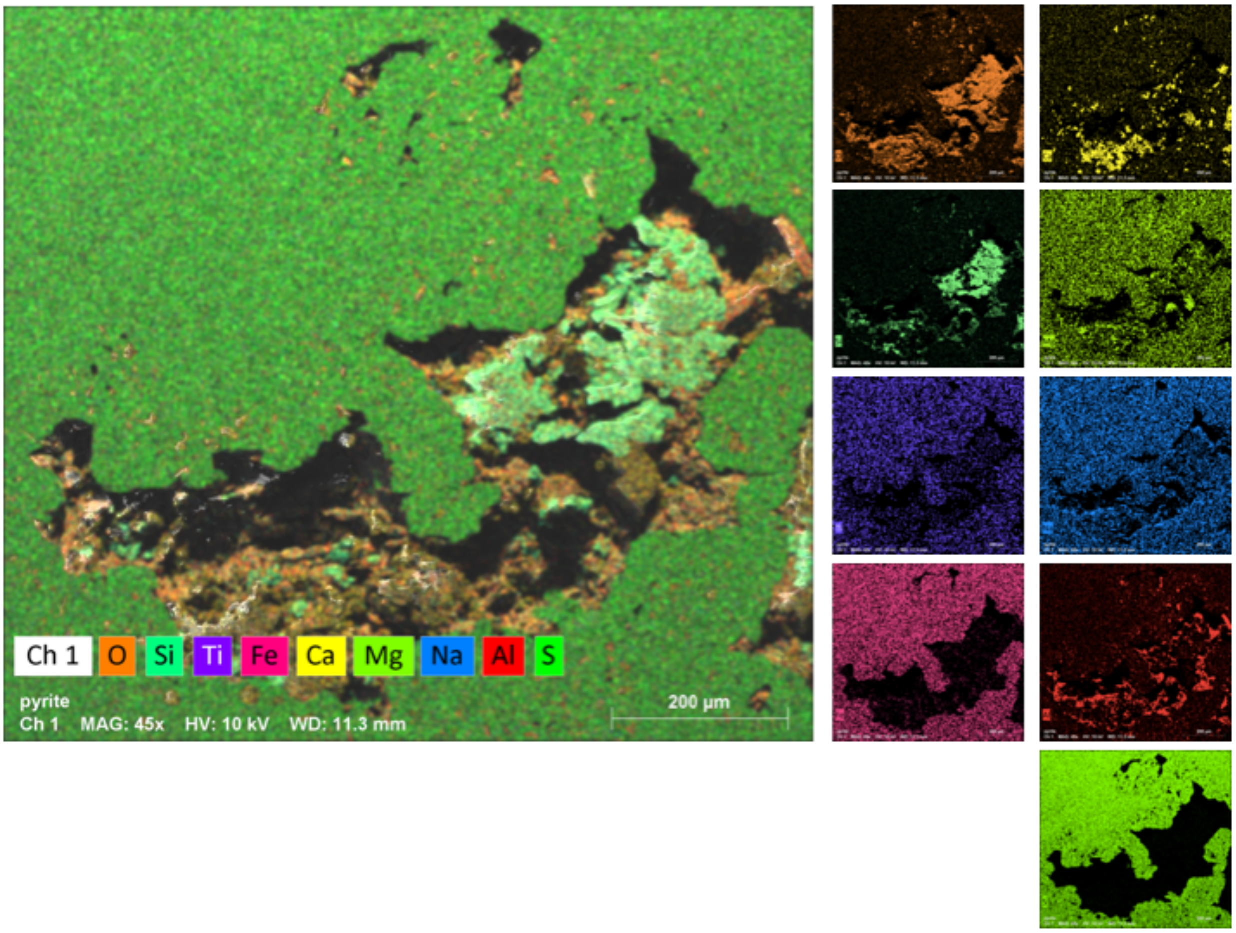

Figure 50: EDS map with elemental composition of pyrite. Images on the side are partial EDS elements maps representing oxygen, silicon, titanium, iron, calcium, magnesium, sodium, aluminum and sulfur, respectively (from top to bottom).

### *5.1.9 Pyrrhotite*

The resulted EDS map (Figure 51) provides an estimation of the chemical composition of pyrrhotite sample and its inclusions. The individual element maps are illustrated on the side. The elements detected by the method in this sample were oxygen, sulfur, iron and copper. As expected, iron and sulfur are present in the matrix, which is composed by pyrrhotite. Three mineral inclusions could be observed by the EDS maps. The inclusion shown in pink is an oxygen rich mineral, but no other elements were identified within it. The inclusion shown in dark yellow is a sulfide, but the map did not show other elements for this inclusion. The inclusion shown in yellowish green is composed by sulfur, iron and copper.

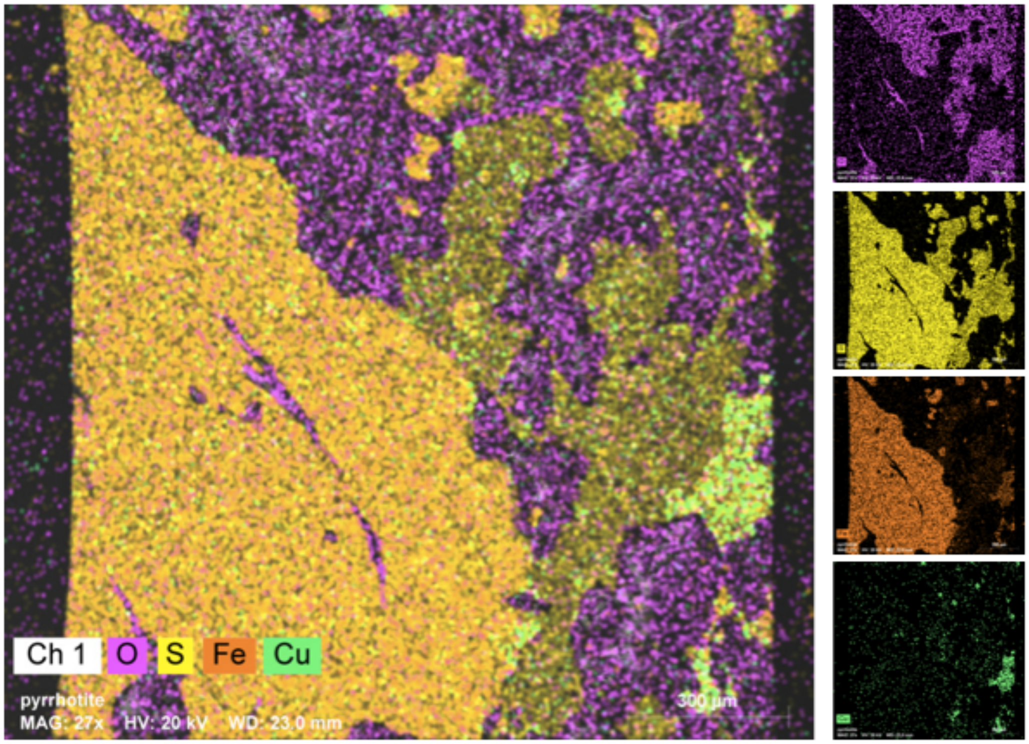

Figure 51: EDS map with elemental composition of pyrrhotite. Images on the side are partial EDS elements maps representing oxygen, sulfur, iron and copper, respectively (from top to bottom).

### *5.1.10 Serpentinite*

The resulted EDS map (Figure 52) provides an estimation of the chemical composition of serpentinite. The individual element maps are illustrated on the side. The elements detected by the method in this sample were iron, oxygen, silicon, aluminum, magnesium, chromium, manganese, cobalt and nickel. The matrix is composed by iron, oxygen, silicon, magnesium, chromium, manganese, cobalt and nickel. The porphyroblast is formed by aluminum and oxygen but other elements were not clearly distinguished.

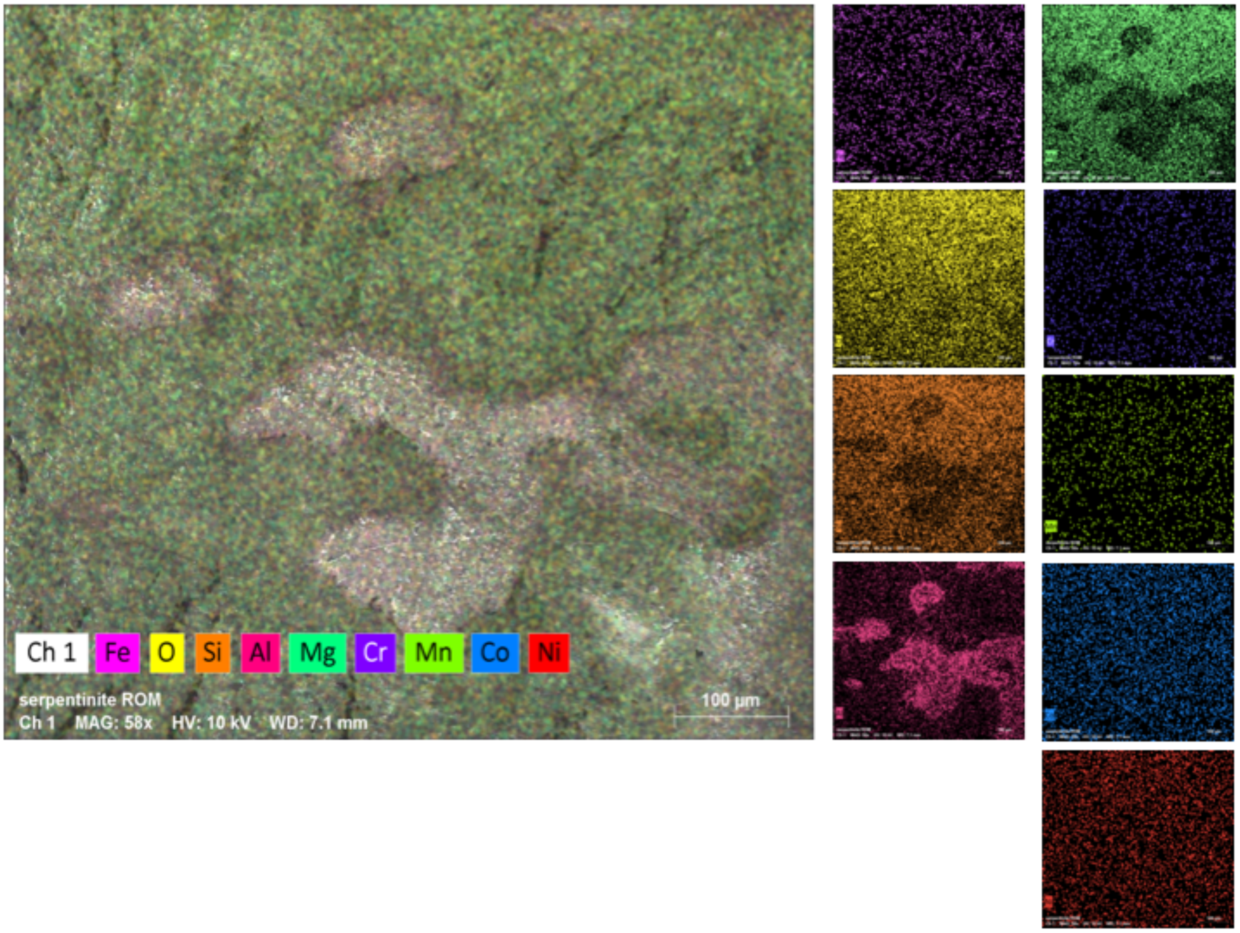

Figure 52: EDS map with elemental composition of serpentinite. Images on the side are partial EDS elements maps representing iron, oxygen, silicon, aluminum, magnesium, chromium, manganese, cobalt and nickel, respectively (from top to bottom).

## 5.2 Voltage versus current graphs

The voltage versus current graphs (VI graphs) for all samples are represented in Appendix A. Three samples of each mineral/rock were analyzed. The experiments were conducted within a temperature range of 10K to 300K, and steps of 10K. However, for some samples the lowest temperature recorded was above 10K due to some technical issues. The "warm-up" plots represent the tests with increasing temperature, while the “cool-down” plots represent the tests with decreasing temperature. The data was plotted by averaging the results of the three samples of each mineral/rock. To observe the linearity of the VI graphs and to understand whether each sample at each temperature would have an ohmic behaviour, a linear regression was conducted for each plot (warm-up and cool-down) of each sample. In order to establish the strength of the linearity, the regression coefficients were tested (such that the null hypothesis is given by $H_0$: $H_0\colon \beta_1 = 0$, and alternative hypothesis $H_a\colon \beta_1 \neq 0$ where $\beta_1$ is the regression coefficient corresponding to the current. The corresponding p-values are reported in Appendix B. All the plots and calculations were done using a MATLAB code (see Appendix C).

According to the corresponding R-squared values and p-values of the aforementioned hypothesis test, chalcopyrite, galena, graphite and pyrrhotite behave as ohmic materials, with R-squared equals one or very close to one (0.99 or over). On the other hand, ilmenite can be considered as non-ohmic material. Hematite reveals an ohmic behavior at 50K and at 230K or over. Magnetite was ohmic only at 60K. Magnetite lodestone is mostly ohmic, except at 20K and from 40K to 70K in the warm-up run; and from 40K to 70 K in the cool-down run. Pyrite was ohmic from 50K and over, while serpentinite was ohmic only at 70K in the warm-up run and at 70K and 80K in the cool-down run.

Uncertainties for resistance were calculated according to the source meter and nanovoltmeter specifications (Keithley Instruments, Inc., 1998) (Keithley Instruments, Inc., 2017) and the results are found in Appendix G.

## 5.3 Resistivity versus temperature graphs

The resistivity versus temperature data was plotted for an increasing temperature experiment run, warm-up, and a decreasing temperature run, cool-down, for each sample. Resistivity was calculated using a MATLAB code (see Appendix C). The dimensions of the samples used in the calculations are represented on Appendix D. The resistivity values for all samples are detailed in Appendix E.

A curved region was observed on the VI graphs for hematite, ilmenite, magnetite, magnetite lodestone, pyrite and serpentinite at certain temperatures and when the sourced current was smaller than 1x10$^{-6}$A. Presumably, this phenomenon could be due to a non-ohmic contact between the sample and the silver epoxy and copper plate connectors. The connection could be acting as a rectifying metal-semiconductor contact, also called Schottky barrier. The Schottky barrier is formed by a difference in the work function between the metal and the semiconductor, where a depletion region is formed on the interface, just as it occurs in diodes (Kao, 2004). Taking this into account, if we only consider the results for applied current over 1x10$^{-6}$A, resistivity values would change. The percentage difference in resistivity comparing values on Appendix E and the recalculated resistivity, where only currents over 1x10$^{-6}$A were considered, can be found in Appendix F.

Uncertainties for resistivity were calculated according to the source meter and nanovoltmeter specifications (Keithley Instruments, Inc., 1998) (Keithley Instruments, Inc., 2017) and the results are found in Appendix G.

### *5.3.1 Chalcopyrite*

The resistivity versus temperature graphs for chalcopyrite are shown in Figure 53. There are some differences between the warm-up and cool-down plot. Nevertheless, the same overall trend was observed. The sample revealed a decrease of resistivity with decrease of temperature from 300K to approximately 230K, for the warm-up run, and from 300K to approximately 190K, for the cool-down run. An increase of resistivity with decrease of temperature was noticed for temperatures below 200K for the warm-up run, and below 180K, for the cool-down run.

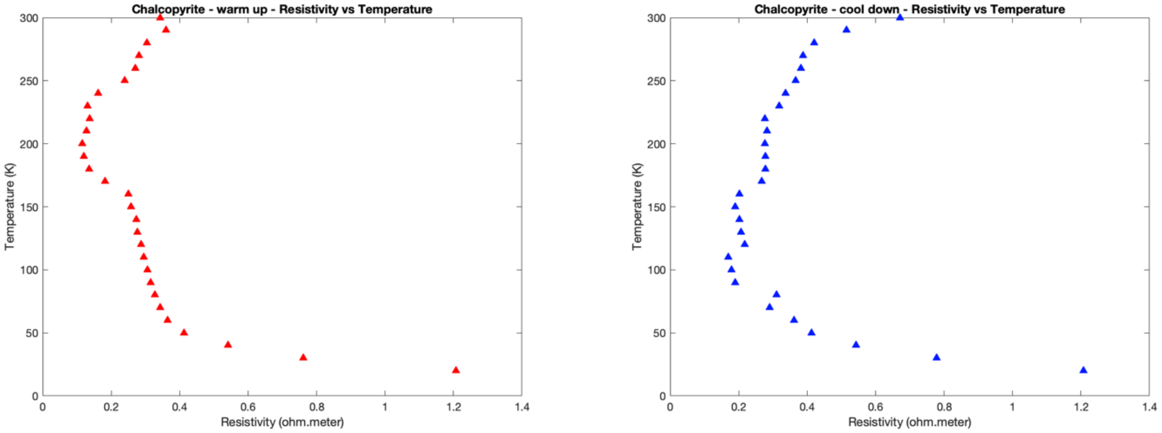

Figure 53: Chalcopyrite resistivity versus temperature graph. Warm-up sequence in red (left) and cool-down in blue (right).

### *5.3.2 Galena*

The resistivity versus temperature graphs for galena are shown in Figure 54. There are very slight differences between the warm-up and cool-down plots. It was observed that resistivity increases as temperature increases. It is worth to mention that this increase occurred in a faster rate at temperatures over 250 K, approximately.

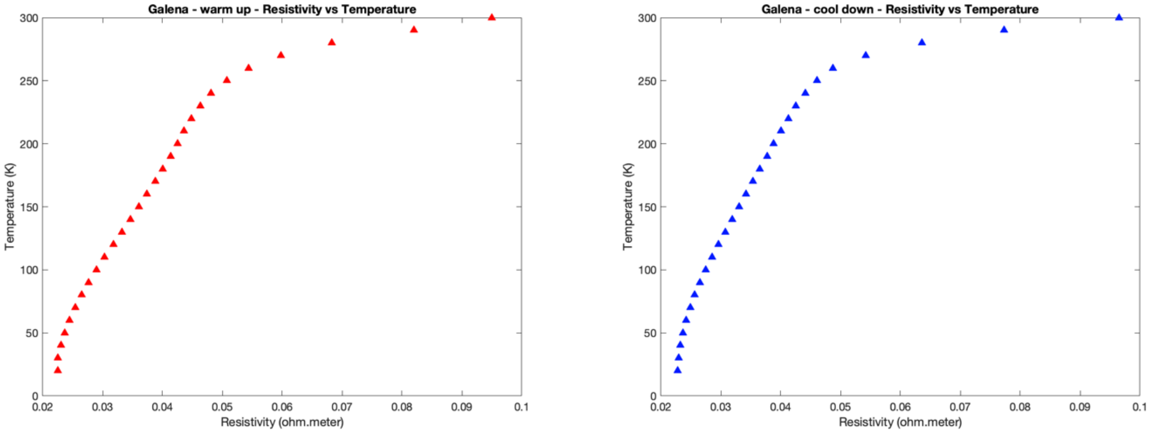

Figure 54: Galena resistivity versus temperature graph. Warm-up sequence in red (left) and cool-down in blue (right).

### *5.3.3 Graphite*

The resistivity versus temperature graphs for graphite are shown in Figure 55. There are some differences between the warm-up and cool-down plots, but both runs follow the same pattern. The sample revealed a decrease of resistivity with decrease of temperature from 300K to approximately 250K followed by an increase of resistivity with increase of temperature for temperatures below 250K.

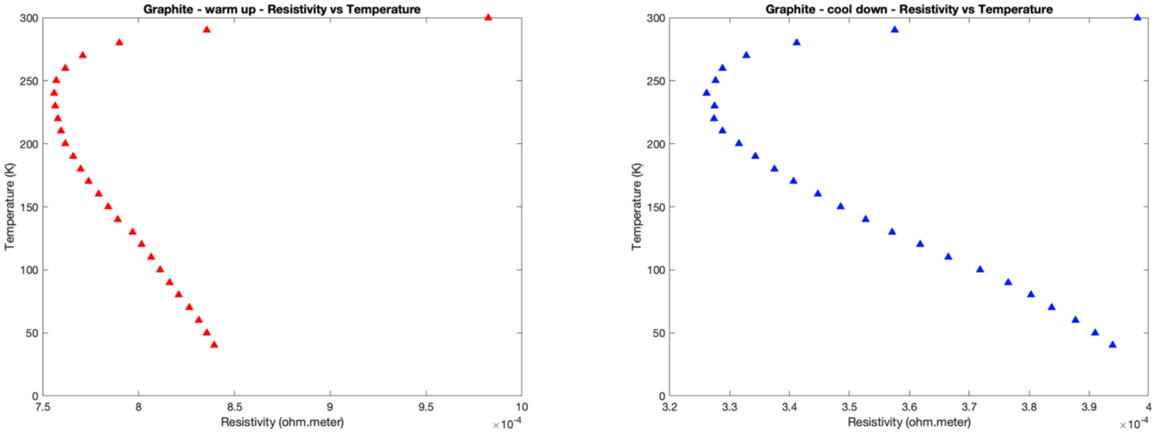

Figure 55: Graphite resistivity versus temperature graph. Warm-up sequence in red (left) and cool-down in blue (right).

### 5.3.4 Hematite

The resistivity versus temperature graphs for hematite are shown in Figure 56. There are some differences between the warm-up and cool-down plots. However, the same overall trend was observed. An increase of resistivity was noticed at temperatures between 300K to 70K. No clear pattern was identified for temperatures below 60K.

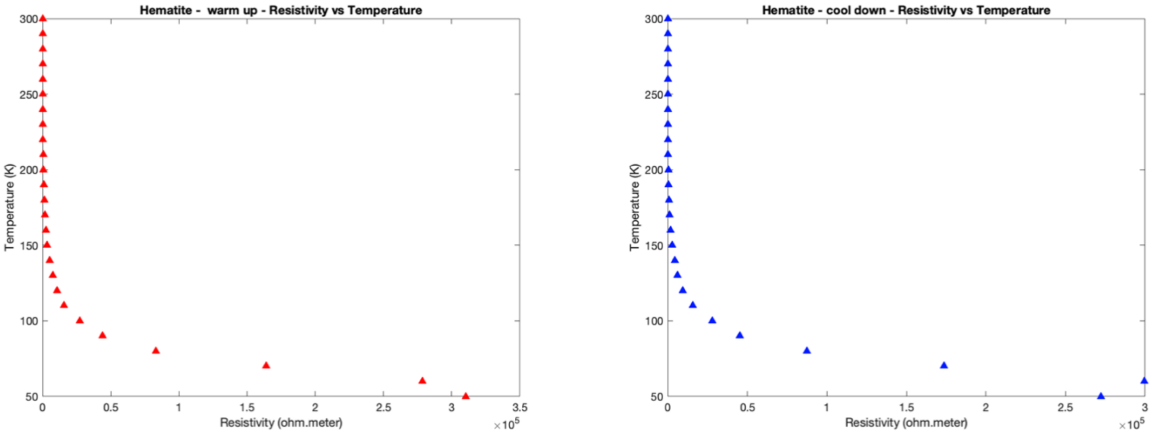

Figure 56: Hematite resistivity versus temperature graph. Warm-up sequence in red (left) and cool-down in blue (right).

### 5.3.5 Ilmenite

The resistivity versus temperature graphs for ilmenite are shown in Figure 57. There are small differences between the warm-up and cool-down plots. Nevertheless, the same overall trend was observed. An increase of resistivity was noticed at temperatures between 300K and 90K.

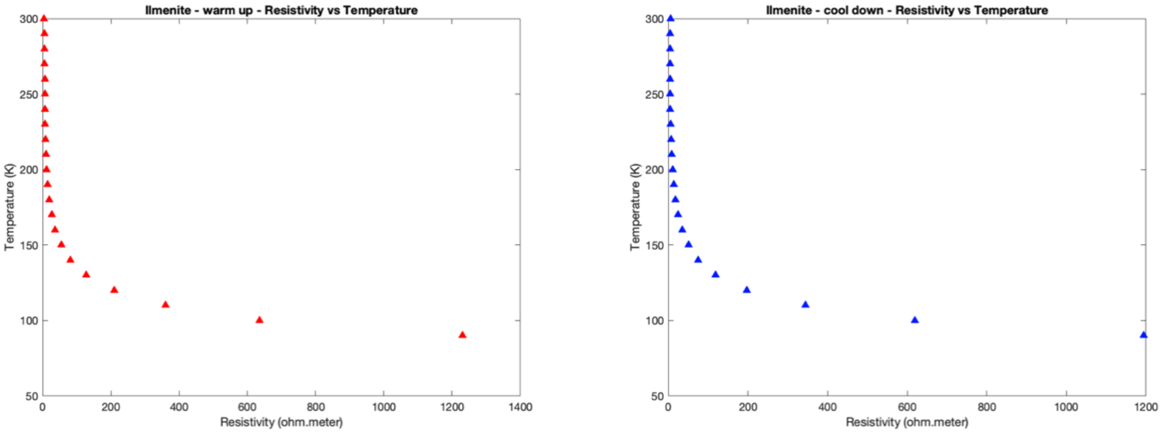

Figure 57: Ilmenite resistivity versus temperature graph. Warm-up sequence in red (left) and cool-down in blue (right).

### 5.3.6 *Magnetite*

The resistivity versus temperature graphs for magnetite are shown in Figure 58. There are some differences between the warm-up and cool-down plot. Nevertheless, the same overall trend was observed. Substantially, resistivity decreases as temperature increases, though no clear pattern was identified at temperatures below 130K.

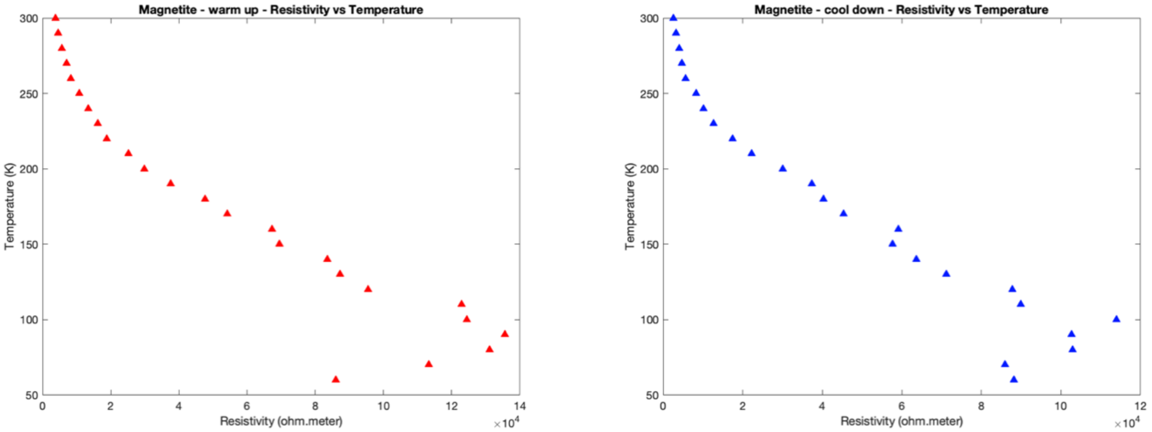

Figure 58: Magnetite resistivity versus temperature graph. Warm-up sequence in red (left) and cool-down in blue (right).

### *5.3.7 Magnetite lodestone*

The resistivity versus temperature graphs for magnetite lodestone are shown in Figure 59. There are some slight differences between the warm-up and cool-down plots, but the same trend was observed. Resistivity increased as temperature decreased from 300K until 30K. Though, resistivity decreased from 30K to 20K.

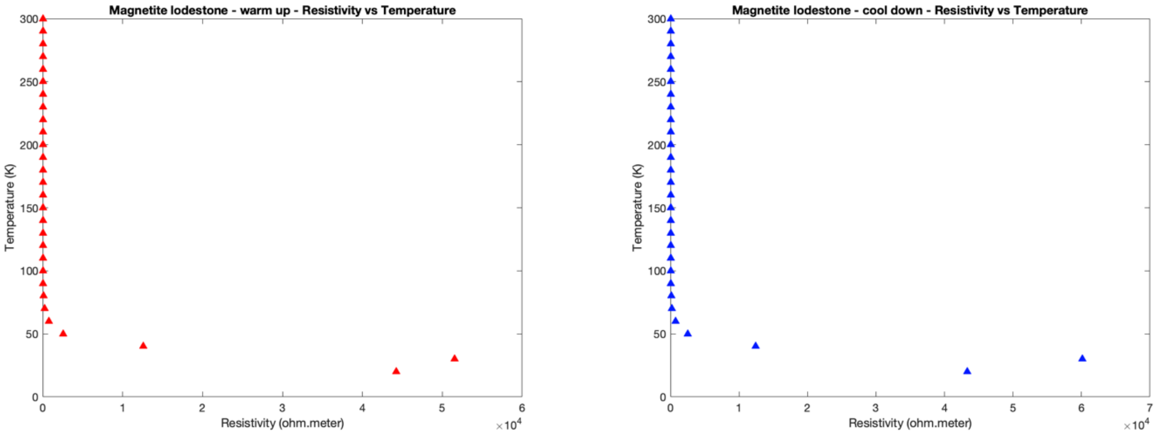

Figure 59: Magnetite lodestone resistivity versus temperature graph. Warm-up sequence in red (left) and cool-down in blue (right).

### *5.3.8 Pyrite*

The resistivity versus temperature graphs for pyrite are shown in Figure 60. There are some slight differences between the warm-up and cool-down plots, however both runs follow the same trend. Resistivity stayed relatively constant from 300K until about 90K, approximately, followed by an increase of resistivity at temperatures below 90K.

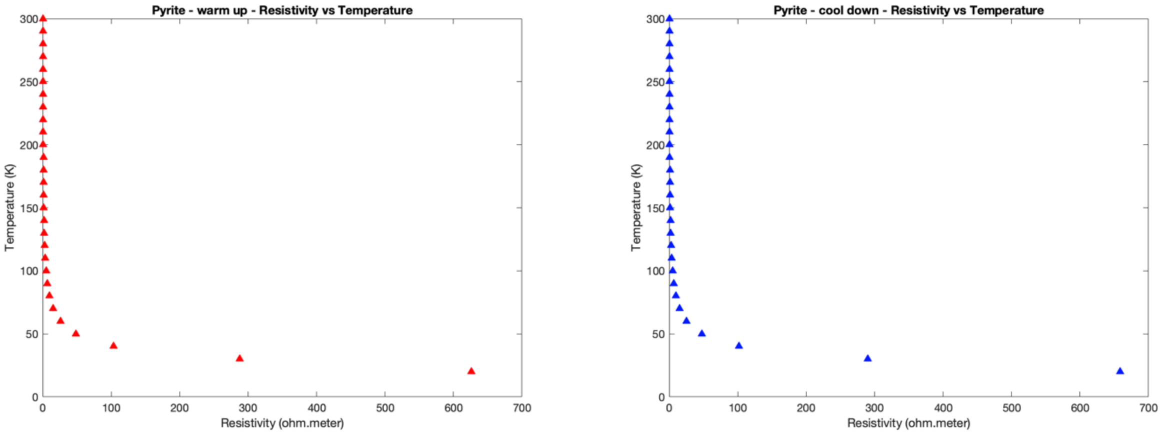

Figure 60: Pyrite resistivity versus temperature graph. Warm-up sequence in red (left) and cool-down in blue (right).

### *5.3.9 Pyrrhotite*

The resistivity versus temperature graphs for pyrrhotite are shown in Figure 61. There are some slight differences between the warm-up and cool-down plots, however both runs follow the same trend. The experiment revealed that the resistivity of the sample increases progressively as temperature decreases.

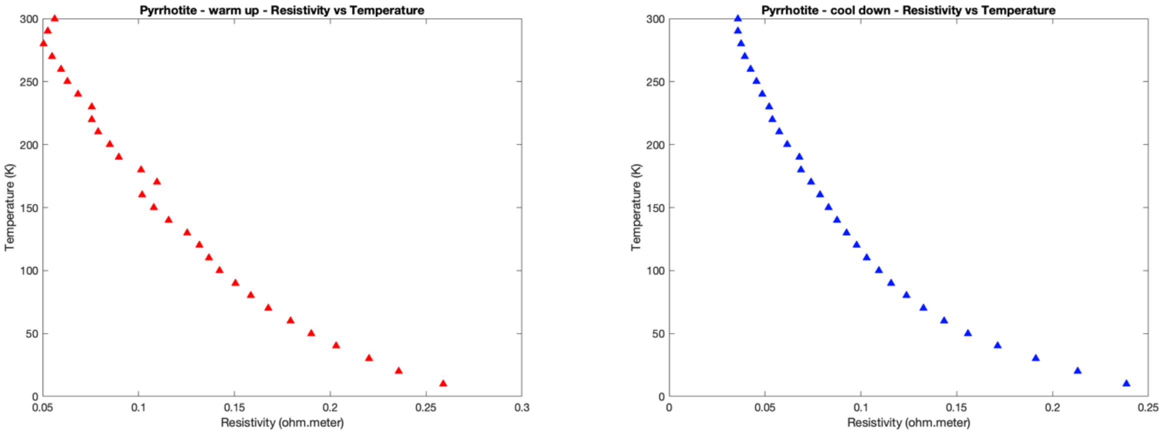

Figure 61: Pyrrhotite resistivity versus temperature graph. Warm-up sequence in red (left) and cool-down in blue (right).

### 5.3.10 *Serpentinite*

The resistivity versus temperature graphs for serpentinite are shown in Figure 62. There are some differences between the warm-up and cool-down plot. Nevertheless, the same overall trend was observed. Generally, for serpentinite resistivity increases as temperature decreases. However, at temperatures below 100K the resistivity and temperature relationship is unclear.

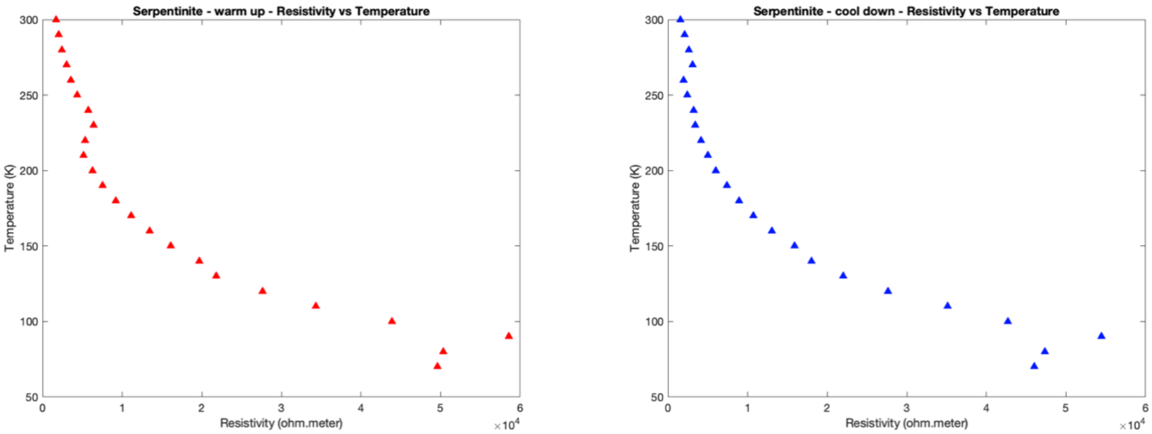

Figure 62: Serpentinite resistivity versus temperature graph. Warm-up sequence in red (left) and cool-down in blue (right).

# 6 Discussion

## 6.1 Sample characterization

Sample characterization is crucial for this work as resistivity is dependant on chemical composition and structure. Notwithstanding that the samples acquired for this work are good grade specimens, impurities and inclusions were observed. These impurities must be taken into account as the overall resistivities can be increased or decreased as a result of its presence considering that its own resistivity might be different than the host mineral. Reflected light petrography was applied for ore sample descriptions, however, it is recommended to prepare thin sections for analysis under transmitted light for characterization of the gangue minerals within the selected samples. EDS maps provided a summary of the elements' distribution of the samples. Comparing the hand specimen, chalcography and petrography descriptions with EDS mapping, we can observe that for chalcopyrite sample EDS mapping detected oxygen (O), sulfur (S), iron (Fe) and copper (Cu) while the minerals sphalerite ($(Zn,Fe)S$), arsenopyrite ($FeAsS$), and pyroxene ($(Ca,Mg,Fe)_2Si_2O_6$) were identified as mineral associations with the descriptive methods. According to Pracejus (2015) chalcopyrite is commonly associated to: anglesite, arsenopyrite, carbonate, galena, hematite, magnetite, pyrite, pyrrhotite, sphalerite, tetrahedrite and tiemannite. On EDS map for chalcopyrite, three inclusions were determined by the spatial distribution of the elements, where three clusters of elements (interpreted as three different inclusions) were distinguished. The first one is composed by iron and sulfur, which could be an indication of sphalerite or arsenopyrite inclusions. The second cluster is composed by iron and oxygen, which could imply and iron oxide mineral, such as hematite and magnetite. The third cluster is composed by sulfur and no other element was associated to it. Therefore, no further conclusion can be made regarding this specific elemental distribution. The distribution of copper, iron and sulfur shows that chalcopyrite is the matrix of the sample.

Galena EDS mapping detected oxygen (O), sulfur (S), lead (Pb), iron (Fe), arsenic (As) and copper (Cu) while the minerals chalcopyrite ($CuFeS_2$), and quartz ($SiO_2$) were identified as mineral associations with the descriptive methods. According to Pracejus (2015) galena is commonly associated to: acanthite, anglesite, barite, calcite, chalcopyrite, dolomite, marcasite, pyrite, quartz, siderite, native silver, sphalerite, tennantite and tetrahedrite. On EDS mapping for galena, one inclusion was determined by the spatial distribution of the elements, where one cluster of elements, interpreted as one inclusion, was distinguished. The cluster is composed by oxygen and copper. Cuprite ($Cu_2O$), is not commonly associated to chalcopyrite. That being said, the results for this cluster are inconclusive. The distribution of lead and sulfur shows that galena is the matrix of the sample.

Graphite EDS mapping detected carbon (C), oxygen (O), magnesium (Mg) and tantalum (Ta). No mineral associations were identified with the descriptive methods. According to (Pracejus, 2015) graphite is commonly associated to: augite, calcite, chalcopyrite, dolomite, magnetite, molybdenite, pyrite, silicates and troilite. The distribution the elements on graphite sample with EDS mapping reveals that oxygen, magnesium and tantalum are contaminants.

Hematite EDS mapping detected oxygen (O), aluminum (Al), silicon (Si), iron (Fe), magnesium (Mg) and sodium (Na) while the minerals quartz ($SiO_2$) relict olivine ($(Mg,Fe)_2SiO_4$) and pyroxene ($(Ca,Mg,Fe)_2Si_2O_6$) were identified as mineral associations with the descriptive methods. According to (Pracejus, 2015) hematite is commonly associated to: barite, goethite, ilmenite, lepidocrocite, magnetite, quartz, rutile, siderite, tiemannite. On EDS mapping for hematite, three inclusions were determined by the spatial distribution of the elements, where three clusters of elements (interpreted as three different inclusions) were distinguished. The first one is composed by oxygen, aluminum, silicon and sodium, which could be an indicative of feldspar. The second cluster is composed by oxygen, aluminum, silicon, iron and magnesium, which could be pyroxene. The third cluster is composed by oxygen, silicon and iron, which could indicate presence of olivine. The distribution of oxygen and reveals that hematite is the matrix of the sample.

Ilmenite EDS mapping detected oxygen (O), silicon (Si), titanium (Ti), iron (Fe), calcium (Ca), magnesium (Mg), sodium (Na) and aluminum (Al) while the minerals quartz ($SiO_2$), rutile ($TiO_2$) and chalcopyrite ($CuFeS_2$) were identified as mineral associations with the descriptive methods. According to (Pracejus, 2015) ilmenite is commonly associated to: apatite, chalcopyrite, galena, hematite, magnetite, pyrite, pyrrhotite, rutile, silicates, ulvite. On EDS mapping for ilmenite, two inclusions were determined by the spatial distribution of the elements, where two clusters of elements (interpreted as two different inclusions) were distinguished. The first one is composed by composed by oxygen, silicon, magnesium and aluminum, which could indicate a silicate (possibly feldspar) with magnesium impurity. The second cluster is associated to the first one with a very similar chemical composition formed by oxygen, silicon, calcium, sodium and aluminum, which could also be a feldspar but a calcium sodium variation. The distribution of oxygen, iron and titanium reveals that ilmenite is the matrix of the sample.

Magnetite EDS mapping detected iron (Fe), oxygen (O), silicon (Si), calcium (Ca), potassium (K) and aluminum (Al) while the minerals quartz ($SiO_2$), hematite ($Fe_2O_3$) and chalcopyrite ($CuFeS_2$) were identified as mineral associations with the descriptive methods. According to (Pracejus, 2015) magnetite is commonly associated to: apatite, chalcopyrite, carbonate, chromite, hematite, ilmenite, pentlandite, pyrite, pyrrhotite, quartz, rutile, silicates, sphalerite and ulvite. On EDS mapping for magnetite, two inclusions were determined by the spatial distribution of the elements, where two clusters of elements (interpreted as two different inclusions) were distinguished. The first one is composed by composed by oxygen, silicon, potassium and aluminum, indicating inclusion of a silicate mineral. The second cluster is formed by calcium and oxygen and could be an indication of a carbonate mineral. The distribution of oxygen and iron reveals that magnetite is the matrix of the sample.

Magnetite lodestone EDS mapping detected oxygen (O), silicon (Si), iron (Fe), calcium (Ca), cobalt (Co) and gold (Au). while the minerals quartz ($SiO_2$), realgar ($As_4S_4$) and sulfide minerals were identified as mineral associations with the descriptive methods. According to (Pracejus, 2015) magnetite is commonly associated to: apatite, chalcopyrite, carbonate, chromite, hematite, ilmenite, pentlandite, pyrite, pyrrhotite, quartz, rutile, silicates, sphalerite and ulvite. On EDS mapping for magnetite lodestone, two inclusions were determined by the spatial distribution of the elements, where two clusters of elements (interpreted as two different inclusions) were distinguished. The first one is composed by oxygen, silicon and gold, which could be quartz with gold contamination. The second cluster is composed by calcium and gold and no other element was associated to it. Therefore, no further conclusion can be made regarding this specific elemental distribution. The distribution of oxygen and iron reveals that magnetite lodestone is the matrix of the sample.

Pyrite EDS mapping detected oxygen (O), silicon (Si), titanium (Ti), iron, calcium, magnesium, sodium, aluminum and sulfur while quartz ($SiO_2$) was identified as mineral association with the descriptive methods. According to (Pracejus, 2015) pyrite is commonly associated to: arsenopyrite, barite, bravoite, calcite, chalcopyrite, fluorite, galena, hematite, marcasite, pyrrhotite, quartz and sphalerite. On EDS mapping for pyrite, two inclusions were determined by the spatial distribution of the elements, where two clusters of elements, interpreted as two inclusions, were distinguished. One of the clusters is composed by oxygen, silicon, magnesium, sodium and aluminum, which could be a feldspar, although it is not a common association with pyrite. Another cluster is formed by oxygen, silicon, magnesium and sodium, which could indicate quartz with magnesium and sodium impurities. The distribution of iron and sulfur shows that pyrite is the matrix of the sample and the dispersion of titanium shows that the element occurs as contaminant in the matrix.

Pyrrhotite EDS mapping detected oxygen (O), sulfur (S), iron (Fe) and copper (Cu) while quartz ($SiO_2$), chalcopyrite ($CuFeS_2$) and sphalerite ($(Zn,Fe)S$) were identified as mineral associations with the descriptive methods. According to (Pracejus, 2015) pyrrhotite is commonly associated to: calcite, chalcopyrite, dolomite, galena, magnetite, marcasite, pentlandite, pyrite, rutile and sphalerite. On EDS mapping for pyrrhotite, three inclusions were determined by the spatial distribution of the elements, where three clusters of elements, interpreted as three inclusions, were distinguished. The first cluster only exhibited oxygen content. Another cluster observed revealed only sulfur content, hence results for these two clusters are inconclusive. A third cluster identified is formed by sulfur, iron and copper, which presumably represents chalcopyrite. The distribution of iron and sulfur shows that pyrrhotite is the matrix of the sample.

Serpentinite EDS mapping detected iron (Fe), oxygen (O), silicon (Si), aluminum (Al), magnesium (Mg), chromium (Cr), manganese (Mn), cobalt (Co) and nickel (Ni) while talc ($Mg_3Si_4O_{10}(OH)_2$), serpentine ($(Mg,Fe,Ni,Al,Zn,Mn)_{2-3}$ $(Si,Al,Fe)_2O_5(OH)_4$), relict olivine ((Fe,Mg)2SiO4) and opaque minerals were identified as mineral associations with the descriptive methods. On EDS mapping for serpentinite, one inclusion was determined by the spatial distribution of the elements, where one cluster of elements, interpreted as one inclusion, was distinguished. The inclusion is composed by aluminum and oxygen. No other elements were observed within the inclusion so no conclusions can be made regarding the mineralogy of the inclusion. The elements iron, oxygen, silicon, magnesium, chromium, manganese, cobalt and nickel which is assumed to represent a mineral from the serpentine group. Nickel, cobalt and chromium are contaminants.

The mineral inclusions inferred by EDS mapping are not precise. The minerals indicated by the method instantiate possible mineral occurrence within the samples analyzed taking into account only the elements identified but the method but not considering the petrogenesis of the samples. More reliable, quantitative, analysis is suggested as future work, such as LA-ICP-MS (Laser Ablation Inductively Coupled Mass Spectrometry).

## 6.2 The Cryogen-Free Magnet System for DC resistivity of rocks and minerals

One of the biggest achievements of the present work is the electrical resistivity results for the samples: chalcopyrite, galena, graphite, hematite, ilmenite, magnetite, magnetite, magnetite lodestone, pyrite, pyrrhotite and serpentinite; at cryogenic temperatures. Such study for these samples for temperature ranging from 10K to 300k has never been performed and it expected to contribute on future planetary missions, such as radar and GPR exploration, where such temperatures can be found. Similar studies though have been done (Brecher, Briggs, & Simons, 1975) but for carbonaceous meteorites with temperature varying from 90K to 300. The method used by the authors, for DC conductivity, was a three-electrode pulse technique at voltages varying from 40V/cm to 100V/cm. Liquid nitrogen was used to cool the system.

The Cryogen-Free Magnet System (CFMS) used for this study is circulated with helium which allows the Variable Temperature Insert (VTI) to reach cryogenic temperatures. The helium is stored in the helium dump and pumped into the system by the oil-free pump. Originally, the recommendation for sample preparation within the CFMS is soldering the sample to sample holder provided or attaching the sample to the sample holder using silver epoxy. Soldering is not an adequate option for rocks and minerals, since the heat may affect the nature of the sample. Many attempts of preparing the samples using silver epoxy to attach the sample to the holder were made. However, this method proved infeasible because the epoxy did not secure the samples very well on the holder. Moreover, it was very challenging to obtain good contacts with this method. As a consequence of that, a method for measuring DC resistivity with the CFMS was developed in this work. The sample preparation method created consists of soldering copper wires to copper plates and then attaching it to two opposite sides of the samples using silver epoxy, where two wires are placed on each side. The sample is connected to the sample platform connecting the wires direct to the platform. This method, proposed by this work, proved efficient for DC resistivity assessment with CFMS.

## 6.3 VI graphs

The dependence of voltage and current was tested by applying a linear regression to the observed data. The model was given by

$$V = \beta_0 + \beta_0 I$$

To establish the linearity between current and voltage ($V$ and $I$ respectively), the significance of $\beta_1$ was tested such that $H_0\colon \beta_1 = 0$, and $H_a\colon \beta_1 \neq 0$ where $\beta_1$ is the regression coefficient corresponding to the current.

The linear regression for chalcopyrite sample resulted in p-values varying from $7.06\text{x}10^{-189}$ to $1.86\text{x}10^{-133}$ (in the case of temperature at 80K and at 230K, respectively) for the warm-up run; and from $4.70\text{x}10^{-195}$ to $8.78\text{x}10^{-129}$ (in the case of temperature at 20K and at 60K, respectively) for the cool-down run. These p-values are effectively 0, thus suggesting that we should reject the null hypothesis. This implies that there is a strong linear relationship in these samples between current and voltage, which is further substantiated by the R-squared values equals 1 for the warm-up and cool-down runs. Cumulatively, we may infer that the chalcopyrite sample has an ohmic behavior from 20K to 300K.

The linear regression for galena sample resulted in p-values varying from $5.20\text{x}10^{-120}$ to $7.30\text{x}10^{-92}$ (in the case of temperature at 20K and at 240K, respectively) for the warm-up run; and from $2.38\text{x}10^{-121}$ to $1.06\text{x}10^{-75}$ (in the case of temperature at 20K and at 300K, respectively) for the cool-down run. These p-values are effectively 0, thus suggesting that we should reject the null hypothesis. This implies that there is a strong linear relationship in these samples between current and voltage, which is further substantiated by the R-squared values equals 1 for the warm-up and cool-down runs. Cumulatively, we may infer that the galena sample has an ohmic behavior from 20K to 300K.

The linear regression for graphite sample resulted in p-values varying from $1.88\text{x}10^{-197}$ to $3.15\text{x}10^{-177}$ (in the case of temperature at 280K and at 290K, respectively) for the warm-up run; and from $6.73\text{x}10^{-208}$ to $3.10\text{x}10^{-171}$ (in the case of temperature at 130K and at 300K, respectively) for the cool-down run. These p-values are effectively 0, thus suggesting that we should reject the null hypothesis. This implies that there is a strong linear relationship in these samples between current and voltage, which is further substantiated by the R-squared values equals to 1 for the warm-up and cool-down run. Cumulatively, we may infer that the graphite sample has an ohmic behavior from 40K to 300K.

The linear regression for hematite sample resulted in p-values varying from $2.75 \times 10^{-73}$ to $1.19 \times 10^{-31}$ (in the case of temperature at 300K and at 80K, respectively) for the warm-up run; and from $6.00 \times 10^{-76}$ to $3.45 \times 10^{-32}$ (in the case of temperature at 300K and at 80K, respectively) for the cool-down run. These p-values are effectively 0, thus suggesting that we should reject the null hypothesis. This implies that there is a strong linear relationship in these samples between current and voltage, which is further substantiated by the R-squared values which range from 0.94 to 1 (in the case of temperature at 80K and at 280K and over, respectively) for the warm-up run; and varying from 0.95 to 1 (in the case of temperature at 70K, 80K and 90K; and at 270K and over, respectively) for the cool-down run. For this work, a good R-squared fit is considered for values over 0.99. Hematite sample revealed R-squared values over 0.99 at 50K on both runs and at 240K and over in the warm-up run and at 230K and over in the cool down run. Providing these considerations, we may infer that the hematite sample does not follow the ohmic relationship at temperatures from 60K to 220K/230K. However, the sample does have an ohmic behavior at 50K and at 230K/240K and over.

The linear regression for ilmenite sample resulted in p-values varying from $3.22 \times 10^{-36}$ to $4.4 \times 10^{-8}$ (in the case of temperature at 240K and at 90K, respectively) for the warm-up run; and from $2.75 \times 10^{-39}$ to $5.35 \times 10^{-8}$ (in the case of temperature at 240K and at 90K, respectively) for the cool-down run. These p-values are very close to 0 ($<0.05$), thus suggesting that we should reject the null hypothesis. This implies that there is a strong linear relationship in these samples between current and voltage. On the other hand, R-squared values range from 0.48 to 0.97 (in the case of temperature at 90K and from 200 to 240K, respectively) for the warm-up run; and varying from 0.48 to 0.98 (in the case of temperature at 90K and from 220 to 250K, respectively) for the cool-down run. Considering that R-squared is lower than 0.99, for this work we interpret that ilmenite does not follow the ohmic relationship between current and voltage for temperature varying from 90K to 300K.

The linear regression for magnetite sample resulted in p-values varying from $7.02 \times 10^{-49}$ to $4.14 \times 10^{-16}$ (in the case of temperature at 60K and at 120K, respectively) for the warm-up run; and from $3.19 \times 10^{-49}$ to $5.91 \times 10^{-16}$ (in the case of temperature at 60K and at 120K, respectively) for the cool-down run. These p-values are effectively 0, thus suggesting that we should reject the null hypothesis. This implies that there is a strong linear relationship in these samples between current and voltage. On the other hand, R-squared values range from 0.75 to 0.99 (in the case of temperature at 120K and 60K, respectively) for the warm-up and the cool-down runs. Taking into account that R-squared values for magnetite are lower than 0.99, we infer that magnetite does not behave as an ohmic material for temperature varying from 70K to 300K. However, it is considered ohmic at 60K where R-squared is 0.99.

The linear regression for magnetite lodestone sample resulted in p-values varying from $8.02 \times 10^{-199}$ to $6.43 \times 10^{-37}$ (in the case of temperature at 160K and at 40K, respectively) for the warm-up run; and from $2.93 \times 10^{-203}$ to $1.34 \times 10^{-37}$ (in the case of temperature at 170K and at 40K, respectively) for the cool-down run. These p-values are effectively 0, thus suggesting that we should reject the null hypothesis. This implies that there is a strong linear relationship in these samples between current and voltage. On the other hand, R-squared values range from 0.97 to 1 (in the case of temperature from 40K to 60K and at 90K and over, respectively) for the warm-up and cool-down runs. It is worth to mention that R-squared for this sample is lower than 0.99 at 20K and from 40K to 70K, in the warm-up run, and from 40K to 70K in the cool-down run. Reasoning from this fact, for this study we infer that magnetite lodestone is mostly ohmic, with the exception of the temperatures which R-squared is lower than 0.99, as previously mentioned.

The linear regression for pyrite sample resulted in p-values varying from $4.50 \times 10^{-205}$ to $9.50 \times 10^{-27}$ (in the case of temperature at 300K and at 20K, respectively) for the warm-up run; and from $2.10 \times 10^{-203}$ to $1.83 \times 10^{-26}$ (in the case of temperature at 300K and at 20K, respectively) for the cool-down run. These p-values are effectively 0, thus suggesting that we should reject the null hypothesis. This implies that there is a strong linear relationship in these samples between current and voltage. On the other hand, R-squared values range from 0.91 to 1 (in the case of temperature at 20K and at 60K and over, respectively) for the warm-up and cool-down runs. It is worth to mention that R-squared for this sample is lower than 0.99 at temperatures from 20K to 50K, for both runs. Reasoning from this fact, for this study we infer that pyrite does not follow the ohmic relationship between current and voltage from 20K to 40K. However, from 60K to 300K, pyrite behaves as an ohmic material, with R-squared equals to or over 0.99.

The linear regression for pyrrhotite sample resulted in p-values varying from $2.17\times10^{-187}$ to $1.15\times10^{-139}$ (in the case of temperature at 80K and at 10K, respectively) for the warm-up run; and from $3.93\times10^{-185}$ to $5.26\times10^{-134}$ (in the case of temperature at 140K and at 10K, respectively) for the cool-down run. These p-values are effectively 0, thus suggesting that we should reject the null hypothesis. This implies that there is a strong linear relationship in these samples between current and voltage, which is further substantiated by the R-squared values equals to 1 for the warm-up and cool-down runs. Cumulatively, we may infer that the pyrrhotite sample has an ohmic behavior from 10K to 300K.

The linear regression for serpentinite sample resulted in p-values varying from $2.97\times10^{-46}$ to $3.78\times10^{-24}$ (in the case of temperature at 70K and at 130K, respectively) for the warm-up run; and from $3.35\times10^{-48}$ to $3.17\times10^{-25}$ (in the case of temperature at 70K and at 130K, respectively) for the cool-down run. These p-values are effectively 0, thus suggesting that we should reject the null hypothesis. This implies that there is a strong linear relationship in these samples between current and voltage. On the other hand, R-squared values range from 0.88 to 0.99 (in the case of temperature at 130K and 70K, respectively) for the warm-up run; and varying from 0.90 to 0.99 (in the case of temperature at 130Kand 140K; and at 70K and 80K, respectively) for the cool-down run. R-squared is 0.99 only at 70 K in the warm-up run and at 70K and 80K in the cool-down run, where serpentinite was considered ohmic. Excluding these exceptions, serpentinite behaves as a non-ohmic material.

## 6.4 Temperature dependence of resistivity

According to (Telford , Geldart, & Sheriff, 2003), minerals and rocks with resistivities between $10^{-8}$ and 1Ωm are considered conductors. Semiconductors have resistivity between 1Ωm and $10^{7}$Ωm. Minerals and rocks with resistivity over $10^{7}$Ωm are considered insulators.

In this study, chalcopyrite sample exhibited a decrease of resistivity with decrease of temperature from 300K to 230K, approximately (for the cool-down run) where resistivity varied from 0.65Ωm to 0.31Ωm; and from 300K to 190K (for the warm-up run) where resistivity varied from 0.33Ωm to 0.18Ωm. Nonetheless, resistivity increased with decrease of temperature from 200K to 20K, (for the warm-up run) where resistivity ranged from 0.11Ωm to 1.17Ωm. In the cool-down run, resistivity increased with decrease of temperature from 180K to 20K, where resistivity ranged from 0.27Ωm to 1.17Ωm. On that premise, chalcopyrite is classified as a conductor within 300K and 30K. Yet, at 20K chalcopyrite is considered a semiconductor, when resistivity is higher than 1Ωm. Telford , Geldart, & Sheriff (2003) reported resistivity range from 1.2x10$^{-5}$Ωm to 0.3Ωm for chalcopyrite, though the temperature at which the experiment was executed, was not specified by the authors.

In galena, resistivity increased with increasing temperature. Resistivity values varied from 0.02Ωm to 0.10Ωm (from 20K to 300K, respectively) in the warm-up run and the cool down runs. According to these values, galena is considered a conductor. The expected resistivity range for galena is 3x10$^{-5}$Ωm to 3x10$^{2}$, according to Telford , Geldart, & Sheriff (2003). The resistivity range obtained in this work is within the literature values. However, the temperature at which resistivity from the literature was acquired is unknown.

In graphite, resistivity decreases as temperature decreases from 300K to 240K, as it varies from 9.82x10$^{-4}$Ωm to 7.56x10$^{-4}$Ωm, respectively, (in the warm-up run) and from 3.98x10$^{-4}$Ωm to 3.26 x10$^{-4}$Ωm, respectively (in the cool-down run). However, it was observed that resistivity increases as temperature decreases within 230K to 40K, where resistivity varies from 7.57x10$^{-4}$Ωm to 8.39x10$^{-4}$Ωm, in the warm-up run, and from 3.28x10$^{-4}$Ωm to 3.94x10$^{-4}$Ωm, in the cool down run. According to that, graphite is classified as conductor. Telford , Geldart, & Sheriff (2003) reported resistivity varying from 10$^{-4}$Ωm to 5x10$^{-3}$Ωm for massive graphite, but the temperature at which these values were obtained was not identified by the authors.

In hematite, resistivity increases as temperature decreases. Resistivity varies from 89.87Ωm to 284410.80Ωm (in the case of temperature at 300K and at 50K, respectively) for the warm-up run; and from 71.005Ωm to 238561.85Ωm (in the case of temperature at 300K and at 50K, respectively) for the cool-down run. Hematite is then classified as semiconductor. Resistivity of hematite was previously reported by Telford , Geldart, & Sheriff (2003), where values vary from 3.5x10$^{-5}$Ωm to 10$^{7}$Ωm. The temperature at which resistivity was obtained was not mentioned by the authors.

In ilmenite, resistivity increases as temperature decreases. Resistivity varies from 4.45Ωm to 572.85Ωm (in the case of temperature at 300K and at 90K, respectively) for the warm-up run; and from 5.74Ωm to 565.71Ωm (in the case of temperature at 300K and at 90K, respectively) for the cool-down run. Taking that into account, ilmenite then classified as a conductor. Resistivity of ilmenite was previously reported by Telford , Geldart, & Sheriff (2003), where values vary from $10^{-3}$Ωm to 50Ωm. The temperature at which resistivity was obtained was not mentioned by the authors.

In magnetite, resistivity increases as temperature decreases from 300K to 130K. Resistivity varies from 3528.15Ωm to 64608.19Ωm (at 300K and at 130K, respectively) for the warm-up run; and from 2431.55Ωm to 53538.41Ωm (at 300K and at 130K, respectively) for the cool-down run. These values indicate that magnetite is a semiconductor. No clear pattern of temperature and resistivity dependence was observed for temperatures below 120K. Resistivity values for magnetite varying from $5\times10^{-5}$Ωm to $5.7\times10^{3}$Ωm was reported by Telford , Geldart, & Sheriff (2003), at unknown temperature.

In magnetite lodestone, resistivity increases as temperature decreases. Resistivity varies from 0.16Ωm to 51524.61Ωm (in the case of temperature at 300K and at 30K, respectively) for the warm-up run; and from 0.17Ωm to 60094.59Ωm (in the case of temperature at 300K and at 30K, respectively) for the cool-down run. A decrease of resistivity was noticed from 30K to 20K, changing from 51524.61Ωm to 44216.67Ωm, for the warm-up run, and from 60094.59Ωm to 43338.06Ωm, for the cool-down run. Against this background, magnetite lodestone can be classified as a conductor or semiconductor, depending on the temperature. For this sample resistivity higher than one was observed from 140K to 20K, which means that the sample is semiconductor within this interval. From 150K to 300K, magnetite lodestone is a conductor. Resistivity values for magnetite varying from $5\times10^{-5}$Ωm to $5.7\times10^{3}$Ωm was reported by Telford , Geldart, & Sheriff (2003), at unknown temperature.

In pyrite, resistivity increases as temperature decreases. Resistivity varies from 0.34Ωm to 626.11Ωm (in the case of temperature at 300K and at 20K, respectively) for the warm-up run; and from 0.29Ωm to 658.25Ωm (in the case of temperature at 300K and at 20K, respectively) for the cool-down run. That said, pyrite can be classified as a conductor or semiconductor, depending on the temperature. For this sample resistivity higher than one was observed from 170K to 20K, which means that the sample is semiconductor within this interval. From 180K to 300K, pyrite is a conductor. Telford , Geldart, & Sheriff (2003) reported resistivity values for pyrite varing from $2.9 \times 10^{-5} \Omega m$ to $1.5 \Omega m$, at unknown temperature.

In pyrrhotite, resistivity increases as temperature decreases. Resistivity varies from 0.06Ωm to 0.26Ωm (in the case of temperature at 300K and at 10K, respectively) for the warm-up run; and from 0.04Ωm to 0.24Ωm (in the case of temperature at 300K and at 10K, respectively) for the cool-down run. Taking that into account, pyrrhotite then classified as a conductor. Resistivity of pyrrhotite was previously presented by Telford , Geldart, & Sheriff (2003), where values vary from $6.5 \times 10^{-6} \Omega m$ to $5 \times 10^{-2} \Omega m$. The temperature at which resistivity was obtained was not mentioned by the authors.

In serpentinite, resistivity increases as temperature decreases from 300K to 100K. Resistivity varies from 1597.50Ωm to 44223.43Ωm (at 300K and at 100K, respectively) for the warm-up run; and from 1385.97Ωm to 35594.34Ωm (at 300K and at 100K, respectively) for the cool-down run. These values indicate that serpentinite is a semiconductor. No clear pattern of temperature and resistivity dependence was observed for temperatures below 100K. The highest resistivity value observed was found at 40K, in the warm-up run, where resistivity was 44223.43 Ωm; and at 60K in the cool-down run, where resistivity was 36444.62Ωm.Telford, Geldart, & Sheriff (2003), do not report resistivity values for serpentinite but they do present resistivy for serpentine, the major rock-forming mineral of serpentinite. The values for serpentine reported by the authours vary from $2 \times 10^{2} \Omega m$ to $3 \times 10^{3} \Omega m$.

The conduction of electrons depends on the number of free electrons and charged holes in the atoms. The valence band is the last energy level within an atom that is filled with electrons. The electrons become free when they move to an outer empty band called conduction band. The difference between conductors, semiconductors and insulators is how apart the valence and conduction bands are. In conductors, the two bands overlap. In semiconductors and insulators there is a gap separating these two bands, which is called band gap. The band gap in insulators are wider than in semiconductors. Taking that into consideration, semiconductors and insulators need more energy to excite electrons enough to reach the conduction band. For these materials, conduction is achieved with heat energy. In other words, conductivity increases as temperature increases and resistivity decreases as temperature increases in semiconductors and insulators. For metals, or conductors, resistivity increases as temperature increases, as electron scattering also increases (Callister & Rethwisch, 2009).

In this work, chalcopyrite, galena, graphite and pyrrhotite were classified as conductors, while hematite, ilmenite, magnetite, and serpentinite as semiconductors. Magnetite lodestone and pyrite are partially conductors and partially semiconductors, depending on the temperature. Magnetite lodestone is semiconductor below 160K and pyrite, bellow 180K. Among the conductors, only galena revealed a typical conductor resistivity over temperature graph, where resistivity increases as temperature increases. Even though the measured resistivity of pyrrhotite is considered of a conductor, its resistivity over temperature graph exhibit a semiconductor trend, with resistivity decreasing as temperature increases. Chalcopyrite and graphite presented ambiguous relationship between resistivity and temperature. A conductor trend was observed for temperature over 160K in chalcopyrite and over 250K in graphite. Below these temperatures, respectively, the samples behaved as semiconductors, showing a decrease of resistivity with increasing temperature. Hematite, ilmenite, magnetite and seperntinite revealed a typical semiconductor relationship between resistivity and temperature.

# 7 Conclusions

Electrical DC resistivity of graphite, serpentinite, oxide minerals (ilmenite, magnetite, and hematite) and sulfide minerals (chalcopyrite, galena, pyrite and pyrrhotite) was assessed using the Cryogen-Free Magnet System (CFMS) at the Planetary Instrumentation Laboratory (PIL) at York University. The measurements were executed at temperatures varying from 10K to 300K, with 10K increment. A method for sample preparation suitable for rocks and minerals for DC resistivity analysis with the CFMS was developed in this work and it is a great contribution for future work. The samples were characterized by hand sample examination and with the use of a petrological microscope. Additionally, EDS mapping was used for chemical elements distribution within the samples. Current versus voltage graphs were generated and linear regression was applied to identify whether the samples would behave as an ohmic material. It was observed that chalcopyrite, galena, graphite and pyrrhotite have an ohmic behavior from 10K, approximately, to 300K; while ilmenite, magnetite and serpentinite do not follow the ohmic relationship between voltage and current. Some of the samples revealed an ohmic pattern depending on the temperature. For instance, magnetite lodestone showed ohmic response between 90K and 300K. Similarly, pyrite presented the same effect from 60K to 300K. Hematite presented ohmic relationship at 290K and 300K. Resistivity results were compared to the results presented by Telford , Geldart, & Sheriff (2003). It is worth to mention that even within the same mineral or rock, resistivity can be very diverse (Parasnis, 1956). This is due to the fact that mineral inclusions, cracks, porous and loose structure, for instance, can affect resistivity (Parasnis, 1956). Temperature dependency of resistivity was analyzed for each sample. In general, it was observed that for most of the samples resistivity increased with decreasing temperature. Galena, on the other hand presented and increase of resistivity with increasing temperature.

This work foments basis for future studies of electrical DC resistivity of rocks and minerals at cryogenic temperatures, in application to possible planetary geophysical missions. Succeeding work should include a bigger variety of samples, including meteorites and other planetary rocks. It is recommended a more accurate chemical composition analysis such as LA-ICP-MS (Laser Ablation Inductively Coupled Mass Spectrometry).

# References

Ali, W., & Shieh, S. R. (2014). Exploring Shallow Subsurface of Mars and Introducing the GPR Technique for Planetary Sciences(Exploring Mars beyond the Surface Features). *Journal of Geology & Geosciences, 3*(1), 1-5.

Angelopoulos, M., Redman, D., Pollard, W. H., Haltigin, T. W., & Dietrich, P. (2014). Lunar ground penetrating radar: Minimizing potential data artifacts caused by signal interaction with a rover body. *Advances in Space Research, 54*, 2059–2072.

Ayala-Cabrera, D., Herrera, M., Montalvo, I., & Pérez-García, R. (2011). Towards the visualization of water supply system components with GPR images. *Mathematical and Computer Modelling, 54*, 1818–1822.

Boivin, A. L., Hickson, D., Tsai, C., Ghent, R. R., & Daly, M. G. (2018). Broadband measurements of the complex permittivity of carbonaceous asteroid regolith analog materials. *Jornal of Geophysical Research: Planets, 123*, 3088-3104.

Brecher, A., Briggs, P. L., & Simons, G. (1975). THE LOW-TEMPERATURE ELECTRICAL PROPERTIES OF CARBONACEOUS METEORITES . *Earth and Planetary Science Letters*, 37-45.

Callister, W. D., & Rethwisch, D. G. (2009). *Materials Science and Engineering: An Introduction* (Vol. 8th edition). Hoboken, NJ, USA: John Wiley & Sons, Inc.

Campbell, B. A. (2002). *Radar remote sensing of planetary surfaces.* Cambridge: The press syndicate of the University of Cambridge.

Cryogenic Ltd. (2014). *Mini Cryogen-Free Magnet System user manual. DC Resistance probe.* London.

Cutnel, J. D., & Johnson, K. W. (1995). *Physics.* New York: John Wiley & Sons, Inc.

Daintith, J. (2010). *A Dictionary of Physics (6 ed.).* Oxford: Oxford University Press.

Daniels, D. J. (2004). *Ground penetrating radar.* London: The Institutuion of Electrical Engineers.

Elachi, C. (1988). *Spaceborne radar remote sensing: applications and techniques.* New York: The Institute of Electrical and Electronics Engineers, Inc.

Fang, G.-Y., Zhou, B., Ji, Y.-C., Zhang, Q.-Y., Shen, S.-X., Li, Y.-X., . . . Wang, S.-Z. (2014). Lunar Penetrating Radar onboard the Chang'e-3 mission. *Research in Astronomy and Astrophysics, 14*(12), 1607–1622.

Feldman, Y., Gusev, Y. A., & Vasilyeva, M. A. (2012). Dielectric relaxation phenomena in complex systems. *Advances in Chemical Physics,, 133*, 1-123.

Ghosh, S. (2010). *Fundamentals of electrical and electronics engineering* (Second ed.). New Delhi: PHI Learning Private Limited.

Giancoli, D. C. (1988). *Physics for scientists and engineers.* New Jersey: Prentice-Hall.

Halliday, D., Resnick, R., & Krane, K. S. (1992). *Physics.* New York: John Wiley & Sons, Inc.

Harding Jr, L. W., Miller, W. D., Swift, R. N., & Wright, C. W. (2001). Aircraft Remote Sensing. *Encyclopedia of Ocean Sciences (Second Edition)* , 138-146.

Hickson, D., Boivin, A., Daly, M. G., Ghent, R., Nolan, M. C., Tait, K., . . . Tsai, C. A. (2018). Near surface bulk density estimates of NEAs from radar observations and permittivity measurements of pwdered geologic material. *Icarus*, 16-24.

Hickson, D., Sotodeh, S., Daly, M. G., Ghent, R., & Nolan, M. C. (2017). Improvements on effective permittivity measurements of powdered alumina: Implications for bulk permittivity properties of asteroid regoliths. *Advances in Space Research*, 472-482.

Kao, K. C. (2004). 6 - Charge Carrier Injection from Electrical Contacts. In K. C. Kao, *Dielectric Phenomena in Solids With Emphasis on Physical Concepts of Electronic Processes* (pp. 327-380). Academic Press .

Keithley Instruments, Inc. (1998). *2400 Series SourceMeter® User's Manual.* Cleveland, Ohio.

Keithley Instruments, Inc. (2017). *Model 2182 and 2182A Nanovoltmeter User's Manual.* Cleveland, Ohio.

Kim, S. S., Carnes, S. R., & Ulmer, C. T. (2012). Miniature Ground Penetrating Radar (GPR) for Martian Exploration: Interrogating the shallow subsurface of Mars from the surface. *Concepts and Approaches for Mars Exploration* .

Kumar, N. (2010). *Comprehensive Physics XII.* New Delhi: Laxmi Publications Pvt Limited.

Kuo, J. (2014). *Electron Microscopy. Methods and Protocols.* (Third ed.). New York: Humana Press.

Parasnis, D. S. (1956). The electrical resistivity of some sulphide and oxide mierals and their ores. *Tenth meeting of the European Association of Exploration Geophysics*, (pp. 249-278). Hamburg.

Persico, R. (2014). *Introduction to Ground Penetrating Radar.* John Wiley & Sons, Inc.

Porcello, L. G., Jordan, R. L., Zelenka, J. S., Adams, G. F., Phillips, R. J., Brown Jr., W. E., . . . Jackson, P. L. (1974). The Apotlo Lunar Sounder Radar System. *PROCEEDINGS OF THE IEEE*, (pp. 769-783).

Pracejus, B. (2015). *The ore minerals under the microscope. An optical guide.* (Second ed., Vol. 3). Muscat, Oman: Elsevier.

Richards, J. A. (2009). *Remote Sensing with Imaging Radar.* Springer Berlin Heidelberg.

Schrott, L., Otto, J.-C., Götz, J., & Geilhausen, M. (2013). Fundamental Classic and Modern Field Techniques in Geomorphology: An Overview. *Treatise on Geomorphology, 14*, 6-21.

Stillman, D., & Olhoeft, G. (2008). Frequency and temperature dependence in electromagnetic properties of martian analog minerals. *Journal of geophysical research*, 1-14.

Telford , W. M., Geldart, L. P., & Sheriff, R. E. (2003). Electrical properties of rocks and minerals. In *Applied geophysics* (pp. 283-292). Cambridge, United Kingdom.

Ulaby, F. T. (2014). *Microwave Radar and Radiometric Remote Sensing.* Artech House.

Vasavada, A. R., Bandfield, J. L., Greenhagen, B. T., Hayne, P. O., Siegler, M. A., Williams, J.-P., & Paige, D. A. (2012). Lunar equatorial surface temperatures and regolith properties from the Diviner Lunar Radiometer Experiment. *Journal of Geophysical Research, 117*(E00H18), 1-12.

# Appendices

## Appendix A: Current versus voltage graphs

### *Chalcopyrite*

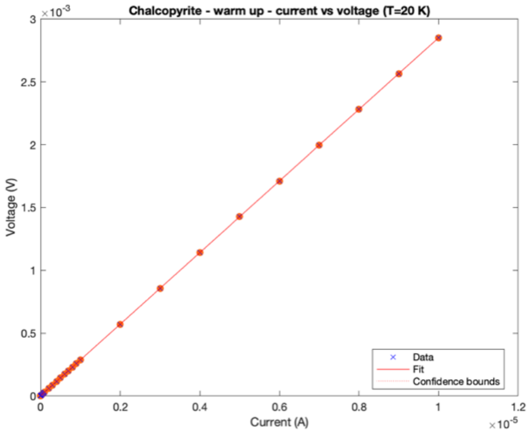

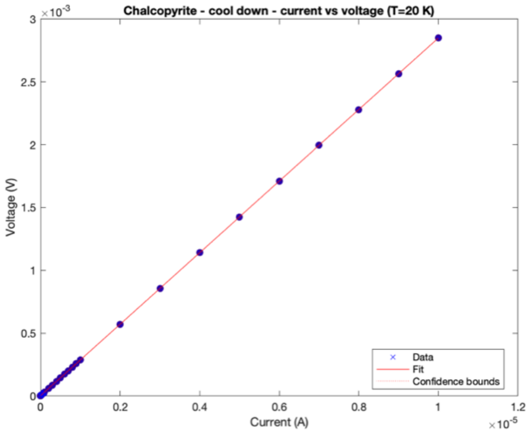

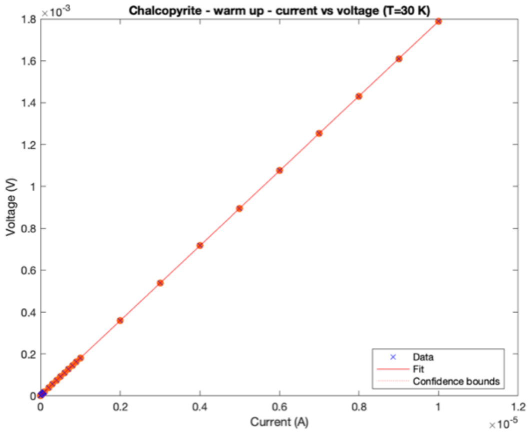

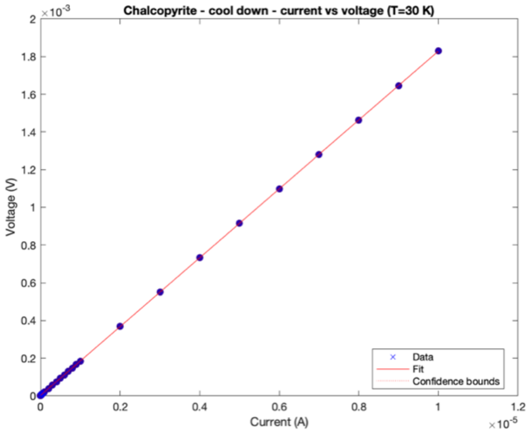

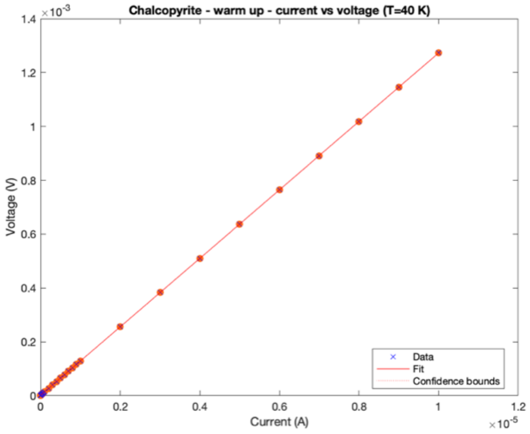

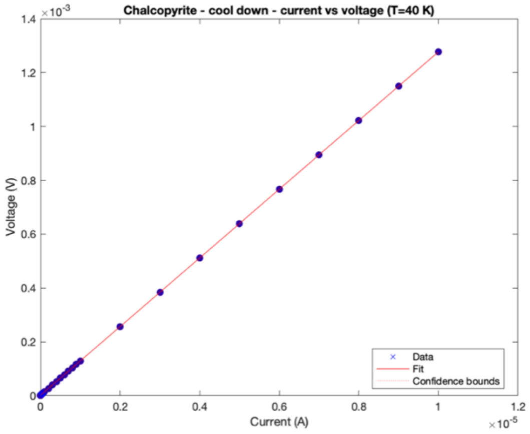

Figure 63: Chalcopyrite voltage versus current graphs. Temperature range: 20K to 40K.

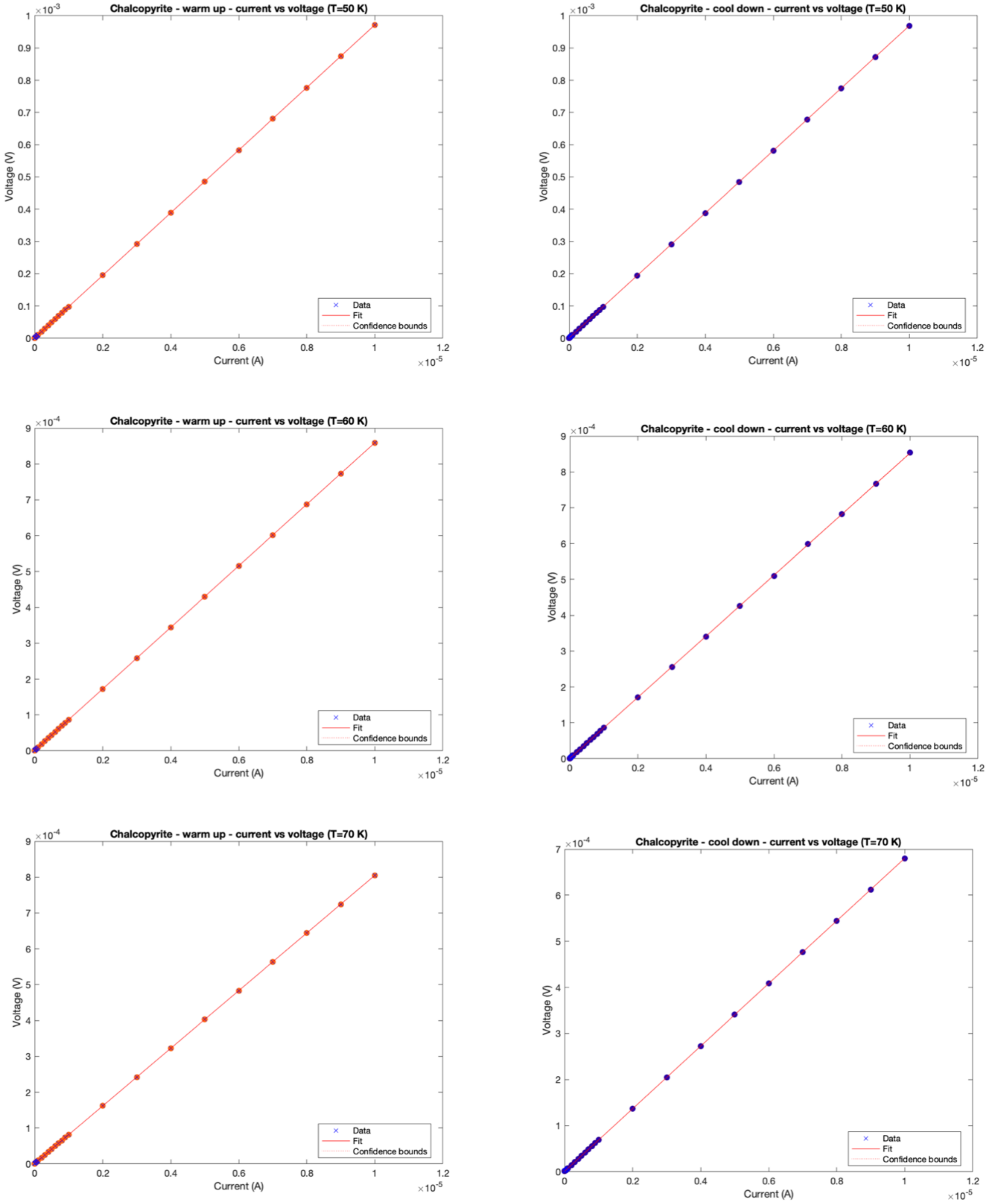

Figure 64: Chalcopyrite voltage versus current graphs. Temperature range: 50K to 70K.

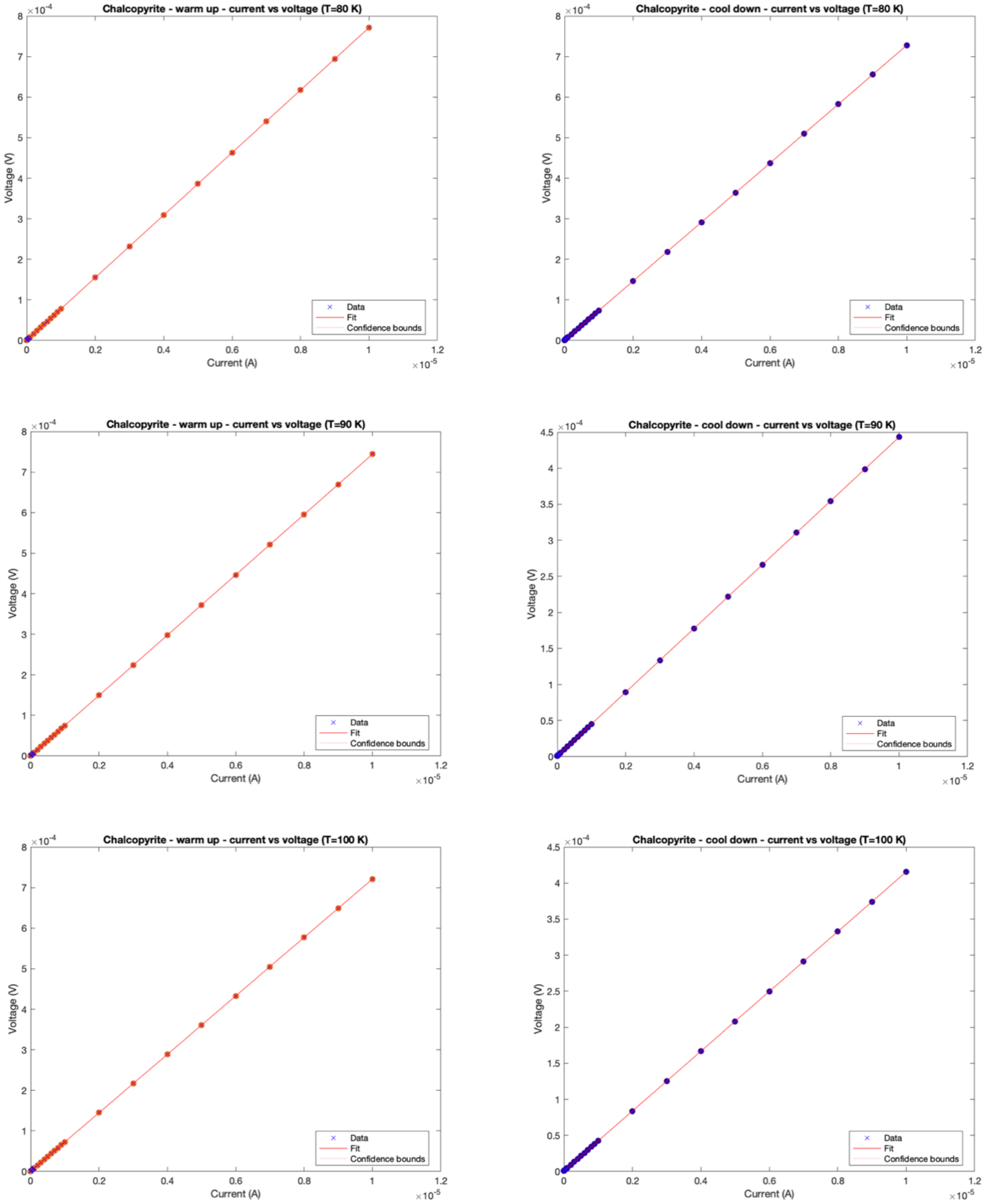

Figure 65: Chalcopyrite voltage versus current graphs. Temperature range: 70K to 100K.

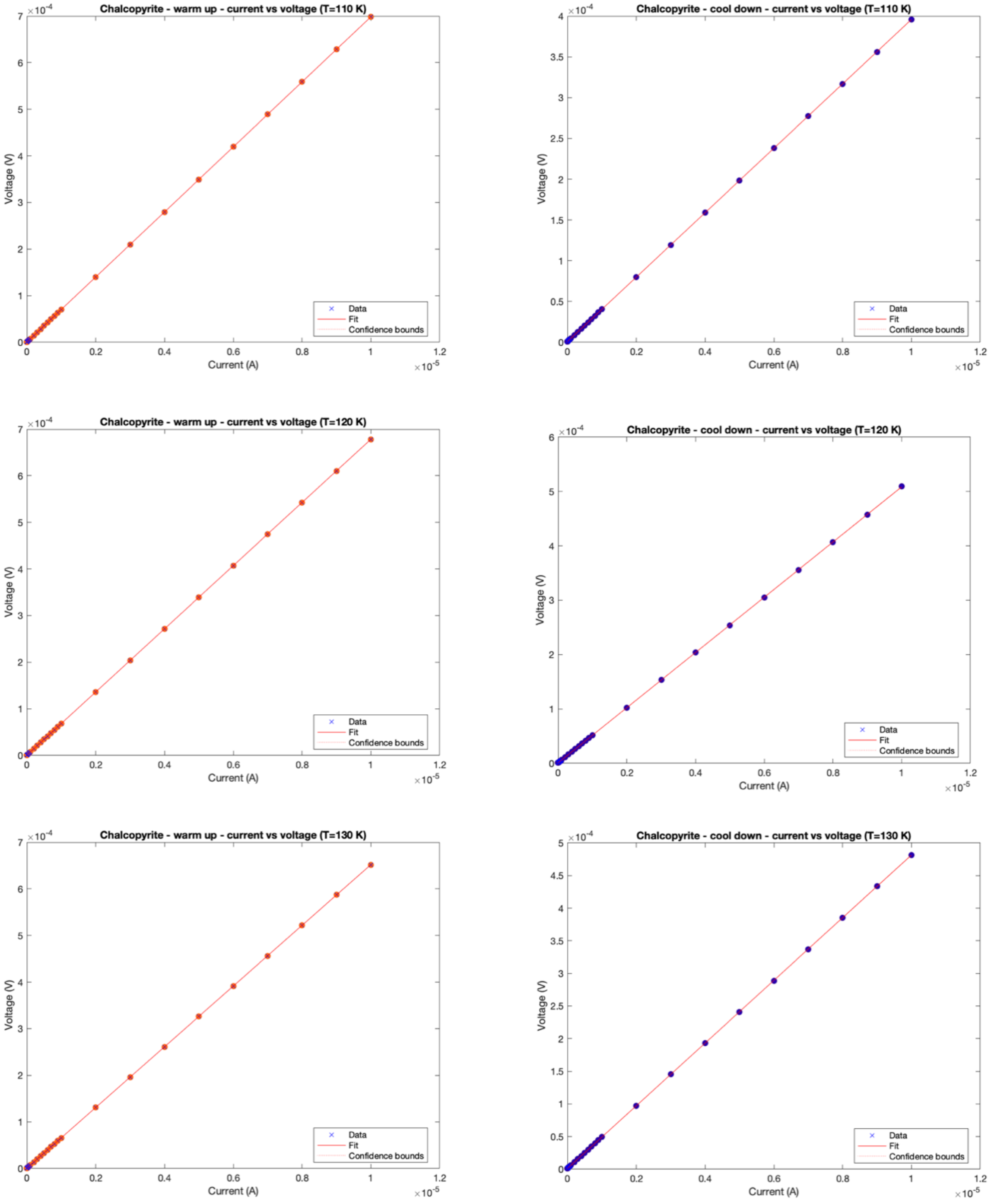

Figure 66: Chalcopyrite voltage versus current graphs. Temperature range: 110K to 130K.

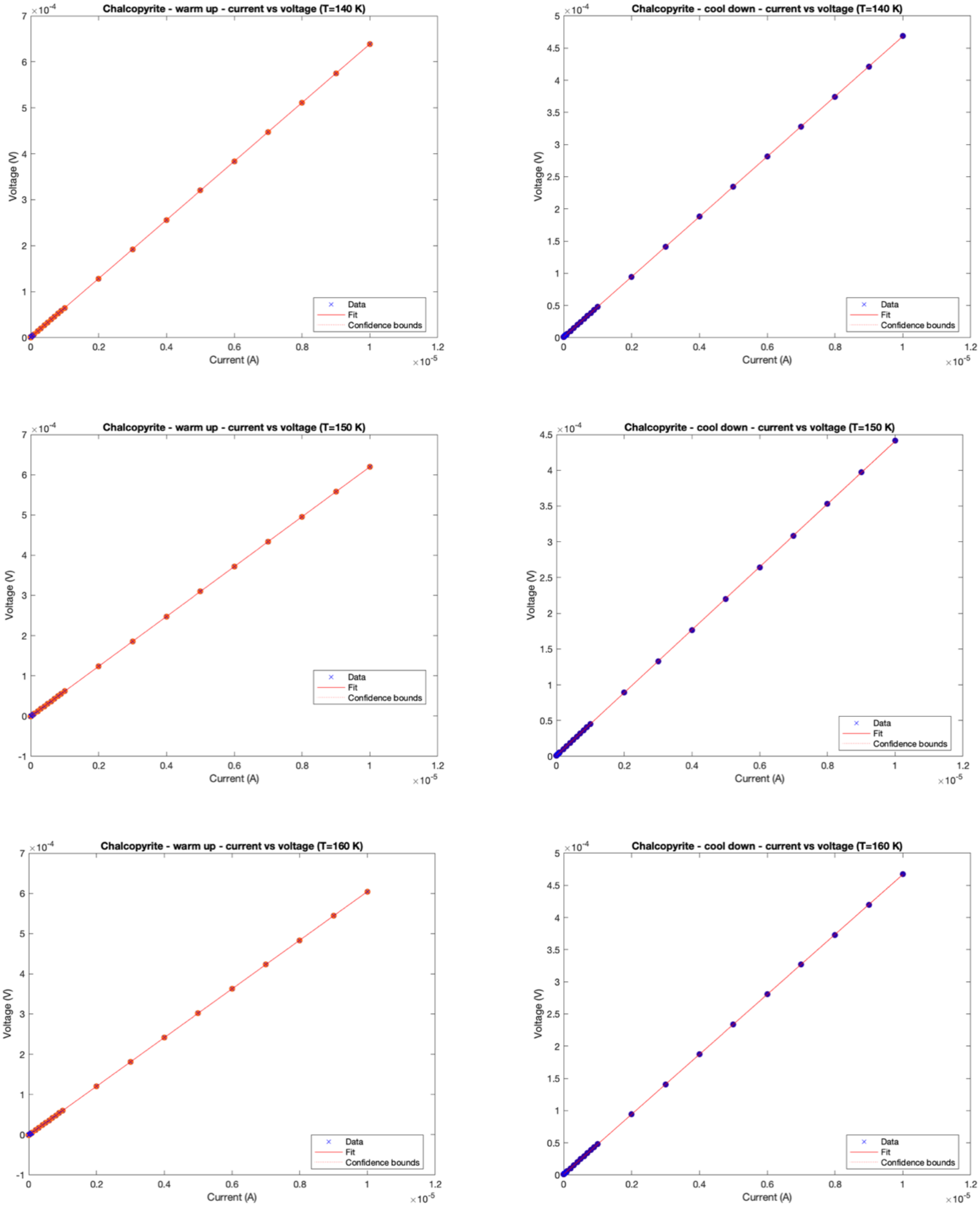
Chalcopyrite - warm up - current vs voltage (T=140 K)

Chalcopyrite - cool down - current vs voltage (T=140 K)

Chalcopyrite - warm up - current vs voltage (T=150 K)

Chalcopyrite - cool down - current vs voltage (T=150 K)

Chalcopyrite - warm up - current vs voltage (T=160 K)

Chalcopyrite - cool down - current vs voltage (T=160 K)

Figure 67: Chalcopyrite voltage versus current graphs. Temperature range: 140K to 160K.

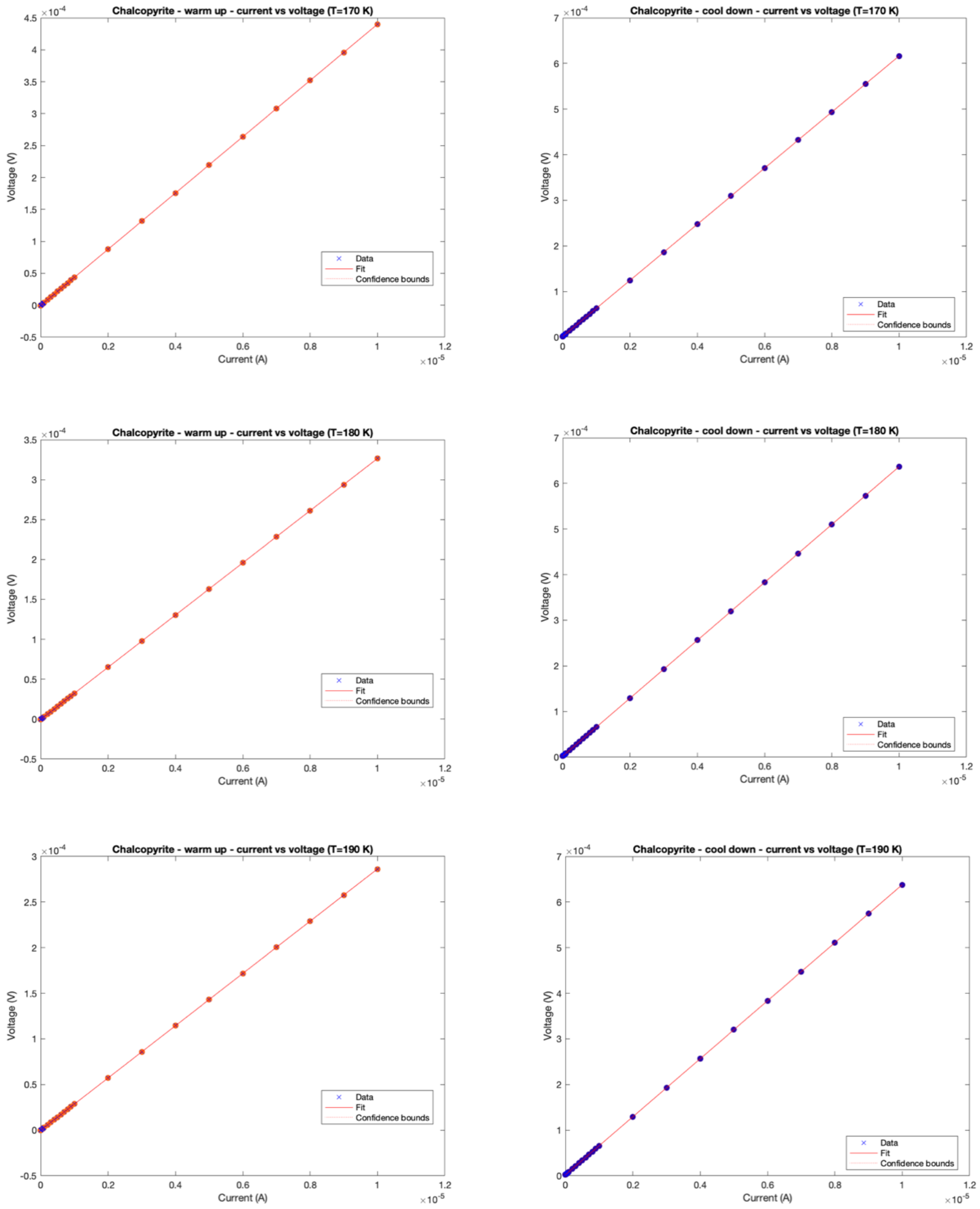

Figure 68: Chalcopyrite voltage versus current graphs. Temperature range: 170K to 190K.

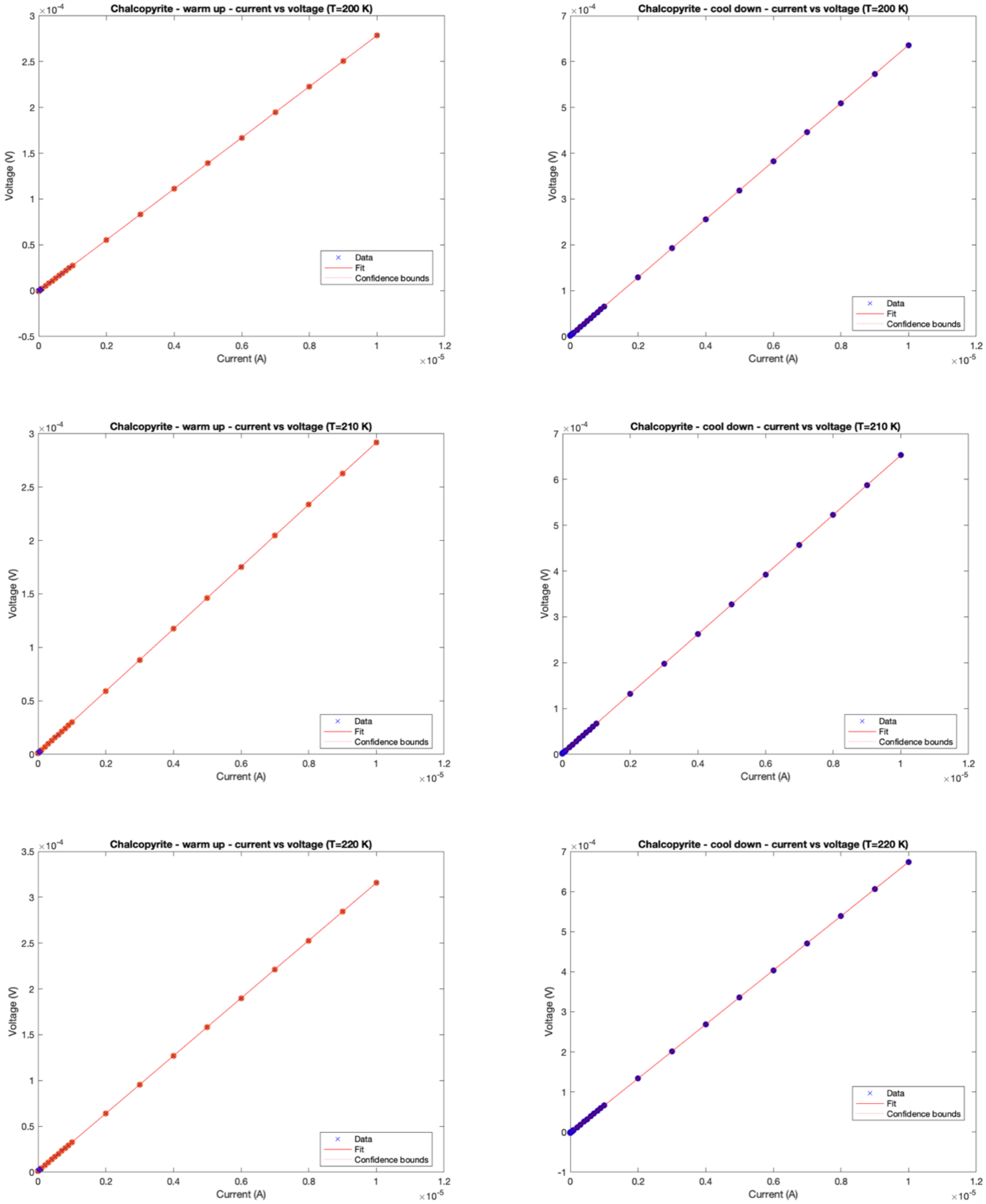

Figure 69: Chalcopyrite voltage versus current graphs. Temperature range: 200K to 220K.

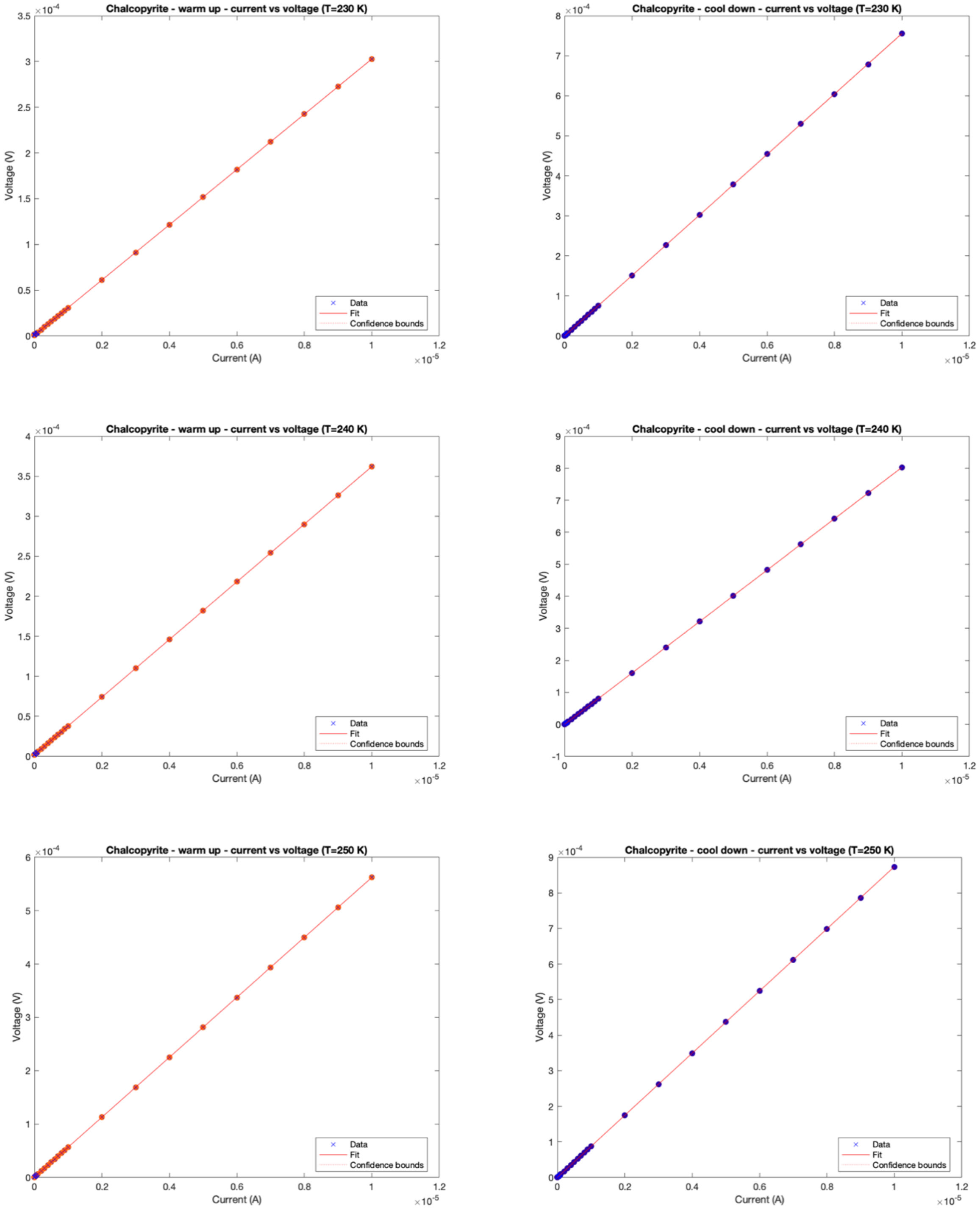

Figure 70: Chalcopyrite voltage versus current graphs. Temperature range: 230K to 250K.

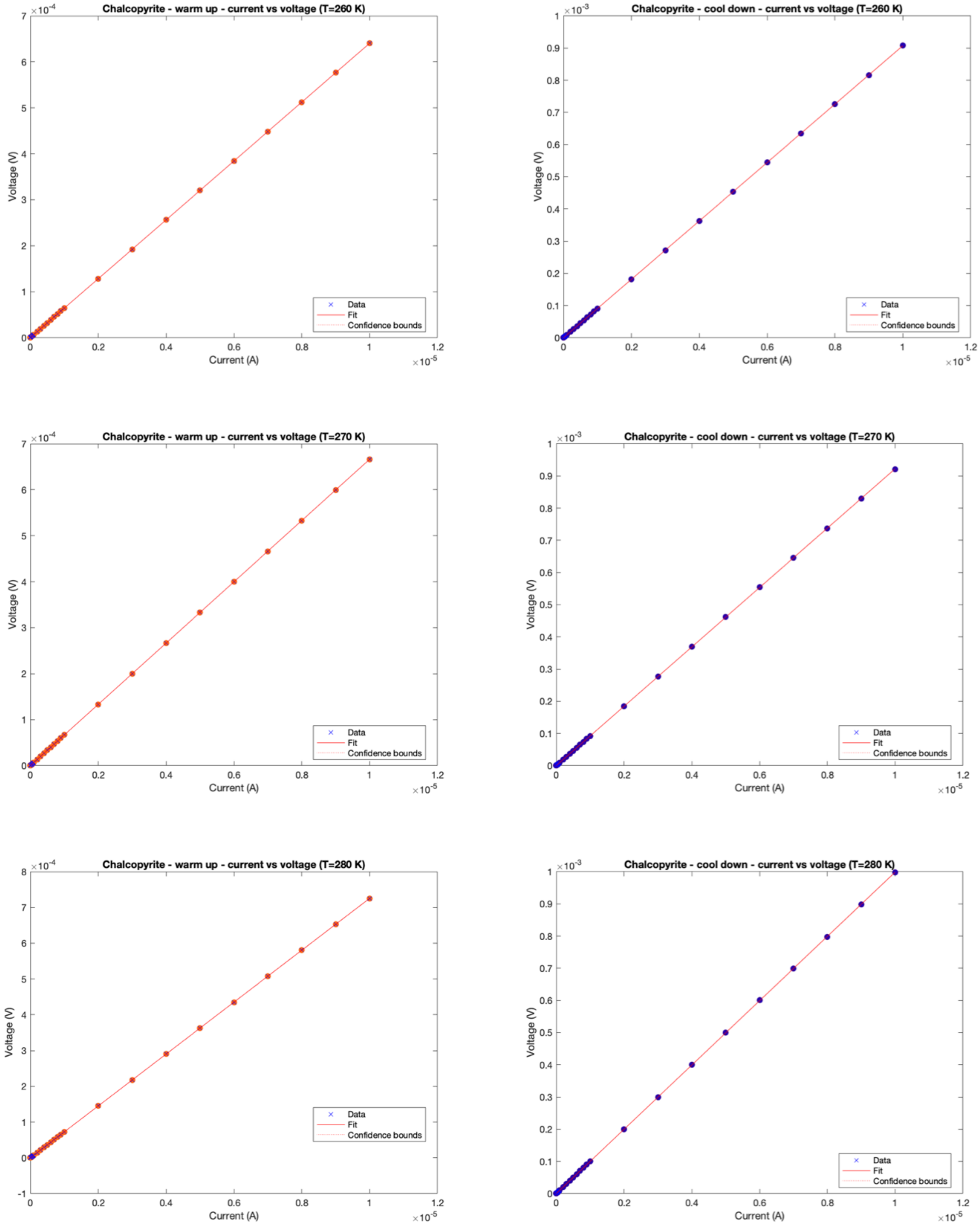

Figure 71: Chalcopyrite voltage versus current graphs. Temperature range: 260K to 280K.

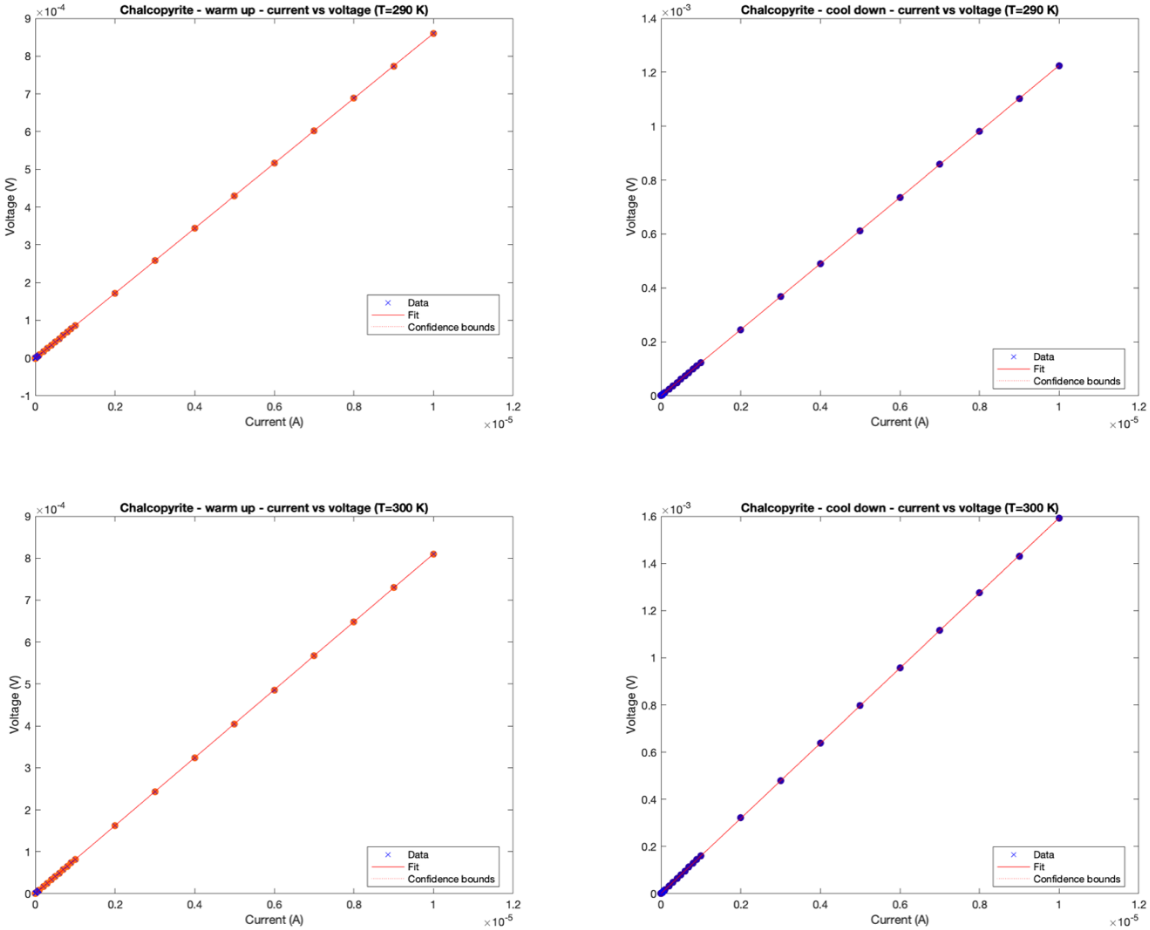
Chalcopyrite - warm up - current vs voltage (T=290 K)

Chalcopyrite - cool down - current vs voltage (T=290 K)

Chalcopyrite - warm up - current vs voltage (T=300 K)

Chalcopyrite - cool down - current vs voltage (T=300 K)

Figure 72: Chalcopyrite voltage versus current graphs. Temperature range: 290K to 300K.

## *Galena*

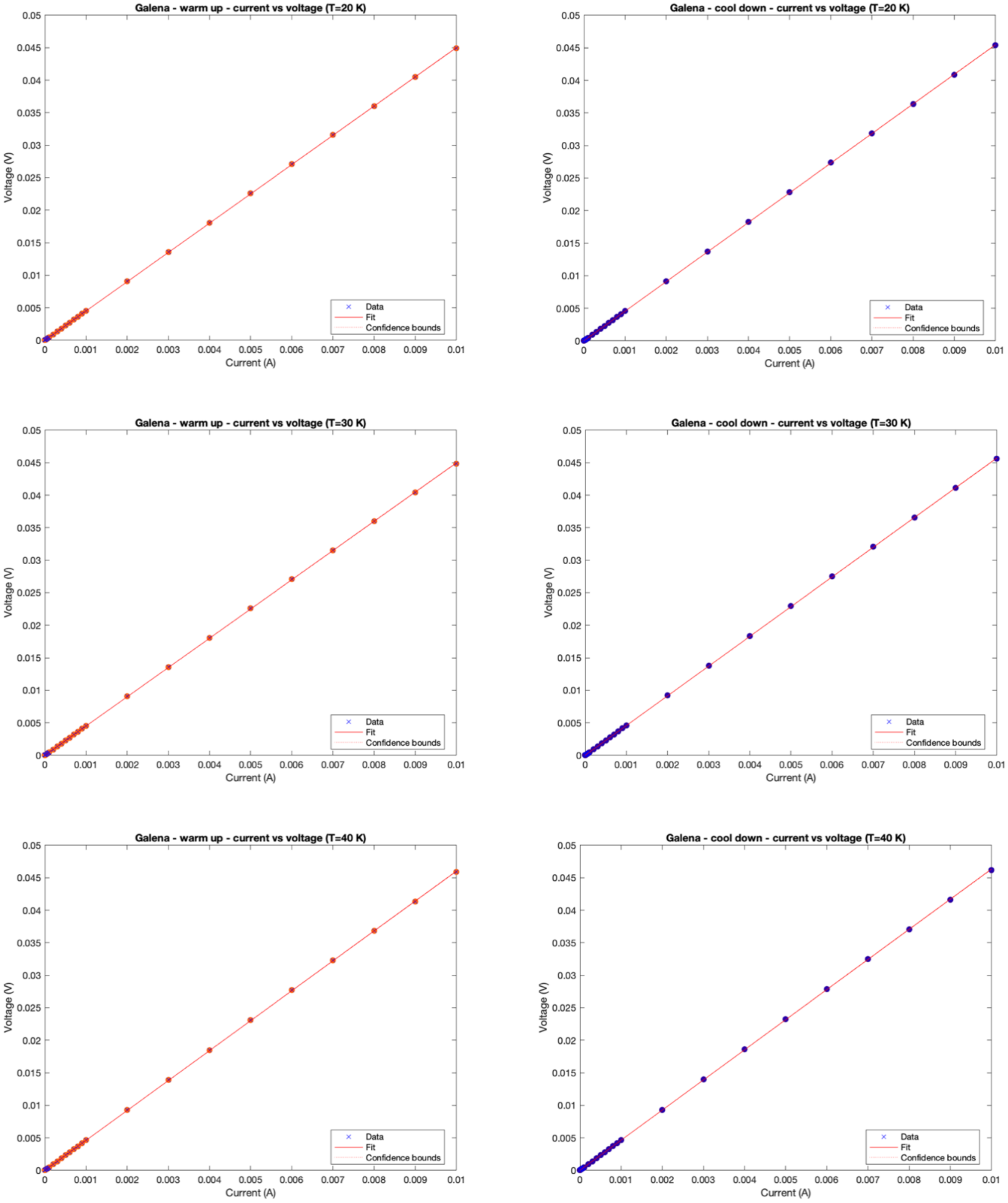

Figure 73: Galena voltage versus current graphs. Temperature range: 20K to 40K.

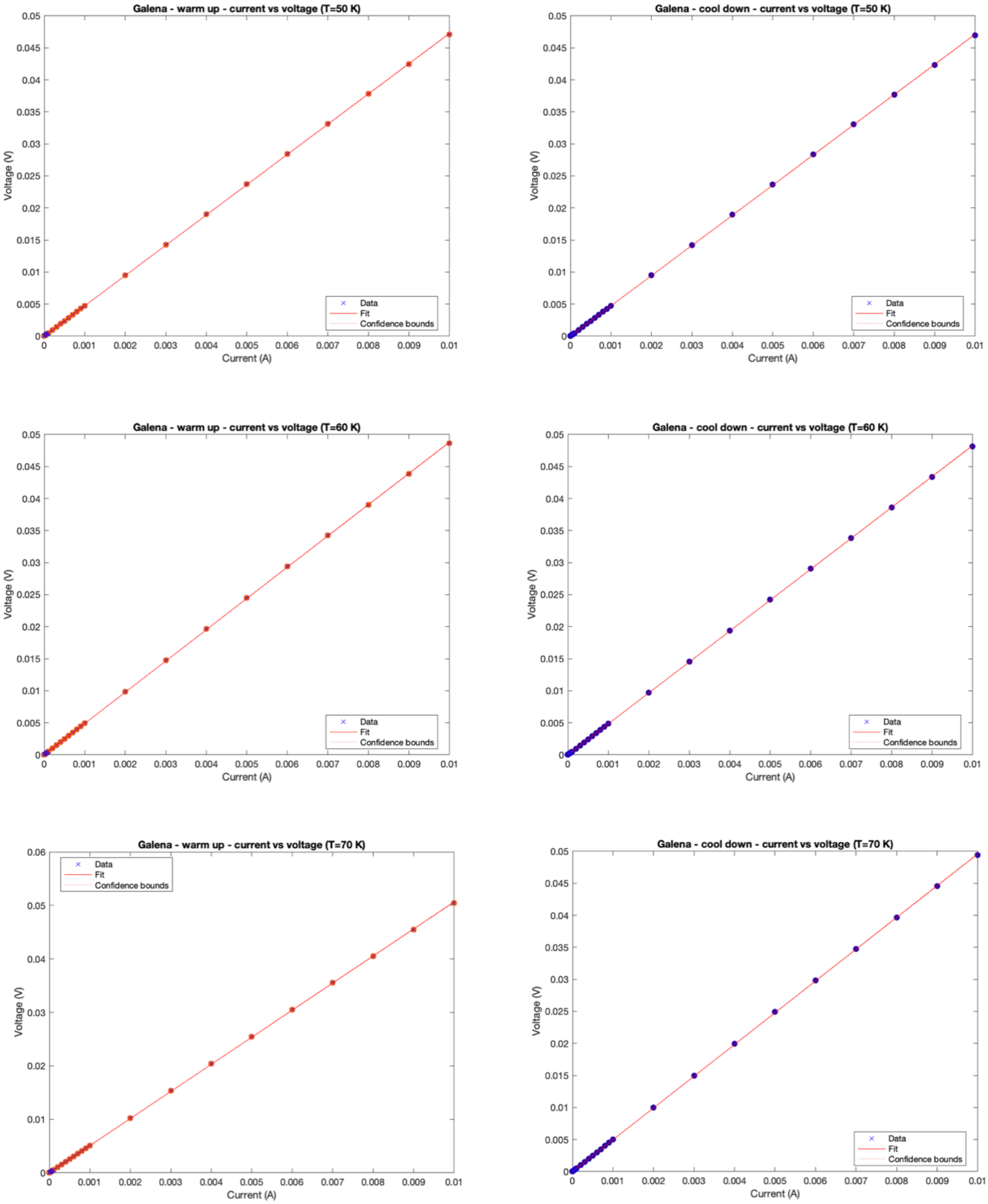

Figure 74: Galena voltage versus current graphs. Temperature range: 50K to 70K.

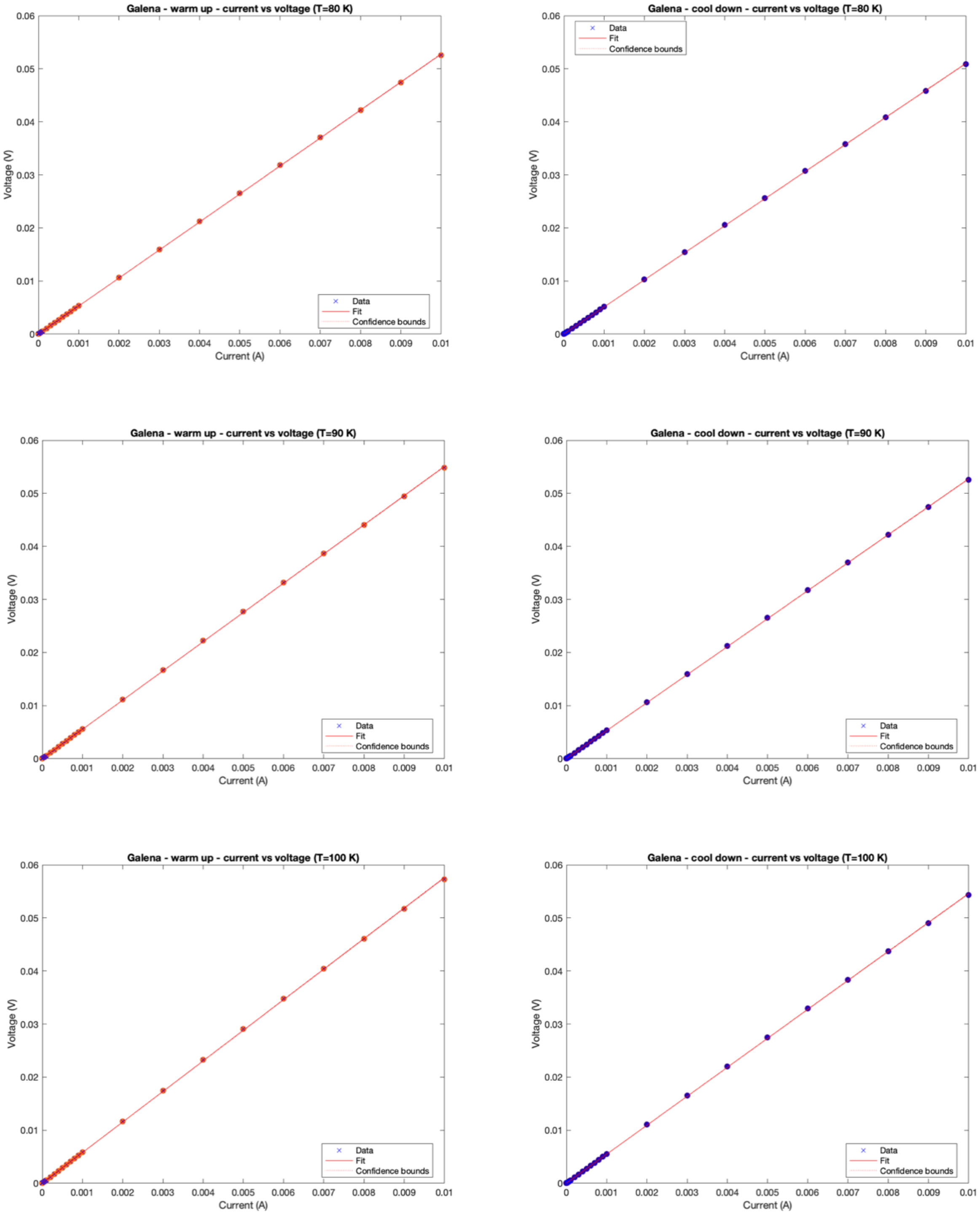

Figure 75: Galena voltage versus current graphs. Temperature range: 80K to 100K.

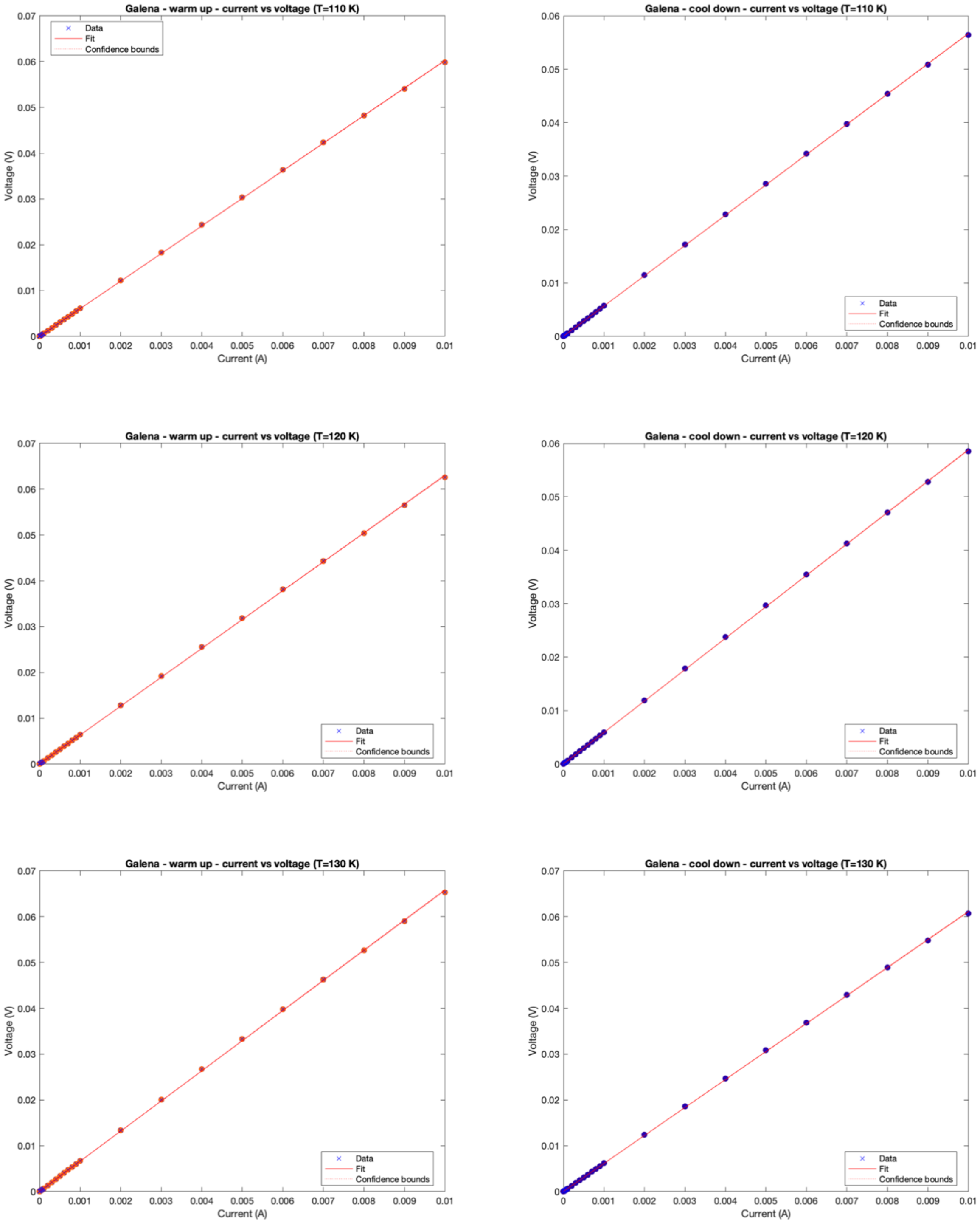

Figure 76: Galena voltage versus current graphs. Temperature range: 110K to 130K.

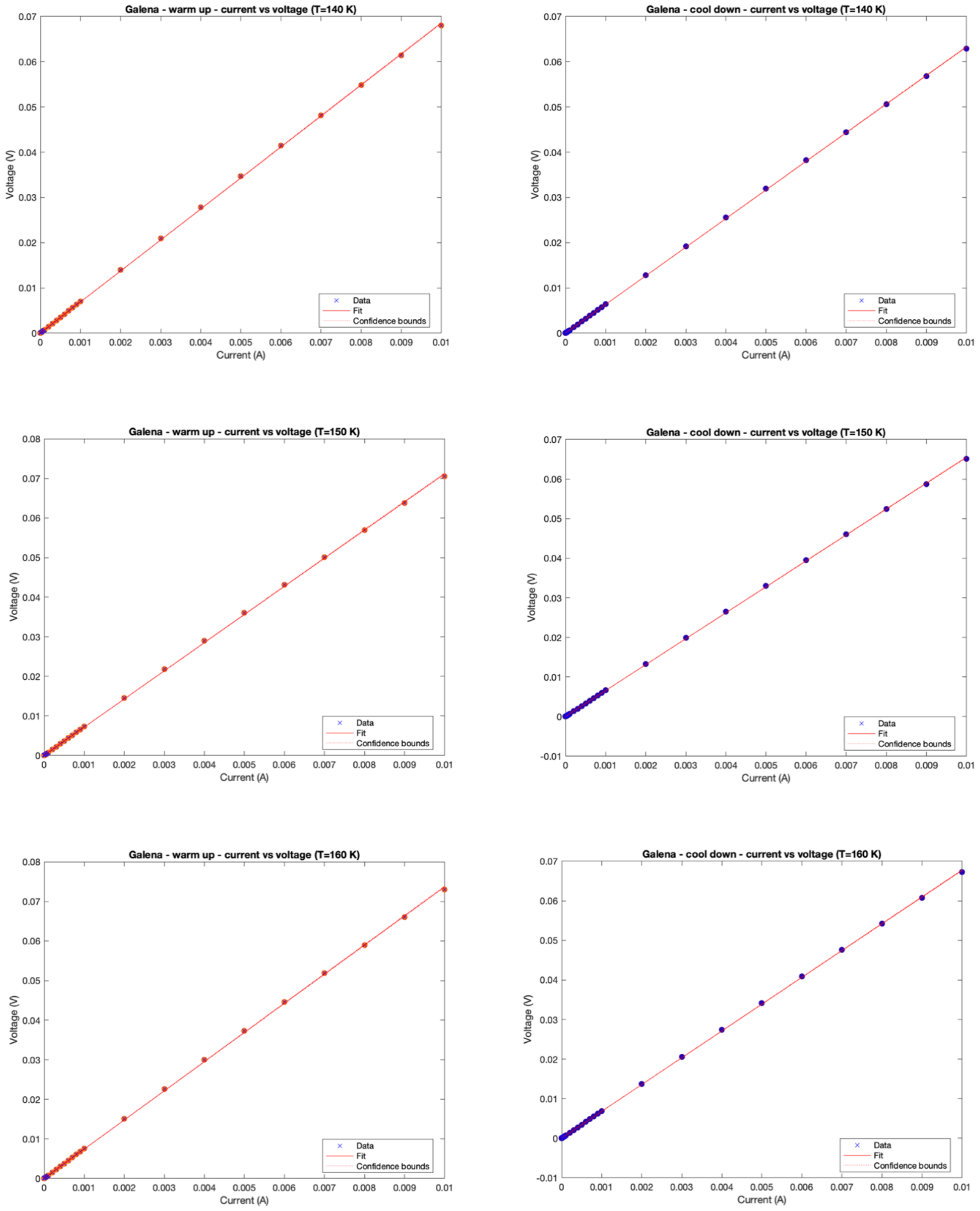

Figure 77: Galena voltage versus current graphs. Temperature range: 140K to 160K.

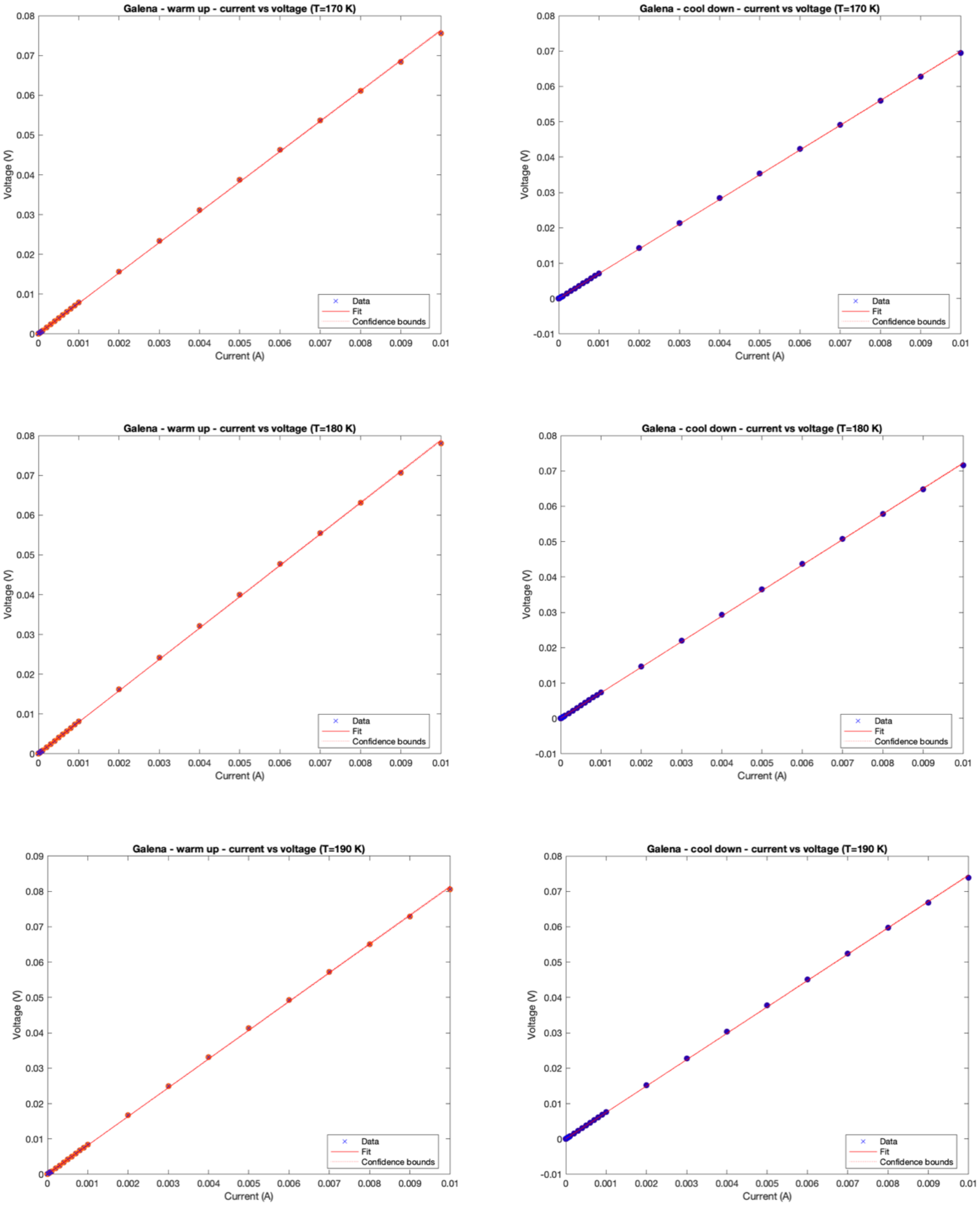

Figure 78: Galena voltage versus current graphs. Temperature range: 170K to 190K.

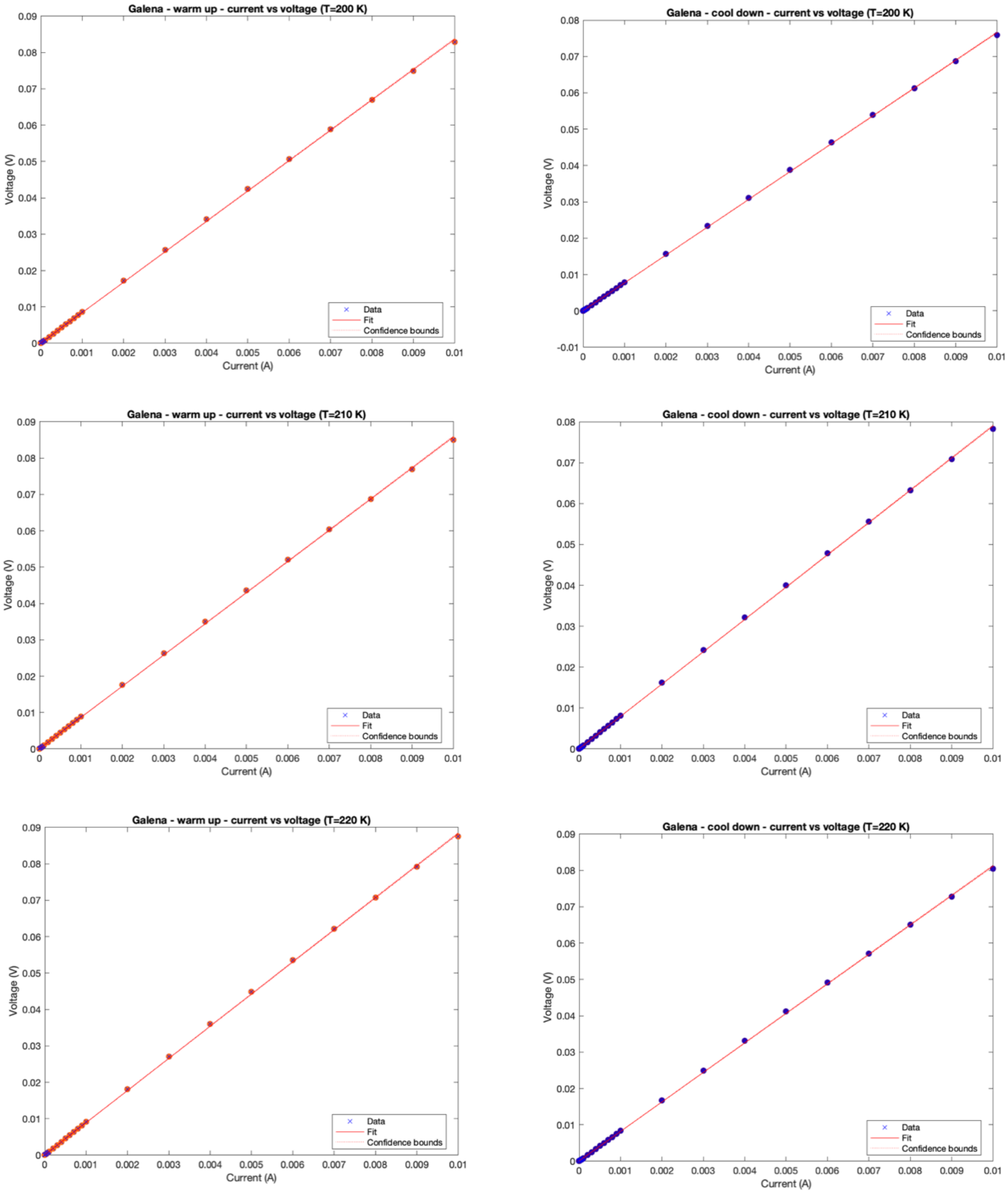
Galena - warm up - current vs voltage (T=200 K)

Galena - cool down - current vs voltage (T=200 K)

Galena - warm up - current vs voltage (T=210 K)

Galena - cool down - current vs voltage (T=210 K)

Galena - warm up - current vs voltage (T=220 K)

Galena - cool down - current vs voltage (T=220 K)

Figure 79: Galena voltage versus current graphs. Temperature range: 200K to 220K.

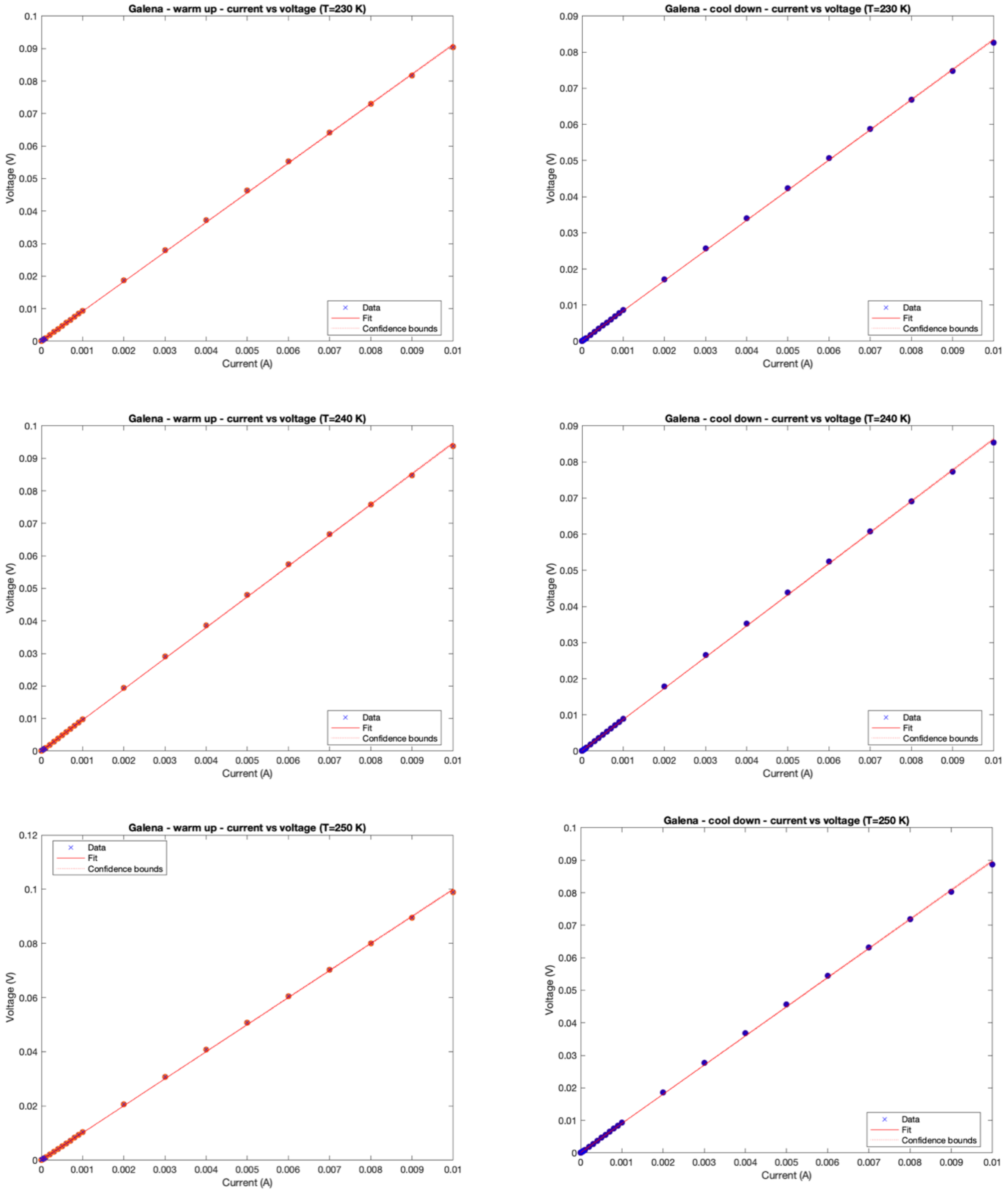

Galena - warm up - current vs voltage (T=230 K)

Galena - cool down - current vs voltage (T=230 K)

Galena - warm up - current vs voltage (T=240 K)

Galena - cool down - current vs voltage (T=240 K)

Galena - warm up - current vs voltage (T=250 K)

Galena - cool down - current vs voltage (T=250 K)

Figure 80: Galena voltage versus current graphs. Temperature range: 230K to 250K.

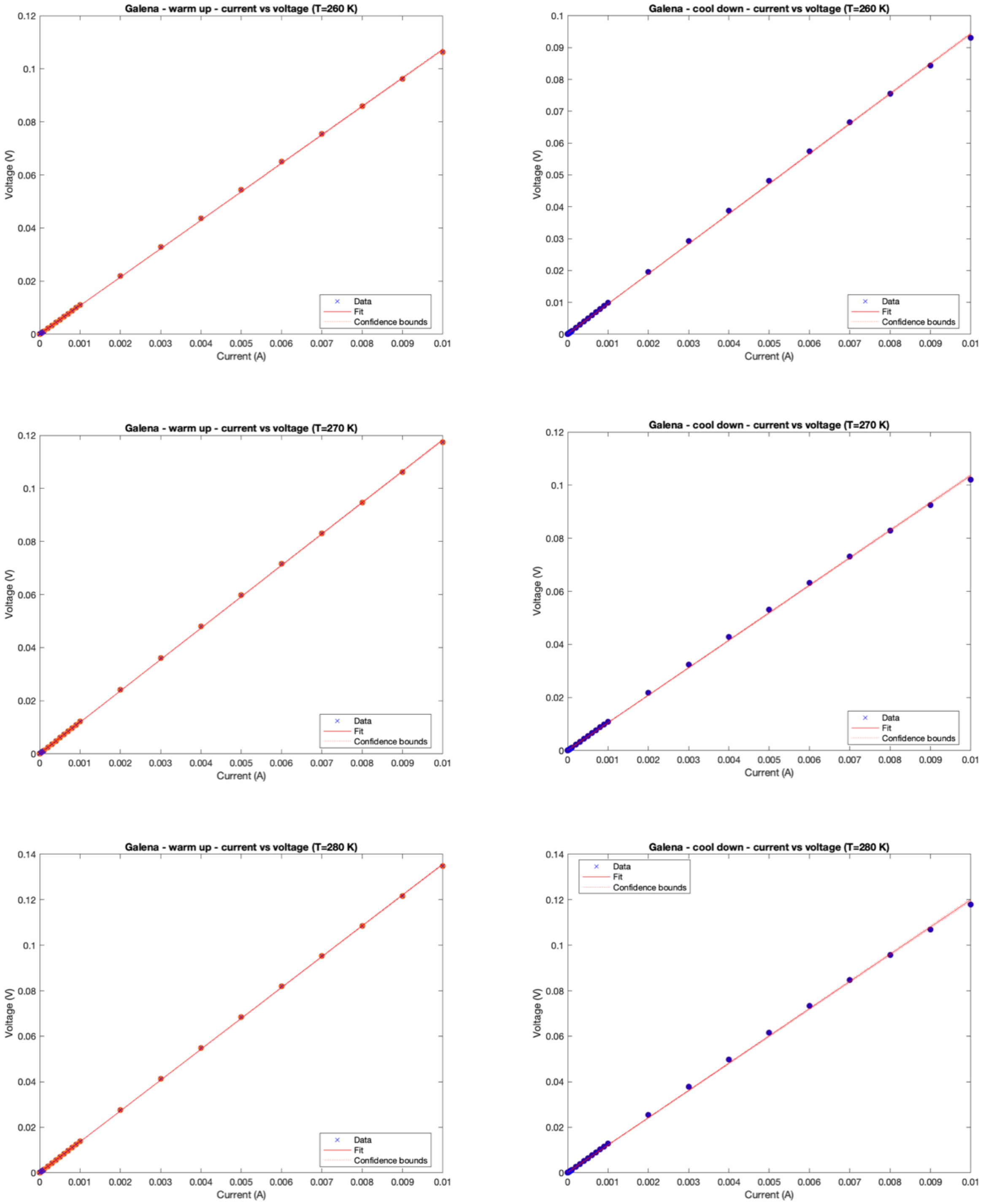

Figure 81: Galena voltage versus current graphs. Temperature range: 260K to 280K.

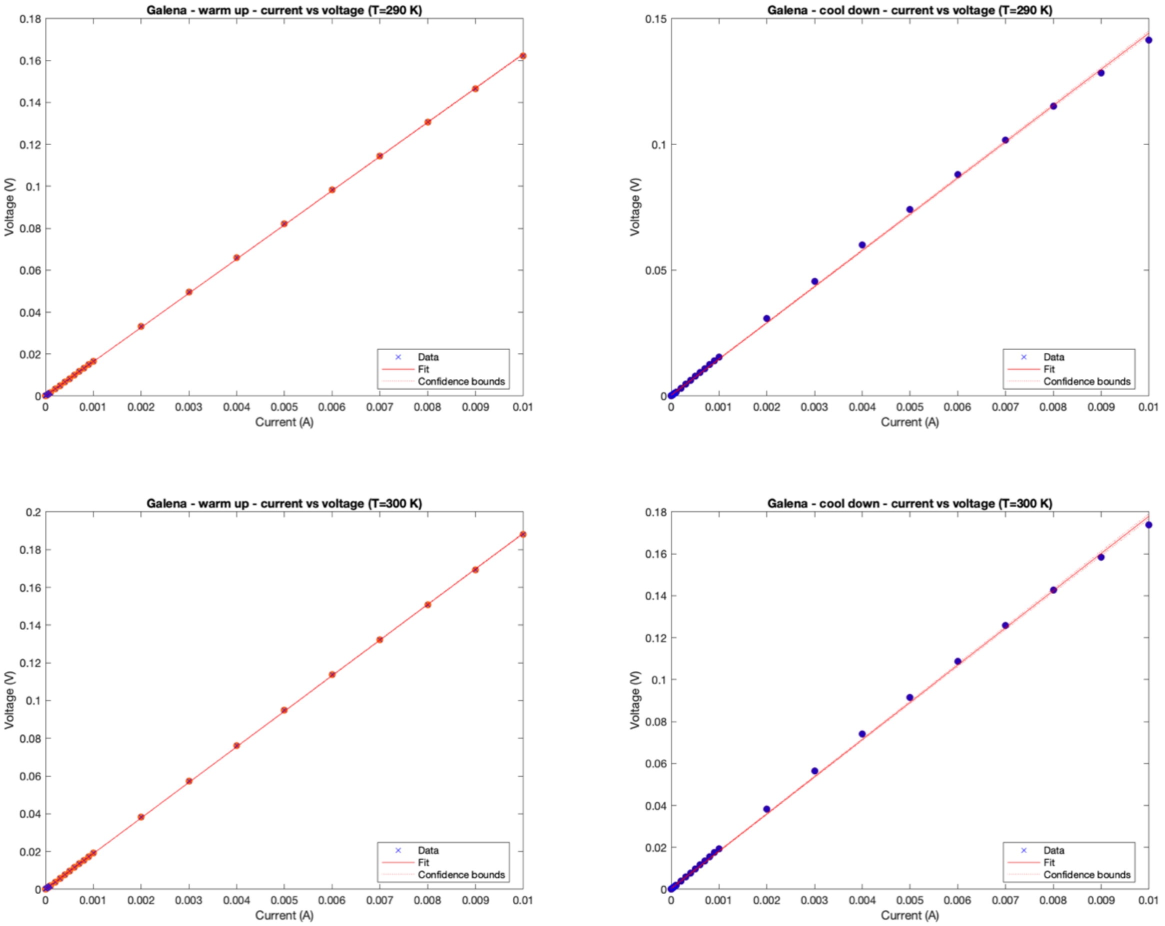
Galena - warm up - current vs voltage (T=290 K)

Galena - cool down - current vs voltage (T=290 K)

Galena - warm up - current vs voltage (T=300 K)

Galena - cool down - current vs voltage (T=300 K)

Figure 82: Galena voltage versus current graphs. Temperature range: 290K to 300K.

### *Graphite*

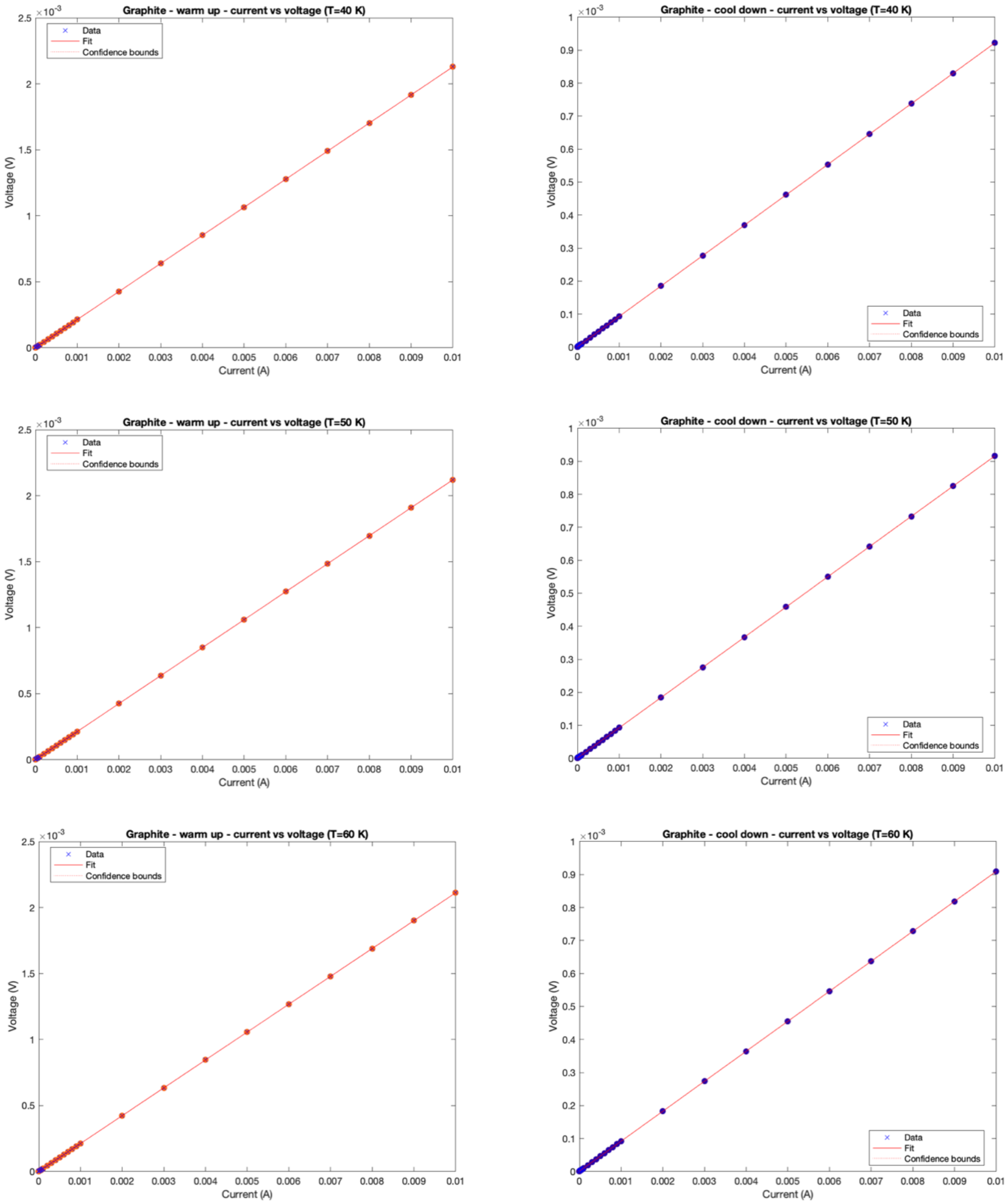

Figure 83: Graphite voltage versus current graphs. Temperature range: 40K to 60K.

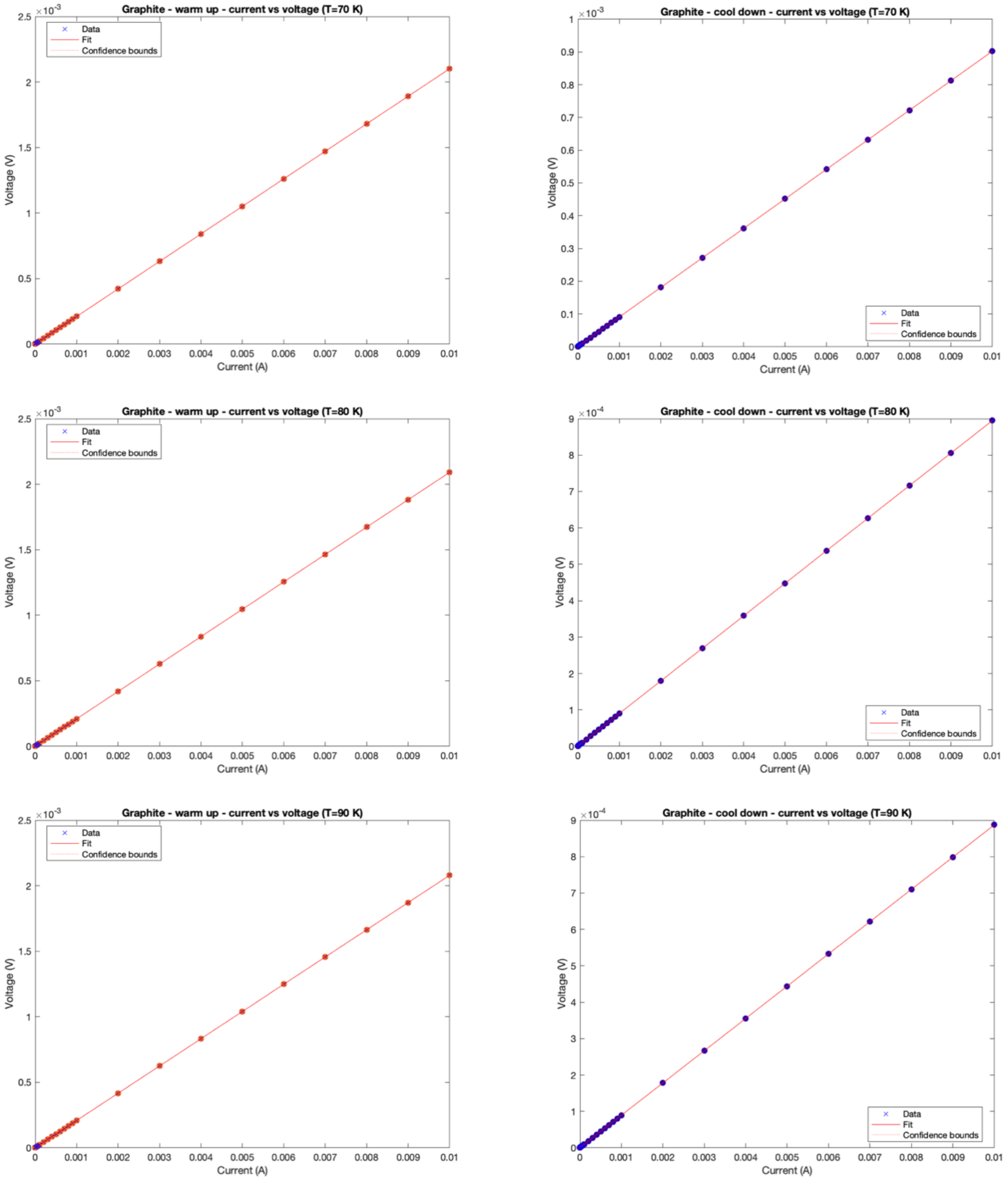
Graphite - warm up - current vs voltage (T=70 K)

Graphite - cool down - current vs voltage (T=70 K)

Graphite - warm up - current vs voltage (T=80 K)

Graphite - cool down - current vs voltage (T=80 K)

Graphite - warm up - current vs voltage (T=90 K)

Graphite - cool down - current vs voltage (T=90 K)

Figure 84: Graphite voltage versus current graphs. Temperature range: 70K to 90K.

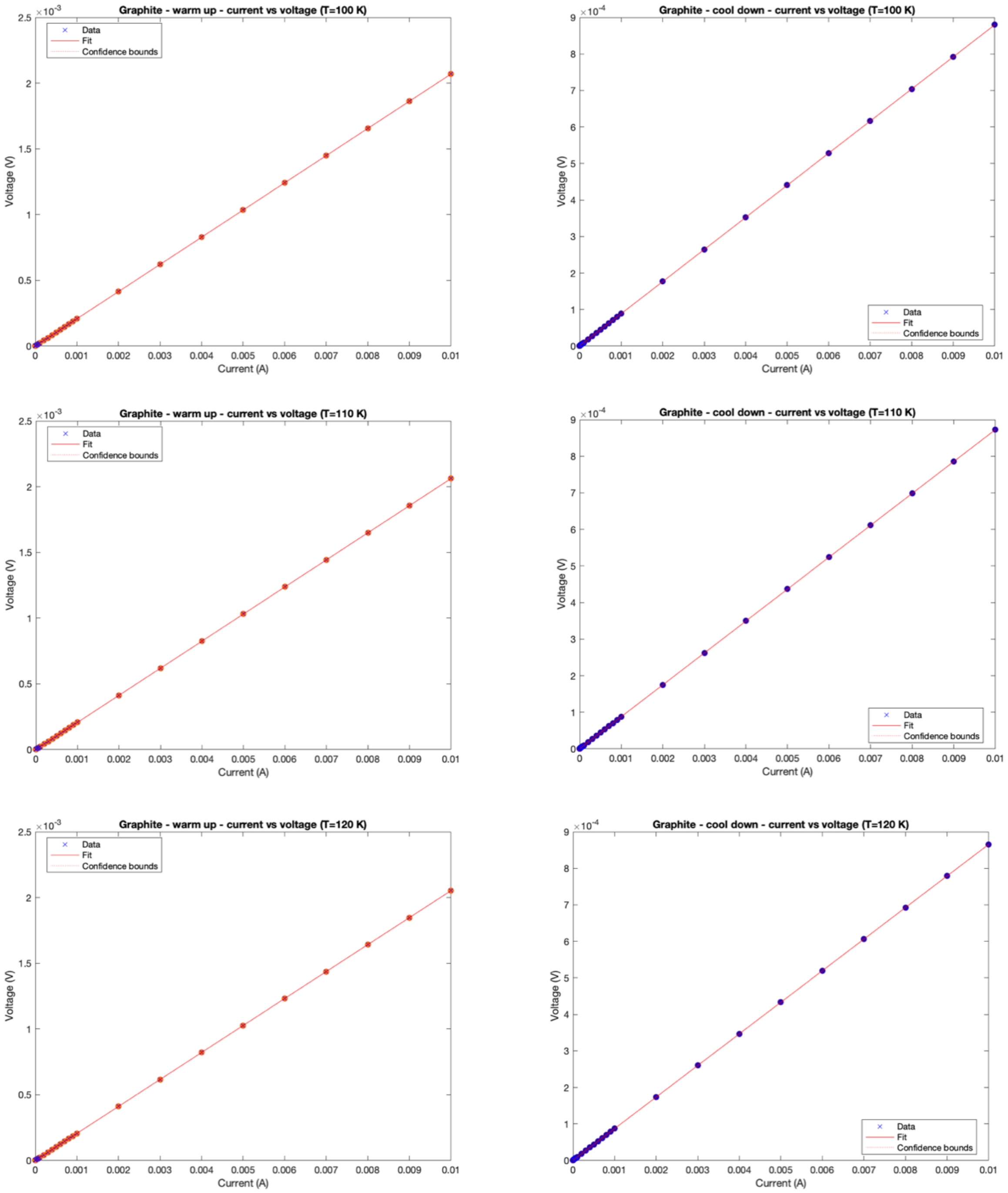

Figure 85: Graphite voltage versus current graphs. Temperature range: 100K to 120K.

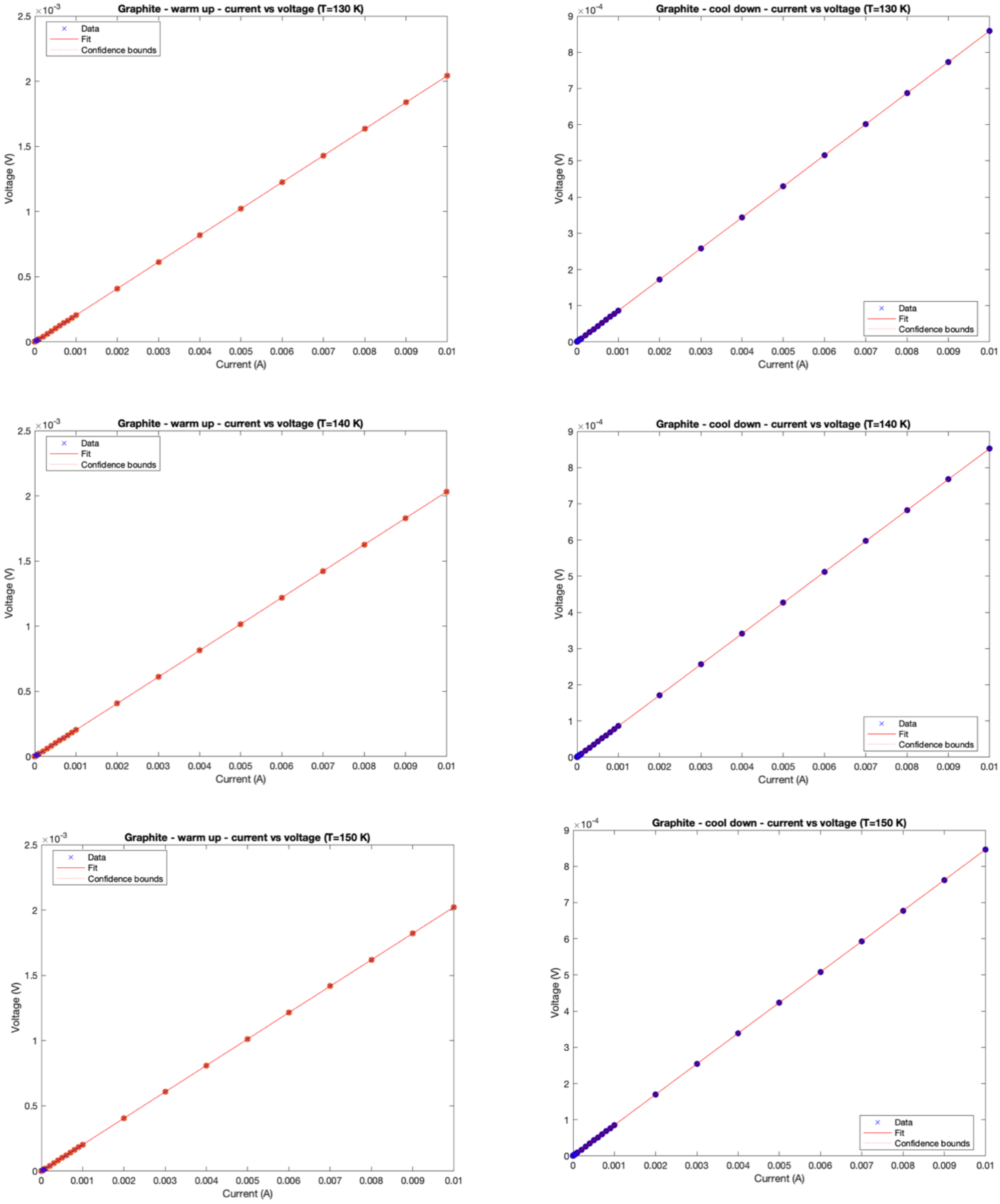

Figure 86: Graphite voltage versus current graphs. Temperature range: 130K to 150K.

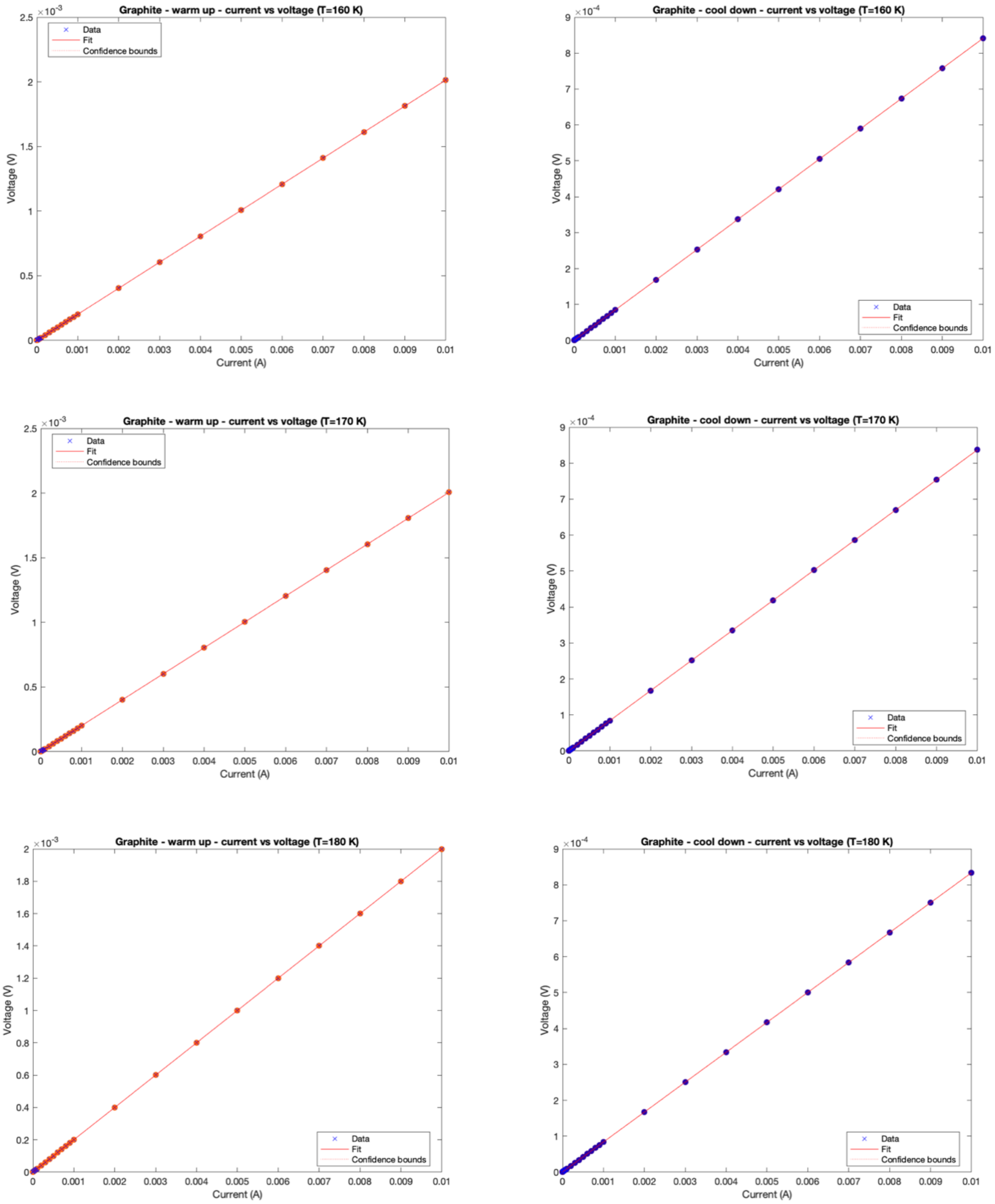

Figure 87: Graphite voltage versus current graphs. Temperature range: 160K to 180K.

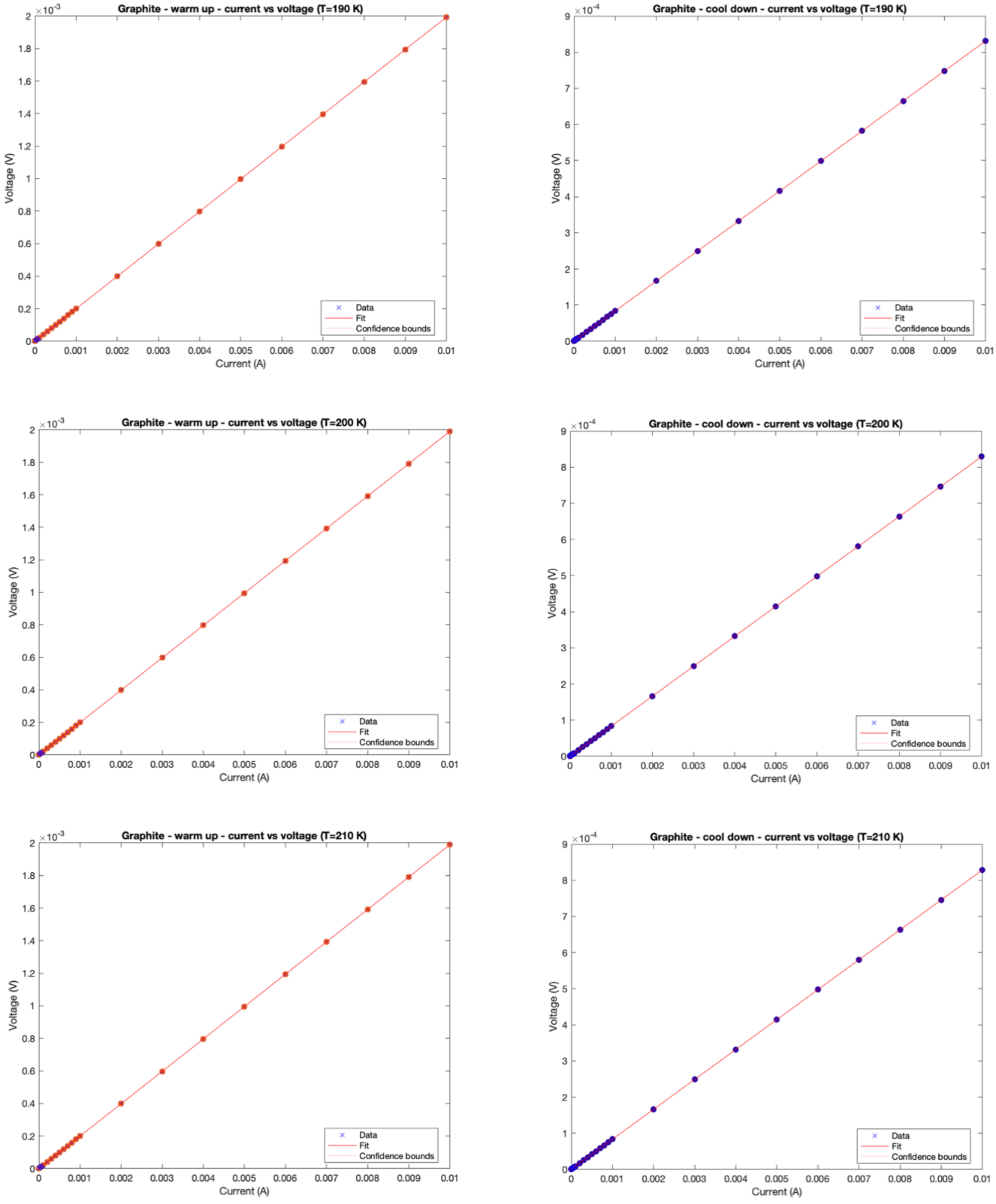

Figure 88: Graphite voltage versus current graphs. Temperature range: 190K to 210K.

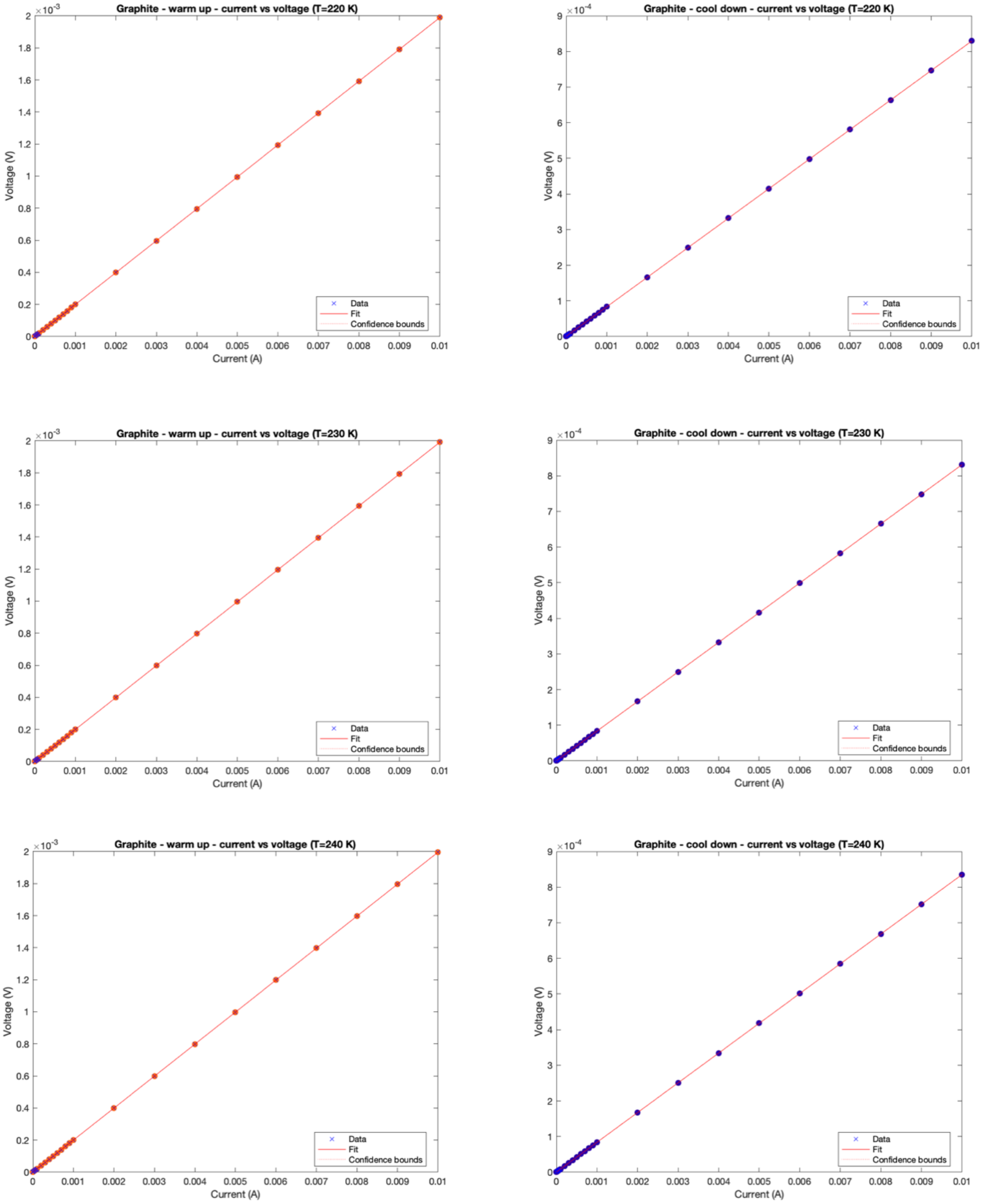

Figure 89: Graphite voltage versus current graphs. Temperature range: 220K to 240K.

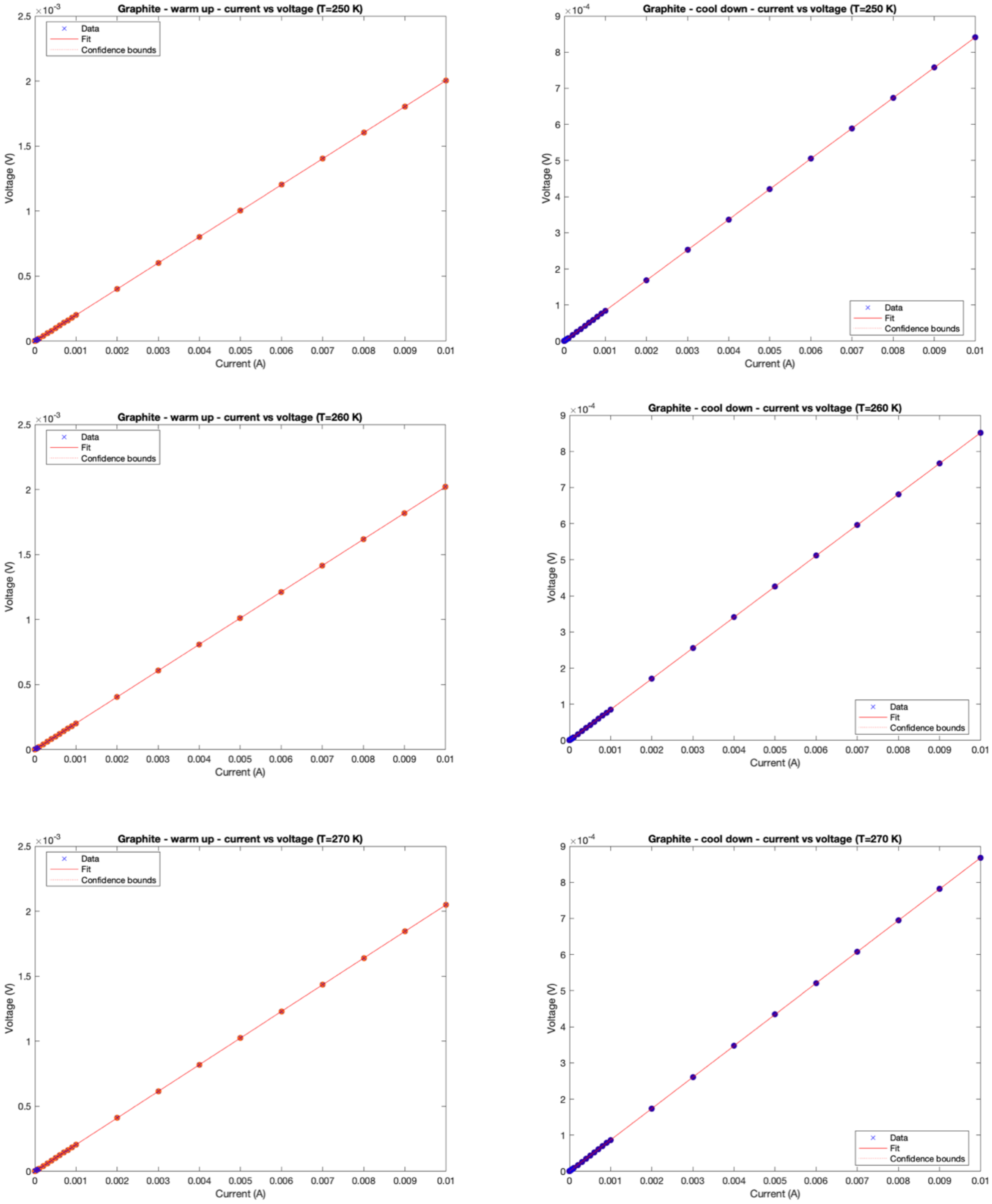

Figure 90: Graphite voltage versus current graphs. Temperature range: 250K to 270K.

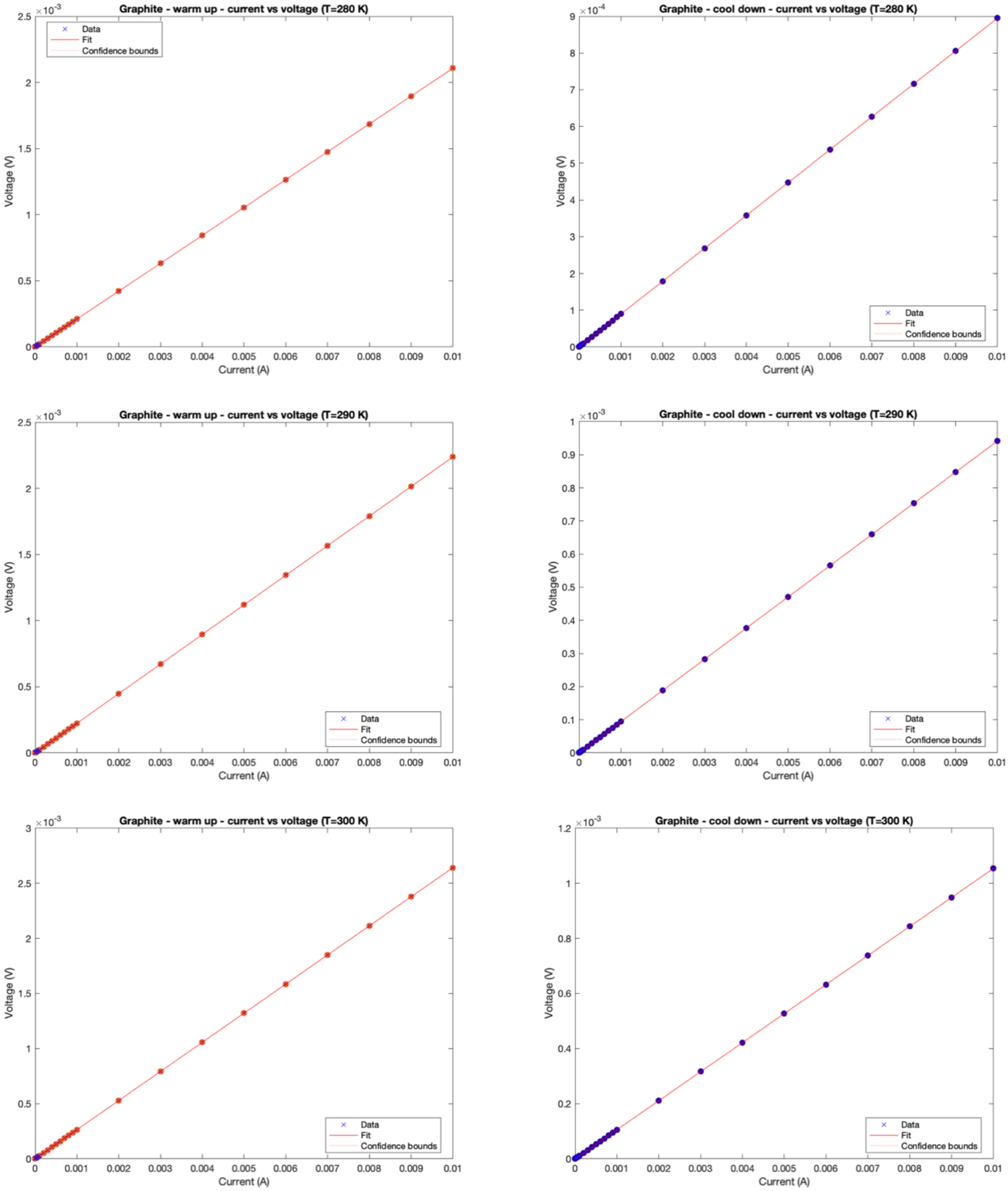
Graphite - warm up - current vs voltage (T=280 K)

Graphite - cool down - current vs voltage (T=280 K)

Graphite - warm up - current vs voltage (T=290 K)

Graphite - cool down - current vs voltage (T=290 K)

Graphite - warm up - current vs voltage (T=300 K)

Graphite - cool down - current vs voltage (T=300 K)

Figure 91: Graphite voltage versus current graphs. Temperature range: 280K to 300K.

### *Hematite*

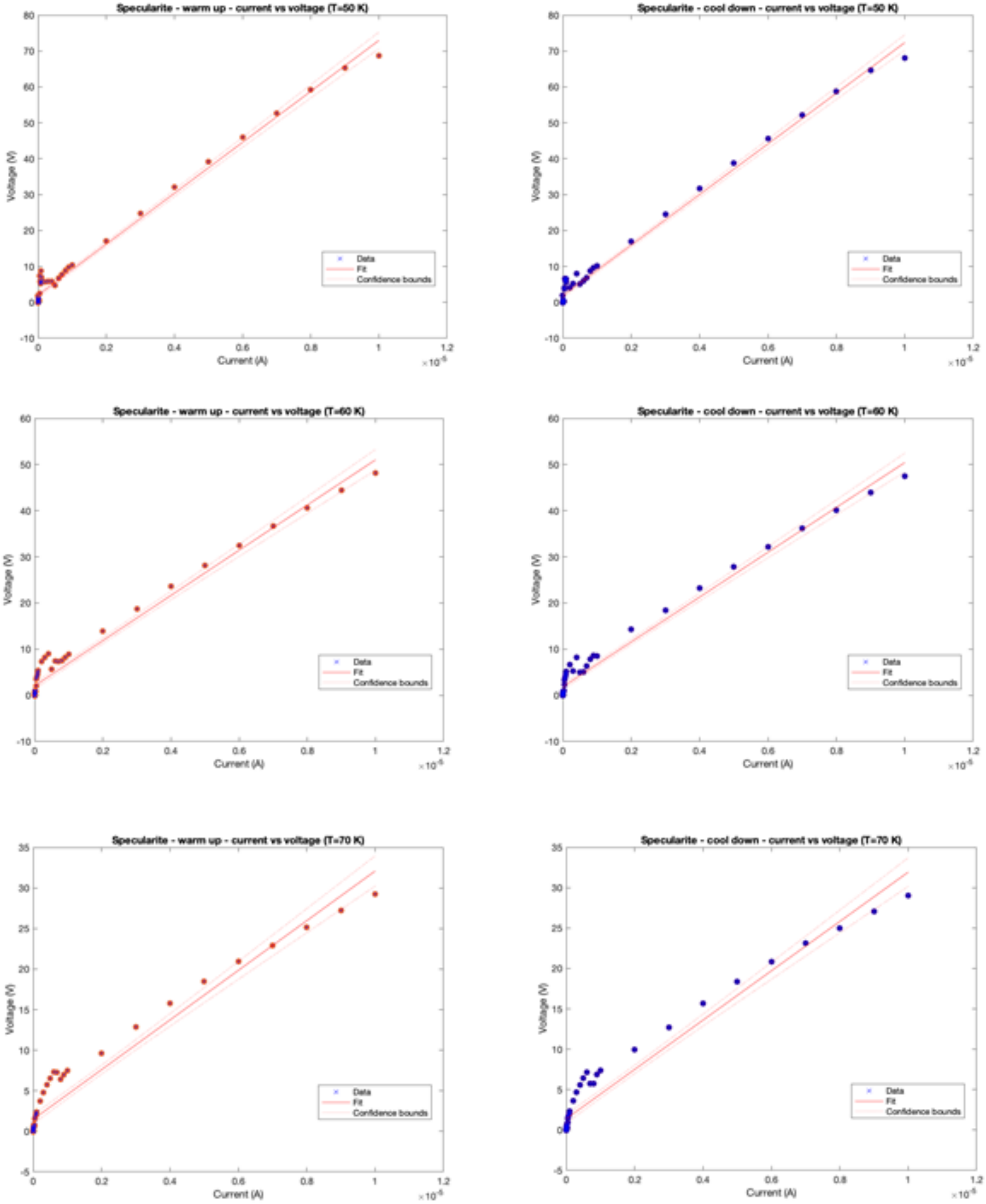
Specularite - warm up - current vs voltage (T=50 K)

Specularite - cool down - current vs voltage (T=50 K)

Specularite - warm up - current vs voltage (T=60 K)

Specularite - cool down - current vs voltage (T=60 K)

Specularite - warm up - current vs voltage (T=70 K)

Specularite - cool down - current vs voltage (T=70 K)

Figure 92: Hematite voltage versus current graphs. Temperature range: 50K to 70K

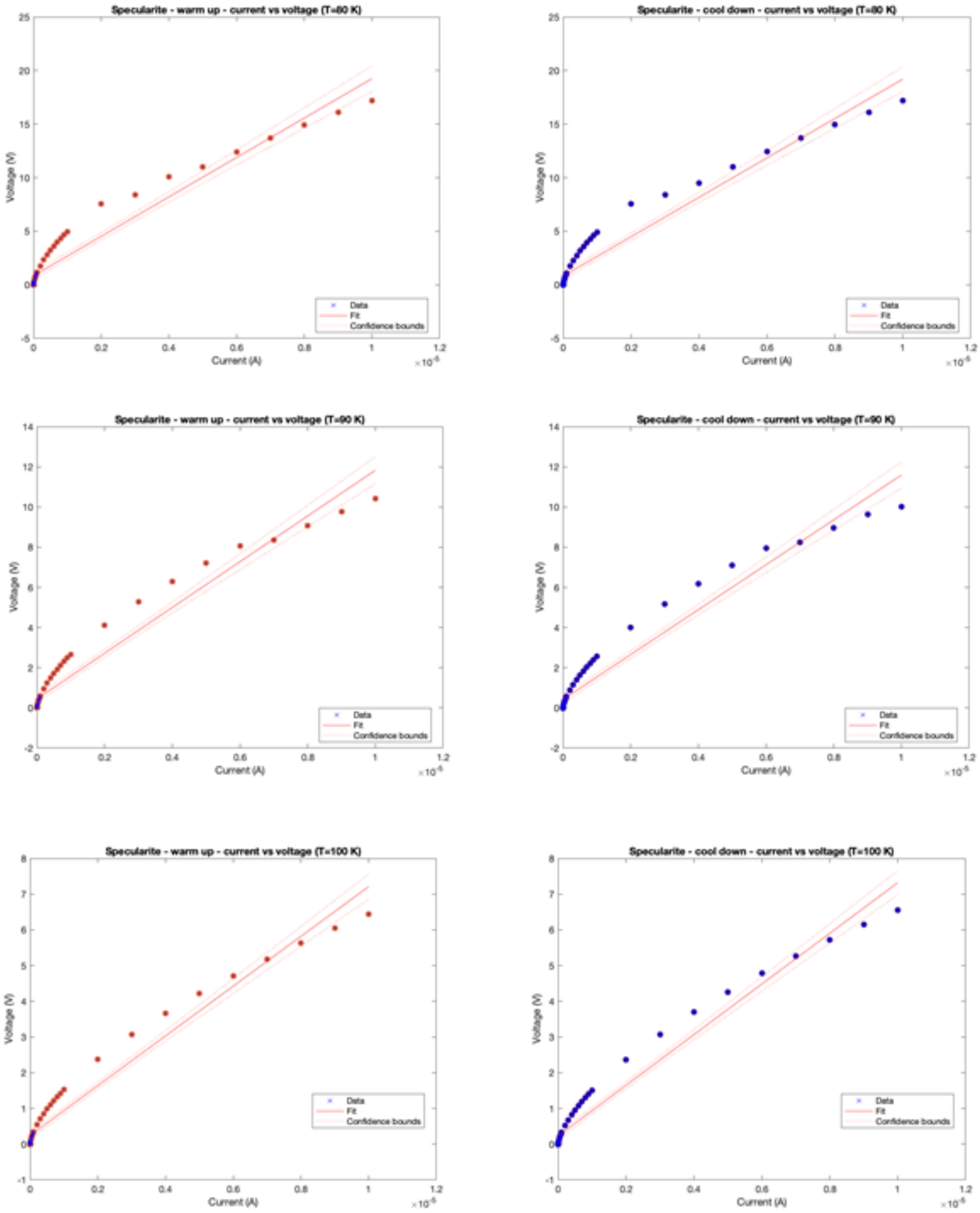

Figure 93: Hematite voltage versus current graphs. Temperature range: 80K to 100K.

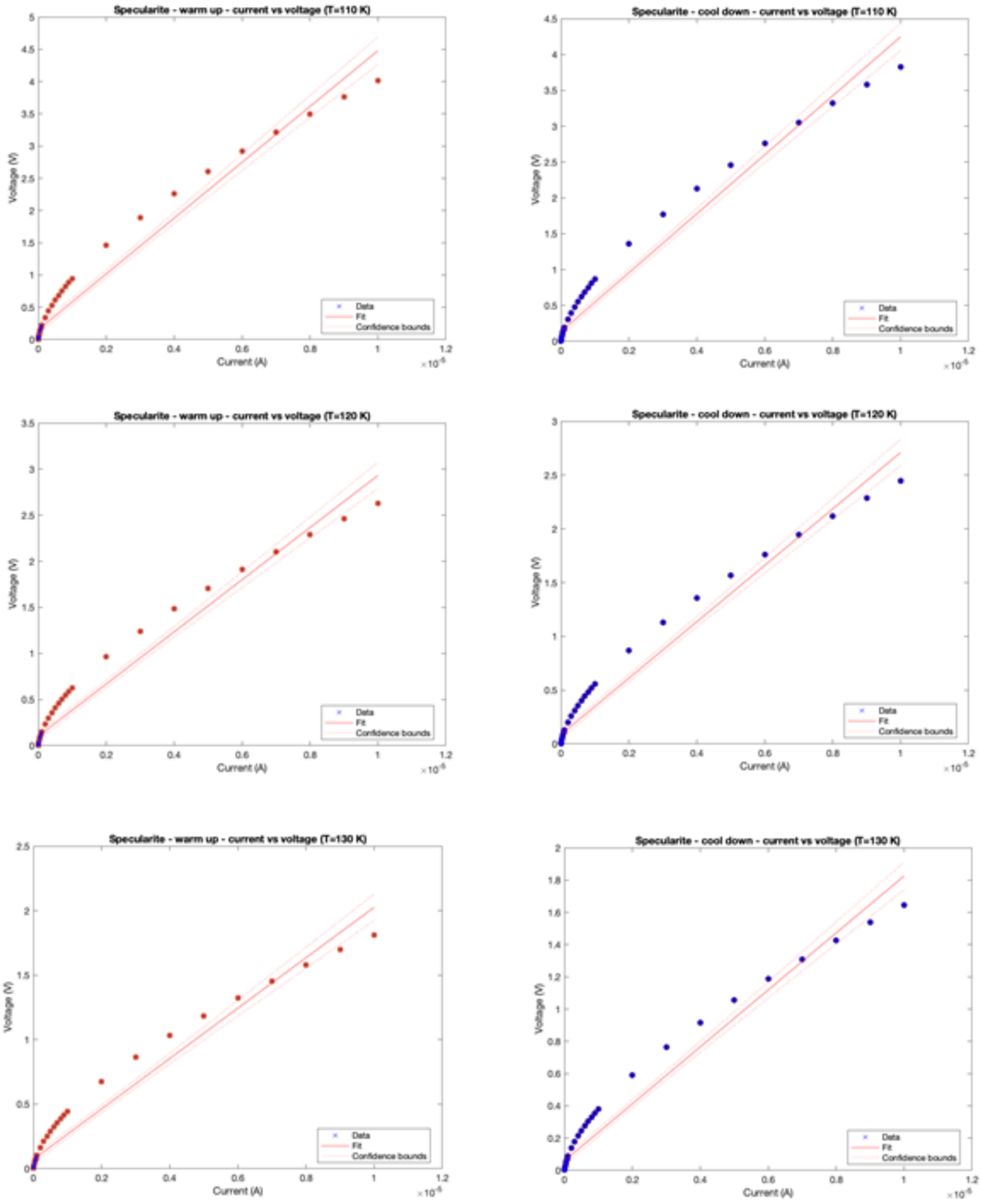

Figure 94: Hematite voltage versus current graphs. Temperature range: 110K to 130K.

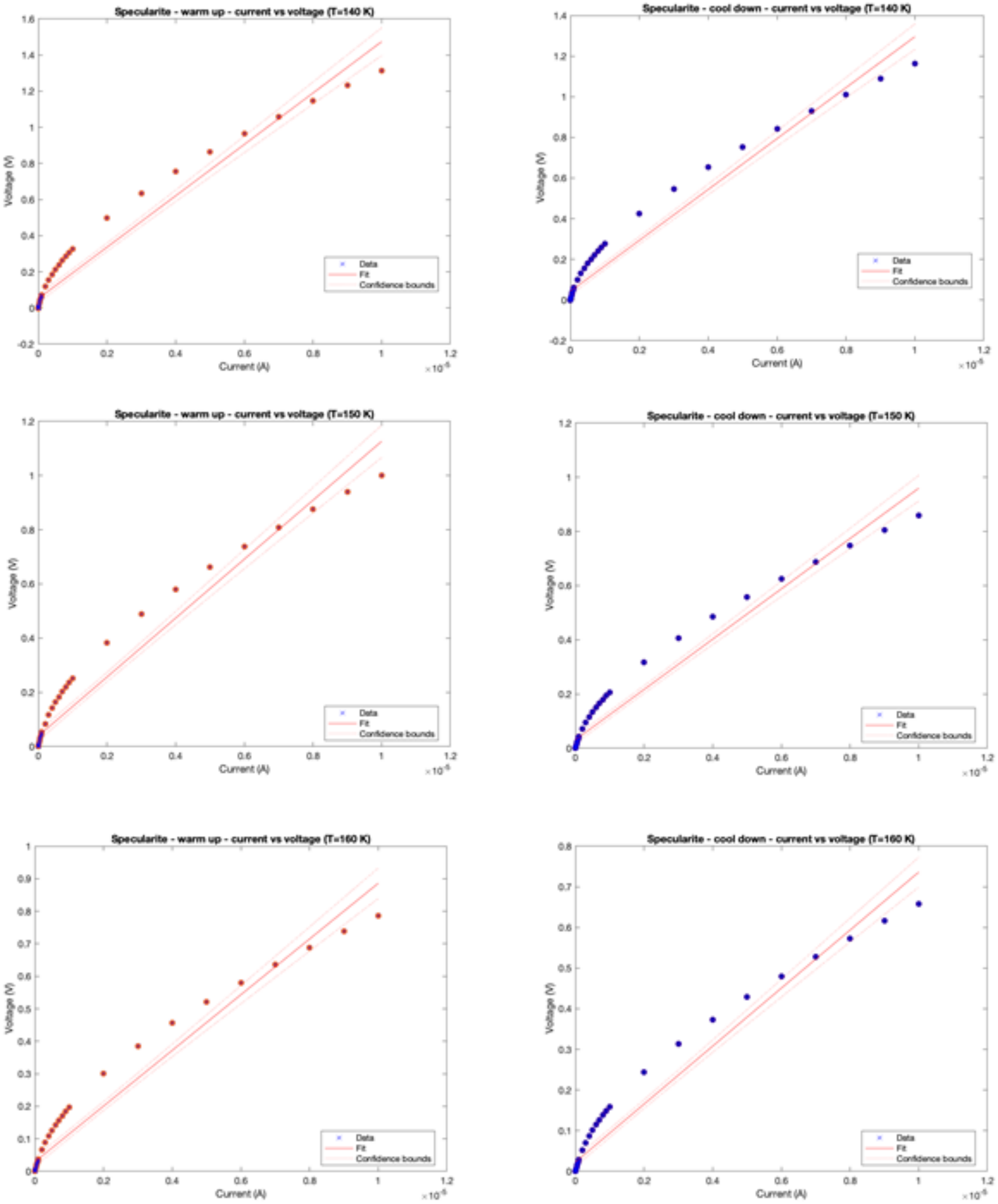

Figure 95: Hematite voltage versus current graphs. Temperature range: 140K to 160K.

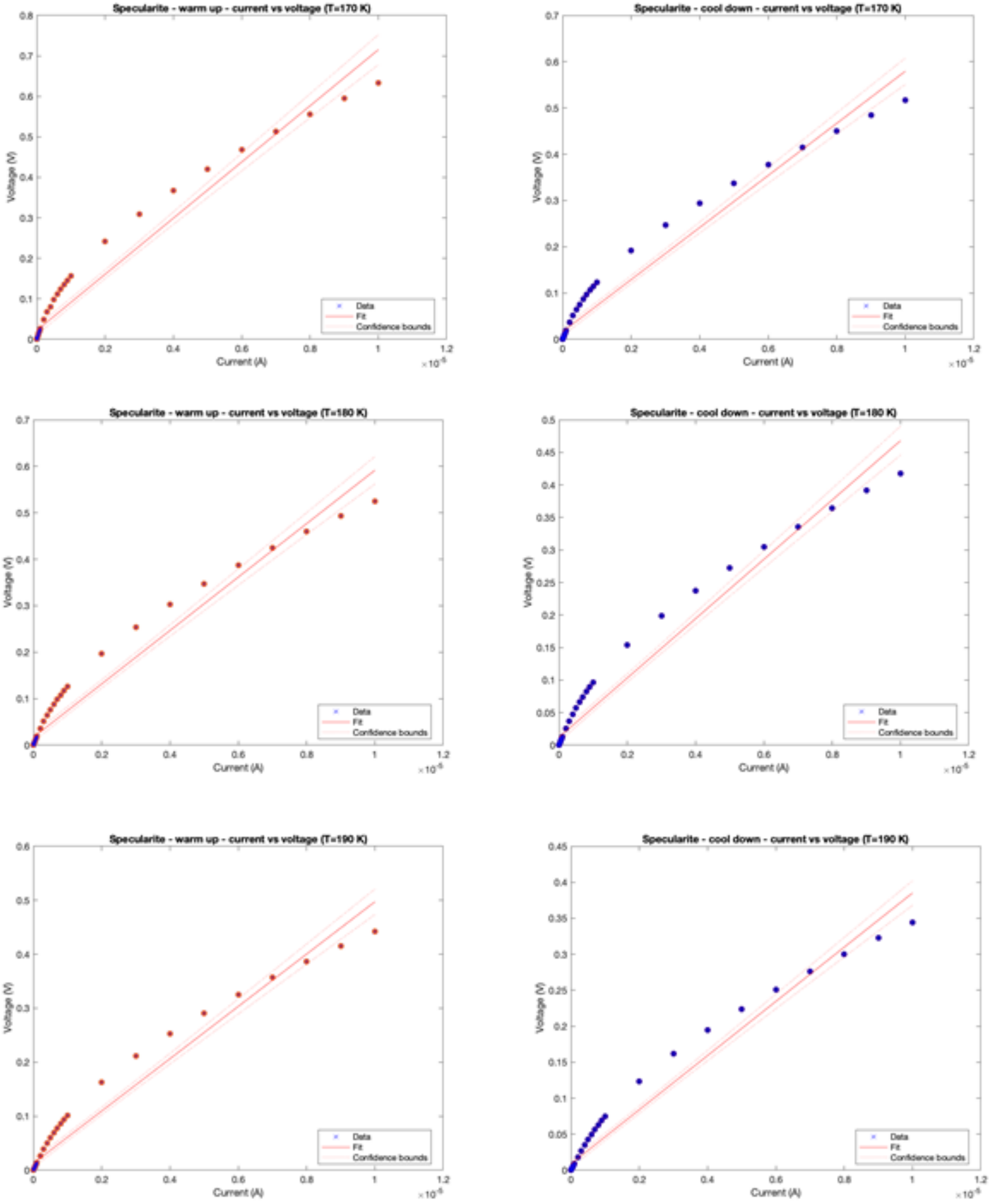

Figure 96: Hematite voltage versus current graphs. Temperature range: 170K to 190K.

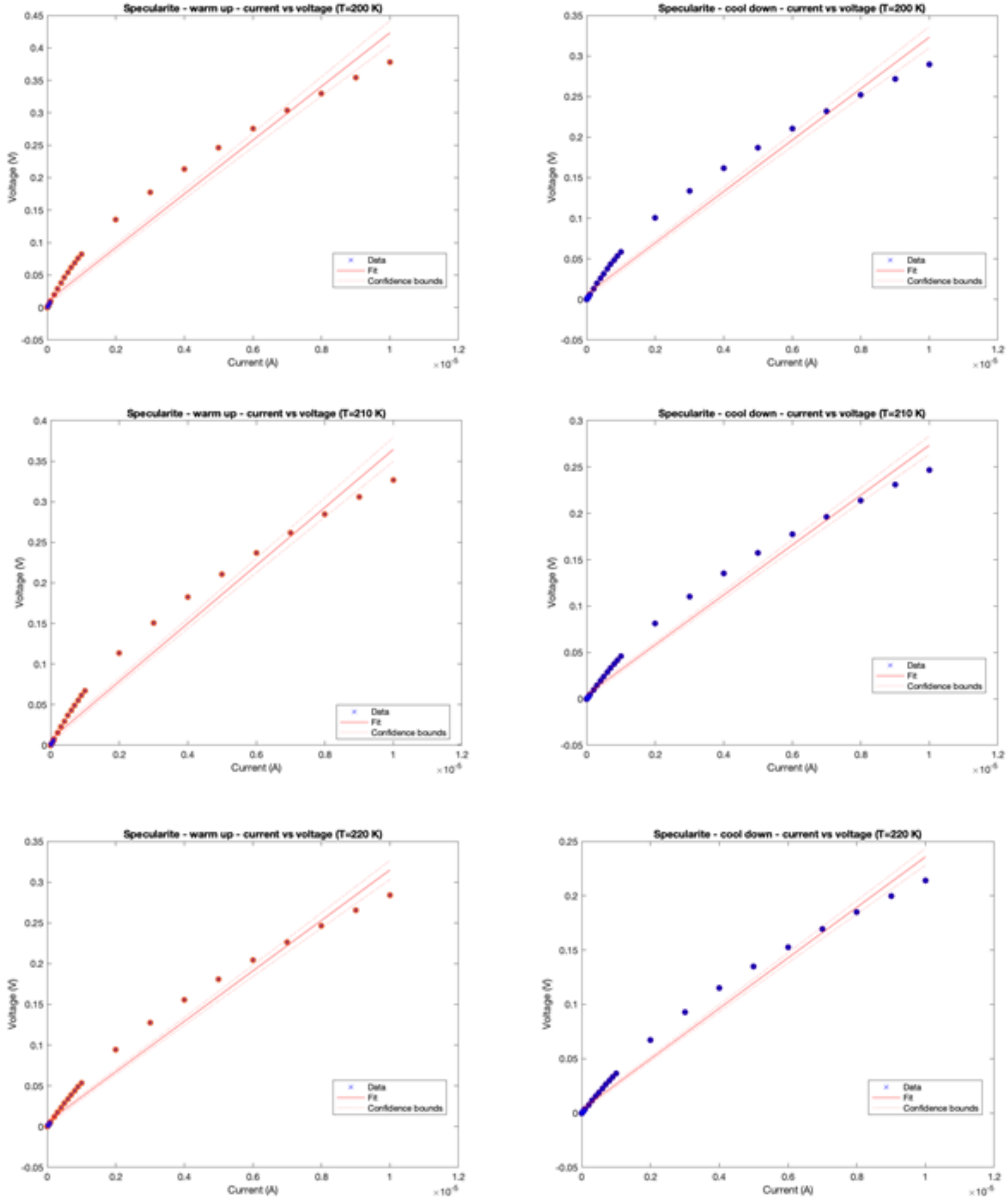

Figure 97: Hematite voltage versus current graphs. Temperature range: 200K to 220K.

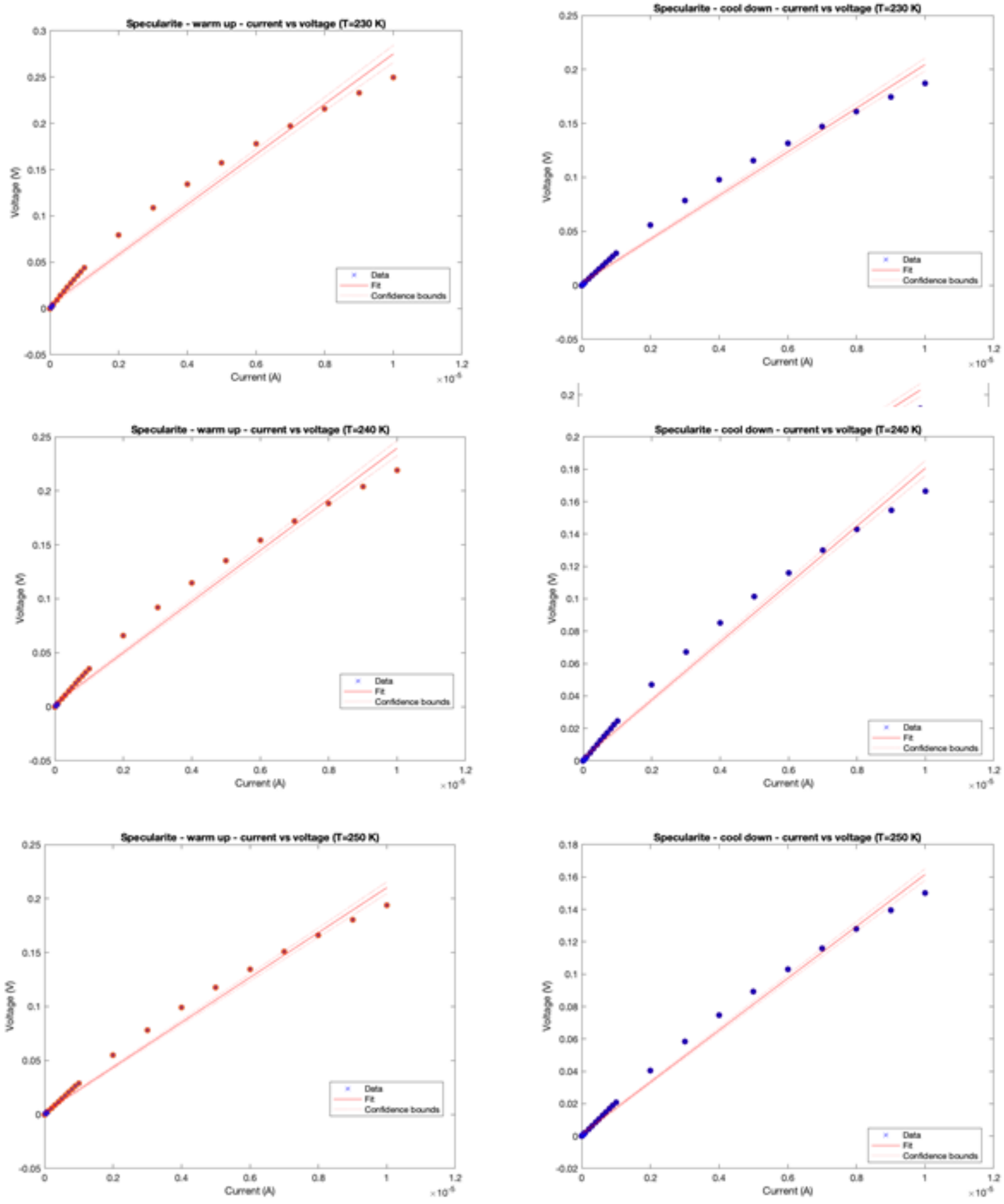

Figure 98: Hematite voltage versus current graphs. Temperature range: 230K to 250K.

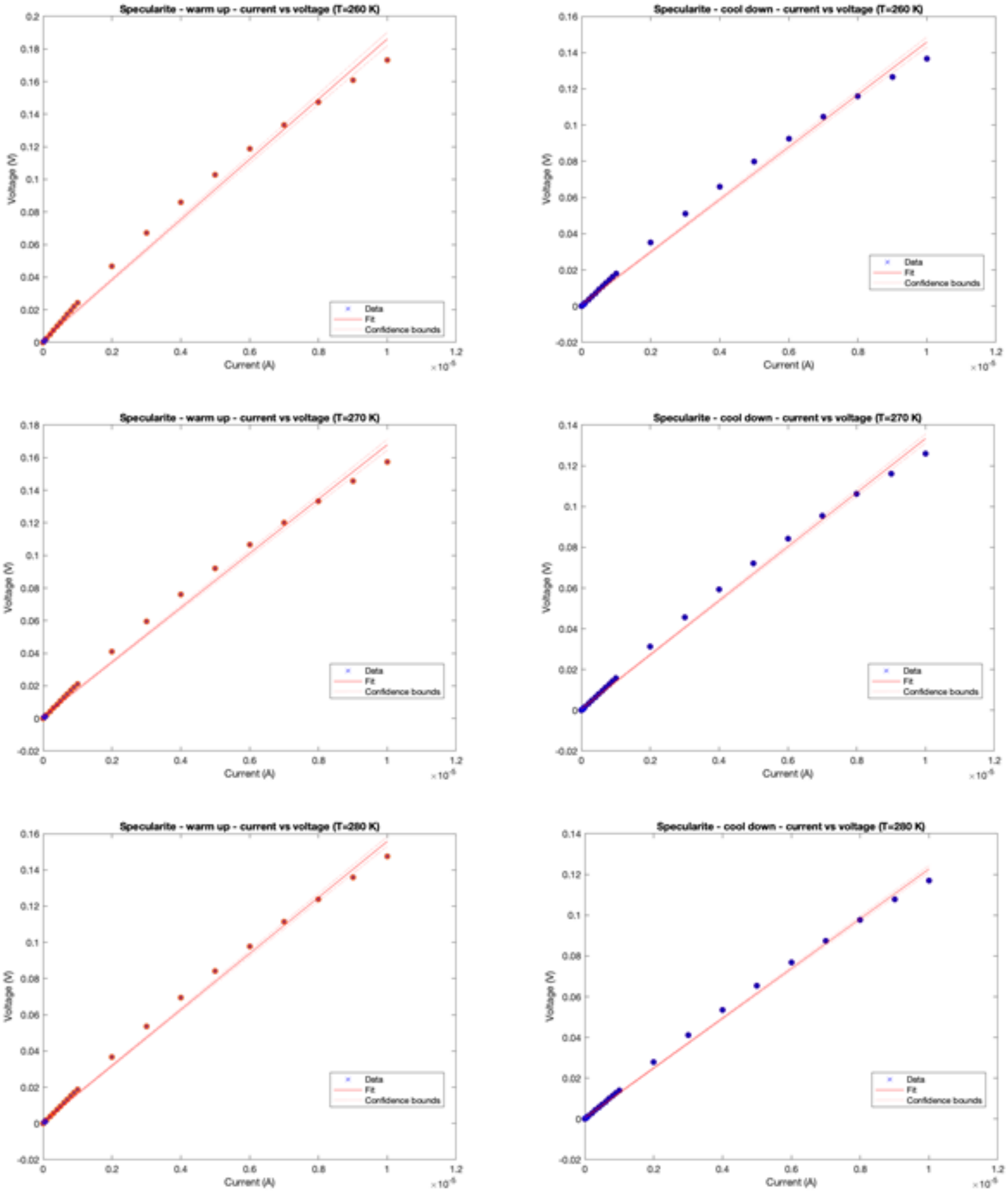

Figure 99: Hematite voltage versus current graphs. Temperature range: 260K to 280K.

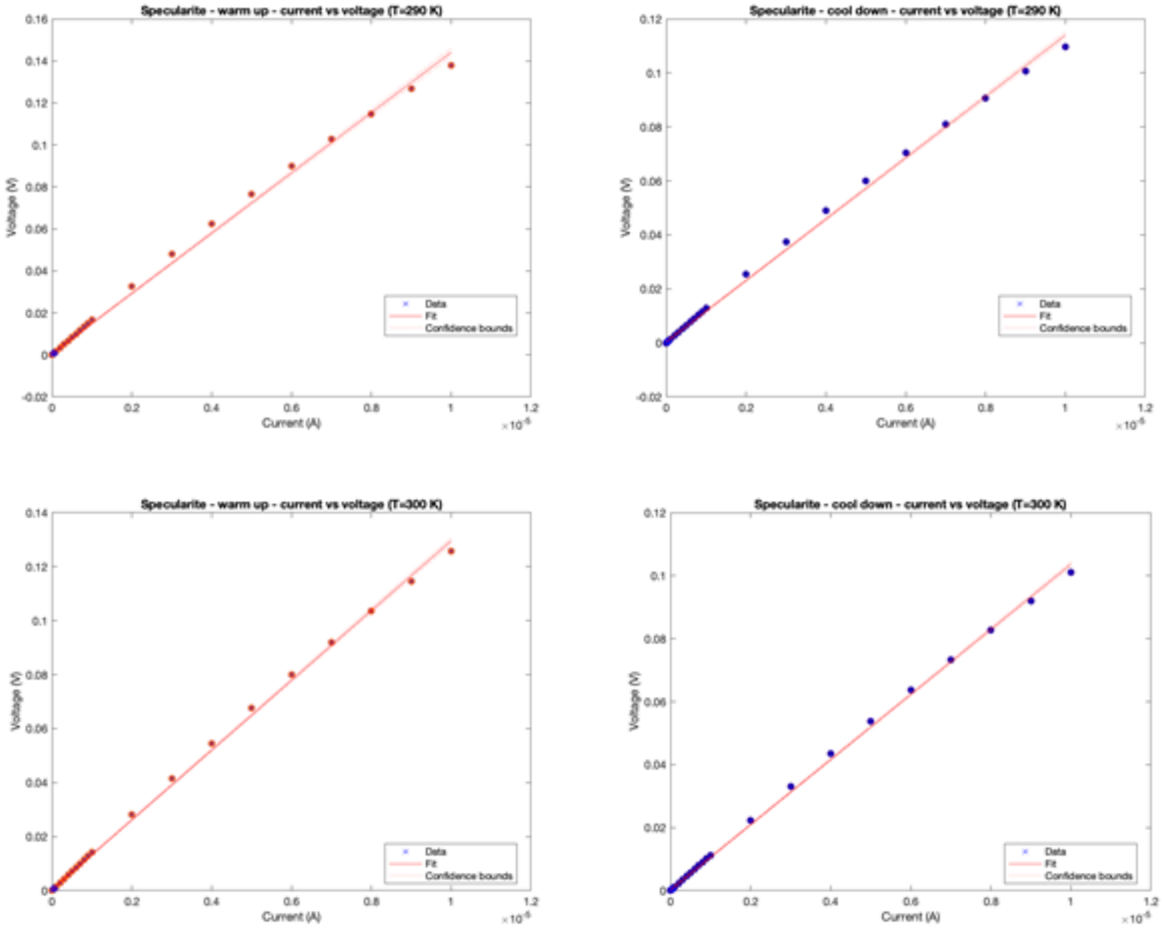

Figure 100: Hematite voltage versus current graphs. Temperature range: 290K to 300K.

## *Ilmenite*

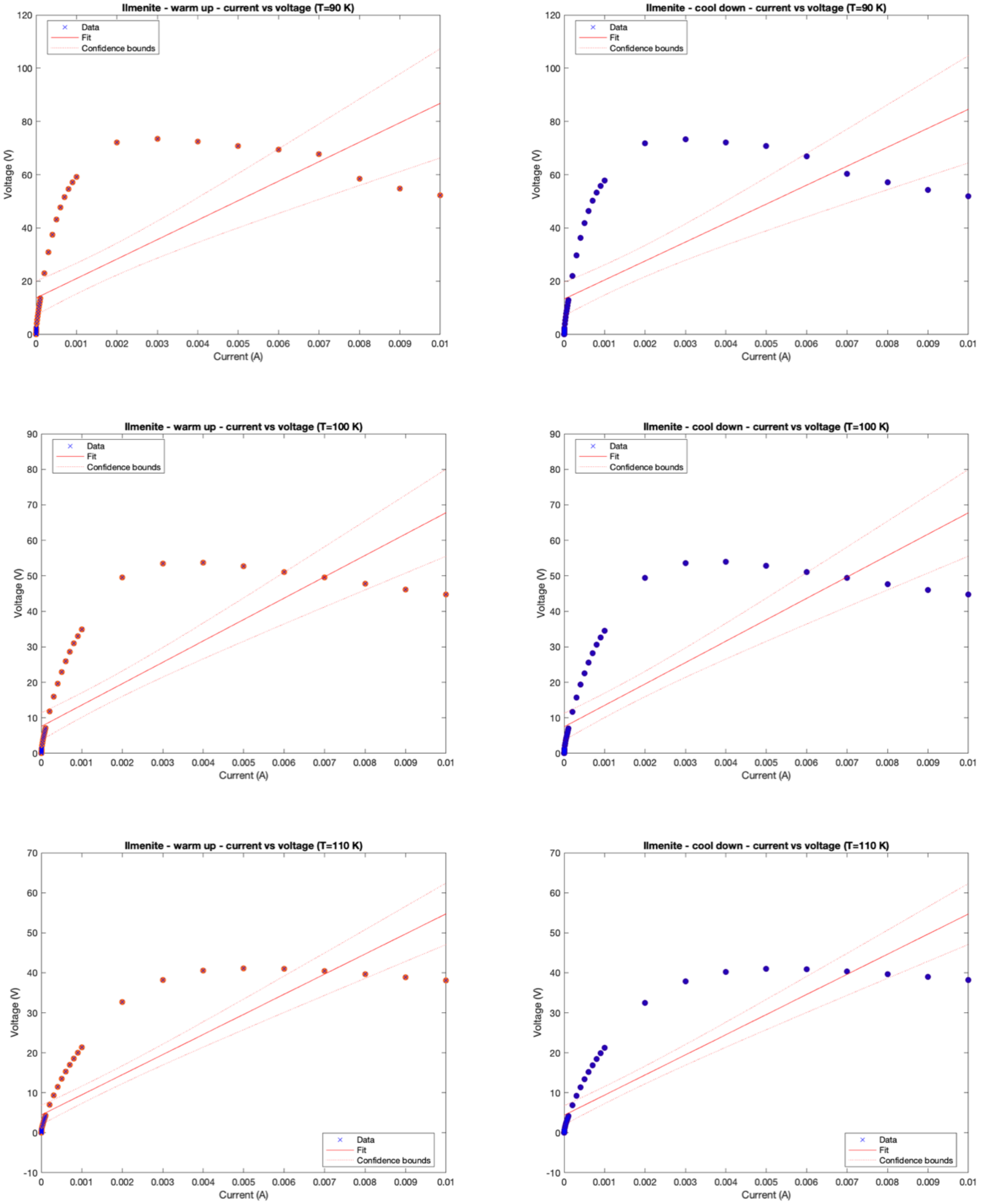

Figure 101: Ilmenite voltage versus current graphs. Temperature range: 90K to 110K.

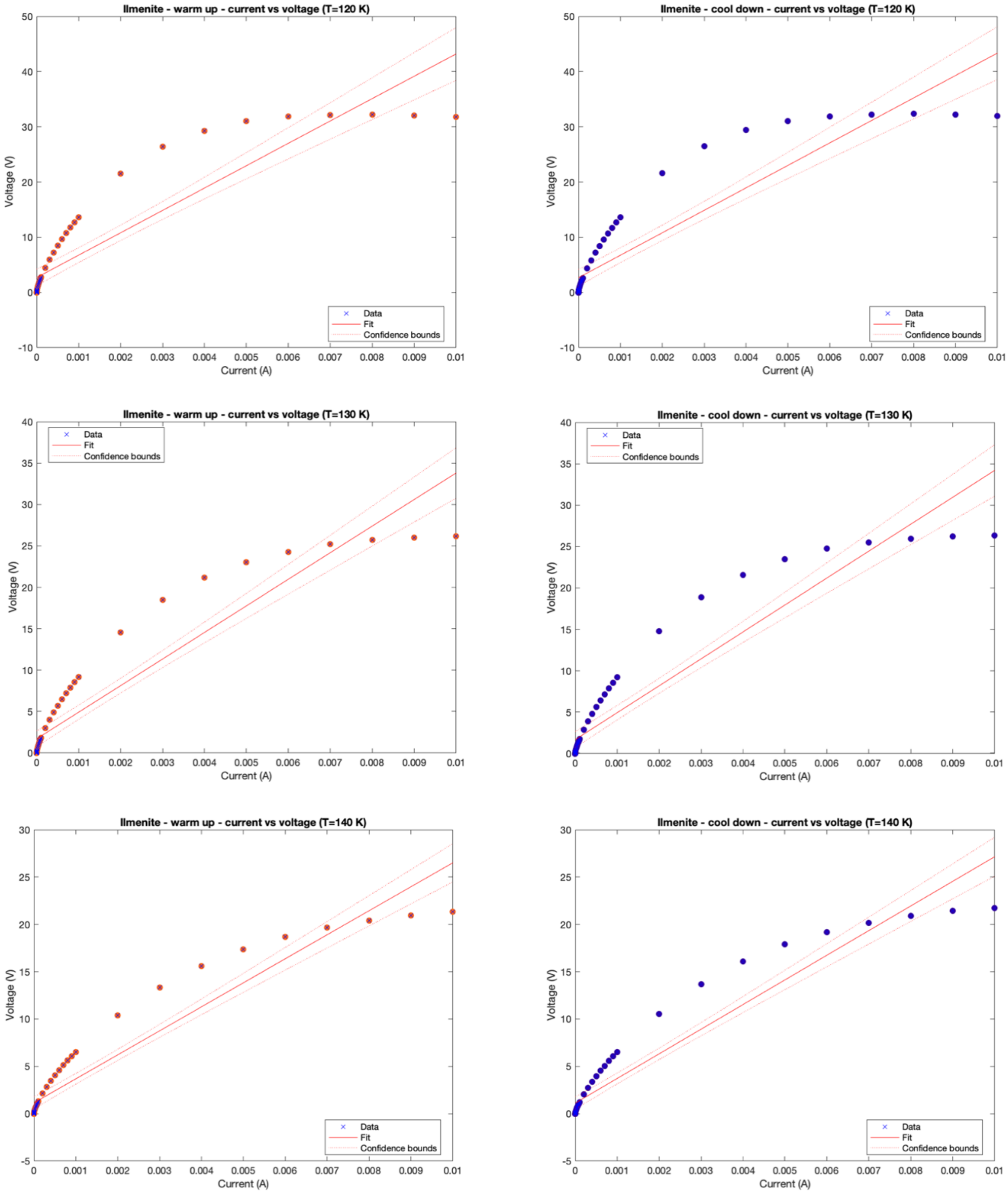
Ilmenite - warm up - current vs voltage (T=120 K)

Ilmenite - cool down - current vs voltage (T=120 K)

Ilmenite - warm up - current vs voltage (T=130 K)

Ilmenite - cool down - current vs voltage (T=130 K)

Ilmenite - warm up - current vs voltage (T=140 K)

Ilmenite - cool down - current vs voltage (T=140 K)

Figure 102: Ilmenite voltage versus current graphs. Temperature range: 120K to 140K.

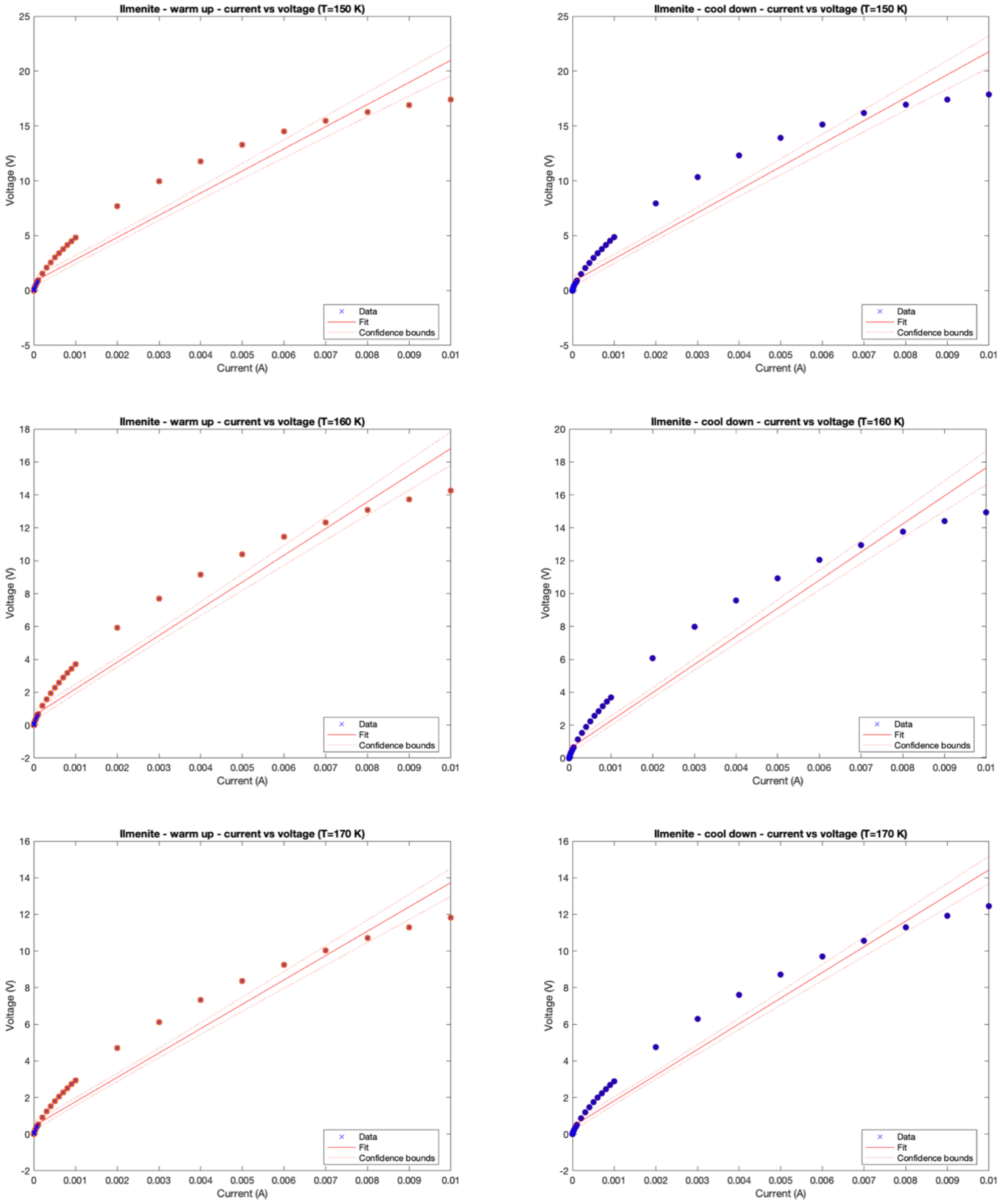

Figure 103: Ilmenite voltage versus current graphs. Temperature range: 150K to 170K.

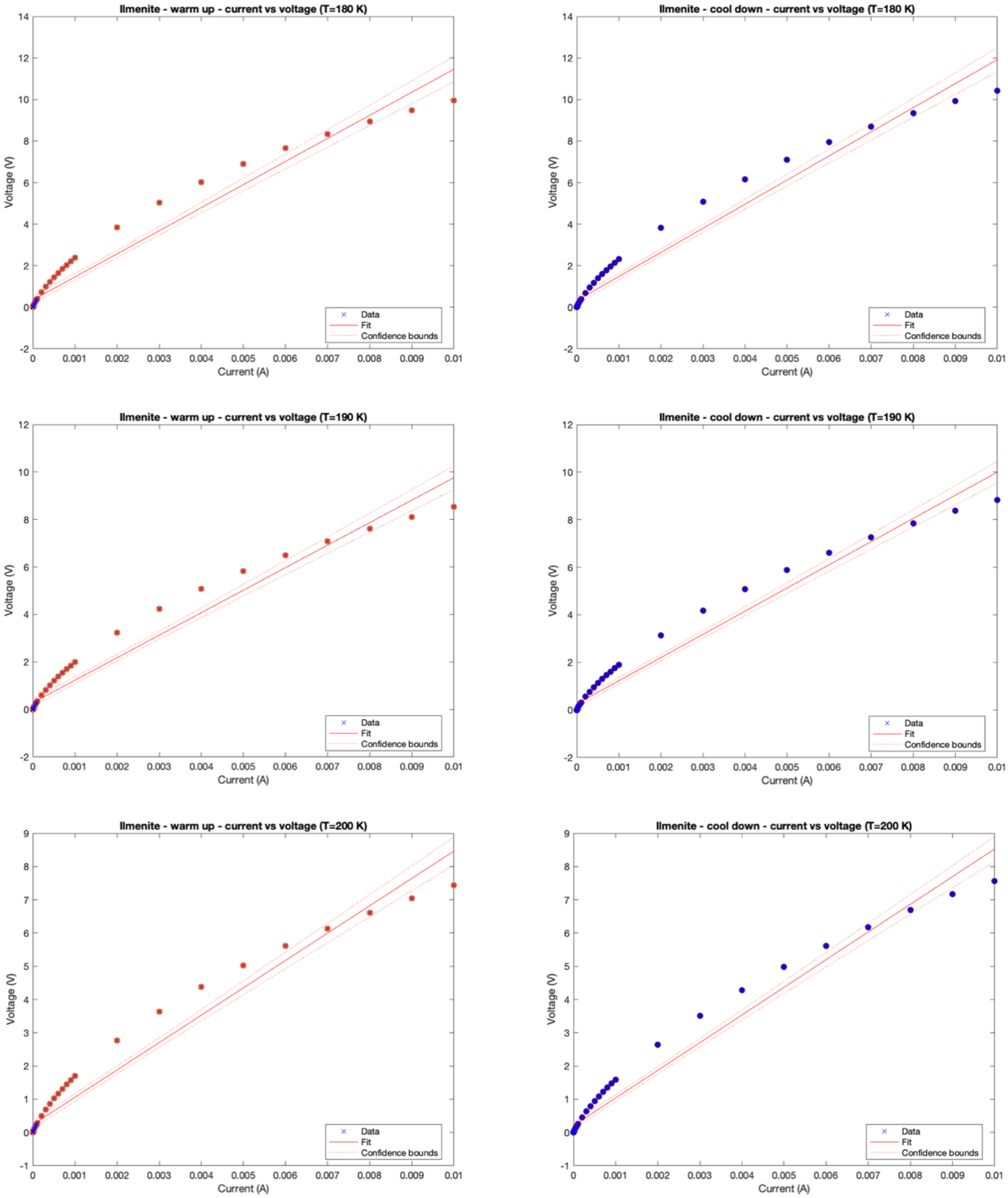

Figure 104: Ilmenite voltage versus current graphs. Temperature range: 180K to 200K.

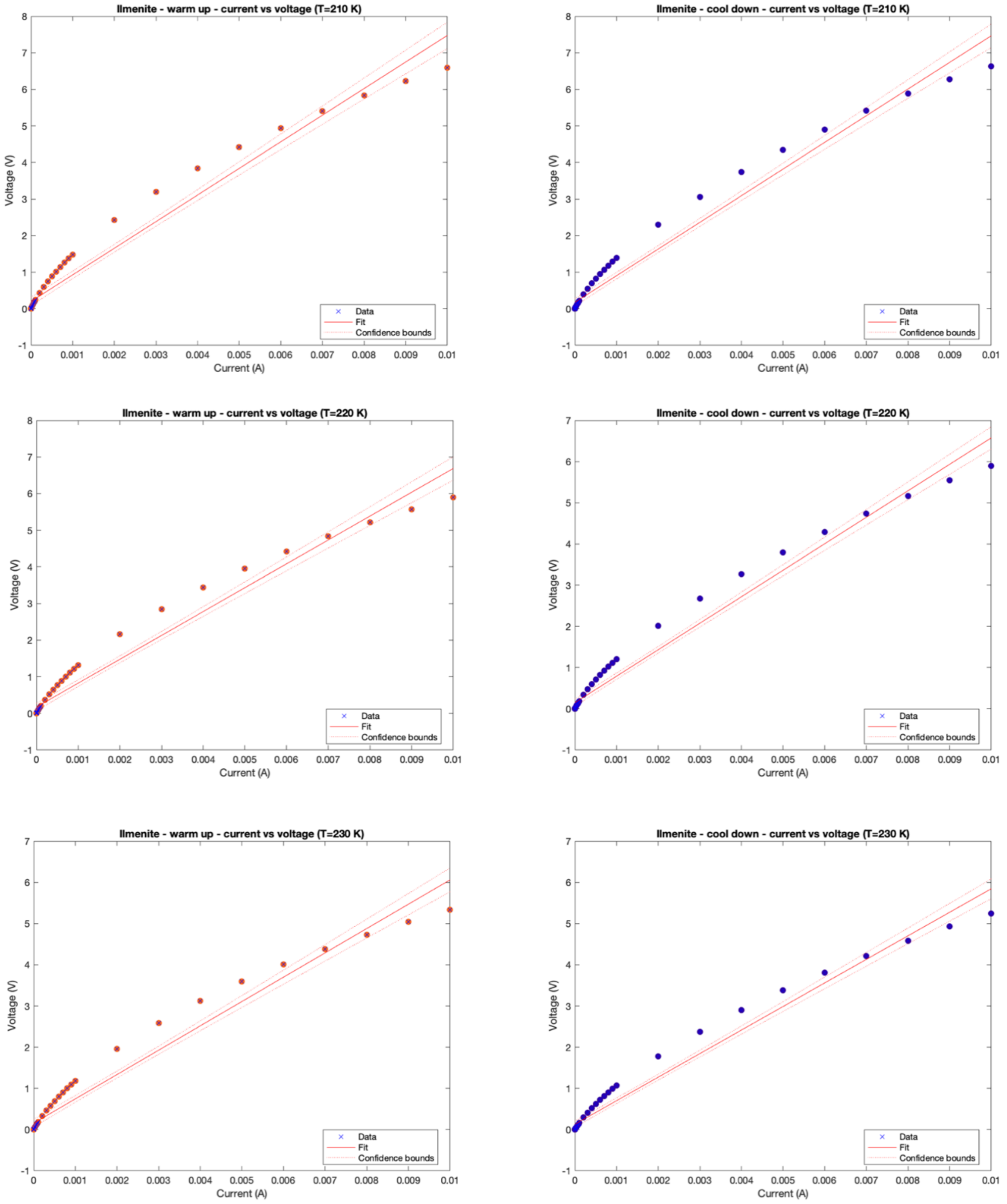

Figure 105: Ilmenite voltage versus current graphs. Temperature range: 210K to 230K.

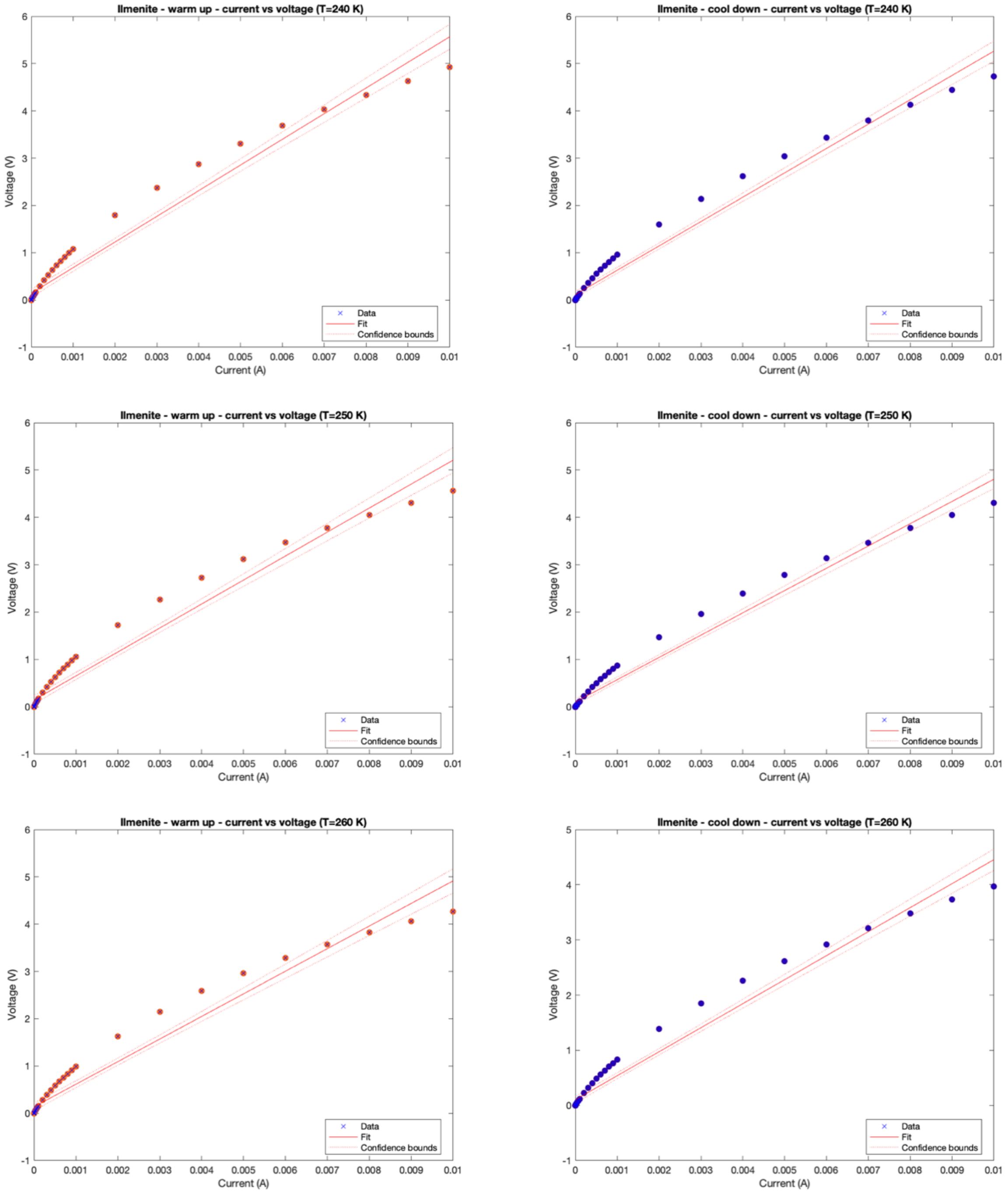

Figure 106: Ilmenite voltage versus current graphs. Temperature range: 240K to 260K.

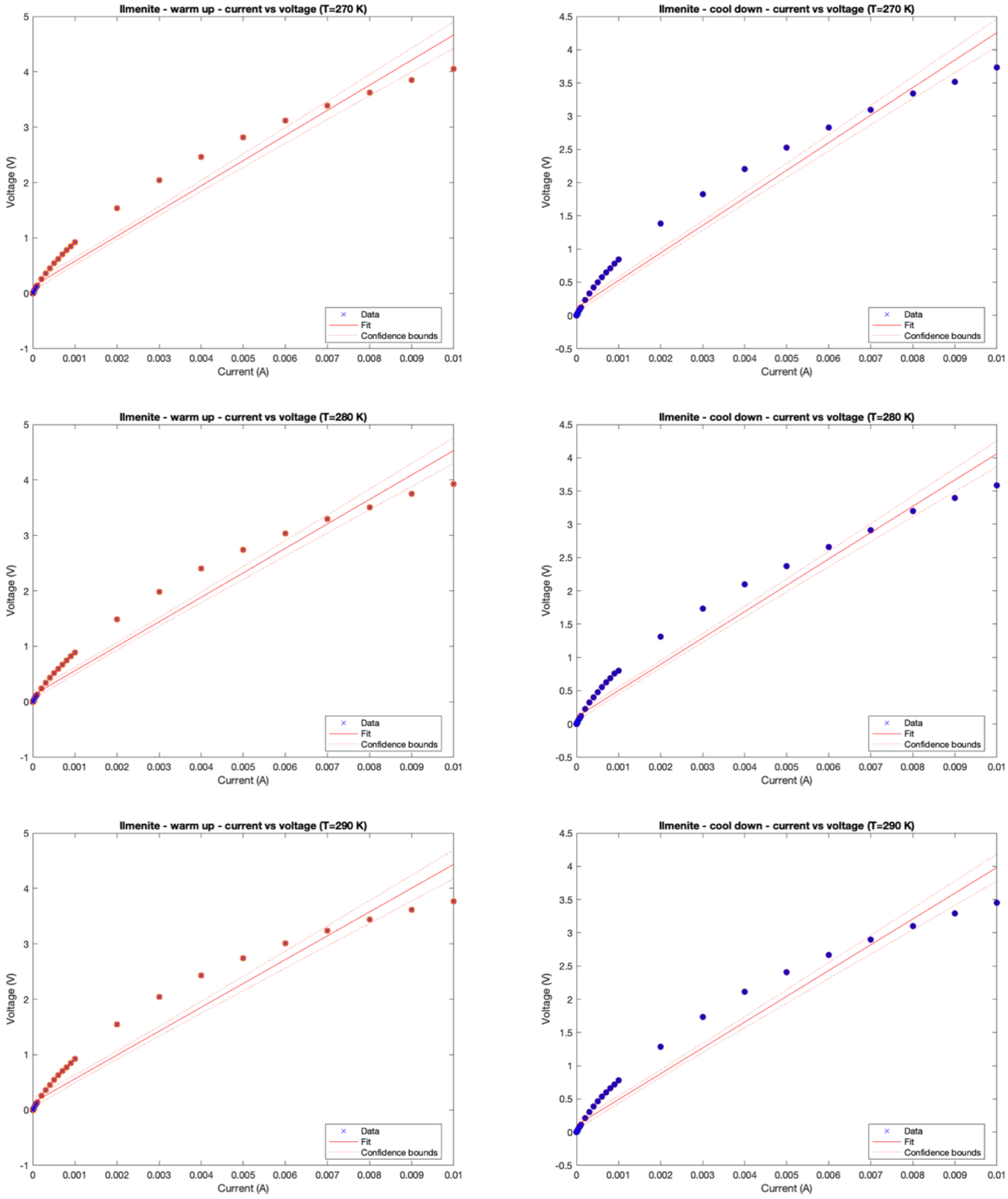

Figure 107: Ilmenite voltage versus current graphs. Temperature range: 270K to 290K.

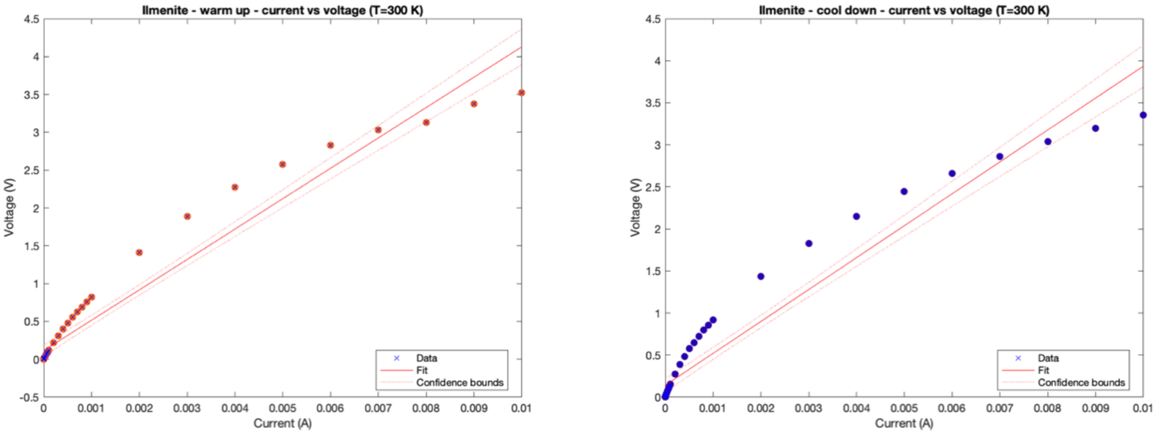

Figure 108: Ilmenite voltage versus current graph. Temperature: 300K.

## *Magnetite*

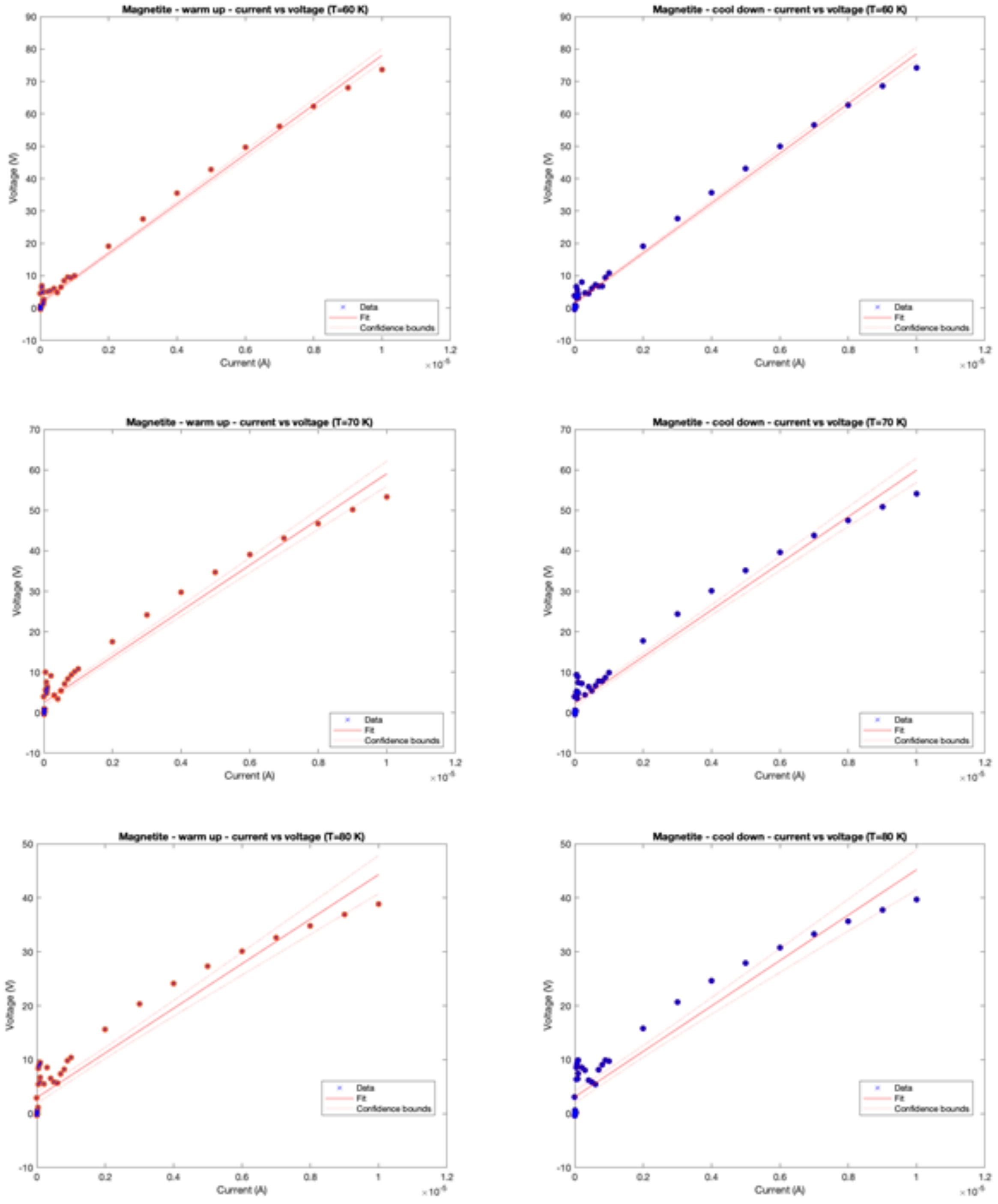

Magnetite - warm up - current vs voltage (T=60 K)

Magnetite - cool down - current vs voltage (T=60 K)

Magnetite - warm up - current vs voltage (T=70 K)

Magnetite - cool down - current vs voltage (T=70 K)

Magnetite - warm up - current vs voltage (T=80 K)

Magnetite - cool down - current vs voltage (T=80 K)

Figure 109: Magnetite versus current graphs. Temperature range: 60K to 80K.

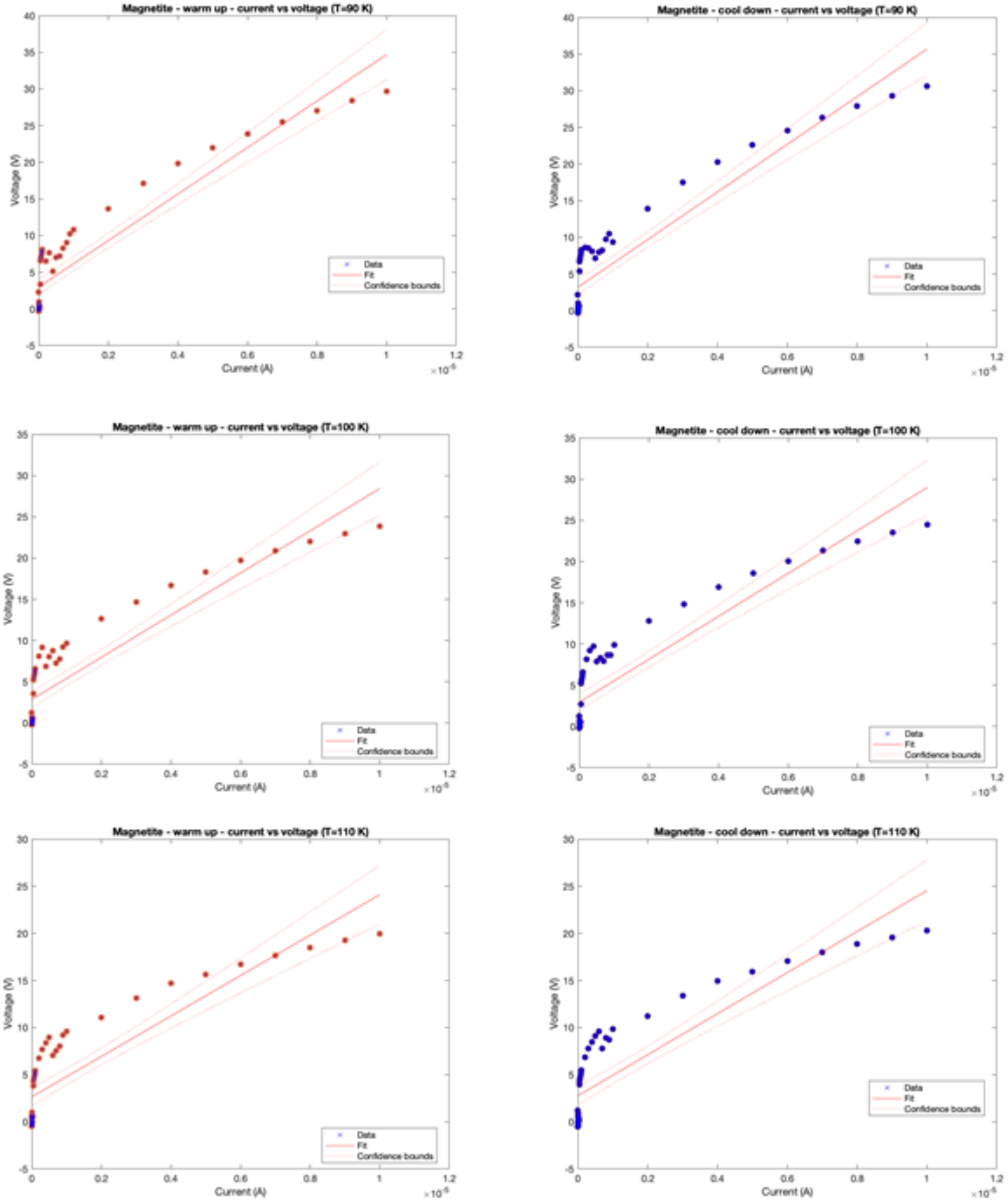

Figure 110: Magnetite voltage versus current graphs. Temperature range: 90K to 110K.

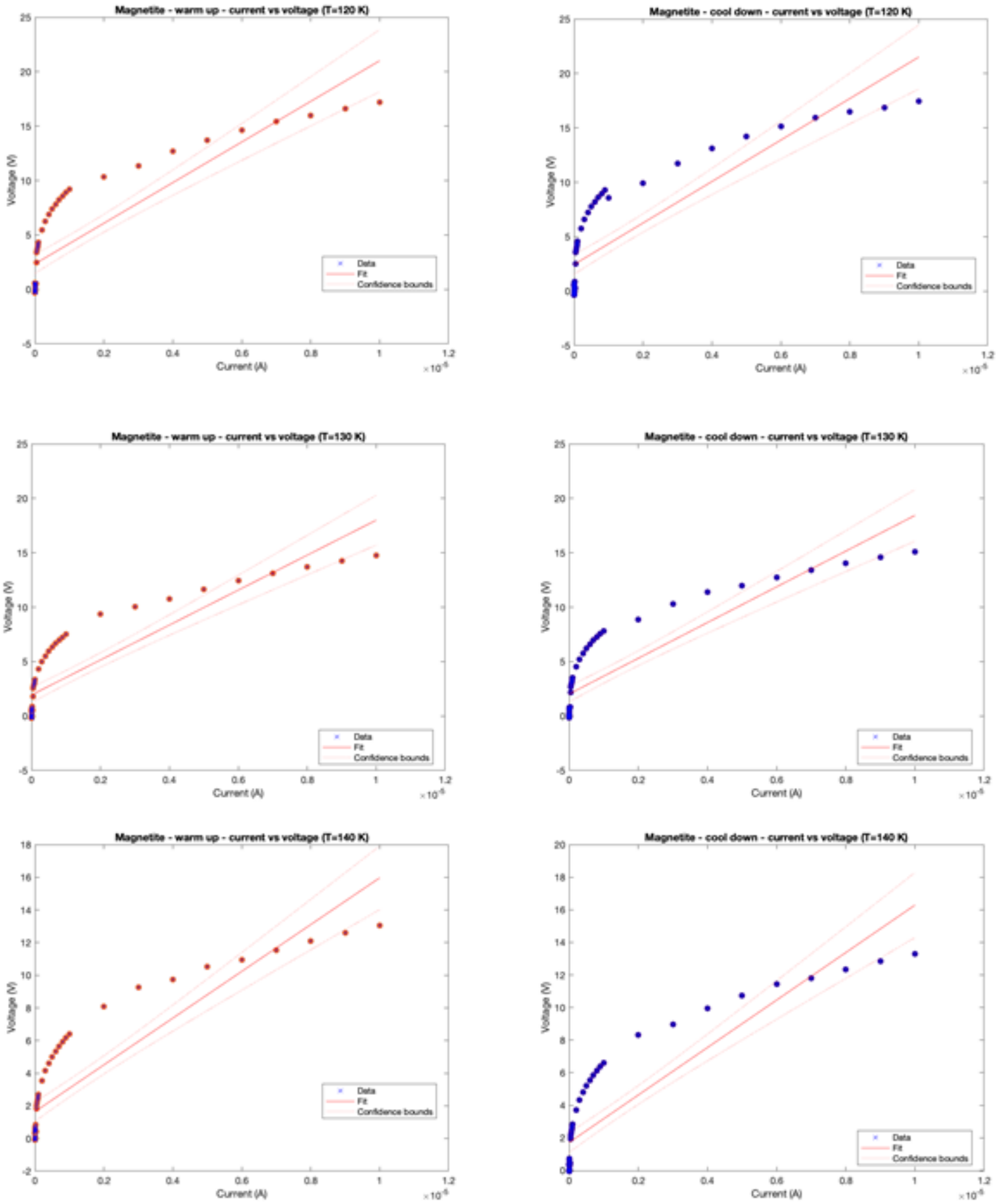

Figure 111: Magnetite voltage versus current graphs. Temperature range: 120K to 140K.

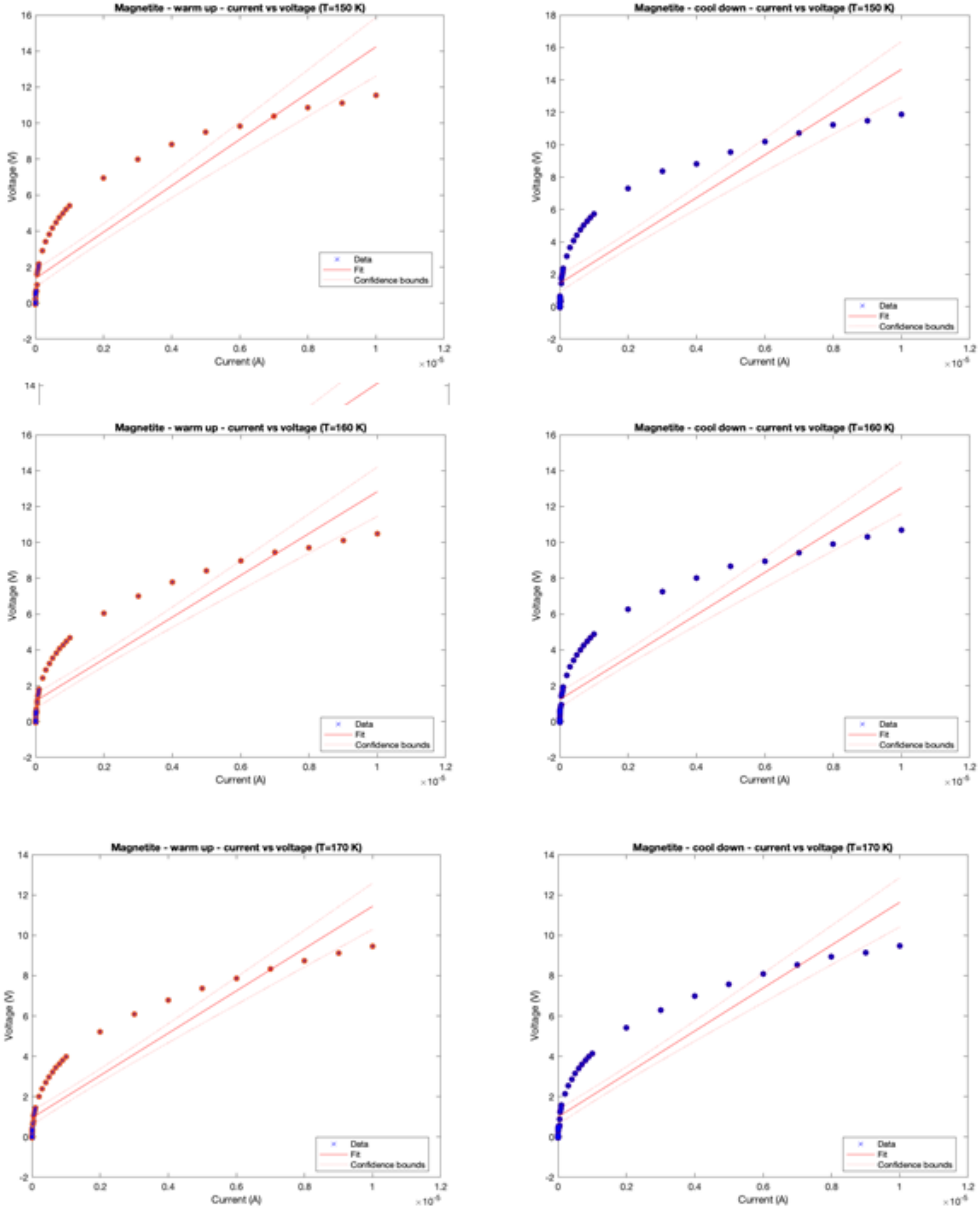

Figure 112: Magnetite voltage versus current graphs. Temperature range: 150K to 170K.

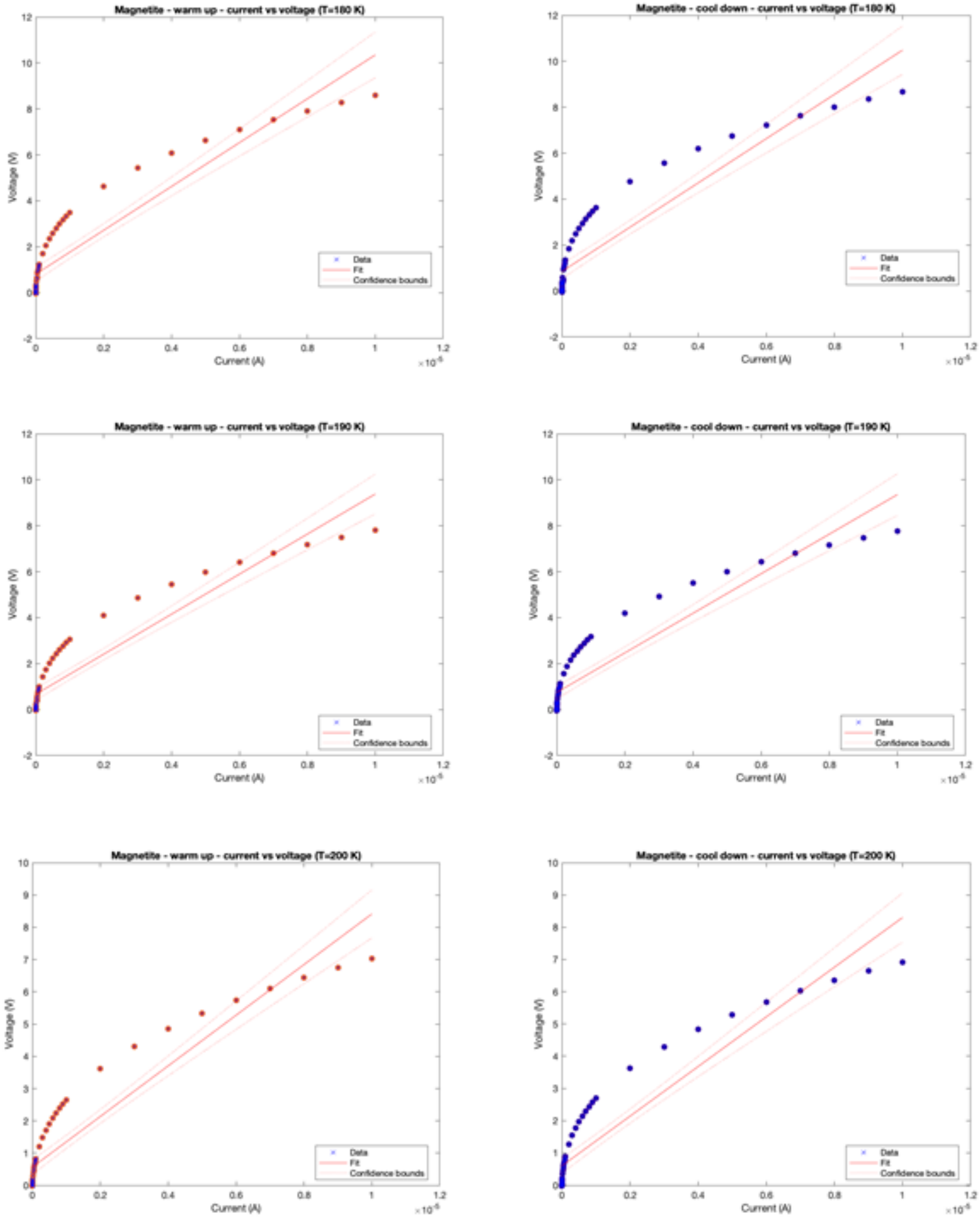

Figure 113: Magnetite voltage versus current graphs. Temperature range: 180K to 200K.

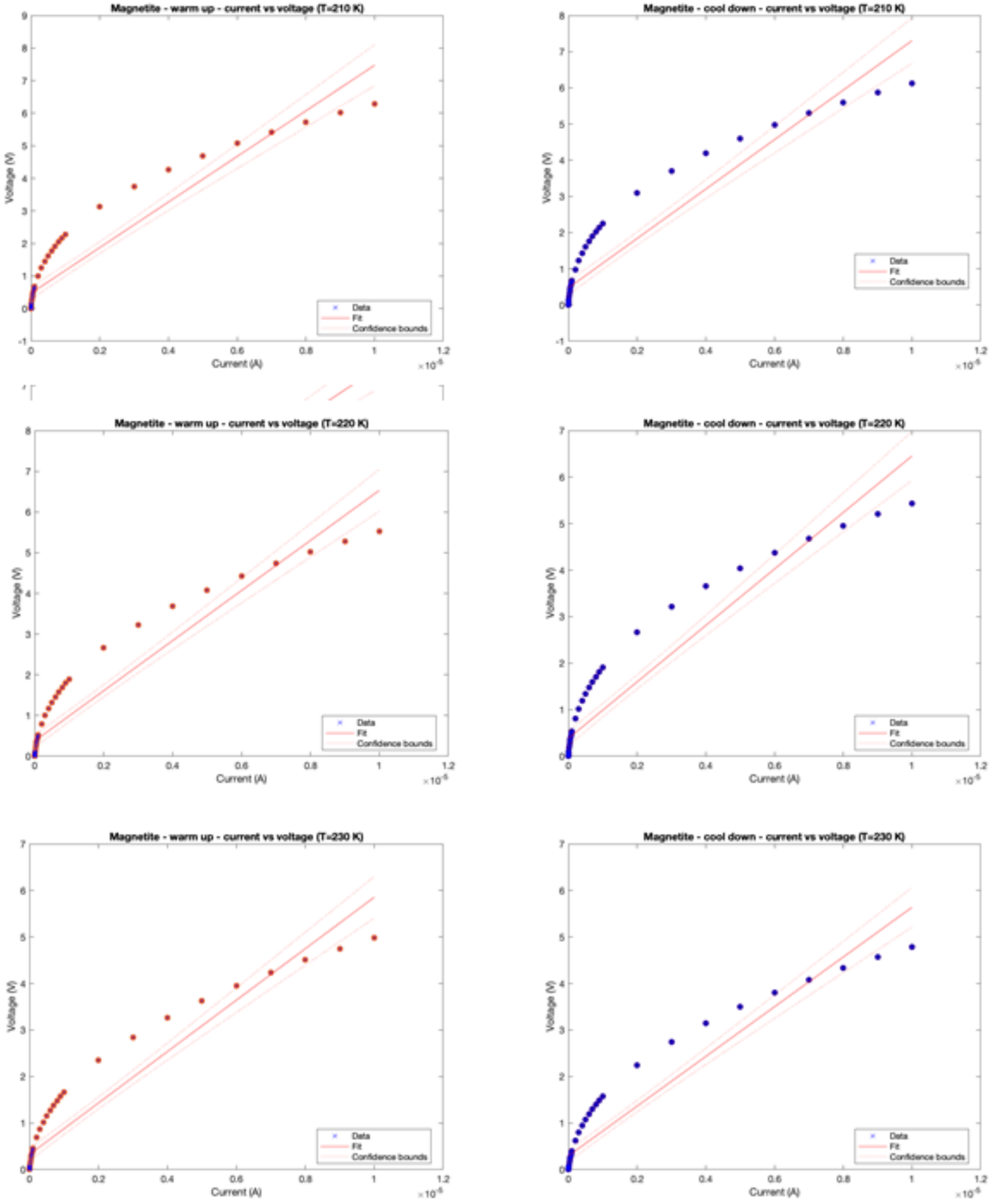

Figure 114: Magnetite voltage versus current graphs. Temperature range: 210K to 230K.

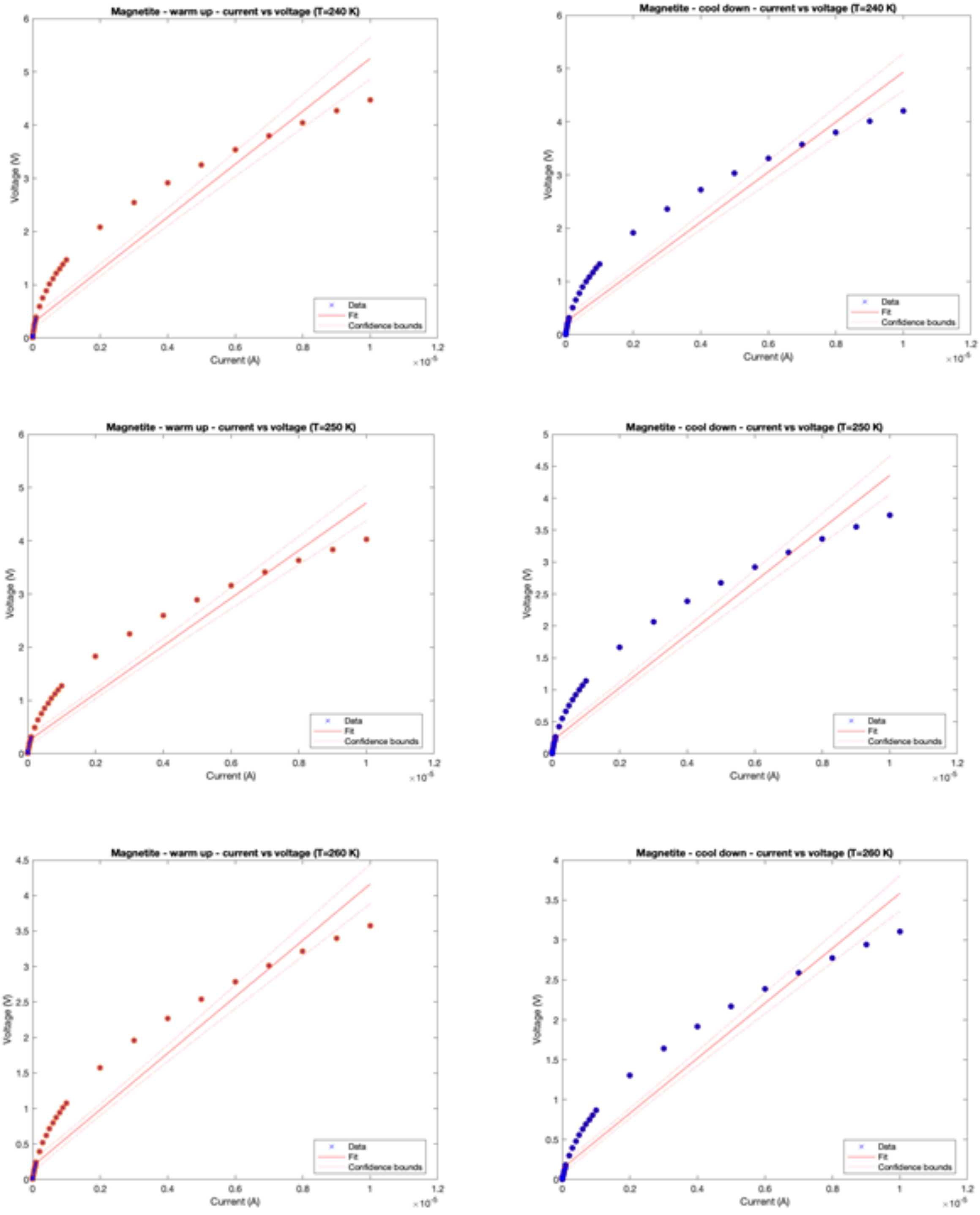

Figure 115: Magnetite voltage versus current graphs. Temperature range: 240K to 260K.

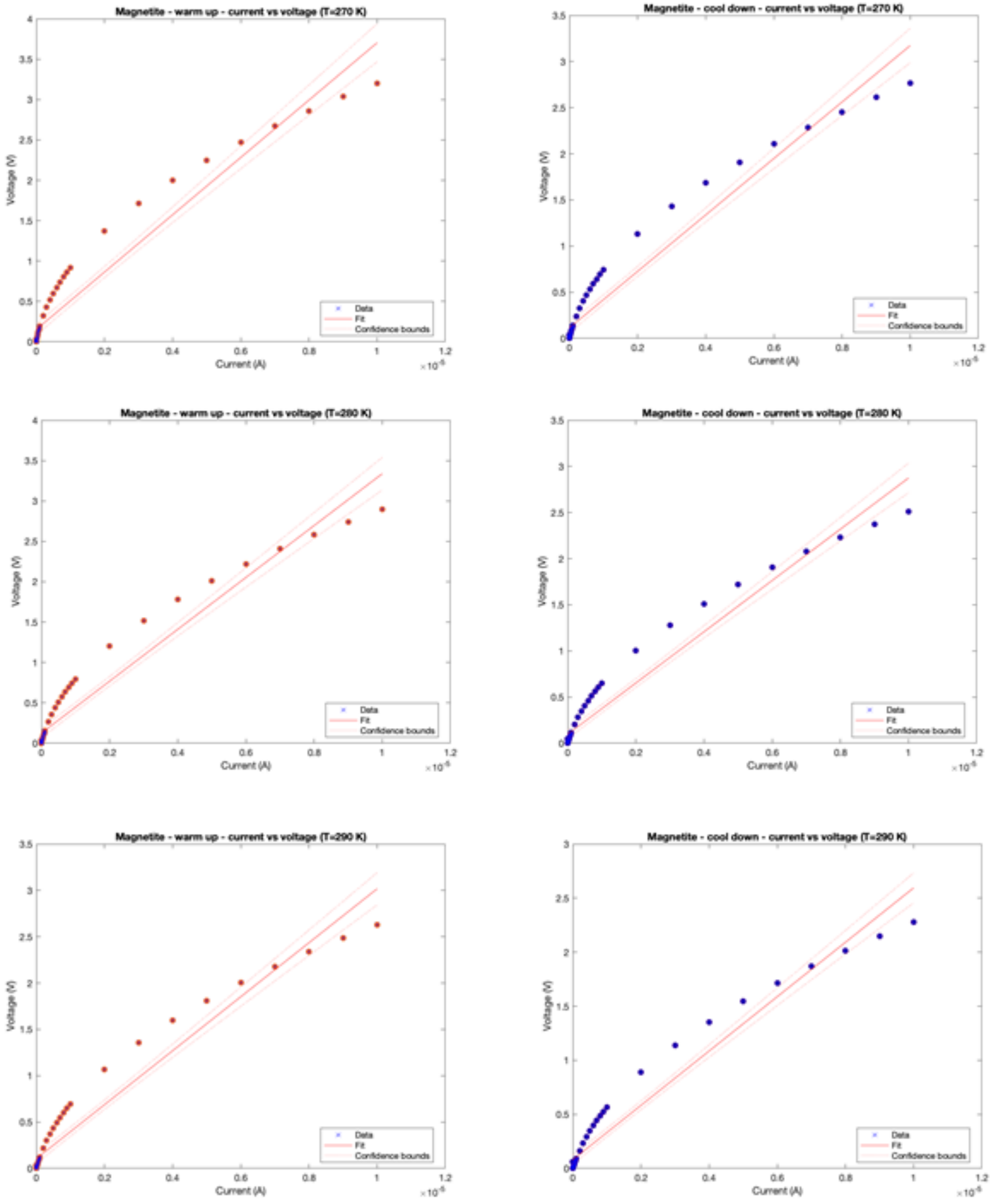

Figure 116: Magnetite voltage versus current graphs. Temperature range: 270K to 290K.

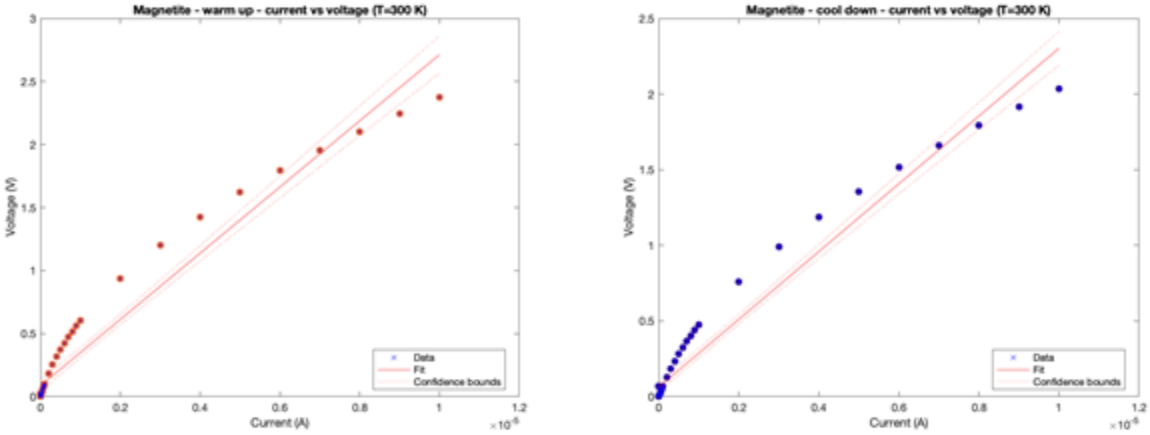

Figure 117: Magnetite voltage versus current graphs. Temperature range: 300K.

### *Magnetite lodestone*

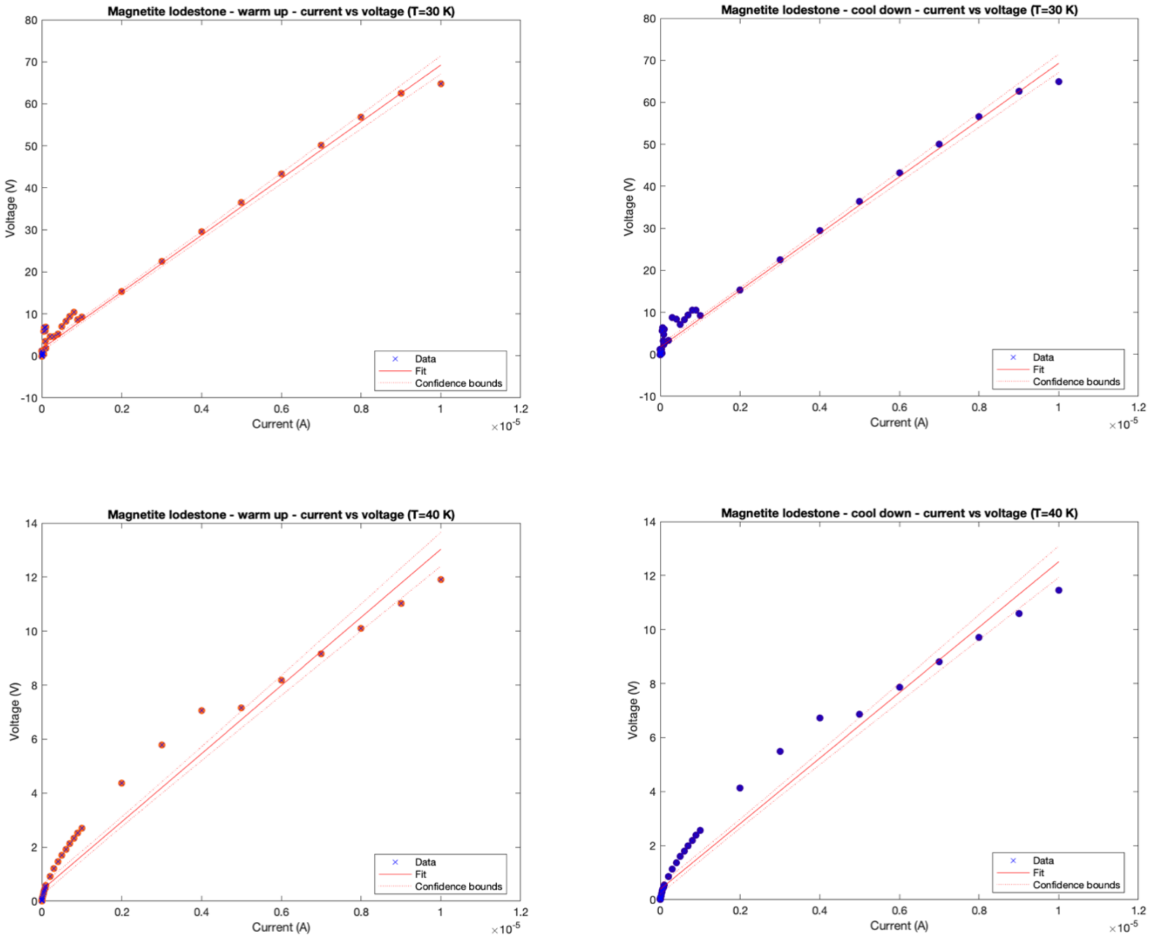

Figure 118: Magnetite lodestone voltage versus current graphs. Temperature range: 30K to 40K.

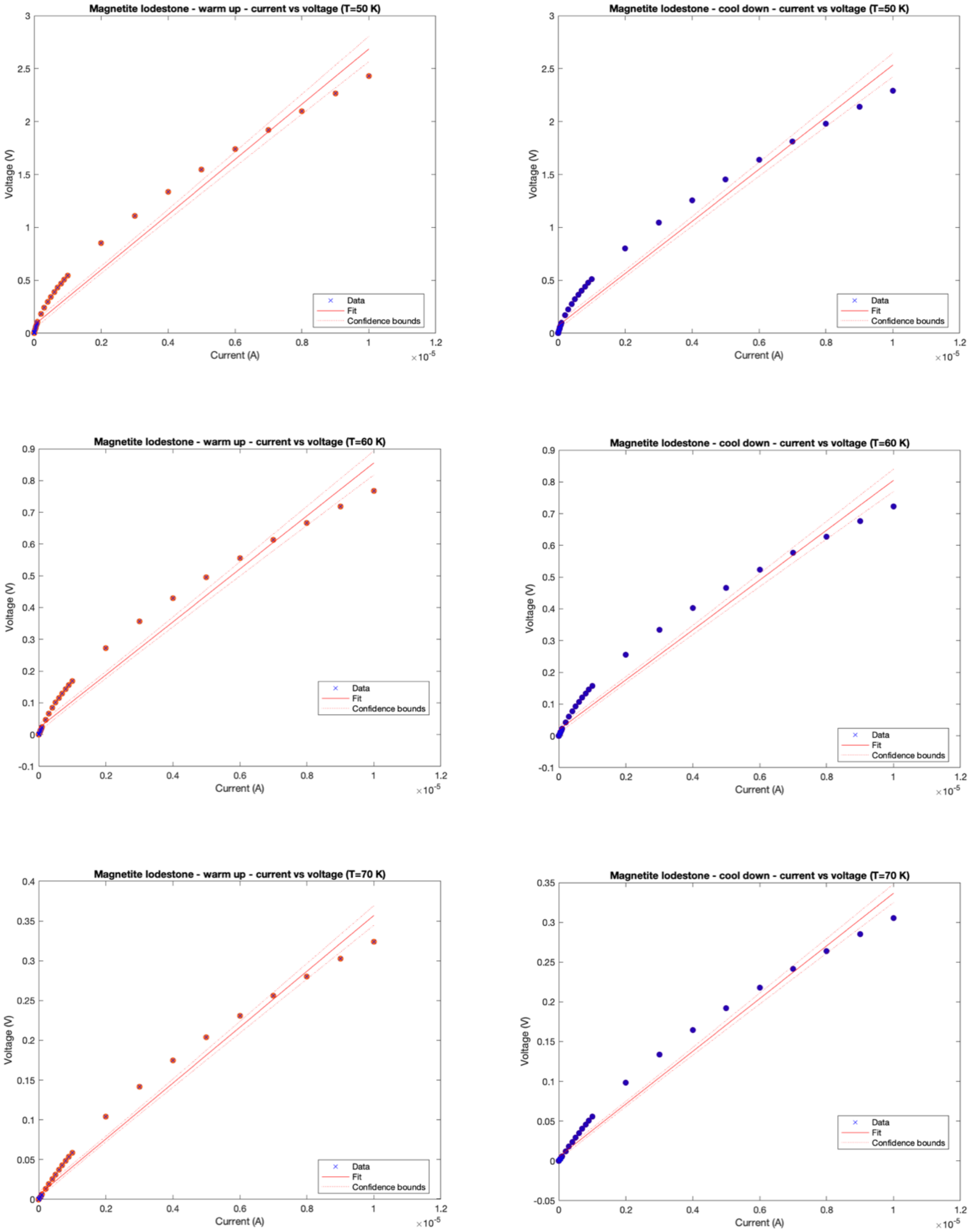
Magnetite lodestone - warm up - current vs voltage (T=50 K)

Magnetite lodestone - cool down - current vs voltage (T=50 K)

Magnetite lodestone - warm up - current vs voltage (T=60 K)

Magnetite lodestone - cool down - current vs voltage (T=60 K)

Magnetite lodestone - warm up - current vs voltage (T=70 K)

Magnetite lodestone - cool down - current vs voltage (T=70 K)

Figure 119: Magnetite lodestone voltage versus current graphs. Temperature range: 50K to 70K.

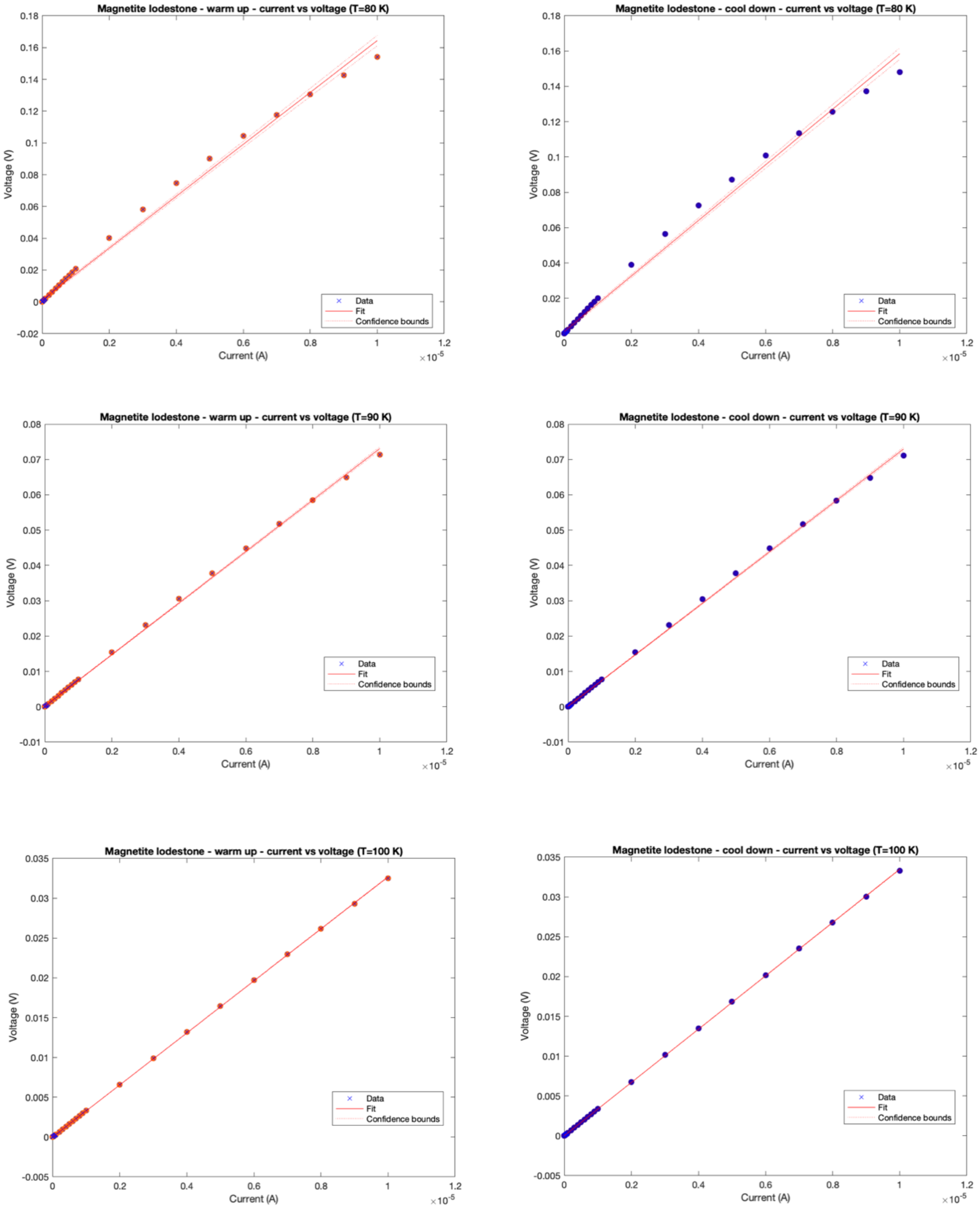

Figure 120: Magnetite lodestone voltage versus current graphs. Temperature range: 80K to 100K.

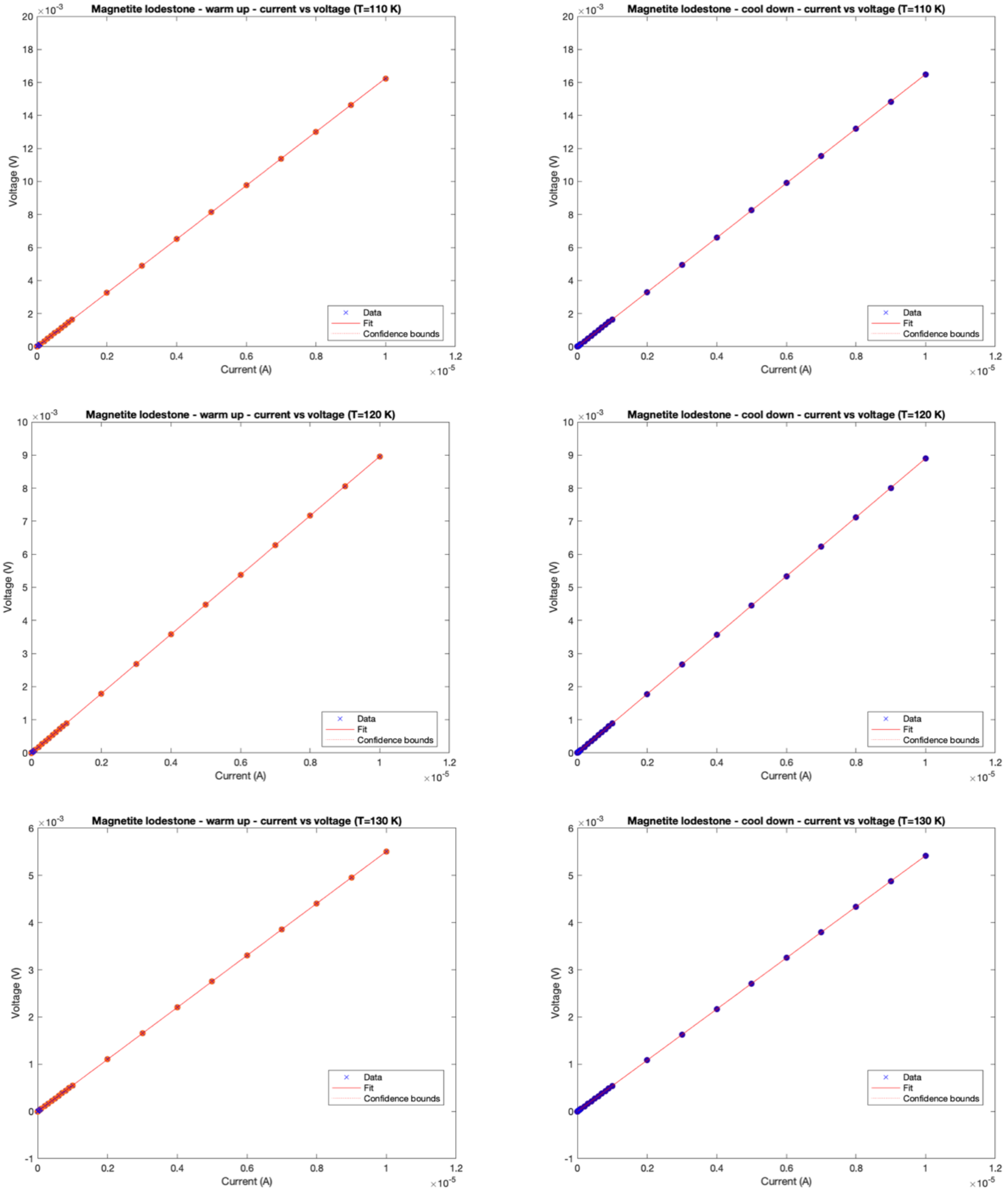
Magnetite lodestone - warm up - current vs voltage (T=110 K)

Magnetite lodestone - cool down - current vs voltage (T=110 K)

Magnetite lodestone - warm up - current vs voltage (T=120 K)

Magnetite lodestone - cool down - current vs voltage (T=120 K)

Magnetite lodestone - warm up - current vs voltage (T=130 K)

Magnetite lodestone - cool down - current vs voltage (T=130 K)

Figure 121: Magnetite lodestone voltage versus current graphs. Temperature range: 110K to 130K.

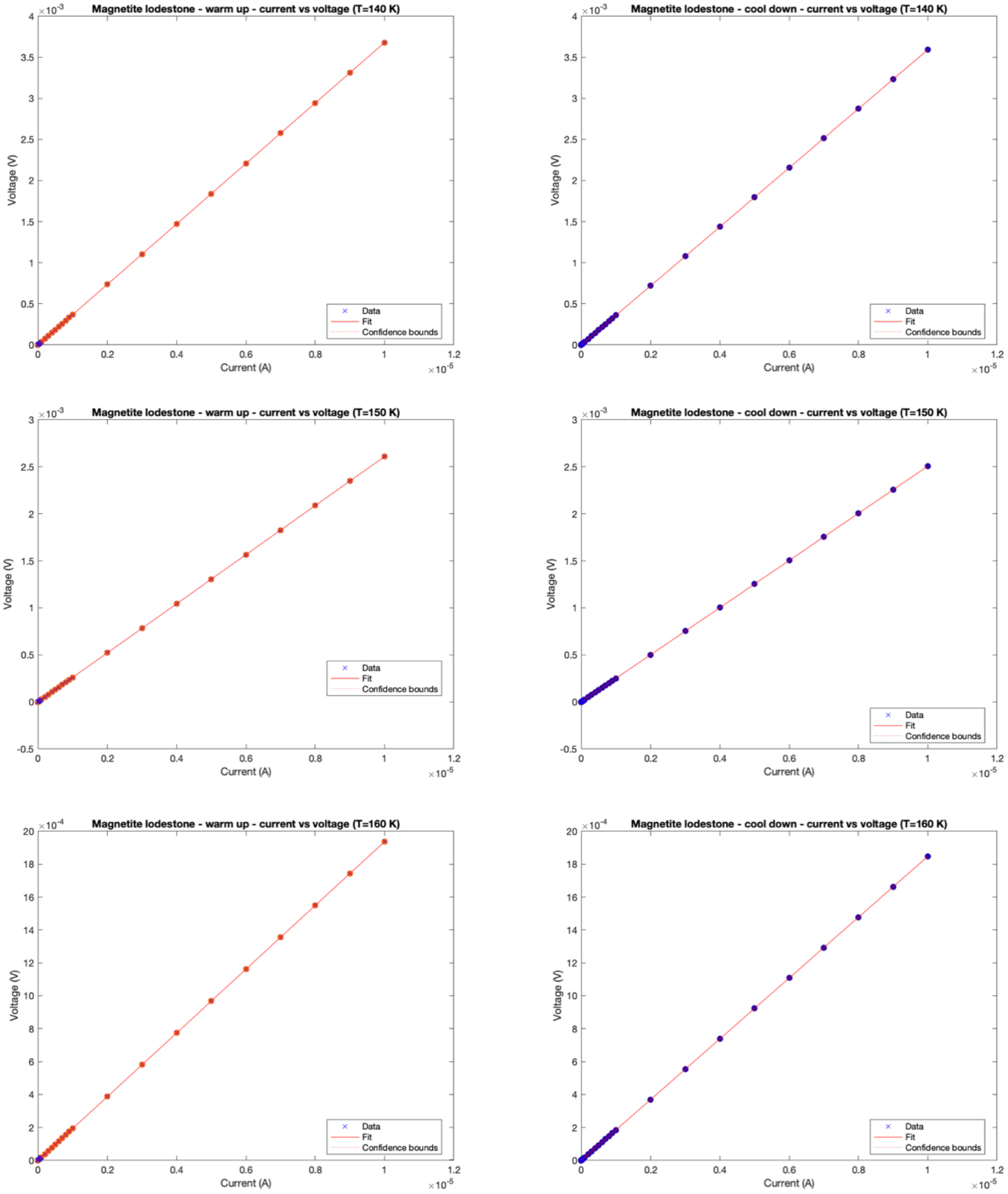

Figure 122: Magnetite lodestone voltage versus current graphs. Temperature range: 140K to 160K.

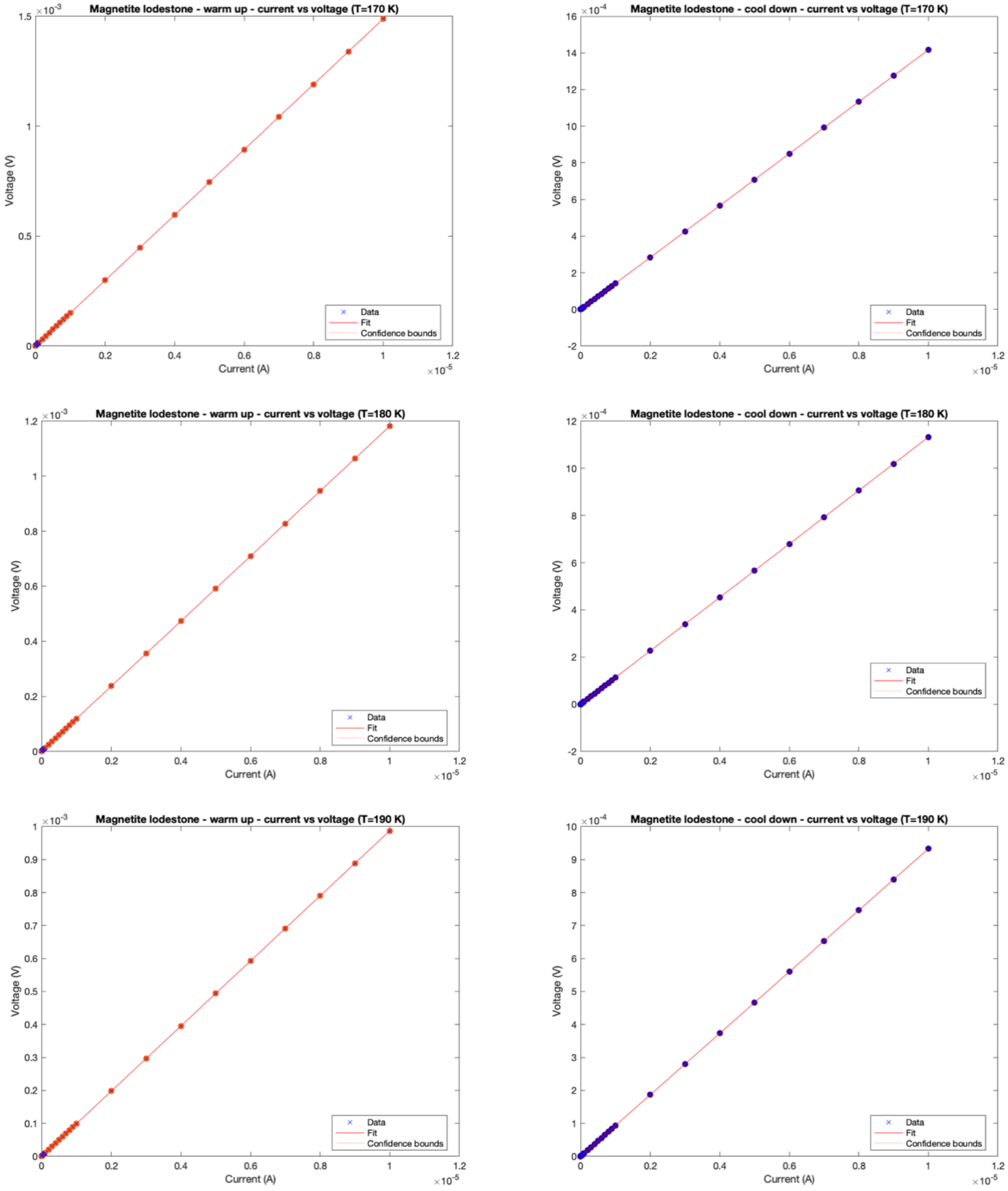

Figure 123: Magnetite lodestone voltage versus current graphs. Temperature range: 170K to 190K.

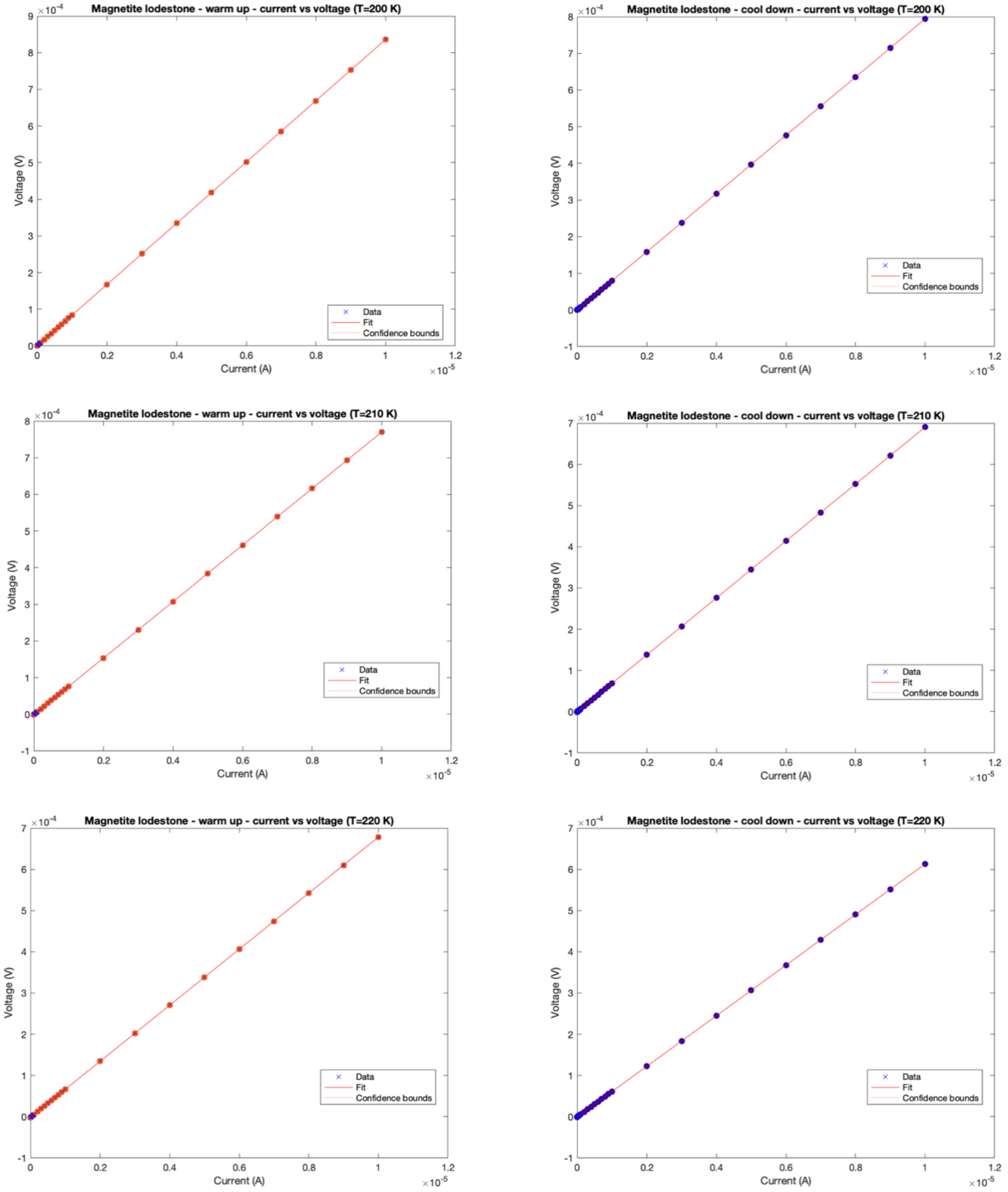

Figure 124: Magnetite lodestone voltage versus current graphs. Temperature range: 200K to 220K.

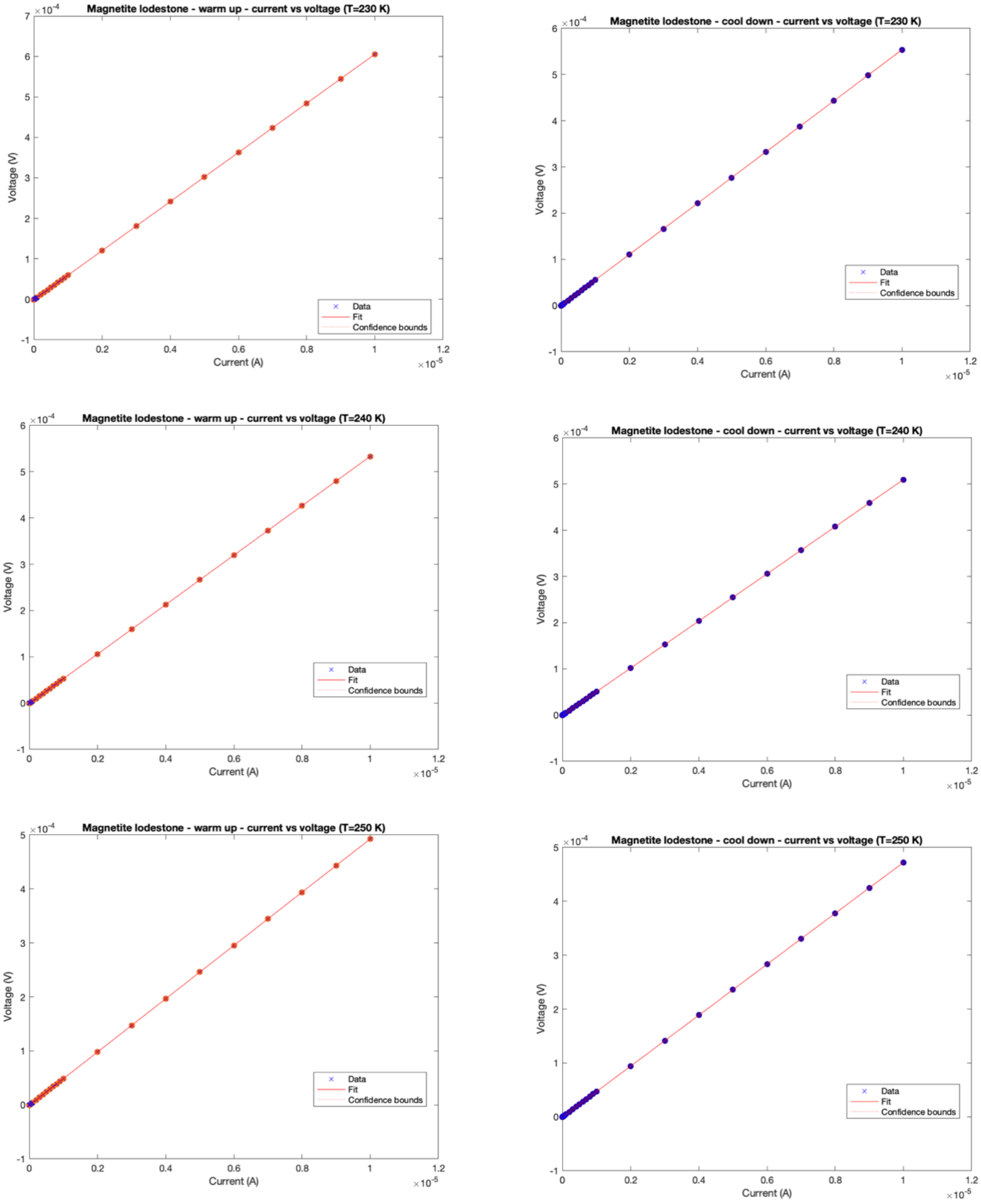

Figure 125: Magnetite lodestone voltage versus current graphs. Temperature range: 230K to 250K.

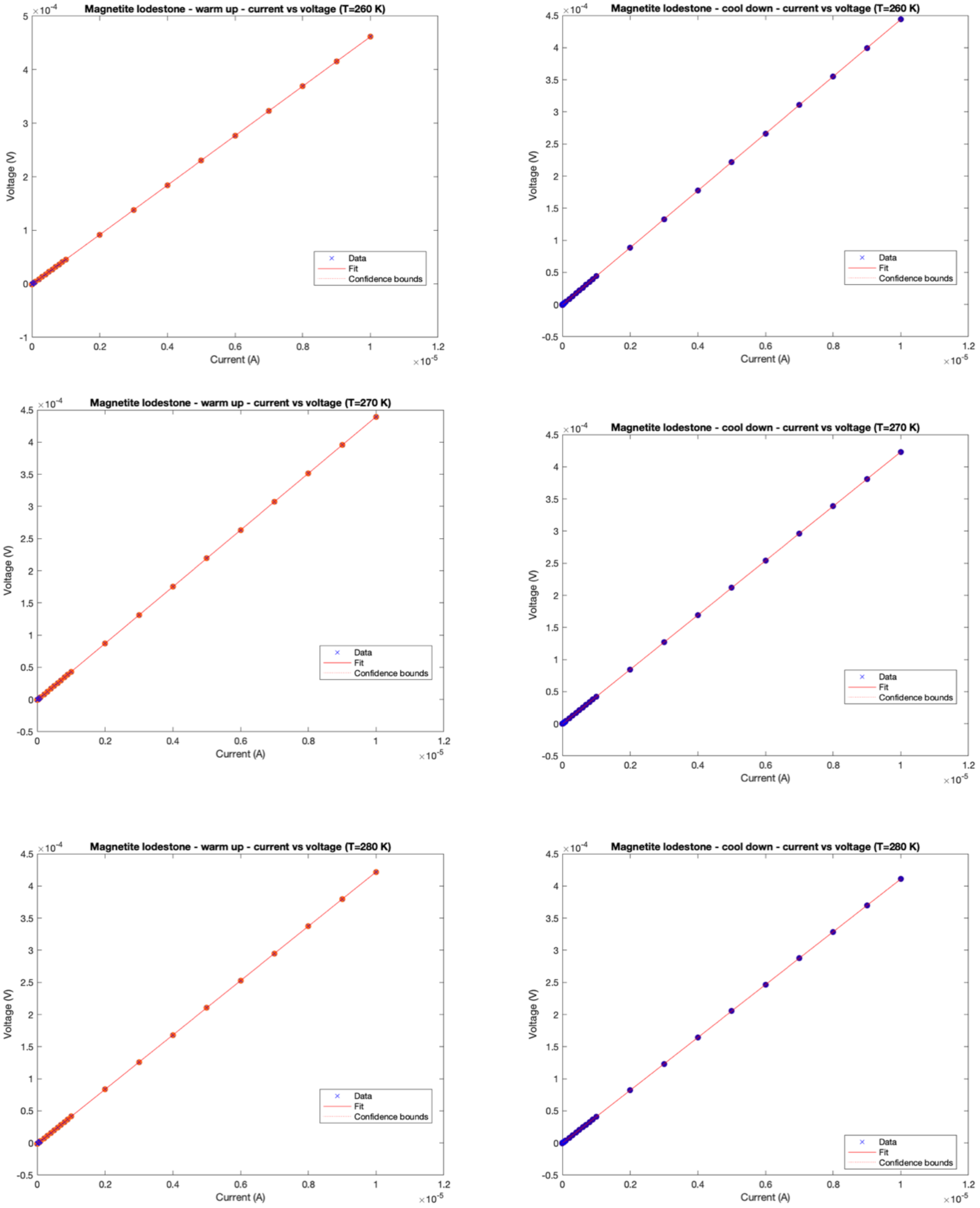

Figure 126: Magnetite lodestone voltage versus current graphs. Temperature range: 260K to 280K.

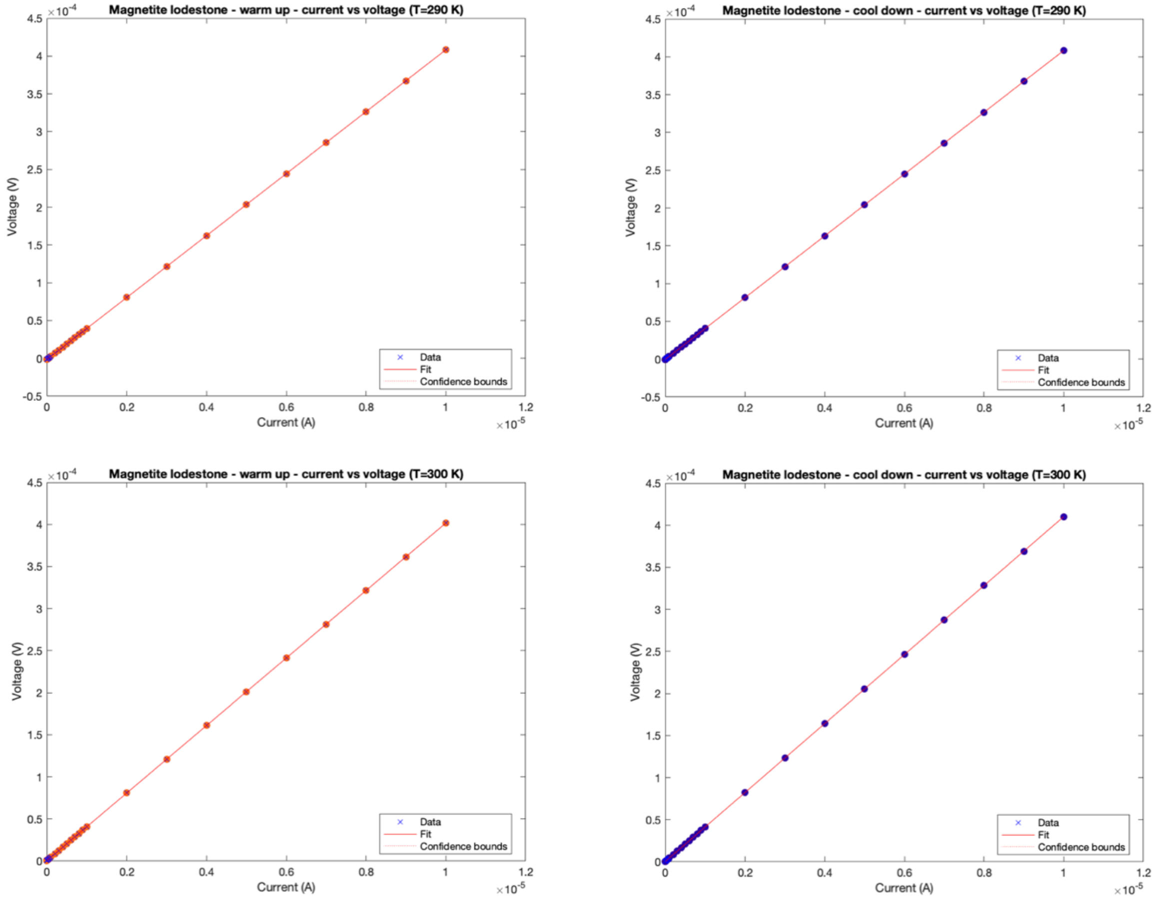
Magnetite lodestone - warm up - current vs voltage (T=290 K)

Magnetite lodestone - cool down - current vs voltage (T=290 K)

Magnetite lodestone - warm up - current vs voltage (T=300 K)

Magnetite lodestone - cool down - current vs voltage (T=300 K)

Figure 127: Magnetite lodestone voltage versus current graphs. Temperature range: 290K to 300K.

### *Pyrite*

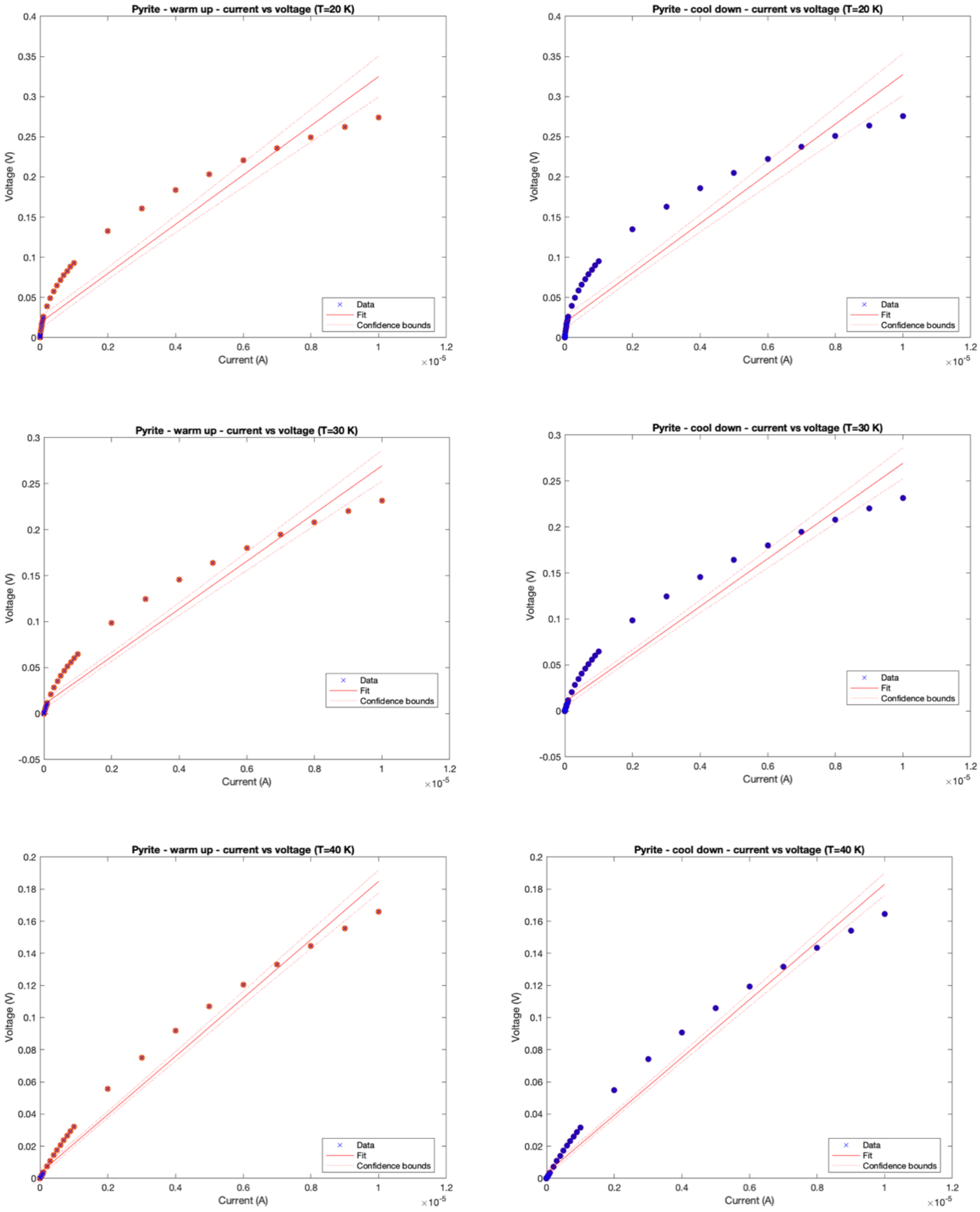

Figure 128: Pyrite voltage versus current graphs. Temperature range: 20K to 40K.

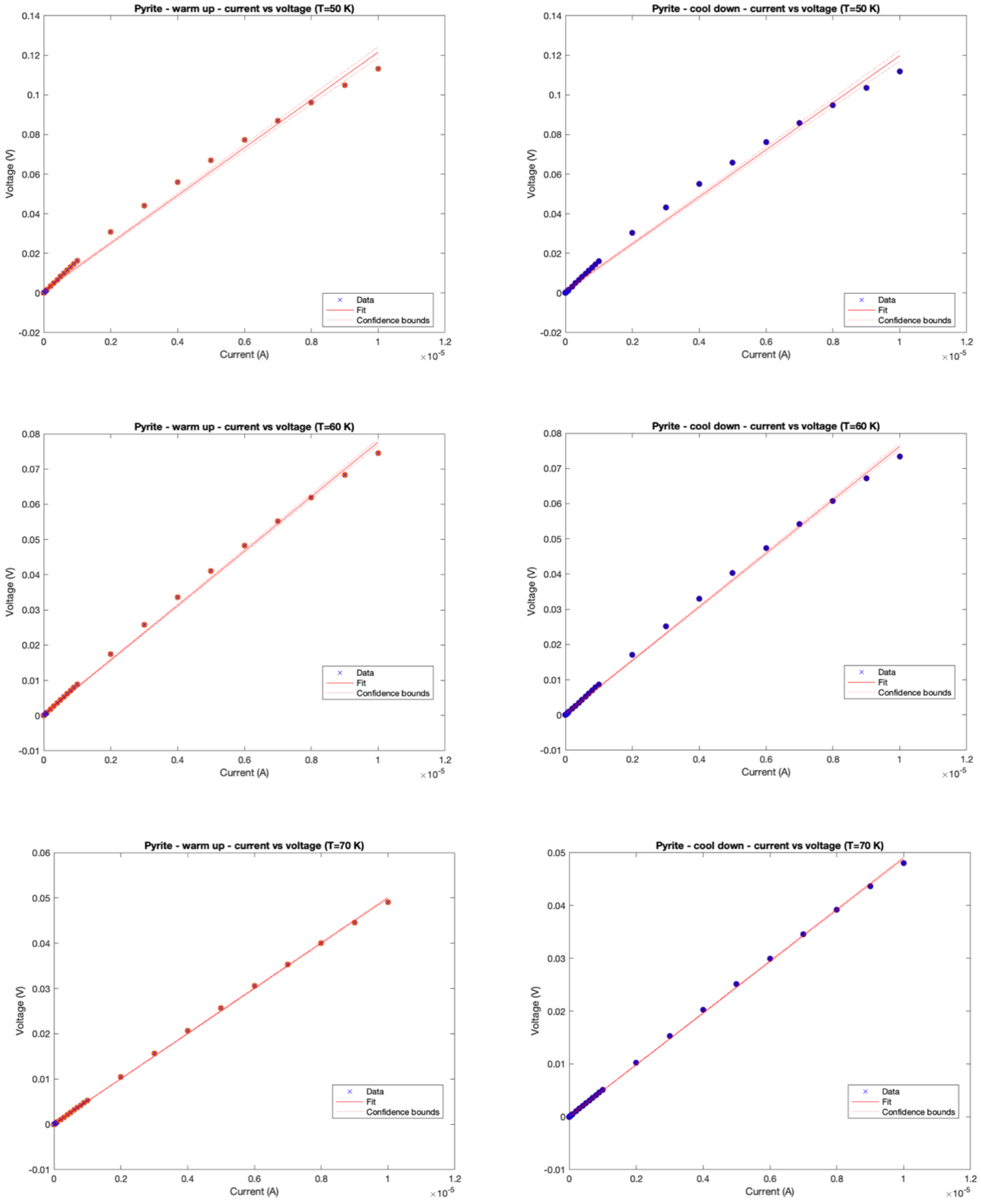

Figure 129: Pyrite voltage versus current graphs. Temperature range: 50K to 70K.

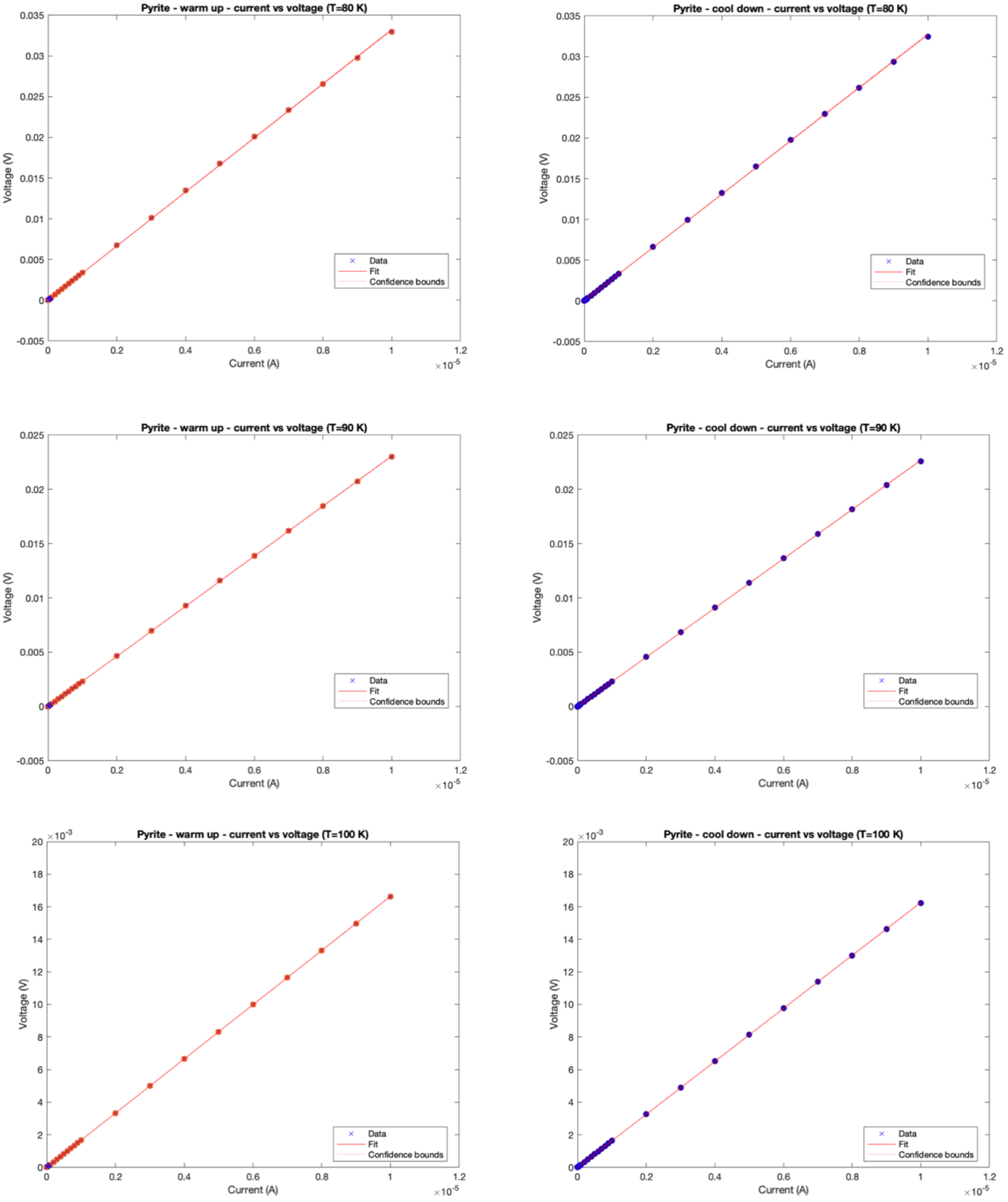
Pyrite - warm up - current vs voltage (T=80 K)

Pyrite - cool down - current vs voltage (T=80 K)

Pyrite - warm up - current vs voltage (T=90 K)

Pyrite - cool down - current vs voltage (T=90 K)

Pyrite - warm up - current vs voltage (T=100 K)

Pyrite - cool down - current vs voltage (T=100 K)

Figure 130: Pyrite voltage versus current graphs. Temperature range: 80K to 100K

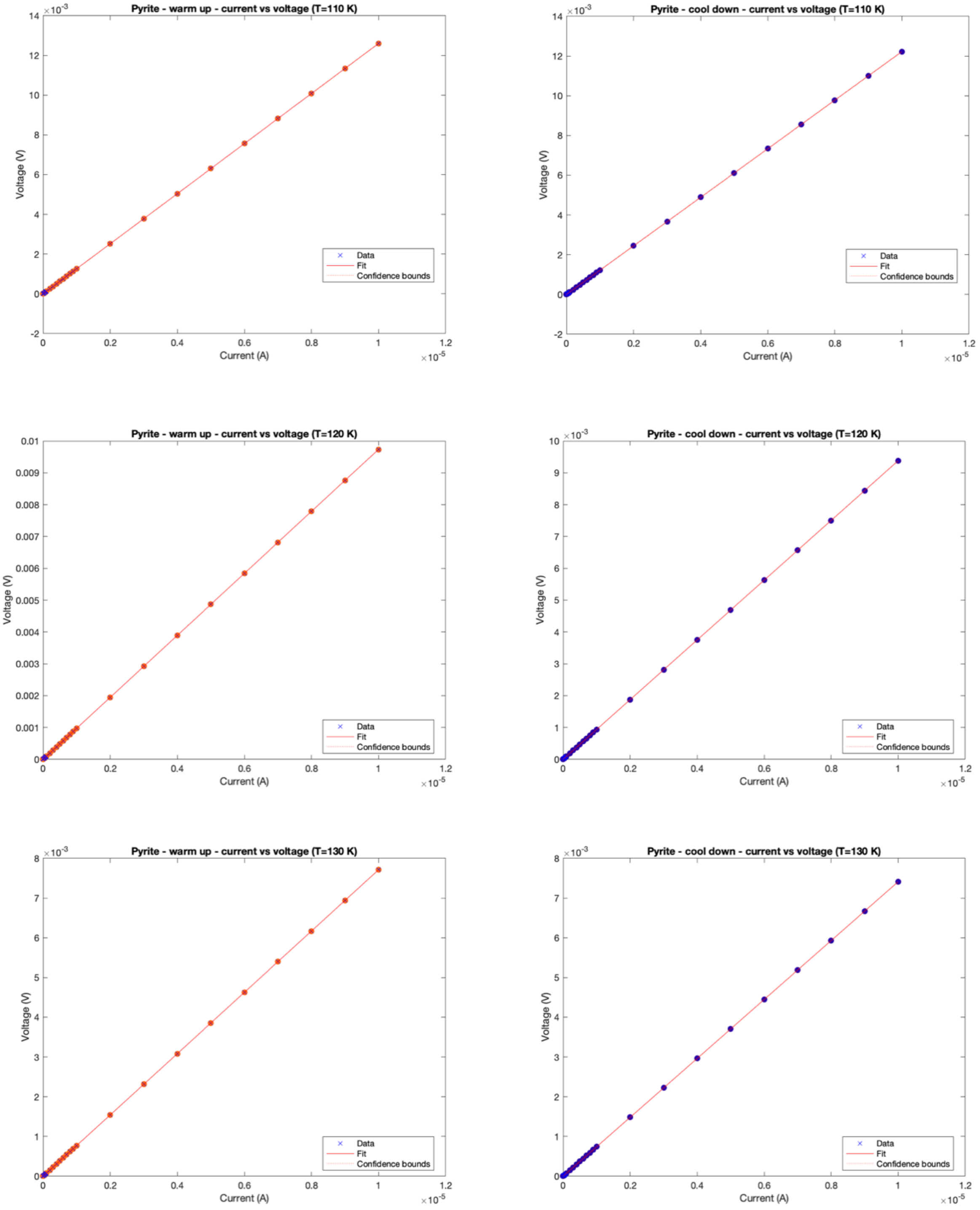

Figure 131: Pyrite voltage versus current graphs. Temperature range: 110K to 130K.

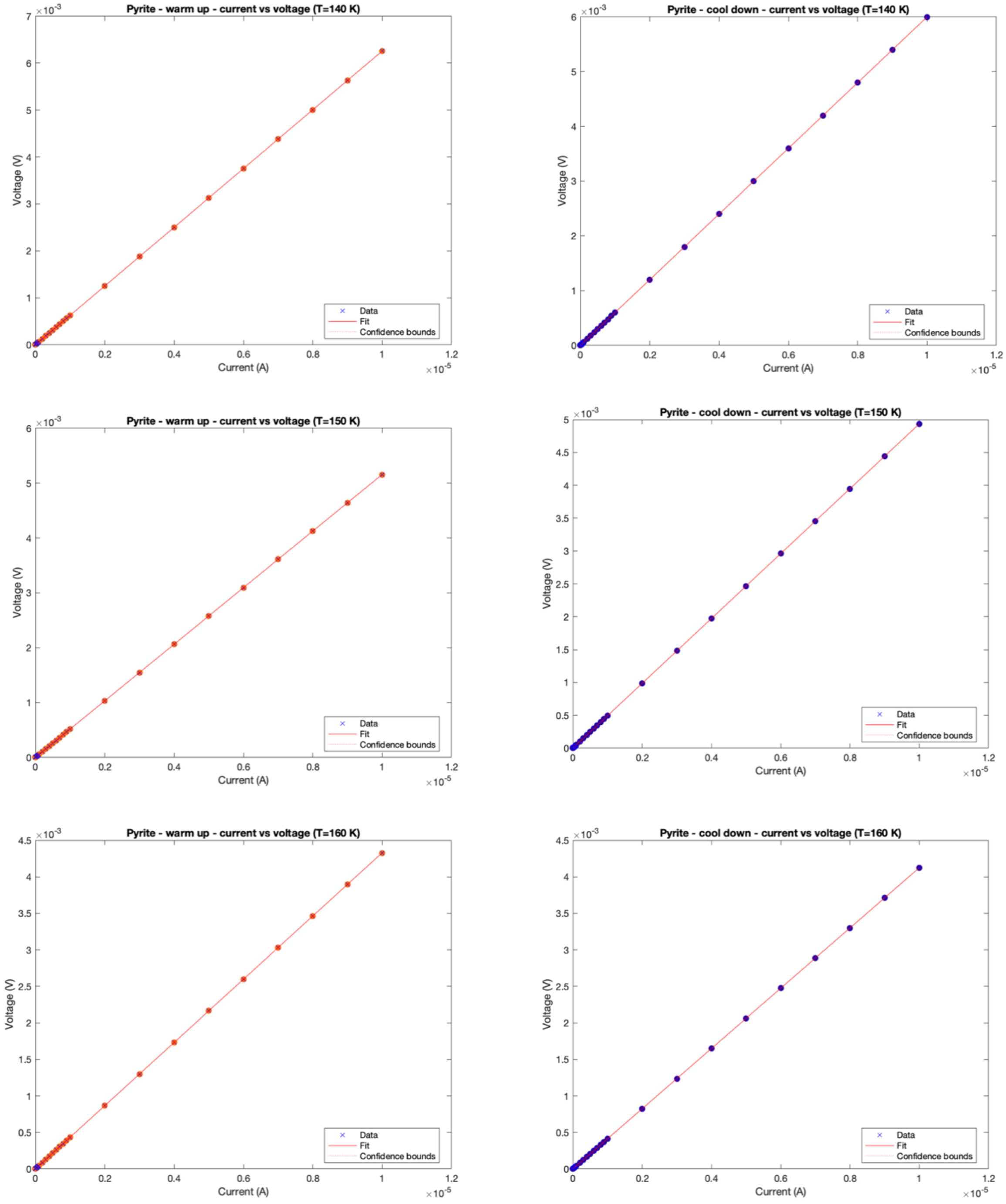

Figure 132: Pyrite voltage versus current graphs. Temperature range: 140K to 160K.

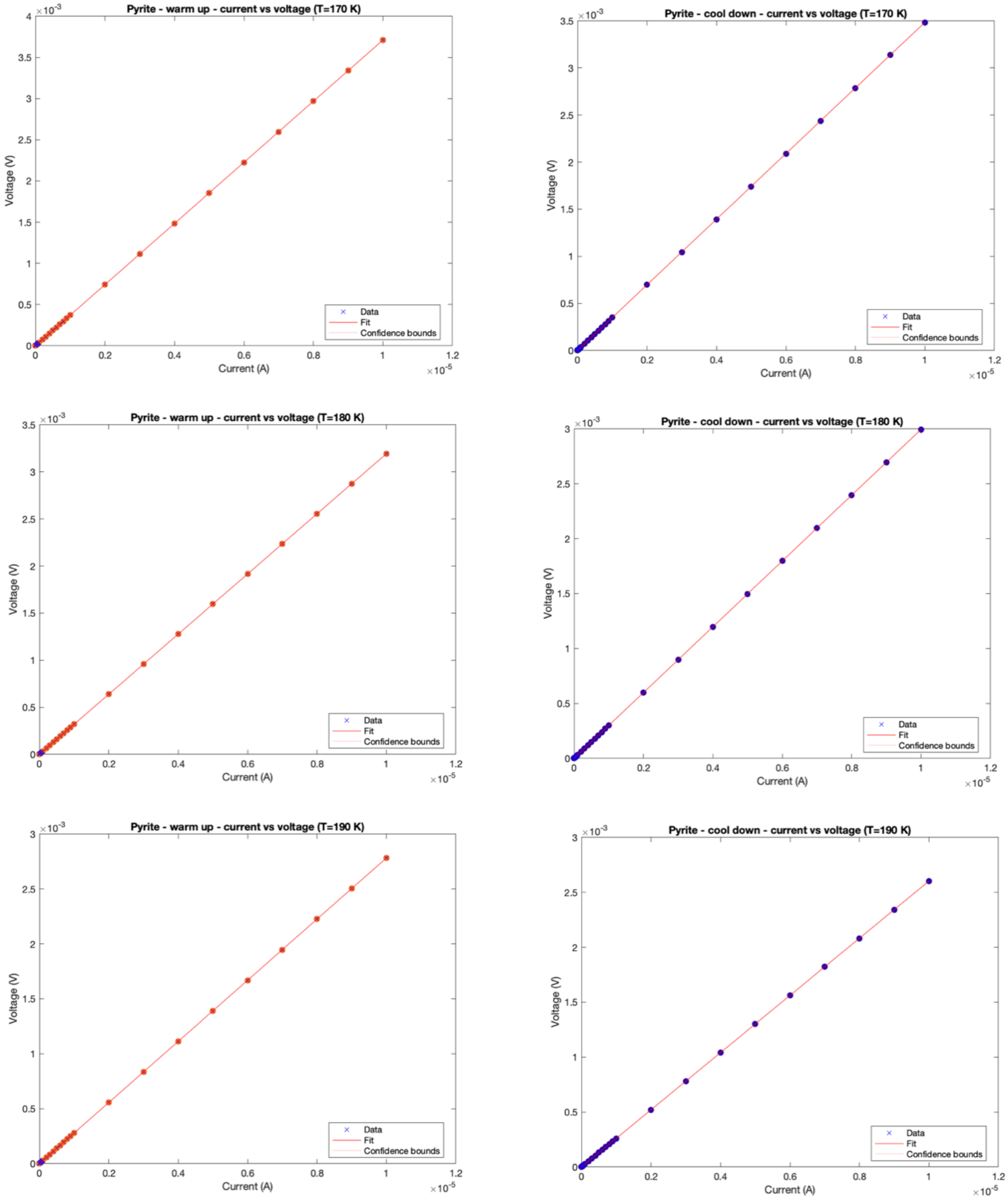

Figure 133: Pyrite voltage versus current graphs. Temperature range: 170K to 190K.

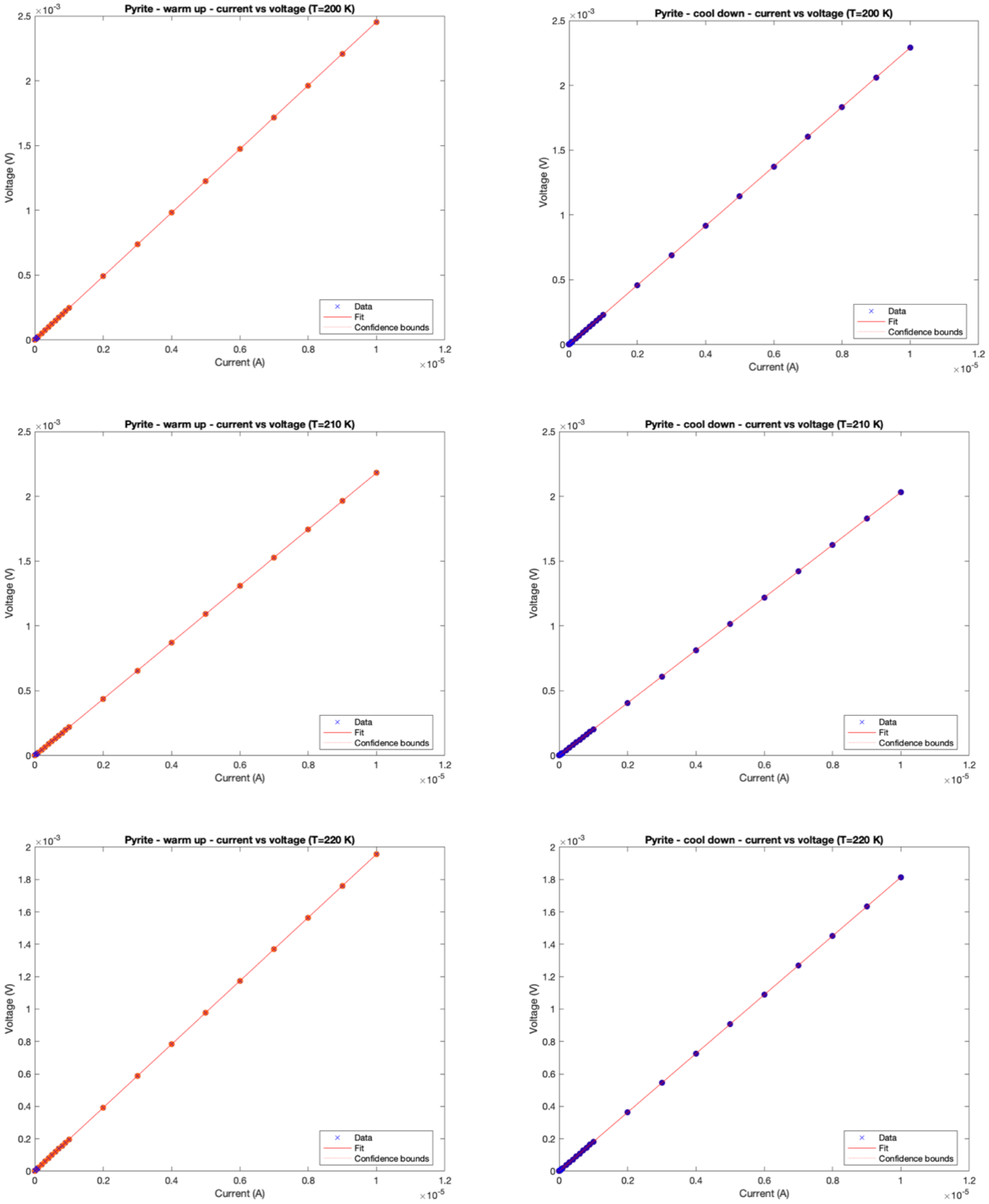

Figure 134: Pyrite voltage versus current graphs. Temperature range: 200K to 220K.

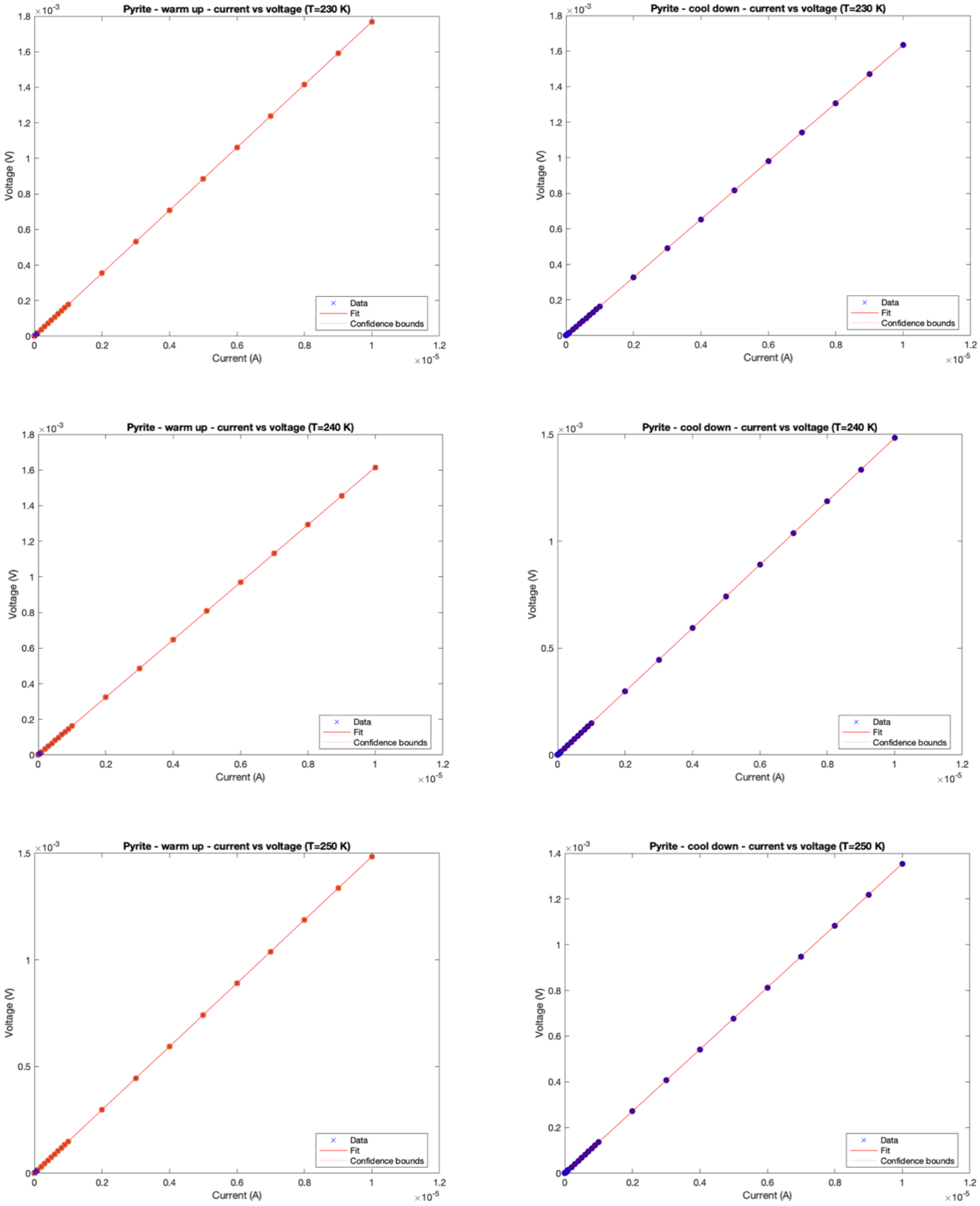

Figure 135: Pyrite voltage versus current graphs. Temperature range: 230K to 250K.

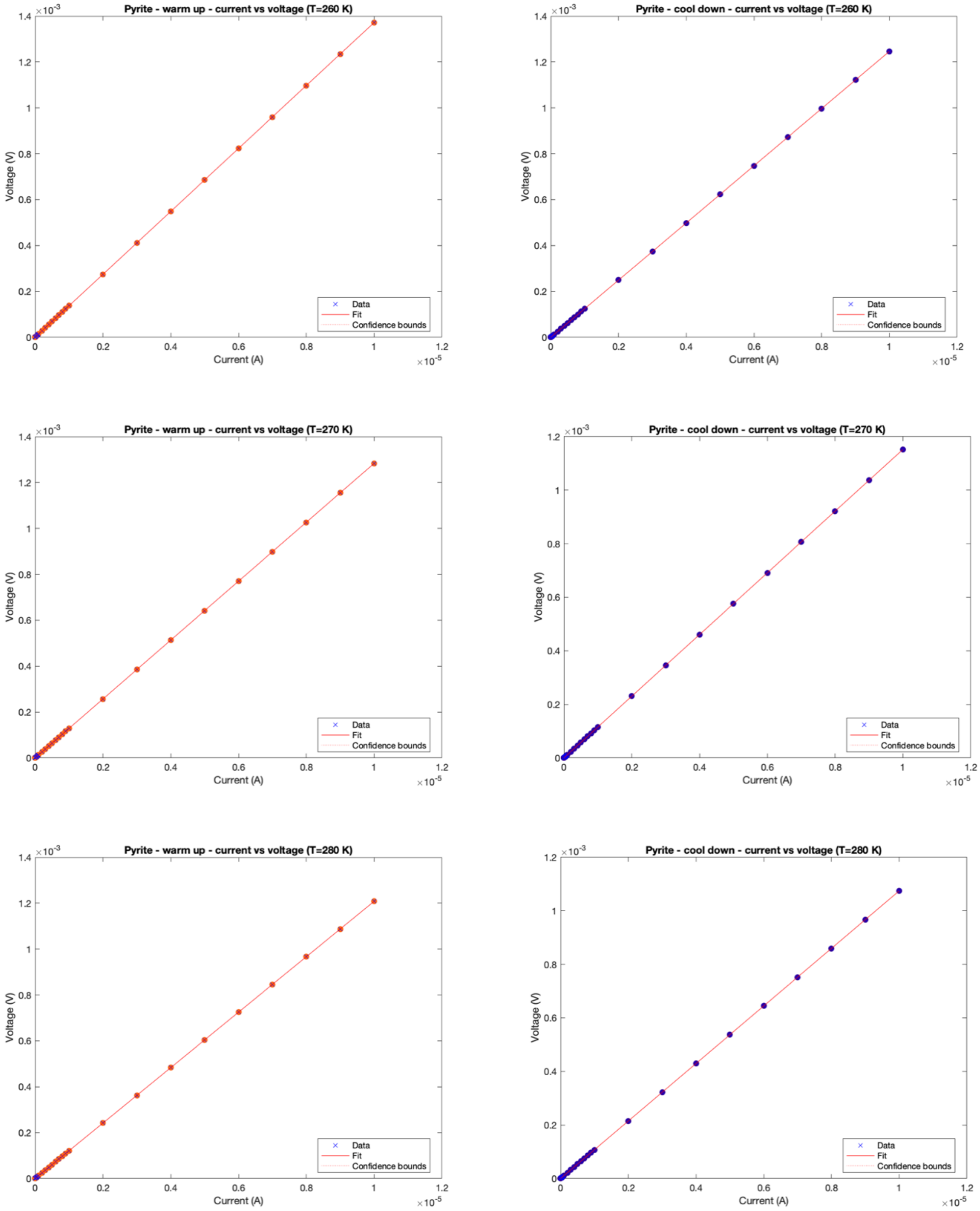

Figure 136: Pyrite voltage versus current graphs. Temperature range: 260K to 280K.

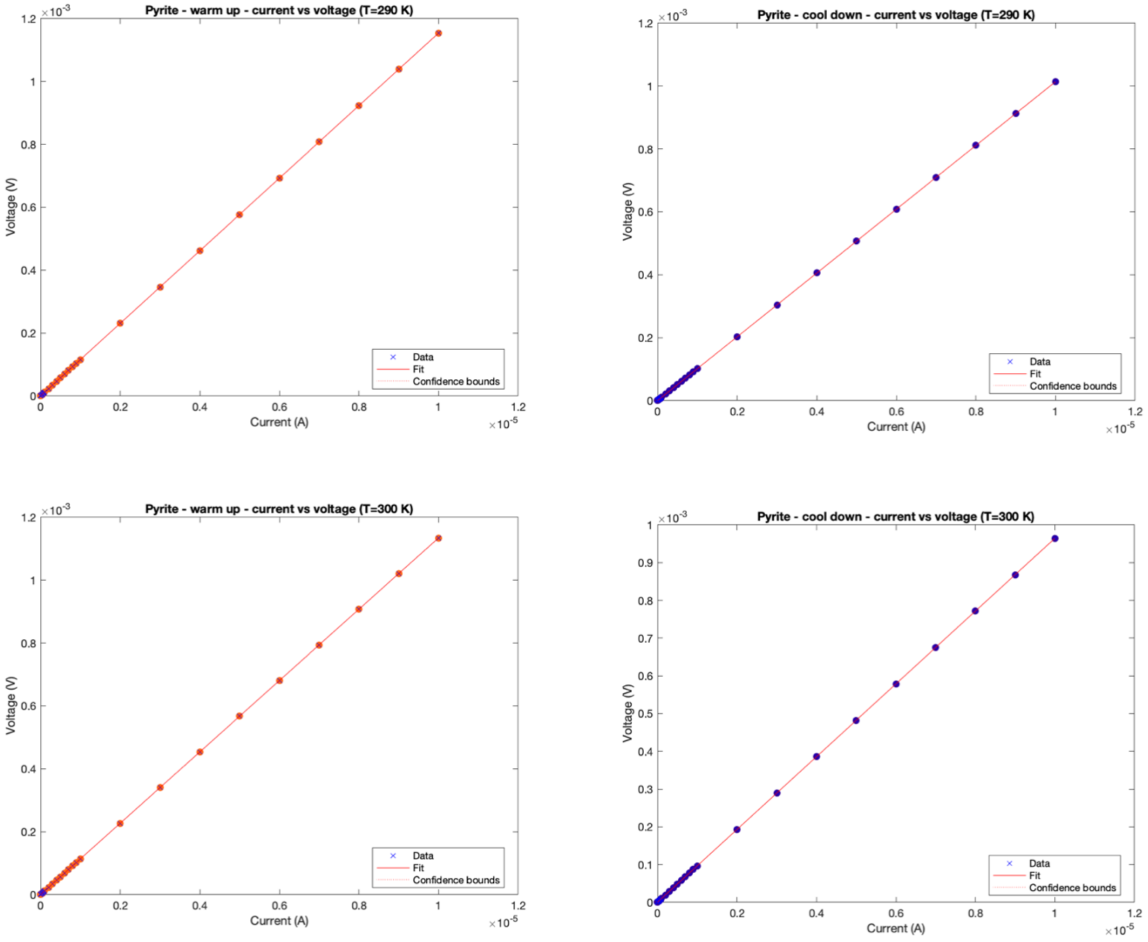

Figure 137: Pyrite voltage versus current graphs. Temperature range: 290K to 300K.

## *Pyrrhotite*

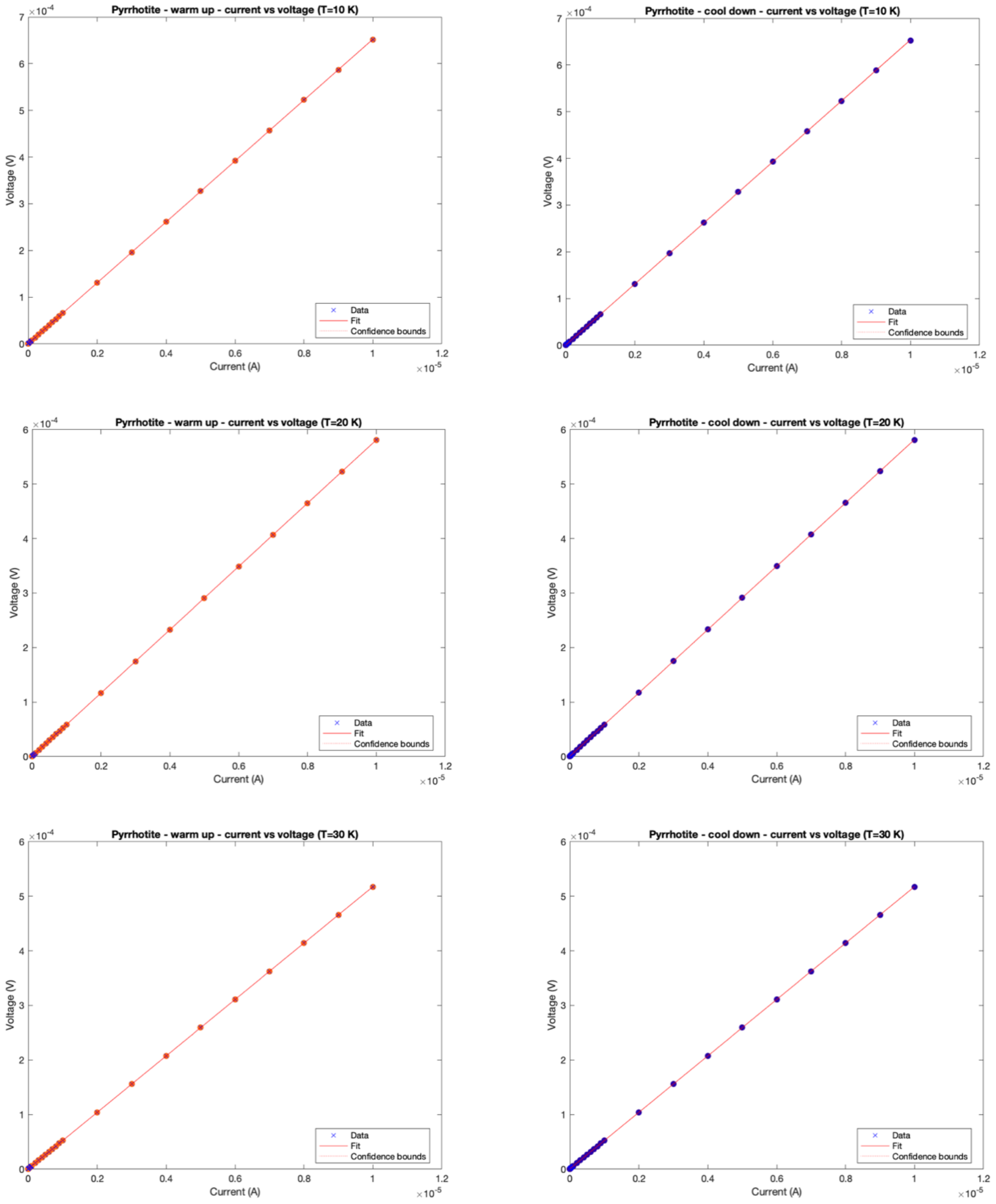

Pyrrhotite - warm up - current vs voltage (T=10 K)

Pyrrhotite - cool down - current vs voltage (T=10 K)

Pyrrhotite - warm up - current vs voltage (T=20 K)

Pyrrhotite - cool down - current vs voltage (T=20 K)

Pyrrhotite - warm up - current vs voltage (T=30 K)

Pyrrhotite - cool down - current vs voltage (T=30 K)

Figure 138: Pyrrhotite voltage versus current graphs. Temperature range: 10K to 30K.

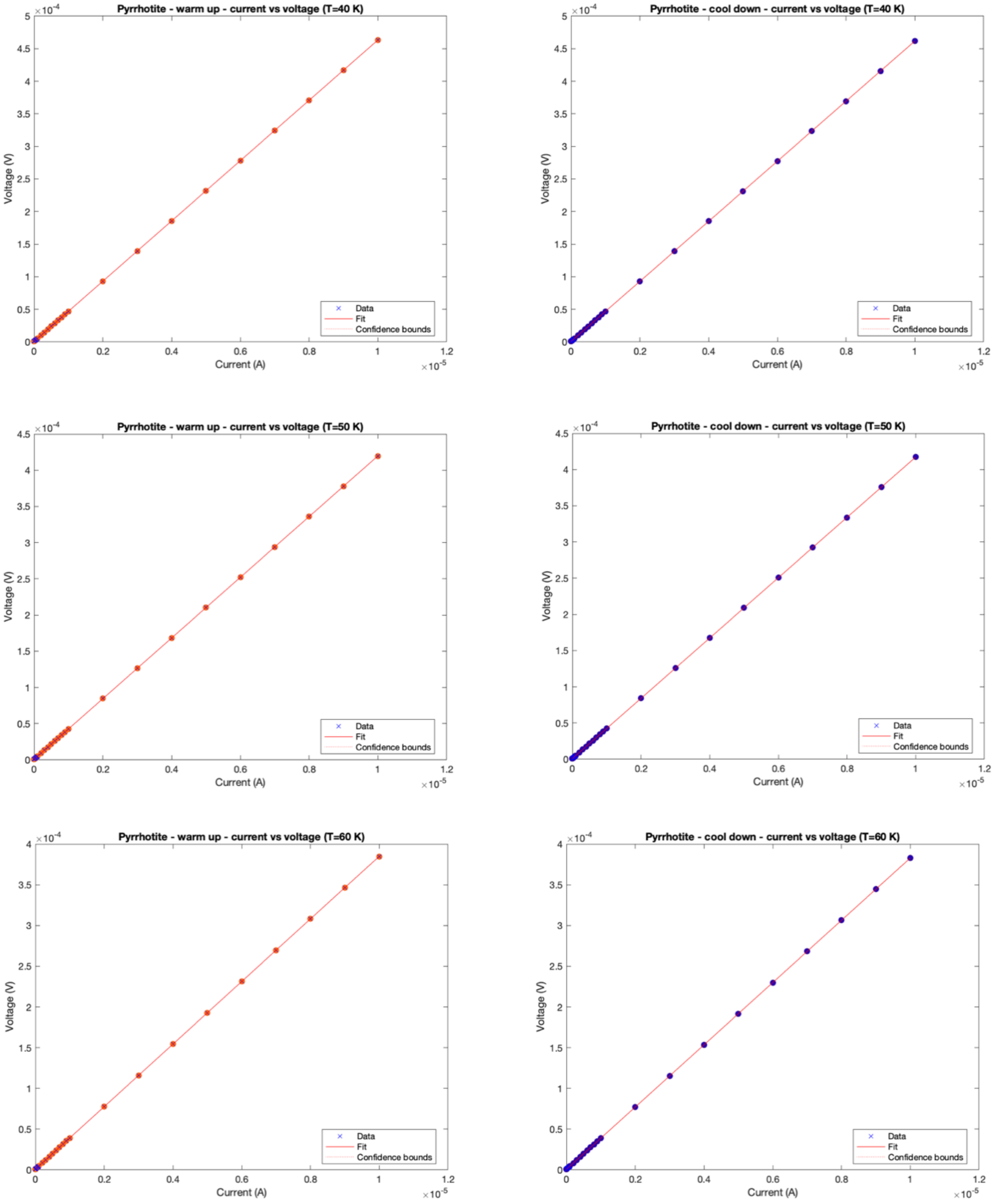

Figure 139: Pyrrhotite voltage versus current graphs. Temperature range: 40K to 60K.

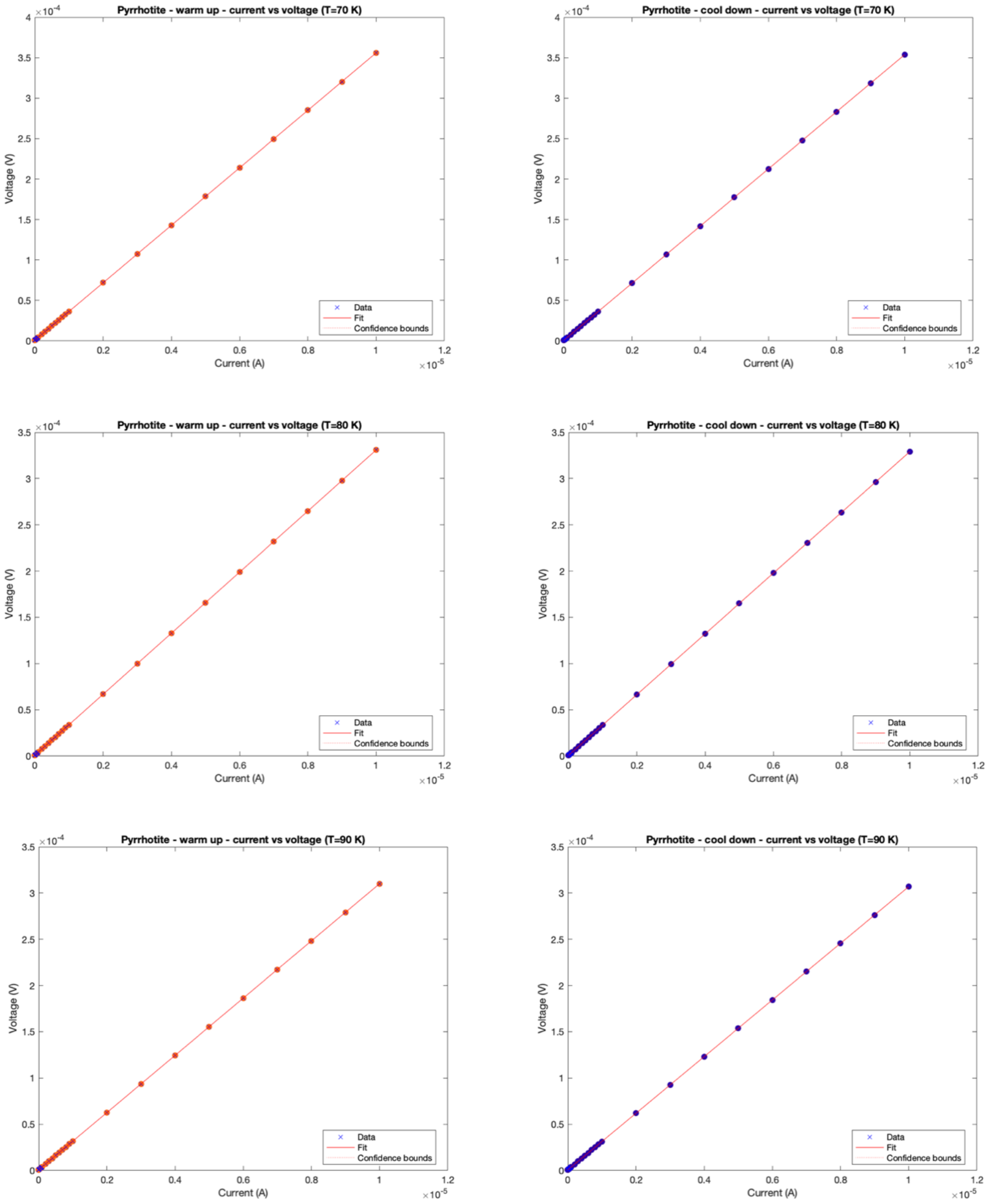

Figure 140: Pyrrhotite voltage versus current graphs. Temperature range: 70K to 90K.

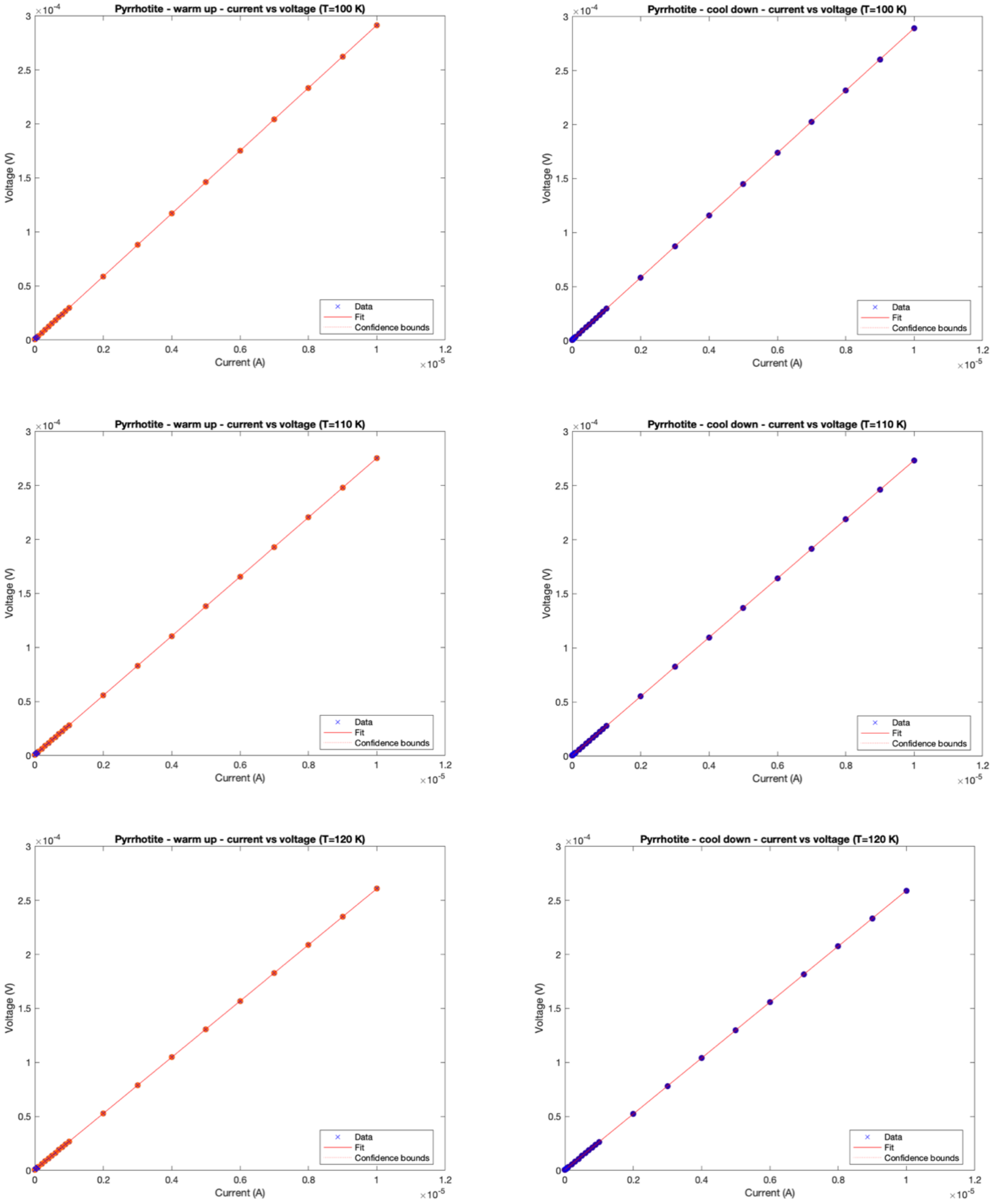

Figure 141: Pyrrhotite voltage versus current graphs. Temperature range: 100K to 120K.

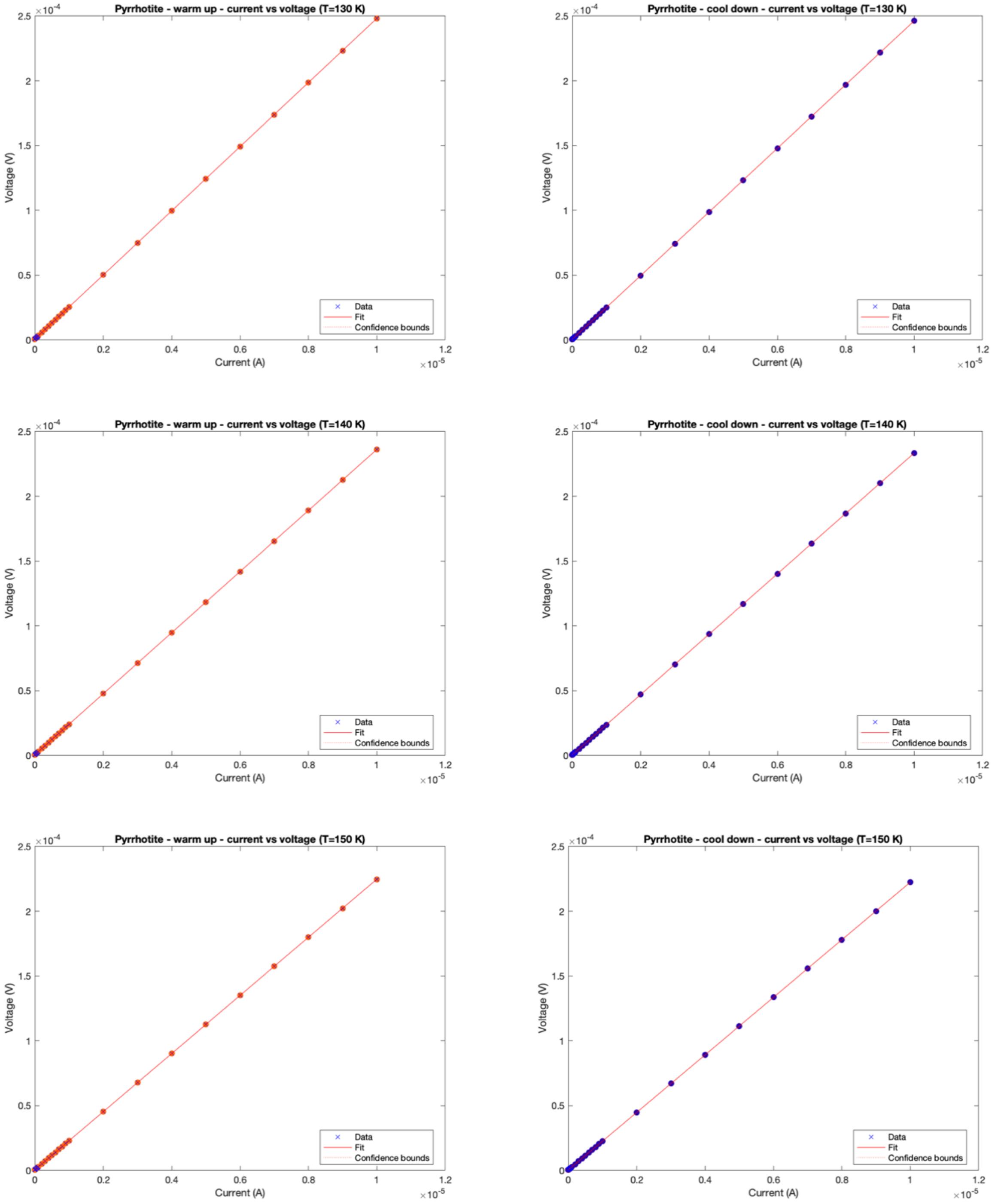

Figure 142: Pyrrhotite voltage versus current graphs. Temperature range: 130K to 150K.

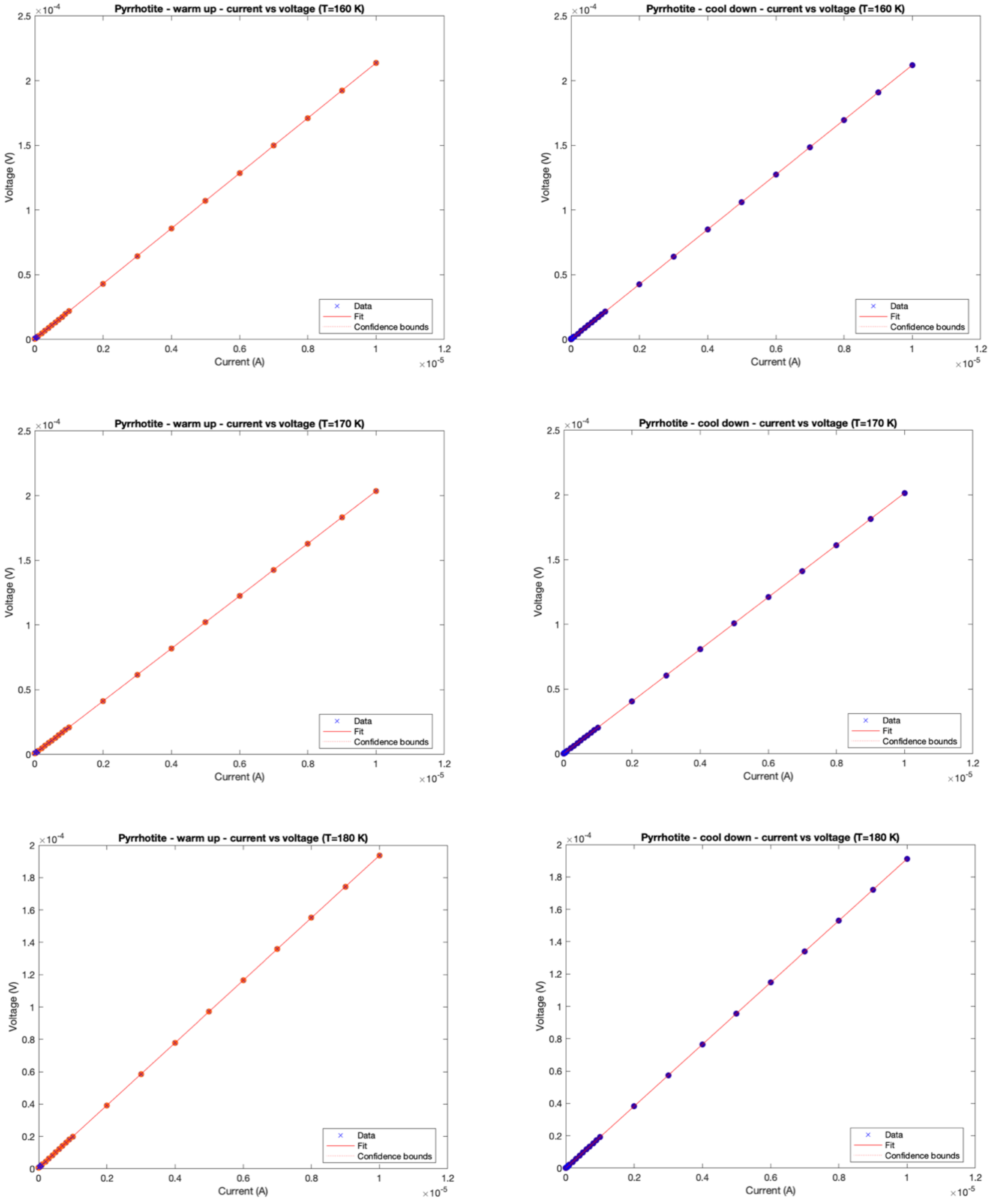
Pyrrhotite - warm up - current vs voltage (T=160 K)

Pyrrhotite - cool down - current vs voltage (T=160 K)

Pyrrhotite - warm up - current vs voltage (T=170 K)

Pyrrhotite - cool down - current vs voltage (T=170 K)

Pyrrhotite - warm up - current vs voltage (T=180 K)

Pyrrhotite - cool down - current vs voltage (T=180 K)

Figure 143: Pyrrhotite voltage versus current graphs. Temperature range: 150K to 180K.

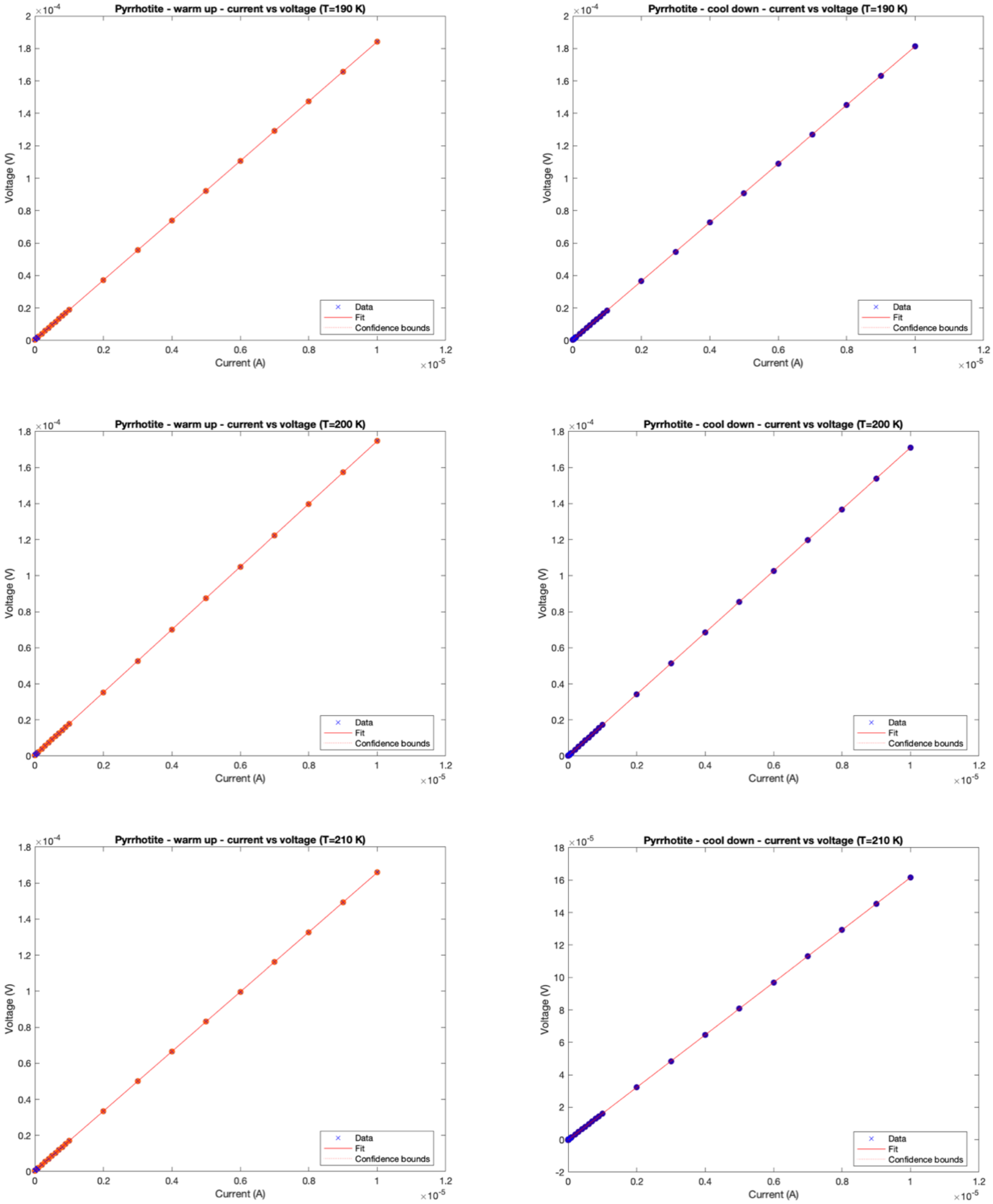

Figure 144: Pyrrhotite voltage versus current graphs. Temperature range: 190K to 210K.

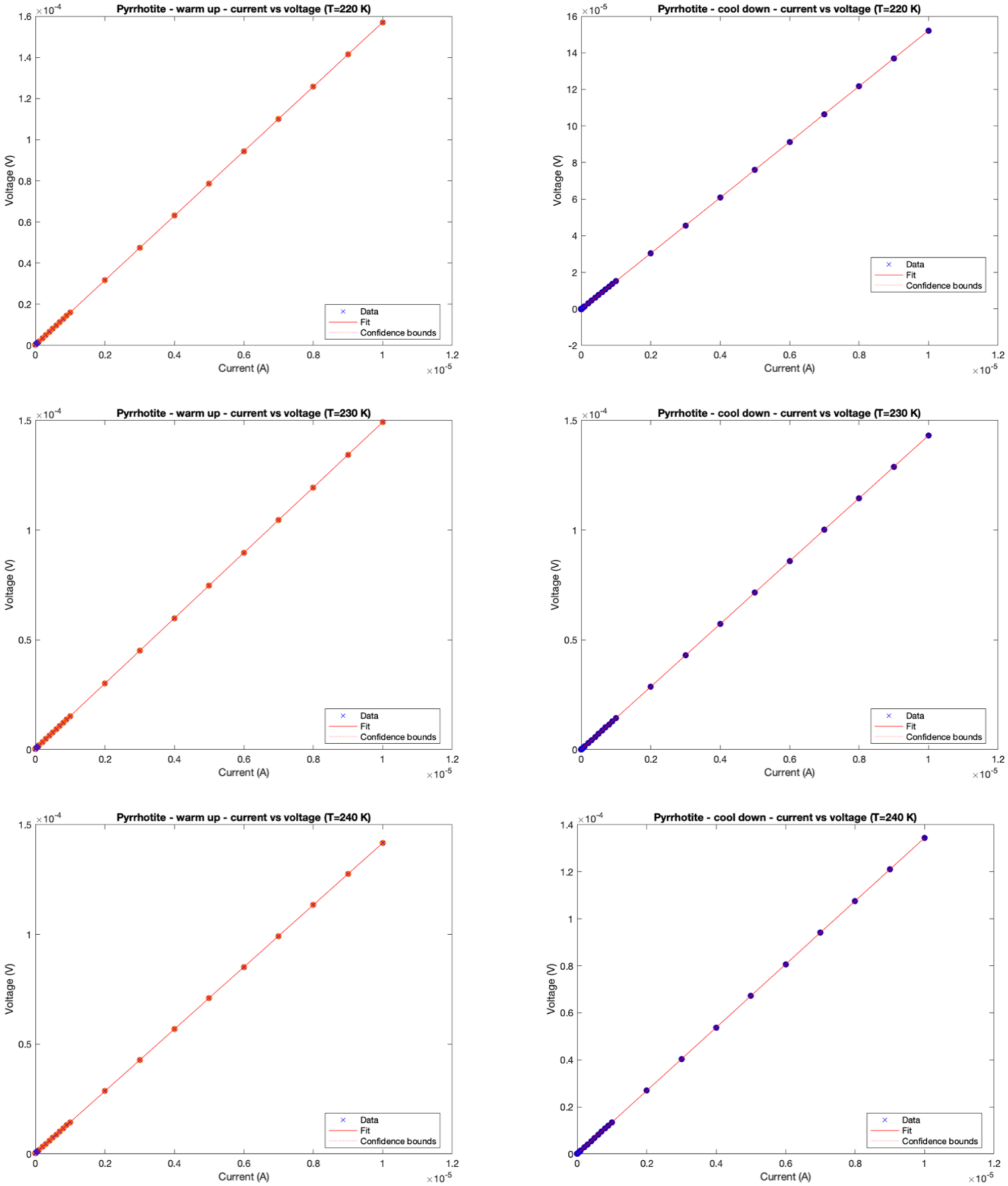

Figure 145: Pyrrhotite voltage versus current graphs. Temperature range: 220K to 240K.

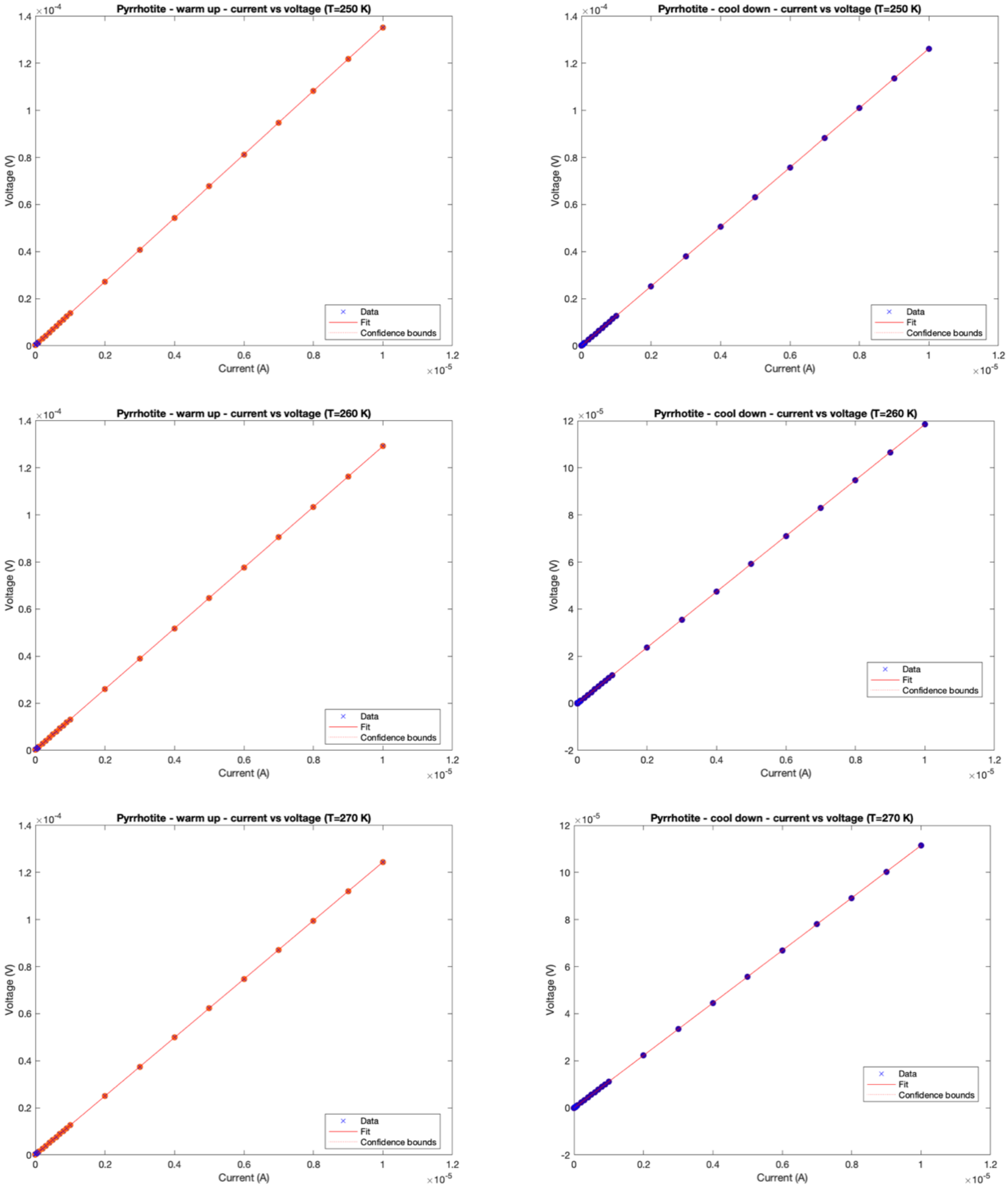
Pyrrhotite - warm up - current vs voltage (T=250 K)

Pyrrhotite - cool down - current vs voltage (T=250 K)

Pyrrhotite - warm up - current vs voltage (T=260 K)

Pyrrhotite - cool down - current vs voltage (T=260 K)

Pyrrhotite - warm up - current vs voltage (T=270 K)

Pyrrhotite - cool down - current vs voltage (T=270 K)

Figure 146: Pyrrhotite voltage versus current graphs. Temperature range: 250K to 270K.

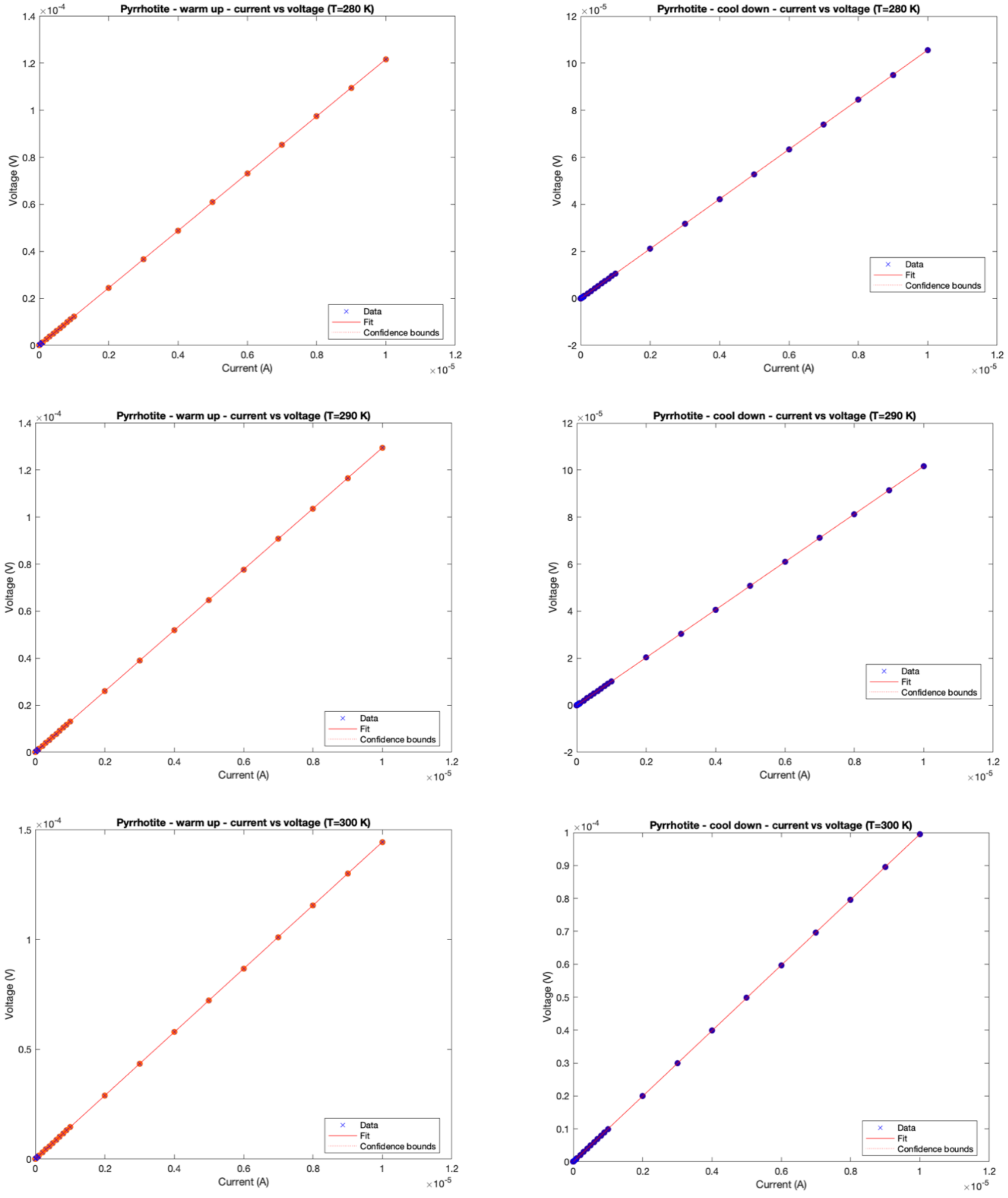
Pyrrhotite - warm up - current vs voltage (T=280 K)

Pyrrhotite - cool down - current vs voltage (T=280 K)

Pyrrhotite - warm up - current vs voltage (T=290 K)

Pyrrhotite - cool down - current vs voltage (T=290 K)

Pyrrhotite - warm up - current vs voltage (T=300 K)

Pyrrhotite - cool down - current vs voltage (T=300 K)

Figure 147: Pyrrhotite voltage versus current graphs. Temperature range: 280K to 300K.

### ***Serpentinite***

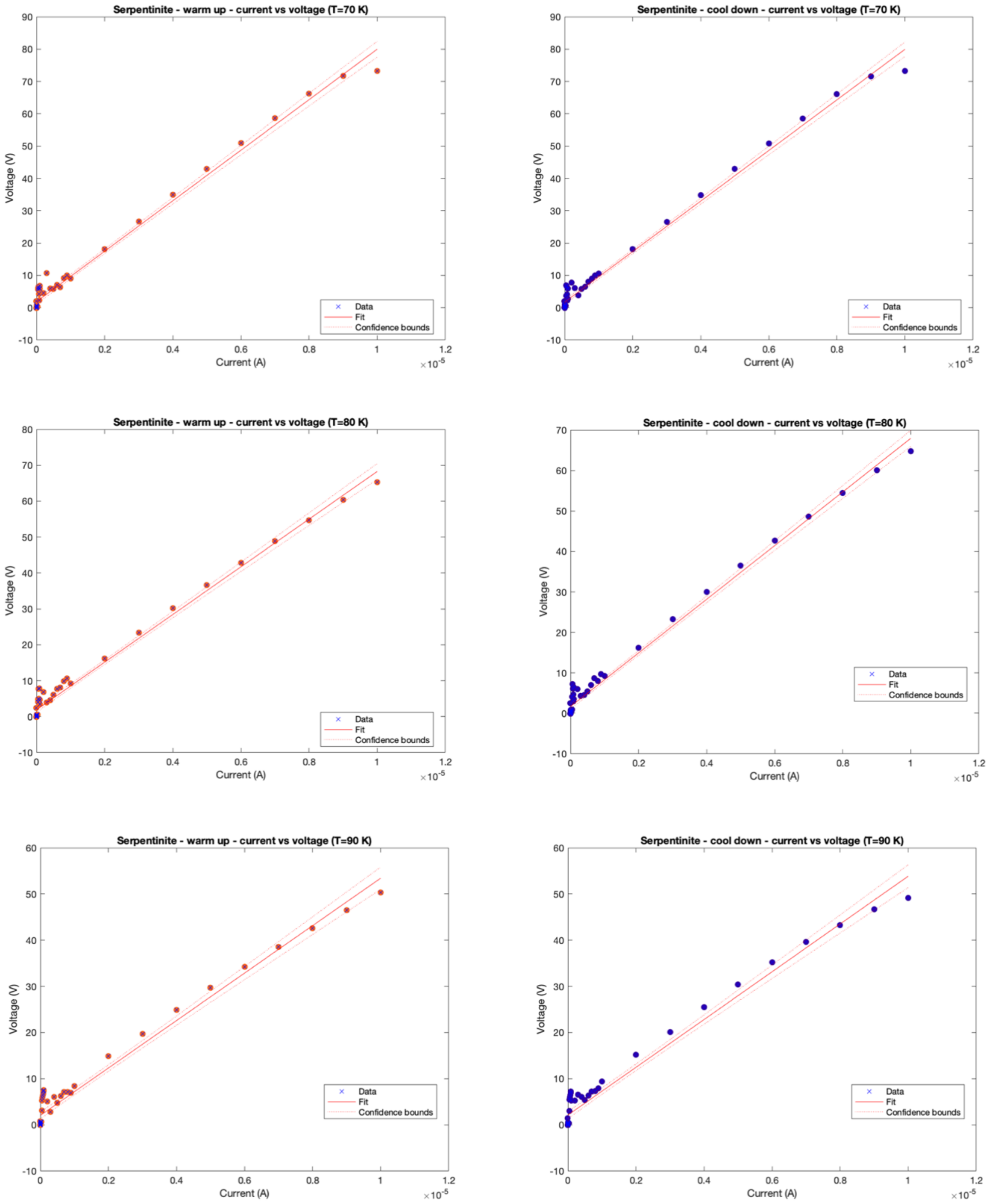

Figure 148: Serpentinite voltage versus current graphs. Temperature range: 70K to 90K.

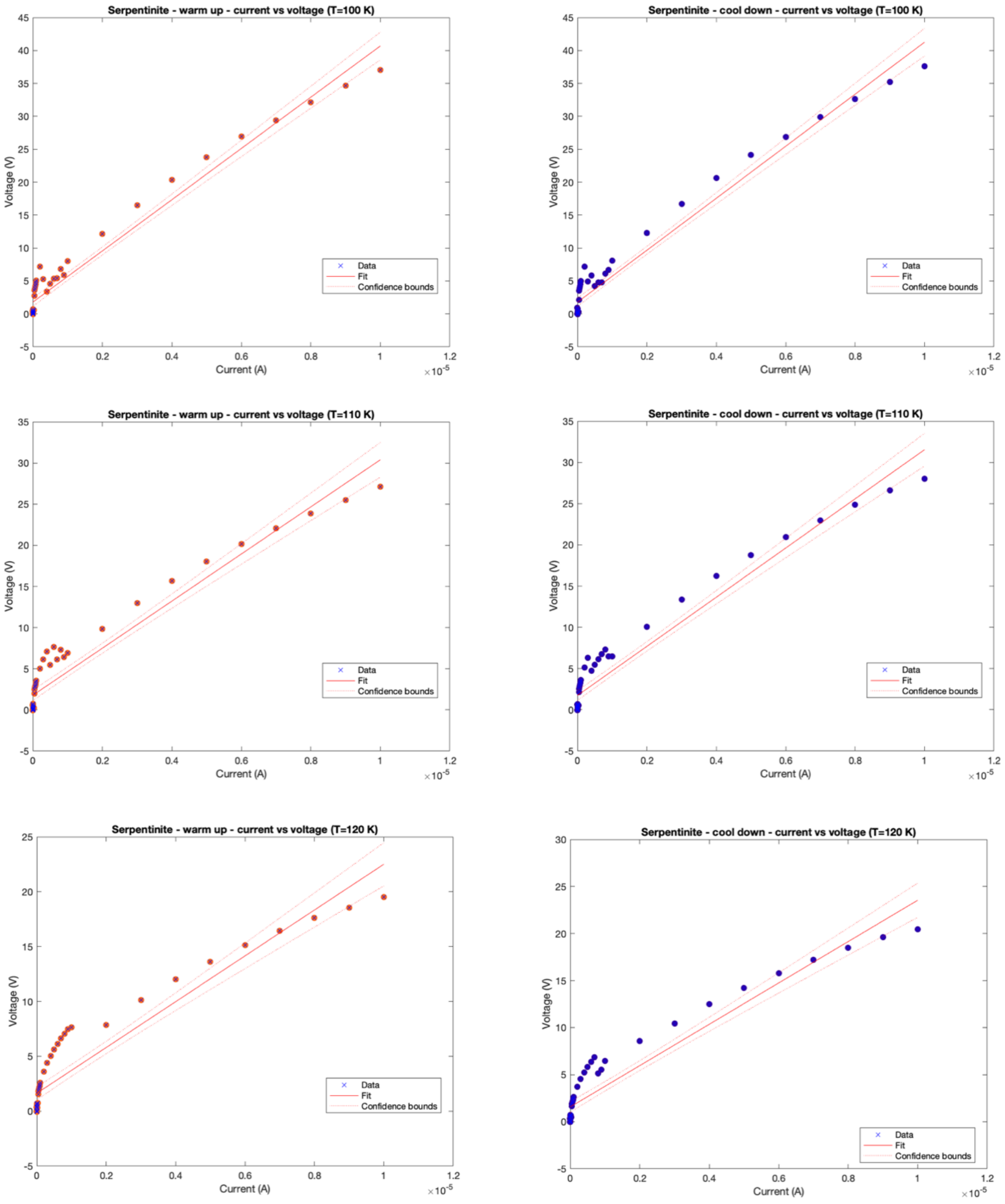

Figure 149: Serpentinite voltage versus current graphs. Temperature range: 100K to 120K.

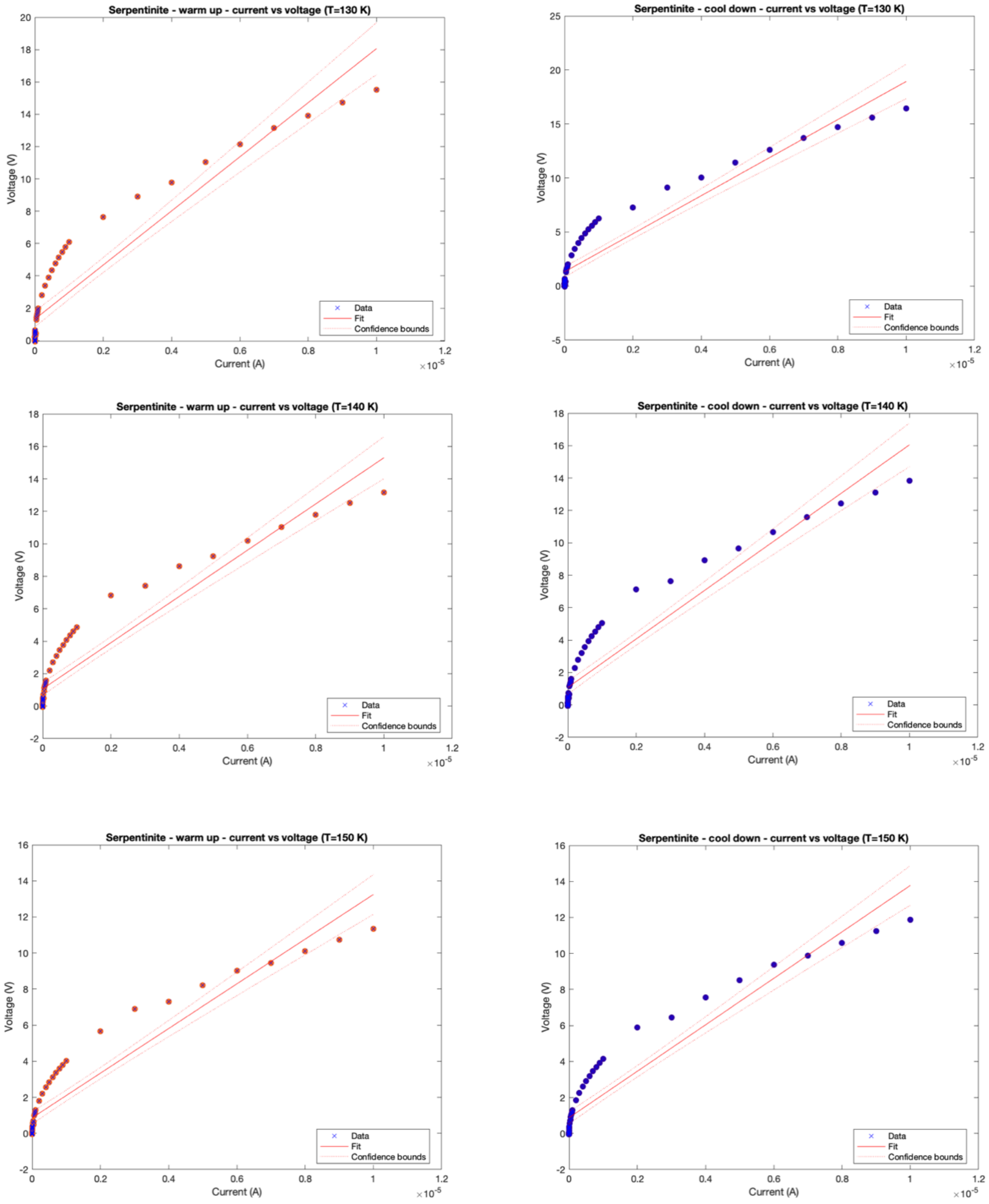

Figure 150: Serpentinite voltage versus current graphs. Temperature range: 130K to 150K.

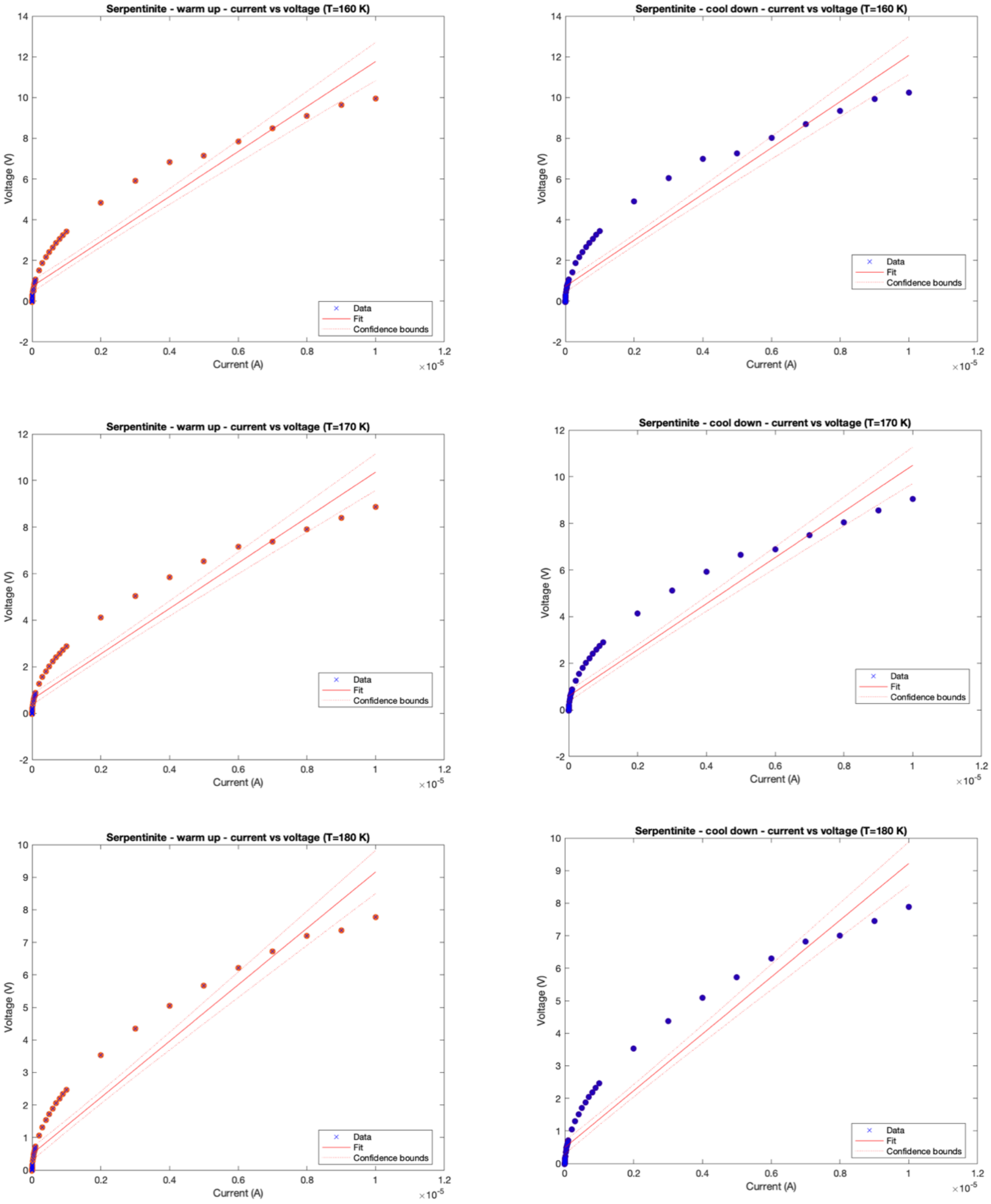

Figure 151: Serpentinite voltage versus current graphs. Temperature range: 160K to 180K.

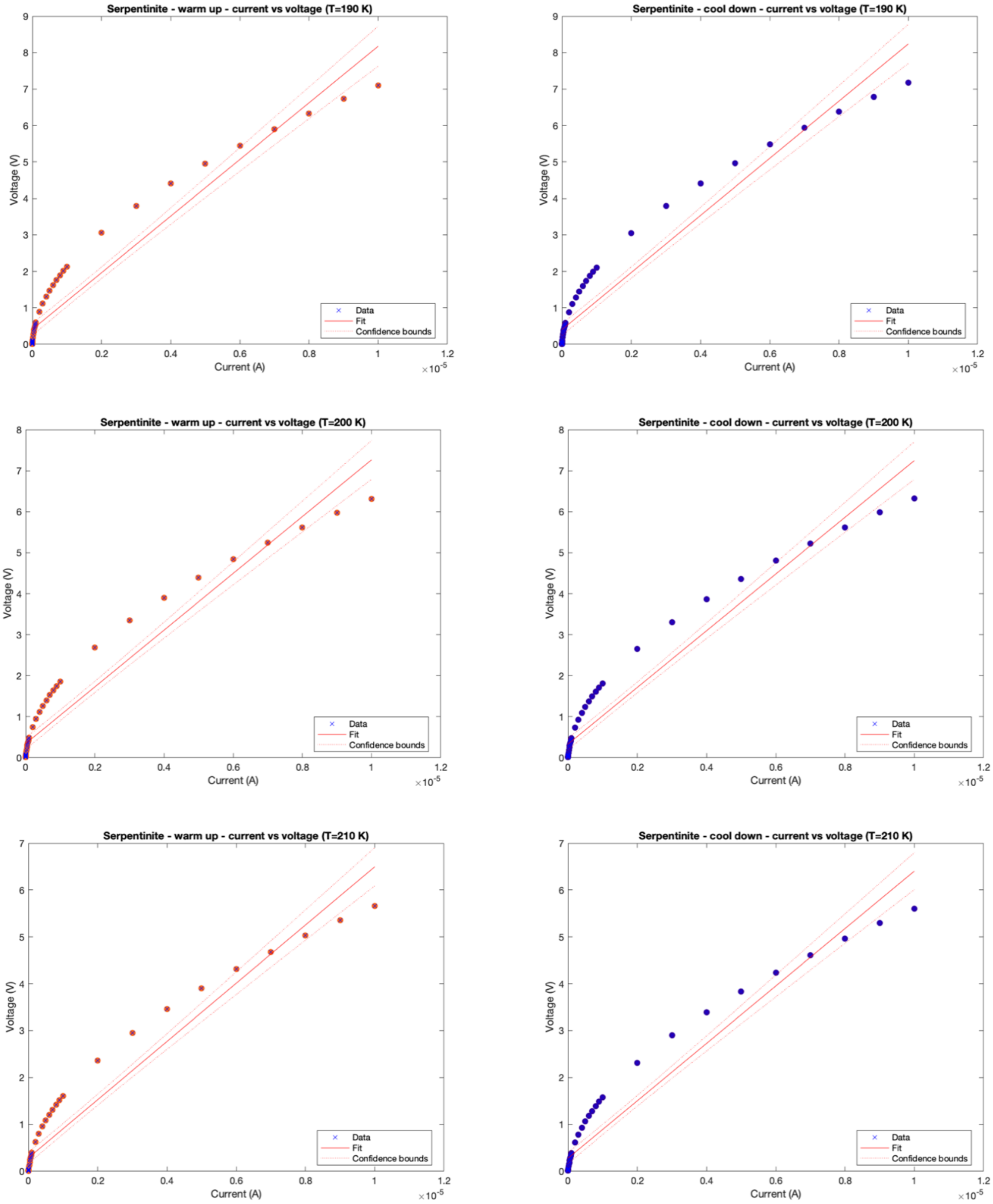

Figure 152: Serpentinite voltage versus current graphs. Temperature range: 190K to 210K.

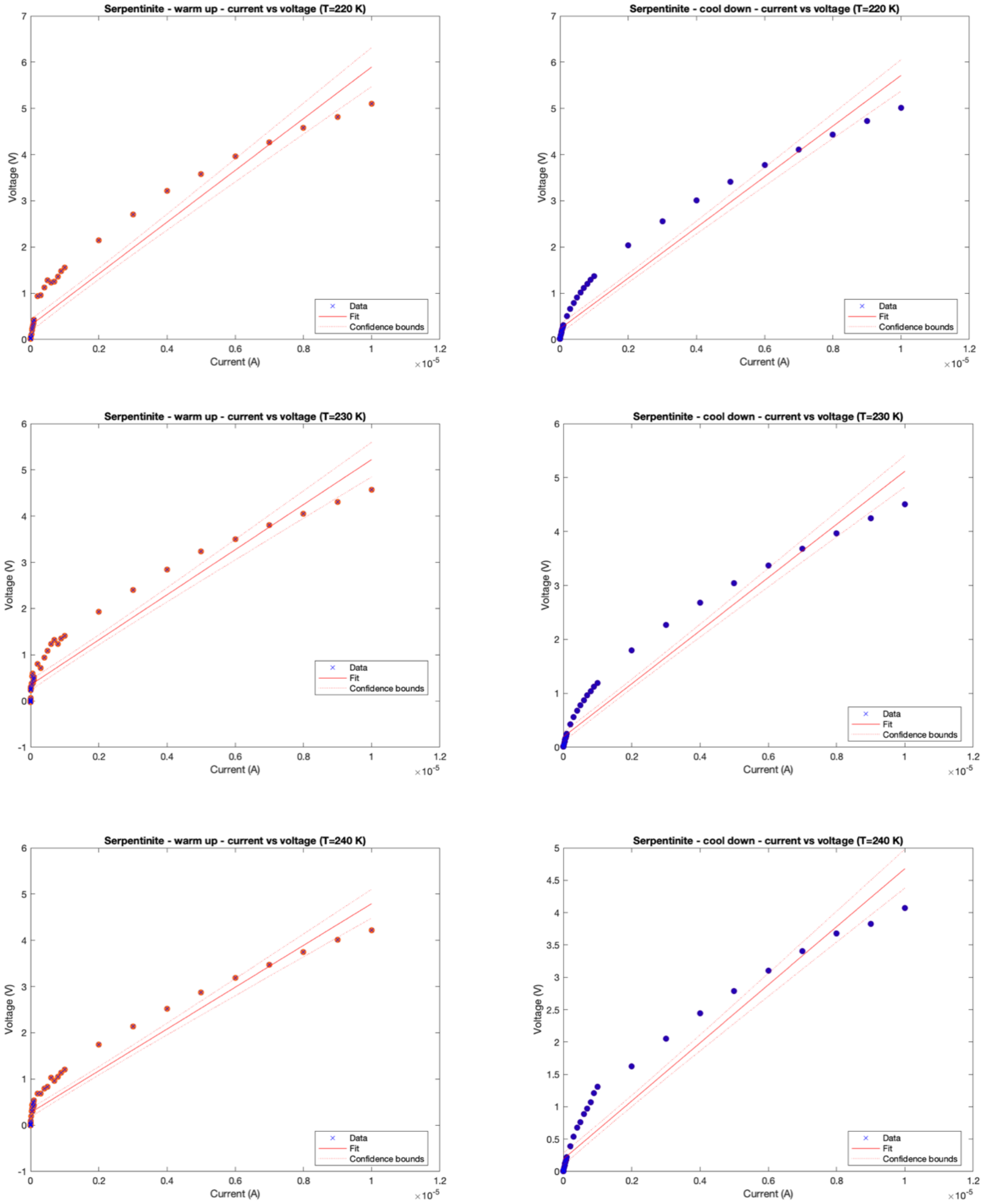
Serpentinite - warm up - current vs voltage (T=220 K)

Serpentinite - cool down - current vs voltage (T=220 K)

Serpentinite - warm up - current vs voltage (T=230 K)

Serpentinite - cool down - current vs voltage (T=230 K)

Serpentinite - warm up - current vs voltage (T=240 K)

Serpentinite - cool down - current vs voltage (T=240 K)

Figure 153: Serpentinite voltage versus current graphs. Temperature range: 220K to 240K.

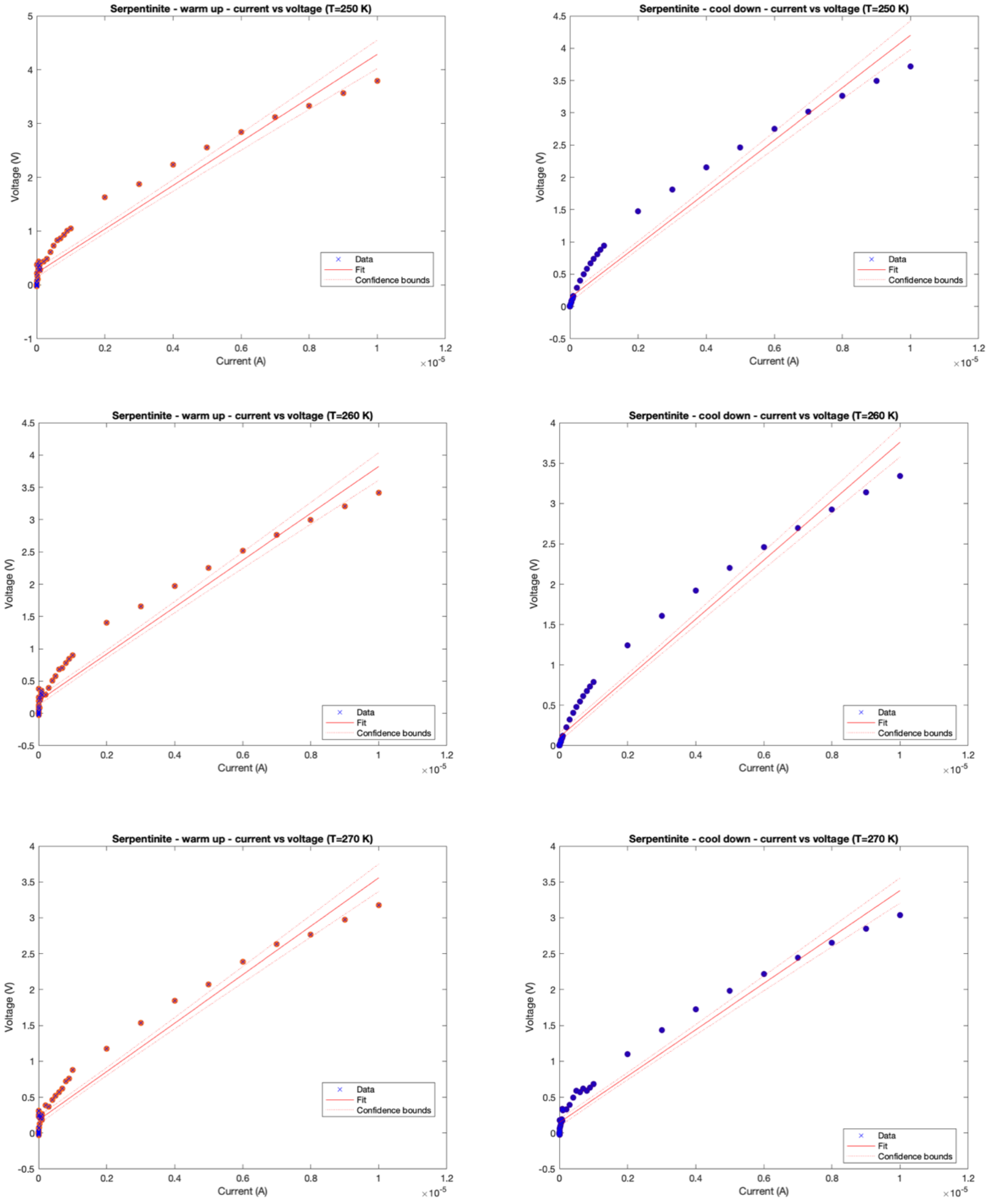

Figure 154: Serpentinite voltage versus current graphs. Temperature range: 250K to 270K.

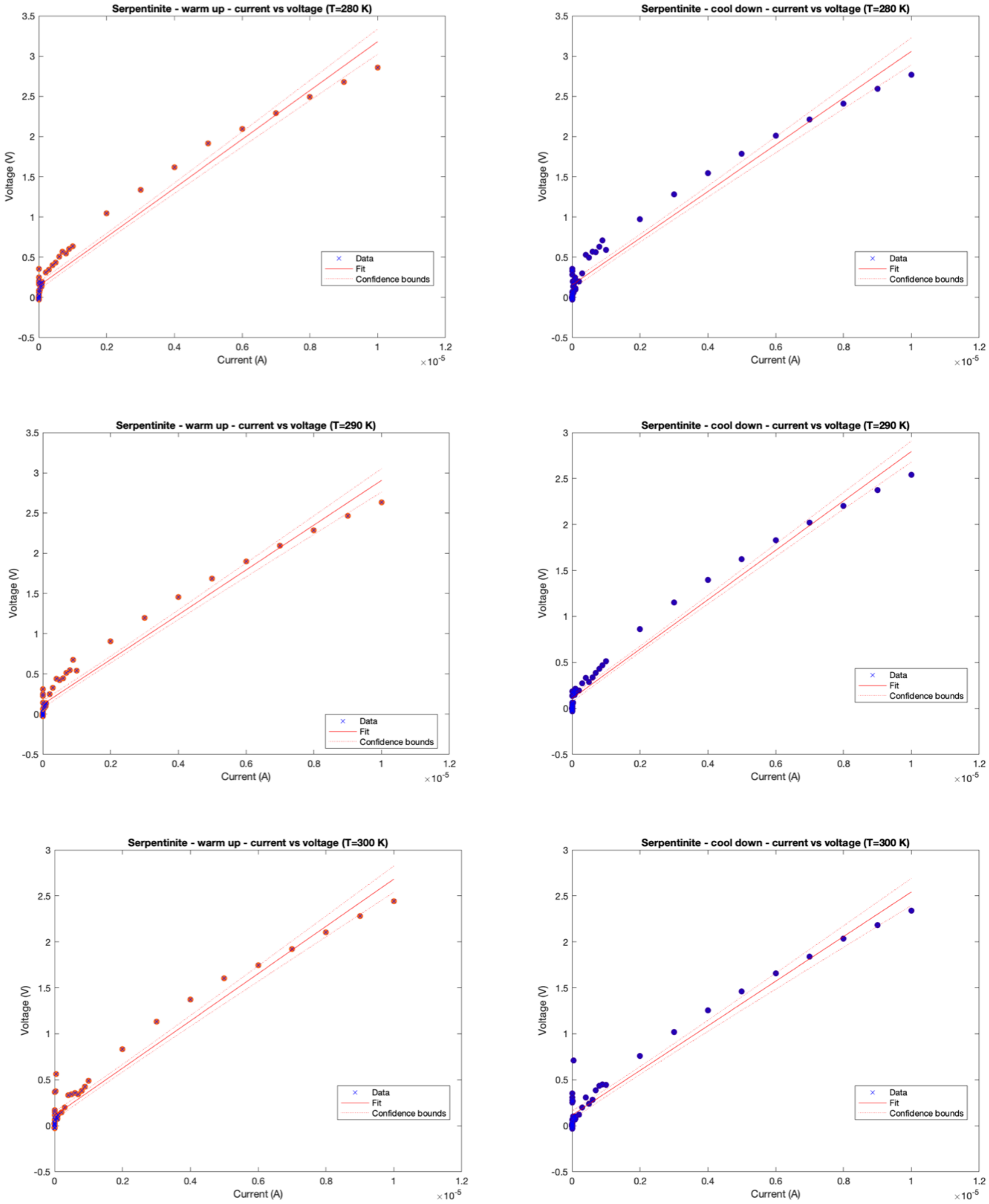

Figure 155: Serpentinite voltage versus current graphs. Temperature range: 280K to 300K.

# Appendix B: Linear regression variables

## *Chalcopyrite*

Table 3: Linear regression variables of chalcopyrite sample (warm-up run).

| Temperature (K) | coefficient estimate | standard error | p-value | r squared |
|---:|---:|---:|---:|---:|
| 20 | 284.80 | 1.00E-02 | 4.03E-175 | 1.00 |
| 30 | 178.63 | 1.67E-02 | 9.39E-155 | 1.00 |
| 40 | 127.08 | 4.57E-03 | 1.19E-174 | 1.00 |
| 50 | 97.03 | 1.17E-02 | 2.44E-149 | 1.00 |
| 60 | 85.82 | 2.65E-03 | 8.49E-178 | 1.00 |
| 70 | 80.38 | 1.93E-03 | 4.17E-183 | 1.00 |
| 80 | 77.04 | 1.40E-03 | 7.06E-189 | 1.00 |
| 90 | 74.32 | 4.72E-03 | 8.47E-163 | 1.00 |
| 100 | 72.03 | 1.47E-03 | 1.73E-186 | 1.00 |
| 110 | 69.77 | 2.87E-03 | 7.91E-172 | 1.00 |
| 120 | 67.77 | 3.01E-03 | 3.09E-170 | 1.00 |
| 130 | 65.12 | 4.31E-03 | 6.70E-162 | 1.00 |
| 140 | 63.77 | 3.87E-03 | 9.98E-164 | 1.00 |
| 150 | 62.00 | 3.14E-03 | 1.79E-167 | 1.00 |
| 160 | 60.52 | 3.71E-03 | 1.67E-163 | 1.00 |
| 170 | 44.05 | 2.16E-03 | 3.56E-168 | 1.00 |
| 180 | 32.69 | 1.49E-03 | 1.12E-169 | 1.00 |
| 190 | 28.64 | 2.86E-03 | 2.31E-153 | 1.00 |
| 200 | 27.89 | 1.29E-03 | 2.27E-169 | 1.00 |
| 210 | 29.07 | 3.00E-03 | 1.11E-152 | 1.00 |
| 220 | 31.46 | 2.74E-03 | 3.20E-156 | 1.00 |
| 230 | 30.19 | 7.83E-03 | 1.86E-133 | 1.00 |
| 240 | 36.00 | 4.52E-03 | 1.37E-148 | 1.00 |
| 250 | 56.15 | 4.45E-03 | 3.54E-158 | 1.00 |
| 260 | 64.00 | 2.95E-03 | 1.75E-169 | 1.00 |
| 270 | 66.61 | 3.88E-03 | 1.31E-164 | 1.00 |
| 280 | 72.55 | 7.31E-03 | 3.77E-153 | 1.00 |
| 290 | 86.04 | 8.29E-03 | 4.42E-154 | 1.00 |
| 300 | 80.95 | 9.90E-03 | 4.03E-149 | 1.00 |

Table 4: Linear regression variables of chalcopyrite sample (cool-down run).

| Temperature (K) | coefficient estimate | standard error | p-value | r squared |
|---:|---:|---:|---:|---:|
| 20 | 284.66 | 3.84E-03 | 4.70E-195 | 1.00 |
| 30 | 182.64 | 6.68E-03 | 2.86E-174 | 1.00 |
| 40 | 127.50 | 3.81E-03 | 1.59E-178 | 1.00 |
| 50 | 96.76 | 1.95E-03 | 9.91E-187 | 1.00 |
| 60 | 85.11 | 2.76E-02 | 8.78E-129 | 1.00 |
| 70 | 67.92 | 5.30E-03 | 1.81E-158 | 1.00 |
| 80 | 72.69 | 7.69E-03 | 3.86E-152 | 1.00 |
| 90 | 44.21 | 2.75E-03 | 3.29E-163 | 1.00 |
| 100 | 41.46 | 1.56E-03 | 9.60E-174 | 1.00 |
| 110 | 39.49 | 2.93E-03 | 1.52E-159 | 1.00 |
| 120 | 50.76 | 1.12E-02 | 9.74E-137 | 1.00 |
| 130 | 48.03 | 6.67E-03 | 1.74E-146 | 1.00 |
| 140 | 46.69 | 5.46E-03 | 4.79E-150 | 1.00 |
| 150 | 43.94 | 1.41E-02 | 6.10E-129 | 1.00 |
| 160 | 46.57 | 1.41E-02 | 3.16E-130 | 1.00 |
| 170 | 61.47 | 4.77E-03 | 1.33E-158 | 1.00 |
| 180 | 63.44 | 6.52E-03 | 9.85E-153 | 1.00 |
| 190 | 63.58 | 4.76E-03 | 2.36E-159 | 1.00 |
| 200 | 63.41 | 5.62E-03 | 8.02E-156 | 1.00 |
| 210 | 65.06 | 9.61E-03 | 3.49E-145 | 1.00 |
| 220 | 67.52 | 9.37E-03 | 1.71E-146 | 1.00 |
| 230 | 75.55 | 2.20E-02 | 4.68E-131 | 1.00 |
| 240 | 80.27 | 1.61E-02 | 9.37E-139 | 1.00 |
| 250 | 87.34 | 5.72E-03 | 3.98E-162 | 1.00 |
| 260 | 90.70 | 7.95E-03 | 4.62E-156 | 1.00 |
| 270 | 92.21 | 1.41E-02 | 1.77E-144 | 1.00 |
| 280 | 99.83 | 1.84E-02 | 1.58E-140 | 1.00 |
| 290 | 122.50 | 1.53E-02 | 1.24E-148 | 1.00 |
| 300 | 159.25 | 4.27E-02 | 9.81E-133 | 1.00 |

## *Galena*

Table 5: Linear regression variables of galena sample (warm-up run).

| temperature (K) | coefficient estimate | standard error | p-value | r squared |
|---|---|---|---|---|
| 20 | 4.50 | 1.77E-03 | 5.20E-120 | 1.00 |
| 30 | 4.50 | 1.87E-03 | 5.54E-119 | 1.00 |
| 40 | 4.60 | 2.10E-03 | 4.22E-117 | 1.00 |
| 50 | 4.72 | 2.33E-03 | 1.65E-115 | 1.00 |
| 60 | 4.88 | 2.63E-03 | 9.29E-114 | 1.00 |
| 70 | 5.07 | 3.07E-03 | 1.88E-111 | 1.00 |
| 80 | 5.28 | 3.61E-03 | 5.16E-109 | 1.00 |
| 90 | 5.51 | 4.24E-03 | 1.27E-106 | 1.00 |
| 100 | 5.76 | 5.09E-03 | 6.98E-104 | 1.00 |
| 110 | 6.02 | 5.95E-03 | 1.17E-101 | 1.00 |
| 120 | 6.30 | 6.96E-03 | 1.94E-99 | 1.00 |
| 130 | 6.58 | 8.01E-03 | 1.73E-97 | 1.00 |
| 140 | 6.85 | 9.14E-03 | 1.16E-95 | 1.00 |
| 150 | 7.12 | 1.01E-02 | 1.71E-94 | 1.00 |
| 160 | 7.37 | 1.08E-02 | 8.53E-94 | 1.00 |
| 170 | 7.63 | 1.19E-02 | 1.28E-92 | 1.00 |
| 180 | 7.88 | 1.22E-02 | 1.21E-92 | 1.00 |
| 190 | 8.13 | 1.28E-02 | 2.78E-92 | 1.00 |
| 200 | 8.37 | 1.30E-02 | 1.40E-92 | 1.00 |
| 210 | 8.59 | 1.31E-02 | 5.35E-93 | 1.00 |
| 220 | 8.83 | 1.34E-02 | 5.05E-93 | 1.00 |
| 230 | 9.12 | 1.43E-02 | 2.06E-92 | 1.00 |
| 240 | 9.47 | 1.53E-02 | 7.30E-92 | 1.00 |
| 250 | 9.99 | 1.59E-02 | 3.86E-92 | 1.00 |
| 260 | 10.72 | 1.58E-02 | 1.17E-93 | 1.00 |
| 270 | 11.82 | 1.50E-02 | 1.15E-96 | 1.00 |
| 280 | 13.56 | 1.39E-02 | 5.75E-101 | 1.00 |
| 290 | 16.31 | 1.39E-02 | 1.12E-104 | 1.00 |
| 300 | 18.86 | 1.37E-02 | 7.27E-108 | 1.00 |

Table 6: Linear regression variables of galena sample (cool-down run).

| temperature (K) | coefficient estimate | standard error | p-value | r squared |
|---|---|---|---|---|
| 20 | 4.55 | 1.68E-03 | 2.38E-121 | 1.00 |
| 30 | 4.57 | 1.85E-03 | 1.91E-119 | 1.00 |
| 40 | 4.63 | 1.94E-03 | 8.16E-119 | 1.00 |
| 50 | 4.71 | 2.16E-03 | 4.92E-117 | 1.00 |
| 60 | 4.83 | 2.39E-03 | 1.83E-115 | 1.00 |
| 70 | 4.96 | 2.66E-03 | 7.59E-114 | 1.00 |
| 80 | 5.10 | 2.91E-03 | 1.33E-112 | 1.00 |
| 90 | 5.27 | 3.25E-03 | 4.33E-111 | 1.00 |
| 100 | 5.46 | 3.76E-03 | 7.36E-109 | 1.00 |
| 110 | 5.67 | 4.27E-03 | 4.75E-107 | 1.00 |
| 120 | 5.88 | 4.88E-03 | 3.89E-105 | 1.00 |
| 130 | 6.11 | 5.59E-03 | 3.27E-103 | 1.00 |
| 140 | 6.33 | 6.01E-03 | 1.94E-102 | 1.00 |
| 150 | 6.55 | 6.68E-03 | 5.17E-101 | 1.00 |
| 160 | 6.77 | 7.33E-03 | 7.84E-100 | 1.00 |
| 170 | 7.00 | 8.19E-03 | 2.83E-98 | 1.00 |
| 180 | 7.22 | 8.91E-03 | 3.22E-97 | 1.00 |
| 190 | 7.45 | 9.94E-03 | 1.15E-95 | 1.00 |
| 200 | 7.66 | 1.03E-02 | 1.96E-95 | 1.00 |
| 210 | 7.90 | 1.15E-02 | 6.47E-94 | 1.00 |
| 220 | 8.12 | 1.25E-02 | 9.50E-93 | 1.00 |
| 230 | 8.35 | 1.37E-02 | 1.63E-91 | 1.00 |
| 240 | 8.63 | 1.56E-02 | 1.44E-89 | 1.00 |
| 250 | 8.97 | 1.75E-02 | 4.10E-88 | 1.00 |
| 260 | 9.43 | 2.05E-02 | 6.60E-86 | 1.00 |
| 270 | 10.35 | 2.68E-02 | 1.89E-82 | 1.00 |
| 280 | 11.98 | 3.62E-02 | 2.54E-79 | 1.00 |
| 290 | 14.39 | 4.73E-02 | 1.22E-77 | 1.00 |
| 300 | 17.75 | 6.43E-02 | 1.06E-75 | 1.00 |

***Graphite***

Table 7: Linear regression variables of graphite sample (warm-up run).

| temperature (K) | coefficient estimate | standard error | p-value | r squared |
|---|---|---|---|---|
| 40 | 0.21 | 3.21E-06 | 3.39E-185 | 1.00 |
| 50 | 0.21 | 2.87E-06 | 2.19E-187 | 1.00 |
| 60 | 0.21 | 2.95E-06 | 1.04E-186 | 1.00 |
| 70 | 0.21 | 2.91E-06 | 6.95E-187 | 1.00 |
| 80 | 0.21 | 2.70E-06 | 2.61E-188 | 1.00 |
| 90 | 0.21 | 2.75E-06 | 7.43E-188 | 1.00 |
| 100 | 0.21 | 2.60E-06 | 7.03E-189 | 1.00 |
| 110 | 0.21 | 2.75E-06 | 1.10E-187 | 1.00 |
| 120 | 0.21 | 2.55E-06 | 4.64E-189 | 1.00 |
| 130 | 0.20 | 2.28E-06 | 3.08E-191 | 1.00 |
| 140 | 0.20 | 2.18E-06 | 5.27E-192 | 1.00 |
| 150 | 0.20 | 2.30E-06 | 7.18E-191 | 1.00 |
| 160 | 0.20 | 2.17E-06 | 6.22E-192 | 1.00 |
| 170 | 0.20 | 2.04E-06 | 4.66E-193 | 1.00 |
| 180 | 0.20 | 2.91E-06 | 6.42E-186 | 1.00 |
| 190 | 0.20 | 2.28E-06 | 8.94E-191 | 1.00 |
| 200 | 0.20 | 2.16E-06 | 8.17E-192 | 1.00 |
| 210 | 0.20 | 2.07E-06 | 1.16E-192 | 1.00 |
| 220 | 0.20 | 2.19E-06 | 1.80E-191 | 1.00 |
| 230 | 0.20 | 2.74E-06 | 4.56E-187 | 1.00 |
| 240 | 0.20 | 2.07E-06 | 1.05E-192 | 1.00 |
| 250 | 0.20 | 2.98E-06 | 1.68E-185 | 1.00 |
| 260 | 0.20 | 3.11E-06 | 8.21E-185 | 1.00 |
| 270 | 0.21 | 2.03E-06 | 1.21E-193 | 1.00 |
| 280 | 0.21 | 1.72E-06 | 1.88E-197 | 1.00 |
| 290 | 0.22 | 5.03E-06 | 3.15E-177 | 1.00 |
| 300 | 0.26 | 5.61E-06 | 2.18E-178 | 1.00 |

Table 8: Linear regression variables of graphite sample (cool-down run).

| temperature (K) | coefficient estimate | standard error | p-value | r squared |
|---:|---:|---:|---:|---:|
| 40 | 0.09 | 7.53E-07 | 1.89E-197 | 1.00 |
| 50 | 0.09 | 5.49E-07 | 1.20E-203 | 1.00 |
| 60 | 0.09 | 5.91E-07 | 5.33E-202 | 1.00 |
| 70 | 0.09 | 1.17E-06 | 3.21E-188 | 1.00 |
| 80 | 0.09 | 5.69E-07 | 1.86E-202 | 1.00 |
| 90 | 0.09 | 6.01E-07 | 3.49E-201 | 1.00 |
| 100 | 0.09 | 4.95E-07 | 7.01E-205 | 1.00 |
| 110 | 0.09 | 5.21E-07 | 1.07E-203 | 1.00 |
| 120 | 0.09 | 5.36E-07 | 5.57E-203 | 1.00 |
| 130 | 0.09 | 4.16E-07 | 6.73E-208 | 1.00 |
| 140 | 0.09 | 5.20E-07 | 2.75E-203 | 1.00 |
| 150 | 0.08 | 6.37E-07 | 4.49E-199 | 1.00 |
| 160 | 0.08 | 5.21E-07 | 5.67E-203 | 1.00 |
| 170 | 0.08 | 1.17E-06 | 1.10E-186 | 1.00 |
| 180 | 0.08 | 4.70E-07 | 7.34E-205 | 1.00 |
| 190 | 0.08 | 4.85E-07 | 3.77E-204 | 1.00 |
| 200 | 0.08 | 6.22E-07 | 3.74E-199 | 1.00 |
| 210 | 0.08 | 6.20E-07 | 3.44E-199 | 1.00 |
| 220 | 0.08 | 7.17E-07 | 2.62E-196 | 1.00 |
| 230 | 0.08 | 6.26E-07 | 4.43E-199 | 1.00 |
| 240 | 0.08 | 9.36E-07 | 3.80E-191 | 1.00 |
| 250 | 0.08 | 6.88E-07 | 1.96E-197 | 1.00 |
| 260 | 0.09 | 1.06E-06 | 5.90E-189 | 1.00 |
| 270 | 0.09 | 1.16E-06 | 1.07E-187 | 1.00 |
| 280 | 0.09 | 1.73E-06 | 3.27E-180 | 1.00 |
| 290 | 0.09 | 2.77E-06 | 7.90E-172 | 1.00 |
| 300 | 0.11 | 3.20E-06 | 3.10E-171 | 1.00 |

***Hematite***

Table 9: Linear regression variables of hematite sample (warm-up run).

| temperature (K) | coefficient estimate | standard error | p-value | r squared |
|---|---|---|---|---|
| 50 | 7096059.47 | 1.25E+05 | 1.33E-45 | 0.99 |
| 60 | 4895624.00 | 1.22E+05 | 1.37E-38 | 0.97 |
| 70 | 3060650.47 | 1.01E+05 | 7.43E-33 | 0.95 |
| 80 | 1840243.31 | 6.49E+04 | 1.19E-31 | 0.94 |
| 90 | 1138968.10 | 3.64E+04 | 1.44E-33 | 0.95 |
| 100 | 696692.57 | 1.91E+04 | 1.08E-36 | 0.97 |
| 110 | 432595.94 | 1.16E+04 | 5.08E-37 | 0.97 |
| 120 | 282903.76 | 7.77E+03 | 1.28E-36 | 0.97 |
| 130 | 195340.36 | 5.55E+03 | 6.00E-36 | 0.96 |
| 140 | 142236.94 | 4.18E+03 | 2.96E-35 | 0.96 |
| 150 | 108719.34 | 3.25E+03 | 6.03E-35 | 0.96 |
| 160 | 85647.90 | 2.55E+03 | 5.26E-35 | 0.96 |
| 170 | 69326.62 | 2.02E+03 | 1.79E-35 | 0.96 |
| 180 | 57484.07 | 1.61E+03 | 3.25E-36 | 0.96 |
| 190 | 48456.12 | 1.28E+03 | 2.20E-37 | 0.97 |
| 200 | 41372.93 | 1.01E+03 | 5.76E-39 | 0.97 |
| 210 | 35719.37 | 8.10E+02 | 1.71E-40 | 0.98 |
| 220 | 30953.44 | 6.34E+02 | 1.45E-42 | 0.98 |
| 230 | 27101.41 | 5.03E+02 | 1.30E-44 | 0.98 |
| 240 | 23660.24 | 3.83E+02 | 2.21E-47 | 0.99 |
| 250 | 20796.41 | 2.92E+02 | 2.51E-50 | 0.99 |
| 260 | 18459.38 | 2.23E+02 | 2.04E-53 | 0.99 |
| 270 | 16670.22 | 1.79E+02 | 7.22E-56 | 0.99 |
| 280 | 15486.24 | 1.39E+02 | 1.39E-59 | 1.00 |
| 290 | 14344.27 | 9.92E+01 | 4.92E-65 | 1.00 |
| 300 | 12918.77 | 6.01E+01 | 2.75E-73 | 1.00 |

Table 10: Linear regression variables of hematite sample (cool-down run).

| temperature (K) | coefficient estimate | standard error | p-value | r squared |
|---:|---:|---:|---:|---:|
| 50 | 7050859.75 | 1.17E+05 | 8.07E-47 | 0.99 |
| 60 | 4857443.83 | 1.10E+05 | 1.80E-40 | 0.98 |
| 70 | 3053137.82 | 9.64E+04 | 7.81E-34 | 0.95 |
| 80 | 1838176.81 | 6.30E+04 | 3.45E-32 | 0.95 |
| 90 | 1117539.33 | 3.56E+04 | 1.22E-33 | 0.95 |
| 100 | 709118.73 | 1.85E+04 | 1.06E-37 | 0.97 |
| 110 | 411400.60 | 1.04E+04 | 2.90E-38 | 0.97 |
| 120 | 262341.65 | 6.69E+03 | 4.04E-38 | 0.97 |
| 130 | 176585.29 | 4.62E+03 | 1.40E-37 | 0.97 |
| 140 | 125260.78 | 3.41E+03 | 8.81E-37 | 0.97 |
| 150 | 92863.31 | 2.58E+03 | 2.35E-36 | 0.96 |
| 160 | 71347.96 | 2.00E+03 | 3.65E-36 | 0.96 |
| 170 | 56280.56 | 1.55E+03 | 1.37E-36 | 0.96 |
| 180 | 45589.70 | 1.21E+03 | 2.29E-37 | 0.97 |
| 190 | 37636.99 | 9.27E+02 | 8.10E-39 | 0.97 |
| 200 | 31678.94 | 7.15E+02 | 1.35E-40 | 0.98 |
| 210 | 26902.64 | 5.41E+02 | 5.98E-43 | 0.98 |
| 220 | 23256.20 | 4.20E+02 | 3.82E-45 | 0.98 |
| 230 | 20211.21 | 3.22E+02 | 9.47E-48 | 0.99 |
| 240 | 17899.52 | 2.51E+02 | 2.30E-50 | 0.99 |
| 250 | 16023.02 | 1.93E+02 | 1.71E-53 | 0.99 |
| 260 | 14485.89 | 1.50E+02 | 1.23E-56 | 0.99 |
| 270 | 13261.46 | 1.20E+02 | 1.58E-59 | 1.00 |
| 280 | 12211.93 | 8.89E+01 | 5.89E-64 | 1.00 |
| 290 | 11356.74 | 6.68E+01 | 2.15E-68 | 1.00 |
| 300 | 10336.64 | 4.23E+01 | 6.00E-76 | 1.00 |

### *Ilmenite*

Table 11: Linear regression variables of ilmenite sample (warm-up run).

| temperature (K) | coefficient estimate | standard error | p-value | r squared |
|---:|---:|---:|---:|---:|
| 90 | 7314.17 | 1.12E+03 | 4.40E-08 | 0.48 |
| 100 | 6021.15 | 6.69E+02 | 1.05E-11 | 0.64 |
| 110 | 5027.77 | 4.19E+02 | 9.00E-16 | 0.76 |
| 120 | 4050.88 | 2.61E+02 | 6.30E-20 | 0.84 |
| 130 | 3210.43 | 1.66E+02 | 9.56E-24 | 0.89 |
| 140 | 2537.03 | 1.10E+02 | 6.87E-27 | 0.92 |
| 150 | 2019.02 | 7.62E+01 | 1.65E-29 | 0.94 |
| 160 | 1623.43 | 5.52E+01 | 1.80E-31 | 0.95 |
| 170 | 1329.87 | 4.20E+01 | 6.96E-33 | 0.96 |
| 180 | 1111.24 | 3.32E+01 | 6.39E-34 | 0.96 |
| 190 | 947.99 | 2.72E+01 | 9.42E-35 | 0.96 |
| 200 | 823.10 | 2.28E+01 | 2.29E-35 | 0.97 |
| 210 | 727.68 | 1.97E+01 | 8.44E-36 | 0.97 |
| 220 | 651.47 | 1.74E+01 | 4.53E-36 | 0.97 |
| 230 | 590.50 | 1.58E+01 | 4.16E-36 | 0.97 |
| 240 | 543.01 | 1.44E+01 | 3.22E-36 | 0.97 |
| 250 | 506.44 | 1.45E+01 | 9.08E-35 | 0.96 |
| 260 | 478.04 | 1.39E+01 | 1.72E-34 | 0.96 |
| 270 | 454.10 | 1.31E+01 | 1.30E-34 | 0.96 |
| 280 | 441.14 | 1.27E+01 | 1.08E-34 | 0.96 |
| 290 | 430.43 | 1.41E+01 | 4.00E-32 | 0.95 |
| 300 | 401.43 | 1.29E+01 | 1.72E-32 | 0.95 |

Table 12: Linear regression variables of ilmenite sample (cool-down run).

| temperature (K) | coefficient estimate | standard error | p-value | r squared |
|---:|---:|---:|---:|---:|
| 90 | 7125.17 | 1.10E+03 | 5.35E-08 | 0.48 |
| 100 | 6028.57 | 6.67E+02 | 9.03E-12 | 0.64 |
| 110 | 5030.78 | 4.15E+02 | 6.19E-16 | 0.76 |
| 120 | 4069.33 | 2.61E+02 | 5.70E-20 | 0.84 |
| 130 | 3251.51 | 1.69E+02 | 1.31E-23 | 0.89 |
| 140 | 2603.56 | 1.12E+02 | 5.08E-27 | 0.92 |
| 150 | 2097.66 | 7.91E+01 | 1.64E-29 | 0.94 |
| 160 | 1708.34 | 5.58E+01 | 3.17E-32 | 0.95 |
| 170 | 1401.84 | 4.10E+01 | 2.39E-34 | 0.96 |
| 180 | 1160.53 | 3.14E+01 | 7.65E-36 | 0.97 |
| 190 | 974.95 | 2.48E+01 | 4.69E-37 | 0.97 |
| 200 | 832.38 | 2.02E+01 | 5.76E-38 | 0.97 |
| 210 | 729.05 | 1.75E+01 | 3.83E-38 | 0.97 |
| 220 | 642.72 | 1.48E+01 | 5.59E-39 | 0.98 |
| 230 | 571.56 | 1.31E+01 | 3.84E-39 | 0.98 |
| 240 | 515.13 | 1.17E+01 | 2.75E-39 | 0.98 |
| 250 | 470.57 | 1.07E+01 | 3.62E-39 | 0.98 |
| 260 | 435.36 | 1.06E+01 | 8.13E-38 | 0.97 |
| 270 | 414.62 | 1.15E+01 | 1.90E-35 | 0.97 |
| 280 | 395.46 | 1.06E+01 | 5.82E-36 | 0.97 |
| 290 | 387.92 | 1.11E+01 | 8.94E-35 | 0.96 |
| 300 | 379.45 | 1.37E+01 | 2.75E-30 | 0.94 |

## *Magnetite*

Table 13: Linear regression variables of magnetite sample (warm-up run).

| temperature (K) | coefficient estimate | standard error | p-value | r squared |
|---:|---:|---:|---:|---:|
| 60 | 7644136.63 | 1.15E+05 | 7.02E-49 | 0.99 |
| 70 | 5652078.05 | 1.68E+05 | 4.86E-35 | 0.96 |
| 80 | 4132875.88 | 1.93E+05 | 3.19E-26 | 0.91 |
| 90 | 3171401.32 | 1.87E+05 | 6.43E-22 | 0.86 |
| 100 | 2556505.46 | 1.78E+05 | 5.85E-19 | 0.81 |
| 110 | 2145423.67 | 1.69E+05 | 6.29E-17 | 0.77 |
| 120 | 1866146.73 | 1.55E+05 | 4.14E-16 | 0.75 |
| 130 | 1605401.20 | 1.25E+05 | 3.53E-17 | 0.78 |
| 140 | 1431899.31 | 1.06E+05 | 5.48E-18 | 0.79 |
| 150 | 1286642.46 | 8.86E+04 | 3.42E-19 | 0.81 |
| 160 | 1167220.93 | 7.49E+04 | 2.09E-20 | 0.83 |
| 170 | 1048937.20 | 6.23E+04 | 8.91E-22 | 0.86 |
| 180 | 954034.17 | 5.42E+04 | 1.44E-22 | 0.87 |
| 190 | 871328.53 | 4.71E+04 | 1.78E-23 | 0.88 |
| 200 | 784654.70 | 4.05E+04 | 2.43E-24 | 0.89 |
| 210 | 700024.35 | 3.42E+04 | 2.42E-25 | 0.90 |
| 220 | 615807.41 | 2.81E+04 | 1.23E-26 | 0.91 |
| 230 | 552802.57 | 2.43E+04 | 2.26E-27 | 0.92 |
| 240 | 497001.07 | 2.13E+04 | 8.19E-28 | 0.92 |
| 250 | 447645.18 | 1.82E+04 | 8.11E-29 | 0.93 |
| 260 | 397472.18 | 1.52E+04 | 5.31E-30 | 0.93 |
| 270 | 355044.40 | 1.28E+04 | 3.59E-31 | 0.94 |
| 280 | 321321.11 | 1.10E+04 | 2.80E-32 | 0.95 |
| 290 | 291259.59 | 9.46E+03 | 2.88E-33 | 0.95 |
| 300 | 262596.60 | 8.05E+03 | 2.00E-34 | 0.96 |

Table 14: Linear regression variables of magnetite sample (cool-down run).

| temperature (K) | coefficient estimate | standard error | p-value | r squared |
|---:|---:|---:|---:|---:|
| 60 | 7689920.20 | 1.14E+05 | 3.19E-49 | 0.99 |
| 70 | 5762146.01 | 1.65E+05 | 7.77E-36 | 0.96 |
| 80 | 4210313.87 | 2.03E+05 | 1.19E-25 | 0.90 |
| 90 | 3247705.84 | 1.95E+05 | 1.46E-21 | 0.85 |
| 100 | 2603127.09 | 1.81E+05 | 5.43E-19 | 0.81 |
| 110 | 2178979.35 | 1.76E+05 | 1.58E-16 | 0.76 |
| 120 | 1905676.54 | 1.60E+05 | 5.91E-16 | 0.75 |
| 130 | 1640768.58 | 1.29E+05 | 5.44E-17 | 0.77 |
| 140 | 1457359.20 | 1.09E+05 | 7.20E-18 | 0.79 |
| 150 | 1320112.94 | 9.38E+04 | 1.18E-18 | 0.80 |
| 160 | 1180324.36 | 7.84E+04 | 8.41E-20 | 0.83 |
| 170 | 1063878.56 | 6.65E+04 | 7.36E-21 | 0.84 |
| 180 | 963107.08 | 5.71E+04 | 8.43E-22 | 0.86 |
| 190 | 860975.51 | 4.93E+04 | 2.00E-22 | 0.86 |
| 200 | 769914.70 | 4.15E+04 | 1.50E-23 | 0.88 |
| 210 | 683358.39 | 3.41E+04 | 5.71E-25 | 0.89 |
| 220 | 606995.04 | 2.86E+04 | 4.55E-26 | 0.90 |
| 230 | 534254.34 | 2.31E+04 | 1.10E-27 | 0.92 |
| 240 | 468954.31 | 1.91E+04 | 8.93E-29 | 0.93 |
| 250 | 415564.61 | 1.63E+04 | 1.43E-29 | 0.93 |
| 260 | 344344.93 | 1.20E+04 | 6.17E-32 | 0.95 |
| 270 | 305931.19 | 1.01E+04 | 7.21E-33 | 0.95 |
| 280 | 277785.08 | 8.74E+03 | 6.59E-34 | 0.95 |
| 290 | 251415.36 | 7.50E+03 | 5.82E-35 | 0.96 |
| 300 | 224008.53 | 6.09E+03 | 8.11E-37 | 0.97 |

### *Magnetite lodestone*

Table 15: Linear regression variables of magnetite lodestone sample (warm-up run).

| temperature (K) | coefficient estimate | standard error | p-value | r squared |
|---:|---:|---:|---:|---:|
| 20 | 8988458.57 | 1.78E+05 | 2.59E-43 | 0.98 |
| 30 | 6753294.83 | 1.18E+05 | 8.68E-46 | 0.99 |
| 40 | 1261697.99 | 3.41E+04 | 6.43E-37 | 0.97 |
| 50 | 260700.54 | 6.50E+03 | 1.39E-38 | 0.97 |
| 60 | 83444.48 | 2.06E+03 | 8.42E-39 | 0.97 |
| 70 | 35138.45 | 6.72E+02 | 5.50E-44 | 0.98 |
| 80 | 16317.25 | 1.76E+02 | 9.06E-56 | 0.99 |
| 90 | 7294.54 | 2.64E+01 | 1.65E-78 | 1.00 |
| 100 | 3266.77 | 2.54E+00 | 1.38E-110 | 1.00 |
| 110 | 1625.29 | 3.32E-01 | 2.02E-138 | 1.00 |
| 120 | 896.00 | 5.87E-02 | 3.83E-162 | 1.00 |
| 130 | 550.56 | 2.14E-02 | 5.02E-173 | 1.00 |
| 140 | 367.87 | 9.40E-03 | 9.48E-182 | 1.00 |
| 150 | 260.88 | 5.26E-03 | 1.04E-186 | 1.00 |
| 160 | 193.62 | 2.18E-03 | 8.02E-199 | 1.00 |
| 170 | 148.68 | 3.56E-03 | 4.27E-183 | 1.00 |
| 180 | 118.11 | 3.28E-03 | 4.78E-180 | 1.00 |
| 190 | 98.71 | 2.66E-03 | 1.19E-180 | 1.00 |
| 200 | 83.54 | 2.76E-03 | 2.12E-176 | 1.00 |
| 210 | 77.07 | 1.36E-03 | 2.01E-189 | 1.00 |
| 220 | 67.96 | 1.04E-03 | 1.57E-192 | 1.00 |
| 230 | 60.63 | 1.35E-03 | 1.34E-184 | 1.00 |
| 240 | 53.40 | 1.29E-03 | 7.03E-183 | 1.00 |
| 250 | 49.33 | 1.00E-03 | 1.68E-186 | 1.00 |
| 260 | 46.22 | 1.34E-03 | 3.39E-179 | 1.00 |
| 270 | 44.03 | 1.34E-03 | 4.25E-178 | 1.00 |
| 280 | 42.29 | 8.23E-04 | 1.94E-187 | 1.00 |
| 290 | 40.96 | 1.14E-03 | 4.60E-180 | 1.00 |
| 300 | 40.10 | 2.05E-03 | 2.67E-167 | 1.00 |

Table 16: Linear regression variables of magnetite lodestone sample (cool-down run).

| temperature (K) | coefficient estimate | standard error | p-value | r squared |
|---:|---:|---:|---:|---:|
| 20 | 9060264.55 | 1.50E+05 | 5.54E-47 | 0.99 |
| 30 | 6755265.66 | 1.19E+05 | 1.26E-45 | 0.99 |
| 40 | 1212719.97 | 3.17E+04 | 1.34E-37 | 0.97 |
| 50 | 246103.69 | 6.07E+03 | 8.37E-39 | 0.97 |
| 60 | 78540.87 | 1.91E+03 | 4.72E-39 | 0.97 |
| 70 | 33129.74 | 6.32E+02 | 4.91E-44 | 0.98 |
| 80 | 15732.13 | 1.77E+02 | 6.92E-55 | 0.99 |
| 90 | 7280.68 | 2.75E+01 | 1.17E-77 | 1.00 |
| 100 | 3346.22 | 2.47E+00 | 1.11E-111 | 1.00 |
| 110 | 1649.28 | 2.43E-01 | 3.18E-145 | 1.00 |
| 120 | 890.09 | 4.77E-02 | 2.54E-166 | 1.00 |
| 130 | 542.00 | 1.42E-02 | 2.69E-181 | 1.00 |
| 140 | 359.17 | 1.34E-02 | 6.40E-174 | 1.00 |
| 150 | 250.63 | 8.99E-03 | 1.09E-174 | 1.00 |
| 160 | 184.70 | 2.79E-03 | 1.01E-192 | 1.00 |
| 170 | 141.67 | 1.29E-03 | 2.93E-203 | 1.00 |
| 180 | 113.25 | 1.65E-03 | 1.67E-193 | 1.00 |
| 190 | 93.29 | 1.46E-03 | 5.32E-192 | 1.00 |
| 200 | 79.41 | 2.04E-03 | 1.30E-181 | 1.00 |
| 210 | 69.03 | 1.61E-03 | 1.08E-183 | 1.00 |
| 220 | 61.31 | 1.58E-03 | 1.32E-181 | 1.00 |
| 230 | 55.40 | 1.79E-03 | 7.61E-177 | 1.00 |
| 240 | 50.99 | 2.05E-03 | 2.80E-172 | 1.00 |
| 250 | 47.22 | 1.94E-03 | 7.40E-172 | 1.00 |
| 260 | 44.39 | 1.56E-03 | 4.11E-175 | 1.00 |
| 270 | 42.33 | 1.67E-03 | 1.08E-172 | 1.00 |
| 280 | 41.10 | 1.11E-03 | 1.52E-180 | 1.00 |
| 290 | 40.86 | 2.22E-03 | 5.36E-166 | 1.00 |
| 300 | 40.98 | 1.31E-03 | 4.88E-177 | 1.00 |

***Pyrite***

Table 17: Linear regression variables of pyrite sample (warm-up run).

| temperature (K) | coefficient estimate | standard error | p-value | r squared |
|---|---|---|---|---|
| 20 | 30646.79 | 1.39E+03 | 9.50E-27 | 0.91 |
| 30 | 25948.47 | 9.15E+02 | 1.22E-31 | 0.94 |
| 40 | 18142.26 | 3.86E+02 | 8.88E-42 | 0.98 |
| 50 | 12043.83 | 1.48E+02 | 3.78E-53 | 0.99 |
| 60 | 7732.60 | 4.99E+01 | 1.83E-66 | 1.00 |
| 70 | 4992.99 | 1.46E+01 | 6.93E-83 | 1.00 |
| 80 | 3319.80 | 3.79E+00 | 1.55E-102 | 1.00 |
| 90 | 2306.20 | 1.06E+00 | 1.94E-121 | 1.00 |
| 100 | 1663.72 | 2.88E-01 | 7.03E-142 | 1.00 |
| 110 | 1259.89 | 1.17E-01 | 8.39E-155 | 1.00 |
| 120 | 973.28 | 2.23E-02 | 4.86E-184 | 1.00 |
| 130 | 771.07 | 2.24E-02 | 4.27E-179 | 1.00 |
| 140 | 625.58 | 1.55E-02 | 2.39E-182 | 1.00 |
| 150 | 515.72 | 1.30E-02 | 4.53E-182 | 1.00 |
| 160 | 432.85 | 4.03E-03 | 8.47E-203 | 1.00 |
| 170 | 370.93 | 4.55E-03 | 4.85E-197 | 1.00 |
| 180 | 319.25 | 3.47E-03 | 1.36E-199 | 1.00 |
| 190 | 278.15 | 2.75E-03 | 1.47E-201 | 1.00 |
| 200 | 245.32 | 2.58E-03 | 2.63E-200 | 1.00 |
| 210 | 218.08 | 3.30E-03 | 1.16E-192 | 1.00 |
| 220 | 195.55 | 2.11E-03 | 1.05E-199 | 1.00 |
| 230 | 176.79 | 2.14E-03 | 2.30E-197 | 1.00 |
| 240 | 161.52 | 1.65E-03 | 6.37E-201 | 1.00 |
| 250 | 148.38 | 1.65E-03 | 4.37E-199 | 1.00 |
| 260 | 137.10 | 2.07E-03 | 1.07E-192 | 1.00 |
| 270 | 128.29 | 1.53E-03 | 1.28E-197 | 1.00 |
| 280 | 120.75 | 1.46E-03 | 2.20E-197 | 1.00 |
| 290 | 115.35 | 1.05E-03 | 2.87E-203 | 1.00 |
| 300 | 113.38 | 9.47E-04 | 4.50E-205 | 1.00 |

Table 18: Linear regression variables of pyrite sample (cool-down run).

| temperature (K) | coefficient estimate | standard error | p-value | r squared |
|---:|---:|---:|---:|---:|
| 20 | 30859.30 | 1.42E+03 | 1.83E-26 | 0.91 |
| 30 | 25947.03 | 9.16E+02 | 1.28E-31 | 0.94 |
| 40 | 17979.51 | 3.78E+02 | 4.70E-42 | 0.98 |
| 50 | 11872.95 | 1.43E+02 | 1.88E-53 | 0.99 |
| 60 | 7597.29 | 4.77E+01 | 4.88E-67 | 1.00 |
| 70 | 4890.47 | 1.40E+01 | 2.14E-83 | 1.00 |
| 80 | 3270.25 | 3.72E+00 | 1.24E-102 | 1.00 |
| 90 | 2267.14 | 9.76E-01 | 6.87E-123 | 1.00 |
| 100 | 1626.13 | 2.72E-01 | 1.48E-142 | 1.00 |
| 110 | 1222.19 | 7.23E-02 | 2.89E-164 | 1.00 |
| 120 | 937.79 | 2.64E-02 | 1.04E-179 | 1.00 |
| 130 | 741.13 | 8.55E-03 | 2.42E-198 | 1.00 |
| 140 | 599.80 | 1.94E-02 | 7.17E-177 | 1.00 |
| 150 | 493.38 | 8.19E-03 | 9.41E-191 | 1.00 |
| 160 | 412.38 | 1.31E-02 | 3.68E-177 | 1.00 |
| 170 | 348.45 | 7.41E-03 | 1.40E-185 | 1.00 |
| 180 | 299.44 | 8.01E-03 | 8.43E-181 | 1.00 |
| 190 | 260.23 | 5.20E-03 | 6.61E-187 | 1.00 |
| 200 | 228.99 | 7.07E-03 | 8.26E-178 | 1.00 |
| 210 | 203.06 | 2.87E-03 | 3.96E-194 | 1.00 |
| 220 | 181.36 | 3.29E-03 | 6.22E-189 | 1.00 |
| 230 | 163.32 | 3.25E-03 | 5.49E-187 | 1.00 |
| 240 | 148.32 | 1.75E-03 | 7.25E-198 | 1.00 |
| 250 | 135.40 | 1.85E-03 | 9.00E-195 | 1.00 |
| 260 | 124.56 | 1.60E-03 | 4.39E-196 | 1.00 |
| 270 | 115.18 | 1.75E-03 | 1.34E-192 | 1.00 |
| 280 | 107.40 | 1.68E-03 | 4.77E-192 | 1.00 |
| 290 | 101.37 | 2.63E-03 | 1.89E-181 | 1.00 |
| 300 | 96.42 | 8.72E-04 | 2.10E-203 | 1.00 |

***Pyrrhotite***

Table 19: Linear regression variables of pyrrhotite sample (warm-up run).

| temperature (K) | coefficient estimate | standard error | p-value | r squared |
|---|---|---|---|---|
| 10 | 65.18 | 1.25E-02 | 1.15E-139 | 1.00 |
| 20 | 58.05 | 5.82E-03 | 2.79E-153 | 1.00 |
| 30 | 51.69 | 2.68E-03 | 5.64E-167 | 1.00 |
| 40 | 46.24 | 1.94E-03 | 2.09E-171 | 1.00 |
| 50 | 41.89 | 1.42E-03 | 8.40E-176 | 1.00 |
| 60 | 38.40 | 8.61E-04 | 1.70E-184 | 1.00 |
| 70 | 35.52 | 1.97E-03 | 1.33E-165 | 1.00 |
| 80 | 33.01 | 6.44E-04 | 2.17E-187 | 1.00 |
| 90 | 30.93 | 1.63E-03 | 1.03E-166 | 1.00 |
| 100 | 29.08 | 7.17E-04 | 1.65E-182 | 1.00 |
| 110 | 27.47 | 7.48E-04 | 2.00E-180 | 1.00 |
| 120 | 26.01 | 9.22E-04 | 6.20E-175 | 1.00 |
| 130 | 24.74 | 7.65E-04 | 8.90E-178 | 1.00 |
| 140 | 23.56 | 8.58E-04 | 2.33E-174 | 1.00 |
| 150 | 22.42 | 1.17E-03 | 6.62E-167 | 1.00 |
| 160 | 21.32 | 1.29E-03 | 8.99E-164 | 1.00 |
| 170 | 20.28 | 6.21E-04 | 5.56E-178 | 1.00 |
| 180 | 19.31 | 7.82E-04 | 3.72E-172 | 1.00 |
| 190 | 18.37 | 8.45E-04 | 1.72E-169 | 1.00 |
| 200 | 17.42 | 1.56E-03 | 1.33E-155 | 1.00 |
| 210 | 16.54 | 1.49E-03 | 1.76E-155 | 1.00 |
| 220 | 15.67 | 1.04E-03 | 7.19E-162 | 1.00 |
| 230 | 14.88 | 7.31E-04 | 3.99E-168 | 1.00 |
| 240 | 14.13 | 5.79E-04 | 6.36E-172 | 1.00 |
| 250 | 13.50 | 7.77E-04 | 7.83E-165 | 1.00 |
| 260 | 12.89 | 1.13E-03 | 5.49E-156 | 1.00 |
| 270 | 12.42 | 8.39E-04 | 1.74E-161 | 1.00 |
| 280 | 12.16 | 9.34E-04 | 8.38E-159 | 1.00 |
| 290 | 12.94 | 1.32E-03 | 6.19E-153 | 1.00 |
| 300 | 14.44 | 1.24E-03 | 1.57E-156 | 1.00 |

Table 20: Linear regression variables of pyrrhotite sample (cool-down run).

| temperature (K) | coefficient estimate | standard error | p-value | r squared |
|---:|---:|---:|---:|---:|
| 10 | 65.33 | 1.65E-02 | 5.26E-134 | 1.00 |
| 20 | 58.13 | 6.17E-03 | 4.42E-152 | 1.00 |
| 30 | 51.69 | 2.83E-03 | 7.24E-166 | 1.00 |
| 40 | 46.09 | 1.48E-03 | 5.73E-177 | 1.00 |
| 50 | 41.65 | 1.48E-03 | 7.74E-175 | 1.00 |
| 60 | 38.20 | 1.38E-03 | 1.74E-174 | 1.00 |
| 70 | 35.31 | 1.26E-03 | 8.06E-175 | 1.00 |
| 80 | 32.85 | 1.93E-03 | 1.94E-164 | 1.00 |
| 90 | 30.62 | 7.51E-04 | 1.29E-182 | 1.00 |
| 100 | 28.86 | 8.04E-04 | 5.88E-180 | 1.00 |
| 110 | 27.28 | 7.97E-04 | 5.55E-179 | 1.00 |
| 120 | 25.86 | 7.62E-04 | 8.66E-179 | 1.00 |
| 130 | 24.57 | 7.85E-04 | 4.33E-177 | 1.00 |
| 140 | 23.29 | 5.06E-04 | 3.93E-185 | 1.00 |
| 150 | 22.20 | 7.98E-04 | 1.21E-174 | 1.00 |
| 160 | 21.17 | 8.55E-04 | 3.17E-172 | 1.00 |
| 170 | 20.13 | 5.76E-04 | 2.02E-179 | 1.00 |
| 180 | 19.12 | 1.18E-03 | 2.12E-163 | 1.00 |
| 190 | 18.09 | 7.41E-04 | 6.37E-172 | 1.00 |
| 200 | 17.10 | 9.09E-04 | 1.72E-166 | 1.00 |
| 210 | 16.17 | 1.03E-03 | 1.10E-162 | 1.00 |
| 220 | 15.22 | 9.69E-04 | 1.01E-162 | 1.00 |
| 230 | 14.31 | 8.96E-04 | 4.52E-163 | 1.00 |
| 240 | 13.43 | 8.99E-04 | 1.10E-161 | 1.00 |
| 250 | 12.62 | 8.25E-04 | 3.65E-162 | 1.00 |
| 260 | 11.85 | 7.15E-04 | 7.61E-164 | 1.00 |
| 270 | 11.15 | 4.26E-04 | 2.14E-173 | 1.00 |
| 280 | 10.57 | 5.76E-04 | 5.65E-166 | 1.00 |
| 290 | 10.17 | 3.88E-04 | 2.19E-173 | 1.00 |
| 300 | 9.95 | 7.28E-04 | 7.88E-160 | 1.00 |

### *Serpentinite*

Table 21: Linear regression variables of serpentinite sample (warm-up run).

| temperature (K) | coefficient estimate | standard error | p-value | r squared |
|---:|---:|---:|---:|---:|
| 70 | 7813805.41 | 1.34E+05 | 2.97E-46 | 0.99 |
| 80 | 6637228.77 | 1.19E+05 | 3.18E-45 | 0.98 |
| 90 | 5137355.69 | 1.31E+05 | 4.24E-38 | 0.97 |
| 100 | 3889586.64 | 1.15E+05 | 3.22E-35 | 0.96 |
| 110 | 2860334.36 | 1.15E+05 | 3.77E-29 | 0.93 |
| 120 | 2086683.93 | 1.07E+05 | 1.76E-24 | 0.89 |
| 130 | 1673615.87 | 8.72E+04 | 3.78E-24 | 0.88 |
| 140 | 1423792.42 | 7.05E+04 | 4.18E-25 | 0.89 |
| 150 | 1238195.76 | 5.99E+04 | 1.49E-25 | 0.90 |
| 160 | 1104325.02 | 5.09E+04 | 1.79E-26 | 0.91 |
| 170 | 976373.27 | 4.28E+04 | 2.11E-27 | 0.92 |
| 180 | 866561.73 | 3.60E+04 | 1.91E-28 | 0.92 |
| 190 | 776736.88 | 2.98E+04 | 5.43E-30 | 0.93 |
| 200 | 692013.77 | 2.58E+04 | 1.44E-30 | 0.94 |
| 210 | 621049.63 | 2.21E+04 | 1.86E-31 | 0.94 |
| 220 | 559068.19 | 2.29E+04 | 1.11E-28 | 0.93 |
| 230 | 487557.33 | 2.03E+04 | 2.35E-28 | 0.92 |
| 240 | 452088.41 | 1.69E+04 | 1.83E-30 | 0.94 |
| 250 | 406074.35 | 1.44E+04 | 1.64E-31 | 0.94 |
| 260 | 363096.51 | 1.16E+04 | 1.26E-33 | 0.95 |
| 270 | 337676.10 | 1.04E+04 | 2.62E-34 | 0.96 |
| 280 | 303556.63 | 8.57E+03 | 4.57E-36 | 0.96 |
| 290 | 278492.09 | 7.91E+03 | 6.11E-36 | 0.96 |
| 300 | 257093.12 | 7.76E+03 | 9.82E-35 | 0.96 |

Table 22: Linear regression variables of serpentinite sample (cool-down run).

| temperature (K) | coefficient estimate | standard error | p-value | r squared |
|---:|---:|---:|---:|---:|
| 70 | 7820675.59 | 1.22E+05 | 3.35E-48 | 0.99 |
| 80 | 6627338.17 | 1.08E+05 | 2.70E-47 | 0.99 |
| 90 | 5172759.35 | 1.34E+05 | 8.65E-38 | 0.97 |
| 100 | 3947373.13 | 1.14E+05 | 1.28E-35 | 0.96 |
| 110 | 2980404.98 | 1.08E+05 | 4.27E-31 | 0.94 |
| 120 | 2197194.46 | 9.89E+04 | 6.74E-27 | 0.91 |
| 130 | 1761669.90 | 8.67E+04 | 3.17E-25 | 0.90 |
| 140 | 1497490.75 | 7.33E+04 | 2.53E-25 | 0.90 |
| 150 | 1289677.32 | 5.97E+04 | 2.26E-26 | 0.91 |
| 160 | 1134753.30 | 5.08E+04 | 5.38E-27 | 0.91 |
| 170 | 989795.11 | 4.25E+04 | 7.90E-28 | 0.92 |
| 180 | 873063.42 | 3.60E+04 | 1.37E-28 | 0.92 |
| 190 | 783835.99 | 2.92E+04 | 1.58E-30 | 0.94 |
| 200 | 691323.88 | 2.50E+04 | 3.74E-31 | 0.94 |
| 210 | 612509.90 | 2.14E+04 | 8.13E-32 | 0.94 |
| 220 | 548200.90 | 1.85E+04 | 1.52E-32 | 0.95 |
| 230 | 492566.46 | 1.59E+04 | 2.05E-33 | 0.95 |
| 240 | 448723.36 | 1.63E+04 | 4.89E-31 | 0.94 |
| 250 | 406527.47 | 1.21E+04 | 6.10E-35 | 0.96 |
| 260 | 365344.86 | 9.98E+03 | 9.84E-37 | 0.97 |
| 270 | 323266.31 | 9.53E+03 | 3.41E-35 | 0.96 |
| 280 | 290350.02 | 9.14E+03 | 6.74E-34 | 0.95 |
| 290 | 268637.26 | 6.22E+03 | 4.34E-40 | 0.97 |
| 300 | 242721.97 | 8.02E+03 | 6.17E-33 | 0.95 |

# Appendix C: MATLAB code

```
%%Sample 1
k1=0;
k2=0;
k3=0;
sample_name=input('Input the sample name + (cool-down / warm-up) = ','s');

temp=[30 40 50 60 70 80 90 100 110 120 130 140 150 160 170 180 190 200 210
220 230 240 250 260 270 280 290 300];
for i = temp
    k1=k1+1;
filename = strcat('T',num2str(i),'magnetite1_cooldown.dat');
fileID = fopen(filename);
[~,~,~,col4_1,~,~,~,col7_1,~,~,~,~,~,~,~,~,~,~] =
textread(filename,'%f%f%f%f%f%f%f%f%f%f%f%f%f%f%f%f','headerlines',1);
fclose(fileID);
length_flag = length(col4_1);

I_s = col4_1;
%new current values



I_new_1(:,k1) = (I_s);
clear I_s

V_nv = col7_1;

%new voltage values

V_new_1(:,k1)=(V_nv);
clear V_nv

end

%%Sample 2
```

```
for i = temp
    k2=k2+1;
filename = strcat('T',num2str(i),'magnetite2_cooldown.dat');
fileID = fopen(filename);
[~,~,~,col4_2,~,~,col7_2,~,~,~,~,~,~,~,~,~] =
textread(filename,'%f%f%f%f%f%f%f%f%f%f%f%f%f%f%f%f','headerlines',1);
fclose(fileID);
length_flag = length(col4_2);

I_s = col4_2;

%new current values


I_new_2(:,k2) = (I_s);
clear I_new

V_nv = col7_2;
%new voltage values

V_new_2(:,k2)=(V_nv);

clear V_new

end

%%Sample 3
for i = temp
    k3=k3+1;
filename = strcat('T',num2str(i),'magnetite3_cooldown.dat');
fileID = fopen(filename);
[~,~,~,col4_3,~,~,col7_3,~,~,~,~,~,~,~,~,~] =
textread(filename,'%f%f%f%f%f%f%f%f%f%f%f%f%f%f%f%f','headerlines',1);
fclose(fileID);
length_flag = length(col4_3);

I_s = col4_3;
```

```
%new current values
I_new = zeros(1,size(I_s,1));
I_new(1) = I_s(end);
I_new(2:end) = I_s(1:(end-1));

I_new_3(:,k3) = (I_new);
clear I_new

V_nv = col7_3;
%new voltage values

V_new_3(:,k3)=(V_nv);
clear V_new

end
L = input('Insert the length of the sample (mm) = ');
L = (10^-3).*L;
W = input('Insert the width of the sample (mm) = ');
T = input('Insert the thickness of the sample (mm) = ');
A = W*T;
A = (10^-6).*A;
L_A = L./A;

%%regression
for i=1:k3
Inew_100=[I_new_1(:,i)];
Vnew_100=[V_new_1(:,i),V_new_2(:,i),V_new_3(:,i)];
V_100_average=mean(Vnew_100,2);

mdl1=fitlm(Inew_100(:,1),V_100_average);
tbl1(i,:)=mdl1.Coefficients(2,:);
r_sq(i)=mdl1.Rsquared.Ordinary;
sse(i)=mdl1.SSE;

I = (Inew_100);
V = V_100_average;
```

```
R(:,i) = V./I;



% cool-down color = [0.2 0 0.6]
%warmup color = [1 0.4 0.1]

figure
p=plot(Inew_100(:,1),V_100_average,'r');

p.LineStyle = 'none';
p.LineWidth = 0.15;
p.Marker = 'o';
p.MarkerEdgeColor = [0.2 0 0.6];
p.MarkerFaceColor = [0.2 0 0.6];

hold on
plot(mdl1);

title (strcat(num2str(sample_name),' - current vs voltage
(T=',num2str(temp(i)),' K)'));
xlabel('Current (A)')
ylabel ('Voltage (V)')
saveas(gcf,strcat('VxI_T_',num2str(temp(i)),'_',sample_name,'.png'));

end

[r,~]=find(R<0);

R(r,:)=[];

%Calculating resistivity (rho)%

rho = R./(L_A);
B_rho = rmoutliers(rho,'median');
RHO=mean(B_rho);
sigma = 1./(B_rho);
```

```
% cool-down color = [0 0.1 1]
%warmup color = 'r'

figure
p= plot(RHO,temp);

p.LineStyle = 'none';
p.Marker = '^';
p.MarkerEdgeColor = [0 0.1 1];
p.MarkerFaceColor = [0 0.1 1];

title (strcat(num2str(sample_name),' - Resistivity vs Temperature'));
xlabel('Resistivity (ohm.meter)')
ylabel('Temperature (K)')
saveas(gcf,strcat('rho_T_','_',sample_name,'.png'));




% first column is coefficient estiamte
%second column is standard error
%third column is t-stat
% fourth column is p-value
% fifth column is r squared
% sixth column is SSE (sum of squared errors)
% each row is a given temperature defined in variable temp at the beginning

final_table=[table2array(tbl1),(r_sq'),(sse')];
```

# Appendix D: Samples dimensions

Table 23: Measurements of length, width and thickness of the samples.

| Samples | Length (mm) | width (mm) | thickness (mm) | Samples | Length (mm) | width (mm) | thickness (mm) |
|---|---|---|---|---|---|---|---|
| **chalcopyrite** | | | | **magnetite crystaline** | | | |
| 1 | 3.75 | 2.78 | 4.59 | 1 | 1.52 | 3.98 | 2.23 |
| 2 | 3.62 | 3.62 | 5.34 | 2 | 1.71 | 3.24 | 2.1 |
| 3 | 2.94 | 3.7 | 2.55 | 3 | 1.87 | 2.76 | 3.79 |
| mean | 3.44 | 3.37 | 4.16 | mean | 1.70 | 3.33 | 2.71 |
| **galena** | | | | **magnetite lodestone** | | | |
| 1 | 2.83 | 3.38 | 3.99 | 1 | 2.6 | 2.64 | 3.45 |
| 2 | 2.23 | 4.17 | 2.24 | 2 | 3.19 | 3.22 | 3.46 |
| 3 | 1.87 | 3.38 | 3.15 | 3 | 3.26 | 4.69 | 3.33 |
| mean | 2.31 | 3.64 | 3.13 | mean | 3.02 | 3.52 | 3.41 |
| **graphite** | | | | **pyrite** | | | |
| 1 | 3.02 | 3.65 | 2.78 | 1 | 3.31 | 2.97 | 3.42 |
| 2 | 2.95 | 3.85 | 3 | 2 | 3.15 | 2.5 | 3.23 |
| 3 | 2.56 | 3.91 | 2.44 | 3 | 3.44 | 3.28 | 3.19 |
| mean | 2.84 | 3.80 | 2.74 | mean | 3.30 | 2.92 | 3.28 |
| **hematite SPECULAR** | | | | **pyrrhotite** | | | |
| 1 | 2.18 | 3.47 | 3.52 | 1 | 3.12 | 3.82 | 3.87 |
| 2 | 1.42 | 3.63 | 4.12 | 2 | 3.12 | 3.11 | 3.18 |
| 3 | 2.77 | 3.69 | 3.31 | 3 | 2.59 | 3.16 | 2.33 |
| mean | 2.12 | 3.60 | 3.65 | mean | 2.94 | 3.36 | 3.13 |
| **ilmenite** | | | | **serpentinite ROM** | | | |
| 1 | 2.28 | 2.46 | 2.73 | 1 | 3.76 | 2.8 | 2.29 |
| 2 | 2.21 | 1.98 | 2.93 | 2 | 1.79 | 2.71 | 2.71 |
| 3 | 2.22 | 4 | 3.17 | 3 | 2.22 | 2.45 | 1.92 |
| mean | 2.24 | 2.81 | 2.94 | mean | 2.59 | 2.65 | 2.31 |

# Appendix E: Resistivity values

Table 24: Resistivity values of the samples at each temperature (warm-up run).

| Resistivity (Ω・m) - Warm up run | | | | | | | | | | |
|---|---|---|---|---|---|---|---|---|---|---|
| temperature (K) | Chalcopyrite | Galena | Graphite | Hematite specular | Ilmenite | Magnetite | Magnetite lodestone | Pyrite | Pyrrhotite | Serpentinite |
| 10 | | | | | | | | | 0.26 | |
| 20 | 1.17 | 0.02 | | | | | 44216.62 | 626.11 | 0.24 | |
| 30 | 0.74 | 0.02 | | | | | 51524.61 | 287.71 | 0.22 | |
| 40 | 0.53 | 0.02 | 8.39E-04 | | | | 12546.31 | 103.41 | 0.20 | |
| 50 | 0.40 | 0.02 | 8.36E-04 | 284410.80 | | | 2530.00 | 48.27 | 0.19 | |
| 60 | 0.35 | 0.02 | 8.31E-04 | 267344.37 | | 75803.85 | 742.90 | 25.76 | 0.18 | |
| 70 | 0.33 | 0.03 | 8.26E-04 | 167738.98 | | 82528.64 | 240.73 | 15.22 | 0.17 | 39182.51 |
| 80 | 0.32 | 0.03 | 8.21E-04 | 82311.31 | | 86876.05 | 82.70 | 9.75 | 0.16 | 33459.06 |
| 90 | 0.31 | 0.03 | 8.16E-04 | 43544.42 | 572.85 | 79097.25 | 30.93 | 6.70 | 0.15 | 38244.28 |
| 100 | 0.30 | 0.03 | 8.11E-04 | 27452.38 | 305.16 | 85495.23 | 13.13 | 4.82 | 0.14 | 31044.43 |
| 110 | 0.29 | 0.03 | 8.07E-04 | 15639.12 | 183.73 | 89996.17 | 6.47 | 3.65 | 0.14 | 25797.52 |
| 120 | 0.28 | 0.03 | 8.02E-04 | 10392.64 | 116.50 | 68447.34 | 3.56 | 2.83 | 0.13 | 21788.26 |
| 130 | 0.27 | 0.03 | 7.97E-04 | 7532.59 | 77.87 | 64608.19 | 2.19 | 2.25 | 0.13 | 17331.47 |
| 140 | 0.26 | 0.03 | 7.89E-04 | 5034.64 | 54.12 | 60164.00 | 1.46 | 1.83 | 0.12 | 16498.37 |
| 150 | 0.25 | 0.04 | 7.84E-04 | 3434.38 | 38.86 | 54616.21 | 1.04 | 1.52 | 0.11 | 13526.00 |
| 160 | 0.24 | 0.04 | 7.79E-04 | 2368.08 | 28.45 | 52076.77 | 0.77 | 1.28 | 0.10 | 11338.39 |
| 170 | 0.18 | 0.04 | 7.74E-04 | 1628.55 | 21.63 | 42967.32 | 0.60 | 1.10 | 0.11 | 9383.83 |
| 180 | 0.13 | 0.04 | 7.70E-04 | 1159.06 | 16.89 | 39130.84 | 0.48 | 0.95 | 0.10 | 7773.81 |
| 190 | 0.12 | 0.04 | 7.66E-04 | 835.04 | 13.47 | 31179.25 | 0.40 | 0.83 | 0.09 | 6372.77 |
| 200 | 0.11 | 0.04 | 7.62E-04 | 613.43 | 11.03 | 24724.35 | 0.34 | 0.73 | 0.09 | 5401.25 |
| 210 | 0.12 | 0.04 | 7.59E-04 | 471.06 | 9.21 | 21808.53 | 0.30 | 0.65 | 0.08 | 4457.43 |
| 220 | 0.13 | 0.04 | 7.58E-04 | 363.22 | 7.81 | 16052.76 | 0.26 | 0.59 | 0.08 | 4668.35 |
| 230 | 0.13 | 0.05 | 7.57E-04 | 287.58 | 6.80 | 13709.15 | 0.23 | 0.53 | 0.08 | 5428.68 |
| 240 | 0.16 | 0.05 | 7.56E-04 | 225.85 | 6.04 | 11432.78 | 0.21 | 0.49 | 0.07 | 4604.90 |
| 250 | 0.23 | 0.05 | 7.57E-04 | 183.24 | 6.48 | 9375.18 | 0.19 | 0.45 | 0.06 | 3515.84 |
| 260 | 0.26 | 0.05 | 7.62E-04 | 152.62 | 5.95 | 7310.22 | 0.18 | 0.41 | 0.06 | 2681.94 |
| 270 | 0.27 | 0.06 | 7.71E-04 | 132.32 | 5.41 | 6474.92 | 0.17 | 0.39 | 0.05 | 2461.14 |
| 280 | 0.30 | 0.07 | 7.90E-04 | 116.92 | 5.11 | 5210.65 | 0.16 | 0.37 | 0.05 | 2071.10 |
| 290 | 0.35 | 0.08 | 8.36E-04 | 102.14 | 5.34 | 4216.29 | 0.15 | 0.35 | 0.05 | 1837.12 |
| 300 | 0.33 | 0.10 | 9.82E-04 | 89.87 | 4.45 | 3528.15 | 0.16 | 0.34 | 0.06 | 1597.50 |

Table 25: Resistivity values of the samples at each temperature (cool-down run).

| Resistivity (Ω · m) - Cool down run | | | | | | | | | | |
|---|---|---|---|---|---|---|---|---|---|---|
| **temperature (K)** | **Chalcopyrite** | **Galena** | **Graphite** | **Hematite specular** | **Ilmenite** | **Magnetite** | **Magnetite lodestone** | **Pyrite** | **Pyrrhotite** | **Serpentinite** |
| 10 | | | | | | | | | 0.24 | |
| 20 | 1.17 | 0.02 | | | | | 43338.06 | 658.25 | 0.21 | |
| 30 | 0.76 | 0.02 | | | | | 60094.59 | 290.33 | 0.19 | |
| 40 | 0.53 | 0.02 | 3.94E-04 | | | | 12425.14 | 102.04 | 0.17 | |
| 50 | 0.40 | 0.02 | 3.91E-04 | 238561.85 | | | 2494.35 | 47.36 | 0.16 | |
| 60 | 0.35 | 0.02 | 3.88E-04 | 259917.91 | | 72965.54 | 716.98 | 25.19 | 0.14 | |
| 70 | 0.28 | 0.02 | 3.84E-04 | 157016.75 | | 60381.77 | 230.54 | 14.87 | 0.13 | 34153.60 |
| 80 | 0.30 | 0.03 | 3.80E-04 | 77564.82 | | 61650.76 | 80.53 | 9.59 | 0.12 | 28301.32 |
| 90 | 0.18 | 0.03 | 3.76E-04 | 42879.53 | 565.71 | 64690.56 | 30.89 | 6.57 | 0.12 | 28457.23 |
| 100 | 0.17 | 0.03 | 3.72E-04 | 24863.74 | 306.84 | 78808.97 | 13.46 | 4.70 | 0.11 | 25401.17 |
| 110 | 0.17 | 0.03 | 3.67E-04 | 14619.32 | 183.16 | 57344.59 | 6.56 | 3.53 | 0.10 | 23426.24 |
| 120 | 0.21 | 0.03 | 3.62E-04 | 8667.32 | 114.79 | 58490.39 | 3.53 | 2.72 | 0.10 | 19541.48 |
| 130 | 0.20 | 0.03 | 3.57E-04 | 6045.13 | 76.00 | 53538.41 | 2.15 | 2.16 | 0.09 | 15945.76 |
| 140 | 0.20 | 0.03 | 3.53E-04 | 4166.32 | 52.34 | 40350.08 | 1.43 | 1.75 | 0.09 | 13304.49 |
| 150 | 0.18 | 0.03 | 3.49E-04 | 2747.34 | 38.11 | 39815.35 | 0.99 | 1.45 | 0.08 | 12344.57 |
| 160 | 0.20 | 0.03 | 3.45E-04 | 1774.87 | 27.89 | 41383.38 | 0.73 | 1.21 | 0.08 | 10143.75 |
| 170 | 0.26 | 0.04 | 3.41E-04 | 1165.89 | 20.95 | 31569.18 | 0.56 | 1.03 | 0.07 | 8438.43 |
| 180 | 0.27 | 0.04 | 3.37E-04 | 794.65 | 16.07 | 29509.51 | 0.45 | 0.88 | 0.07 | 7033.45 |
| 190 | 0.27 | 0.04 | 3.34E-04 | 560.22 | 12.62 | 28784.85 | 0.37 | 0.77 | 0.07 | 5879.34 |
| 200 | 0.27 | 0.04 | 3.32E-04 | 408.46 | 10.09 | 24262.35 | 0.31 | 0.68 | 0.06 | 4841.99 |
| 210 | 0.27 | 0.04 | 3.29E-04 | 302.90 | 8.51 | 18430.77 | 0.27 | 0.60 | 0.06 | 4112.88 |
| 220 | 0.27 | 0.04 | 3.27E-04 | 235.27 | 7.05 | 14633.06 | 0.24 | 0.54 | 0.05 | 3433.85 |
| 230 | 0.31 | 0.04 | 3.27E-04 | 186.76 | 5.94 | 10814.66 | 0.22 | 0.49 | 0.05 | 2906.76 |
| 240 | 0.33 | 0.04 | 3.26E-04 | 152.87 | 5.09 | 8825.02 | 0.20 | 0.44 | 0.05 | 2773.71 |
| 250 | 0.36 | 0.05 | 3.28E-04 | 128.61 | 4.41 | 7271.16 | 0.19 | 0.40 | 0.05 | 2122.79 |
| 260 | 0.37 | 0.05 | 3.29E-04 | 111.26 | 4.42 | 5055.12 | 0.17 | 0.37 | 0.04 | 1751.83 |
| 270 | 0.38 | 0.05 | 3.33E-04 | 98.01 | 4.66 | 4378.13 | 0.17 | 0.34 | 0.04 | 2297.24 |
| 280 | 0.41 | 0.06 | 3.41E-04 | 87.09 | 4.50 | 3701.76 | 0.16 | 0.32 | 0.04 | 2005.77 |
| 290 | 0.50 | 0.08 | 3.58E-04 | 79.54 | 4.25 | 3032.53 | 0.16 | 0.30 | 0.04 | 1539.36 |
| 300 | 0.65 | 0.10 | 3.98E-04 | 71.01 | 5.74 | 2431.55 | 0.17 | 0.29 | 0.04 | 1385.97 |

## Appendix F: Percentage difference in resistivity

Table 26: Percentage difference in resistivity (warm-up), comparing values on Appendix E and the recalculated resistivity, where only currents over $1x10^{-6}$A were considered.

| % difference in Resistivity (Ω・m) - warm up run | | | | | | |
|---|---|---|---|---|---|---|
| **temperature (K)** | **Hematite specular** | **Ilmenite** | **Magnetite** | **Magnetite lodestone** | **Pyrite** | **Serpentinite** |
| 10 | | | | | | |
| 20 | | | | 197.43 | -78.78 | |
| 30 | | | | 120.90 | -64.08 | |
| 40 | | | | 18.97 | -38.16 | |
| 50 | -82.63 | | | 11.90 | -19.32 | |
| 60 | -86.30 | | -40.35 | -2.37 | -8.16 | |
| 70 | -85.18 | | -54.04 | -7.25 | -2.66 | -48.93 |
| 80 | -80.66 | | -64.22 | -4.01 | -0.43 | -47.55 |
| 90 | -78.23 | 49.29 | -66.54 | -1.15 | 0.21 | -62.05 |
| 100 | -79.58 | 45.81 | -73.48 | -0.38 | 0.33 | -62.18 |
| 110 | -77.81 | 38.35 | -77.55 | -0.34 | 0.13 | -64.52 |
| 120 | -78.06 | 28.76 | -73.44 | -0.36 | -0.12 | -65.56 |
| 130 | -78.95 | 19.32 | -75.95 | -0.32 | -0.44 | -64.05 |
| 140 | -76.95 | 10.86 | -77.27 | -0.23 | -0.81 | -68.23 |
| 150 | -74.08 | 4.06 | -78.10 | -0.03 | -1.21 | -66.72 |
| 160 | -70.48 | -1.75 | -79.74 | 0.10 | -1.64 | -65.27 |
| 170 | -65.50 | -5.89 | -78.59 | 3.46 | -1.97 | -63.64 |
| 180 | -60.20 | -8.94 | -78.99 | 3.46 | -2.27 | -61.80 |
| 190 | -54.07 | -11.01 | -76.45 | 1.47 | -2.56 | -59.14 |
| 200 | -47.56 | -12.25 | -73.68 | 2.86 | -2.92 | -57.46 |
| 210 | -42.00 | -12.92 | -73.90 | -3.72 | -3.16 | -54.40 |
| 220 | -36.23 | -13.19 | -69.53 | -8.12 | -3.44 | -59.83 |
| 230 | -30.89 | -13.23 | -68.34 | -5.89 | -3.73 | -69.09 |
| 240 | -25.03 | -13.13 | -66.12 | -5.78 | -3.73 | -67.36 |
| 250 | -20.53 | -13.46 | -63.41 | -5.84 | -3.89 | -61.88 |
| 260 | -16.95 | -13.34 | -59.15 | -6.20 | -3.94 | -56.10 |
| 270 | -14.58 | -13.09 | -59.56 | -8.13 | -4.05 | -55.60 |
| 280 | -11.62 | -12.76 | -55.36 | -10.41 | -3.96 | -54.75 |
| 290 | -7.90 | -13.20 | -50.64 | -13.69 | -3.94 | -54.61 |
| 300 | -7.51 | -12.45 | -47.64 | 5.67 | -4.30 | -51.54 |

Table 27: Percentage difference in resistivity (cool-down), comparing values on Appendix E and the recalculated resistivity, where only currents over 1x10$^{-6}$A were considered.

| % difference in Resistivity (Ω · m) - cool down run | | | | | | |
|---|---|---|---|---|---|---|
| **temperature (K)** | **Hematite specular** | **Ilmenite** | **Magnetite** | **Magnetite lodestone** | **Pyrite** | **Serpentinite** |
| 10 | | | | | | |
| 20 | | | | 114.90 | -79.56 | |
| 30 | | | | 77.80 | -64.41 | |
| 40 | | | | 39.82 | -38.08 | |
| 50 | -79.52 | | | 18.66 | -19.08 | |
| 60 | -86.08 | | -37.08 | -1.49 | -7.87 | |
| 70 | -84.23 | | -37.24 | -6.72 | -2.47 | -40.38 |
| 80 | -79.65 | | -49.44 | -3.54 | -0.23 | -38.22 |
| 90 | -78.40 | 43.52 | -59.48 | -0.96 | 0.44 | -47.51 |
| 100 | -77.34 | 38.53 | -70.75 | -0.54 | 0.47 | -53.24 |
| 110 | -77.73 | 30.66 | -64.04 | -0.82 | 0.44 | -60.23 |
| 120 | -76.01 | 21.22 | -69.12 | -1.26 | 0.16 | -61.50 |
| 130 | -76.74 | 12.47 | -70.40 | -1.65 | -0.21 | -59.99 |
| 140 | -75.89 | 4.91 | -65.44 | -0.96 | -0.46 | -58.86 |
| 150 | -72.82 | -0.13 | -68.86 | -1.03 | -0.96 | -62.56 |
| 160 | -67.67 | -4.80 | -73.78 | -0.88 | -1.18 | -60.45 |
| 170 | -61.39 | -8.38 | -69.96 | -0.20 | -1.52 | -59.23 |
| 180 | -54.54 | -11.04 | -71.50 | -0.09 | -1.75 | -57.58 |
| 190 | -47.67 | -12.74 | -74.13 | -1.26 | -2.06 | -55.67 |
| 200 | -40.77 | -13.73 | -73.24 | -1.76 | -2.30 | -53.00 |
| 210 | -33.84 | -14.42 | -69.62 | -4.18 | -2.36 | -51.46 |
| 220 | -27.98 | -14.31 | -66.72 | -6.55 | -2.42 | -48.54 |
| 230 | -22.87 | -13.94 | -61.50 | -7.85 | -2.61 | -46.08 |
| 240 | -18.24 | -13.40 | -59.33 | -8.56 | -2.57 | -46.61 |
| 250 | -14.62 | -12.63 | -56.81 | -8.05 | -2.54 | -40.21 |
| 260 | -12.22 | -13.52 | -50.34 | -8.42 | -2.48 | -36.49 |
| 270 | -9.87 | -14.51 | -49.80 | -7.73 | -2.54 | -56.72 |
| 280 | -7.97 | -14.31 | -46.84 | -8.39 | -2.60 | -55.63 |
| 290 | -7.18 | -13.72 | -42.07 | -12.94 | -2.70 | -47.98 |
| 300 | -6.72 | -16.89 | -37.10 | 15.65 | -3.67 | -48.20 |

# Appendix G: Uncertainties

Table 28: Percentage error of resistance measurements

| RESISTANCE: % error range | | | | | | | | | |
|---|---|---|---|---|---|---|---|---|---|
| **Chalcopyrite** | **Galena** | **Graphite** | **Hematite** | **Ilmenite** | **Magnetite** | **Magnetite lodestone** | **Pyrite** | **Pyrrhotite** | **Serpentinite** |
| 0.06 - 55.17 | 0.07 - 0.22 | 0.07 - 7.72 | 0.06 - 55.81 | 0.07 - 0.09 | 0.06 - 55.26 | 0.06 - 55.17 | 0.06 - 55.88 | 0.07 - 56.92 | 0.06 - 56.92 |

Table 29: Percentage error of resistivity values

| RESISTIVITY: % error range | | | | | | | | | |
|---|---|---|---|---|---|---|---|---|---|
| **Chalcopyrite** | **Galena** | **Graphite** | **Hematite** | **Ilmenite** | **Magnetite** | **Magnetite lodestone** | **Pyrite** | **Pyrrhotite** | **Serpentinite** |
| 0.25 - 55.08 | 0.31 - 0.37 | 0.29 - 7.89 | 0.31 - 55.56 | 0.33 - 0.34 | 0.38 - 54.97 | 0.27 - 55.65 | 0.28 - 55.00 | 0.29 - 56.52 | 0.35 - 56.49 |